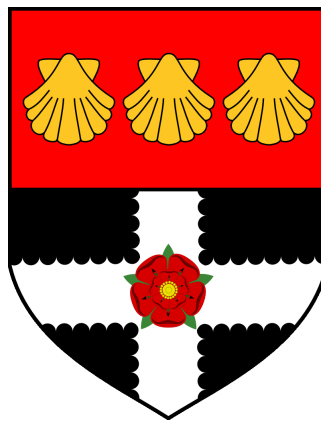


UNIVERSITY OF READING

Department of Meteorology



# Quasi-stationary Convective Systems in the UK

Robert A. Warren

A thesis submitted for the degree of Doctor of Philosophy

June 2014

# Declaration

I confirm that this is my own work and the use of all material from other sources has been properly and fully acknowledged.

---

Signature

---

Date

# Acknowledgements

First and foremost I want to thank my supervisors—Bob Plant, Dan Kirshbaum, and Humphrey Lean—for their support, guidance, advice, and praise over the course of my PhD. I am particularly grateful for the understanding they showed when I was really struggling during my second year, and for their efficiency in providing comments during the writing of this thesis. I also want to thank my monitoring committee, Ellie Highwood and John Methven, for helping to keep the project on track and providing me with a much-needed biannual confidence boost.

Several people provided invaluable assistance with the UM. Among them, I would in particular like to acknowledge Willie McGinty and Peter Clark for their help in respectively getting the UKV and idealised configurations up and running. I would also like to thank Peter for several very long but very interesting conversations regarding various aspects of atmospheric dynamics and numerical modelling. My work further benefited from exchanges with Sylvia Bohnenstengel, Stephen Burt, Emilie Carter, Terry Davies, Brian Golding, Nick Grahame, Carol Halliwell, Will Hand, Chris Holloway, Roy Ker-shaw, Giovanni Leoncini, Adrian Lock, Bruce Macpherson, Thorwald Stein, Dan Suri, Rob Thompson, Simon Vosper, Stu Webster, and Steve Willington. A mention must also go to Andy Heaps, ITmet, and the UM Helpdesk team for dealing with countless problems and queries.

I would like to extend thanks to my colleagues for creating such an enjoyable atmosphere to work in, and providing much-needed distractions in the form of pub visits, games, daft emails, and random conversations. Special mention must go to David McNamara, my neighbour for the entirety of the PhD, for always making me see that things could be worse, and the other members of the panto band—Caroline, Luke, Mark, Matt, Mike, Simon, and Wagner—for the many enjoyable practice sessions and performances. I am additionally grateful to my housemates and fellow PhDs—Angus, Hans, Ray, and Rob—for making our home such a fun place to be. Last but categorically not least, I want to thank my family and my wonderful girlfriend Laura for their love and support, without which I could not have made it through the last few years.

# Abstract

Quasi-stationary convective systems (QSCSs) are lines or clusters of convective cells in which the repeated development of new cells upstream of their predecessors results in near-zero system velocity. These storms can produce extreme precipitation accumulations in a matter of hours, leading in some cases to deadly flash flooding. Little is known about the frequency, regional distribution, environmental characteristics, and formation mechanisms of QSCSs in the UK. Here, this knowledge gap is addressed through a climatology, a case study, and idealised numerical simulations.

First, a five-year climatology of QSCSs in the UK is constructed using a combination of automated and manual analysis of radar imagery. A total of 88 events are identified, giving a mean frequency of 17.6 per year, with the vast majority taking place over land during summertime afternoons. Systems are observed to be more common in the vicinity of coastlines and prominent orography suggesting that these features often play a role in the repeated triggering of convection. A region which appears to be particularly favourable for these storms is the Southwest Peninsula of England. QSCSs are found to occur under a diverse range of synoptic patterns; however, on average their environments feature greater instability and weaker winds than those which typify summertime convective episodes in the UK.

Next, a case study of a QSCS over the Southwest Peninsula is undertaken. The system, which occurred on 21 July 2010, showed remarkable similarity to the flash flood-producing Boscastle storm of 16 August 2004, but did not produce extreme rainfall or flooding itself. This difference is linked to three factors: lower rain rates, a shorter period of stationarity, and distribution of the rainfall over more river catchments. Numerical simulations of the event reveal that, as in the Boscastle case, convection was repeatedly initiated by lifting along a quasi-stationary sea-breeze front (SBF). This feature is under-resolved with a grid length of 1.5 km (the shortest currently used for operational forecasting in the UK) leading to substantial errors in the simulated representation of the QSCS. Major improvements are obtained when the grid length is reduced to 500 m, highlighting the need for continuing increases in model resolution.

The final part of this work uses idealised simulations to investigate the mechanisms by which quasi-stationary SBFs may form over a peninsula. A simple west-to-east orientated strip of land is considered with prescribed vertical profiles of temperature and wind velocity, and a diurnally varying land surface heat flux. Three key mechanisms are identified, all of which likely contribute to the formation of QSCSs over the Southwest Peninsula. These are associated with (1) downstream advection of the north- and south-coast sea breezes in primarily along-peninsula flow, (2) collision of the north- and south-coast sea breezes, and (3) cancellation between a cross-peninsula ambient wind and the sea breeze on the downstream coast. For purely along-peninsula flow, the evolution of the SBFs can be accurately predicted using a simple scaling which relates the front velocity to the surface heat flux integrated along air-parcel trajectories.

# Contents

<b>1</b>	<b>Introduction</b>	<b>1</b>
1.1	Motivation . . . . .	1
1.2	Atmospheric convection . . . . .	2
1.2.1	Basic concepts . . . . .	2
1.2.2	Deep moist convection . . . . .	7
1.2.3	Organisation of DMC . . . . .	8
1.3	Quasi-stationary convective systems . . . . .	9
1.3.1	Definition and characteristics . . . . .	9
1.3.2	Role as flash-flood producers . . . . .	10
1.3.3	Formation of QSCSs . . . . .	10
1.4	Thesis aims and structure . . . . .	14
<b>2</b>	<b>Data and Models</b>	<b>16</b>
2.1	The UK 1 km radar composite product . . . . .	16
2.2	The Met Office Unified Model . . . . .	20
2.2.1	Dynamical core . . . . .	20
2.2.2	Parameterisation schemes . . . . .	22
2.3	Other data sources . . . . .	31
2.3.1	ERA-Interim . . . . .	31
2.3.2	UK rain gauges . . . . .	32
2.3.3	Atmospheric soundings . . . . .	32
<b>3</b>	<b>A climatology of QSCSs in the UK</b>	<b>33</b>
3.1	Introduction . . . . .	33
3.1.1	Background and motivation . . . . .	33
3.1.2	Chapter aims and structure . . . . .	34
3.2	The automatic identification, classification, and tracking of convective storms . . . . .	35
3.2.1	Data sources . . . . .	35
3.2.2	Identification . . . . .	36
3.2.3	Classification . . . . .	37
3.2.4	Tracking . . . . .	40
3.3	Data and methods . . . . .	41

3.4	A climatology of convective storms in the UK . . . . .	50
3.5	Classification of identified events . . . . .	56
3.6	A climatology of QSCSs in the UK . . . . .	63
3.6.1	Geospatial and temporal characteristics . . . . .	63
3.6.2	Environmental characteristics . . . . .	69
3.7	Summary, discussion, and conclusions . . . . .	78
<b>4</b>	<b>Case study of a QSCS over the UK Southwest Peninsula</b>	<b>81</b>
4.1	Introduction . . . . .	81
4.1.1	Background and motivation . . . . .	81
4.1.2	Chapter aims and structure . . . . .	82
4.2	Observational analysis . . . . .	83
4.2.1	Synoptic setting . . . . .	83
4.2.2	Storm evolution and rainfall accumulations . . . . .	85
4.2.3	Comparison with the Boscastle case . . . . .	87
4.3	Numerical model and experiment design . . . . .	91
4.3.1	The UKV model . . . . .	91
4.3.2	Simulation strategy . . . . .	93
4.4	Simulation results . . . . .	93
4.4.1	Control simulation . . . . .	93
4.4.2	Sensitivity tests . . . . .	99
4.4.3	500 m grid-length simulation . . . . .	104
4.4.4	Other runs . . . . .	109
4.5	Summary, discussion, and conclusions . . . . .	111
<b>5</b>	<b>Idealised simulations of peninsula sea breezes</b>	<b>114</b>
5.1	Introduction . . . . .	114
5.1.1	Background and motivation . . . . .	114
5.1.2	Chapter aims and structure . . . . .	115
5.2	The sea-breeze system . . . . .	116
5.2.1	Structure and life cycle . . . . .	116
5.2.2	External controls on sea-breeze evolution . . . . .	117
5.3	Numerical model and experiment design . . . . .	119
5.4	Simulation results . . . . .	124
5.4.1	No background flow . . . . .	124
5.4.2	Along-peninsula background flow . . . . .	127
5.4.3	Sea breeze scaling . . . . .	137
5.4.4	Cross-peninsula flow . . . . .	144
5.4.5	Other wind directions . . . . .	146
5.4.6	The role of coastline geometry . . . . .	147
5.5	Summary, discussion, and conclusions . . . . .	149

<b>6</b>	<b>Conclusions and future work</b>	<b>153</b>
6.1	Conclusions . . . . .	153
6.1.1	Characteristics of QSCSs in the UK . . . . .	153
6.1.2	Formation mechanisms of QSCSs in the UK . . . . .	155
6.1.3	Numerical representation of QSCSs in the UK . . . . .	156
6.2	Future work . . . . .	157
	<b>References</b>	<b>160</b>

# Chapter 1

## Introduction

### 1.1 Motivation

Flash floods represent one of the greatest natural hazards to human life. This is due both to their rapid onset, which leaves little time for dissemination of warnings by authorities and response by those in danger, and high flow velocities, which can carry large debris, destroy buildings and bridges, and trigger mudslides. In a global assessment of flood-related fatalities between 1975 and 2002, Jonkman (2005) found a mortality rate (number of people killed as a percentage of the number affected) for flash floods of 3.6 %. This significantly exceeds that for other types of freshwater flooding and is comparable to values for earthquakes and wind storms. Improving predictions of these events is thus of critical importance.

While there is no universal definition of flash flooding, the term is typically used to describe a rapid rise in stream levels occurring within a short period (minutes to hours) of a heavy rainfall event or following the failure of a natural or man-made obstruction in a watercourse such as a dam or ice jam (Davis 2001). The latter is itself often a consequence of intense precipitation (e.g. Hoxit *et al.* 1978). Thus, most flash flood events result either directly or indirectly from excessive rainfall. However, the role of hydrological factors must not be underestimated. Whether or not a given amount of rain leads to flash flooding depends on its distribution within a watershed and the physical characteristics of that watershed. The latter includes factors such as the slope and cross-sectional area of the stream channel, the infiltration capacity and saturation content of the soil, and vegetation cover/land use (Davis 2001).

Doswell *et al.* (1996) drew attention to the “absurdly simple” concept that the greatest rainfall totals occur where the rainfall rate is highest for the longest period of time<sup>1</sup>. This may be expressed mathematically as

$$P = \bar{R}D \tag{1.1}$$

where  $P$  is the total precipitation at some location,  $\bar{R}$  is the mean rain rate, and  $D$  is the

---

<sup>1</sup>This statement is sometimes referred to as the First Law of Quantitative Precipitation Forecasting.

rainfall duration. One way in which large rainfall totals may occur is when convective storms (typically associated with high  $\bar{R}$ ) repeatedly move across the same area (giving relatively large  $D$ )<sup>2</sup>. This process is known as *echo training*, in reference to the storm system's appearance in radar imagery, with successive echoes traversing the same path like train carriages on a track. Echo training may result when a linearly organised convective system moves approximately parallel to its major axis. In this case, the rainfall duration is limited by the length of the system along its direction of travel. However, if new convective cells develop upstream then  $D$  may be greatly increased. When the formation and assimilation of new cells into the system approximately cancels the downstream movement and decay of old cells, the system velocity approaches zero. The result is a *quasi-stationary convective system* (QSCS; Chappell 1986).

Previous studies have demonstrated that QSCSs are a dominant mode of convective organisation giving rise to precipitation extremes and flash flooding (Section 1.3.2), and have highlighted a variety of mechanisms by which these systems may form (Section 1.3.3). However, the vast majority of this work has been concerned with events in either the USA or countries bordering the Mediterranean Sea. Only a handful of studies have looked at QSCSs in the UK. This partly reflects the comparatively low frequency of rainfall extremes in the UK, itself a consequence of the country's high latitude location and maritime climate which make conditions generally less favourable for very high convective rain rates. Nevertheless, QSCSs do occur in the UK and can lead to devastating flash flooding, as evidenced by the Boscastle storm of 16 August 2004 (Golding *et al.* 2005). In order to improve forecasts of these hazards, it is desirable to gain a better understanding of where, when, and how QSCSs form in the UK. This is the purpose of the present study.

The next section introduces some meteorological concepts relevant to the formation and organisation of atmospheric moist convection (Section 1.2). Following this, existing studies of QSCSs are reviewed, with particular focus on the mechanisms by which these systems may develop (Section 1.3). The final part of this chapter sets out the aims and structure of the rest of the thesis (Section 1.4).

## 1.2 Atmospheric convection

### 1.2.1 Basic concepts

#### Buoyancy

In meteorology, the term 'convection' is used to describe vertical motions associated with an imbalance of forces. Neglecting viscous effects and the Coriolis force, the vertical momentum equation is

---

<sup>2</sup>Extreme rainfall and flash flooding may also be caused by so-called 'high-precipitation' supercell storms (e.g. Smith *et al.* 2001), orographic enhancement of stratiform precipitation (e.g. Sibley 2010), and land-falling tropical cyclones (e.g. Atallah and Bosart 2003) .

$$\frac{dw}{dt} = -\frac{1}{\rho} \frac{\partial p}{\partial z} - g \quad (1.2)$$

where  $w$  is the vertical velocity,  $\rho$  is density,  $p$  is pressure, and  $g$  is the acceleration due to gravity. By defining a horizontally homogeneous base state  $\bar{\rho}(z)$ ,  $\bar{p}(z)$ , where  $\rho = \bar{\rho} + \rho'$  and  $p = \bar{p} + p'$ , which is in hydrostatic balance ( $\frac{\partial \bar{p}}{\partial z} = \bar{\rho}g$ ), we may rewrite Equation 1.2 as

$$\frac{dw}{dt} = -\frac{1}{\rho} \frac{\partial p'}{\partial z} - \frac{\rho'}{\rho} g \quad (1.3)$$

The two terms on the right-hand side of this equation are the vertical perturbation pressure gradient acceleration and the buoyancy acceleration. These are the drivers of atmospheric convection. Thermally direct circulations driven by buoyancy are referred to as *free convection*. On the other hand, *forced convection* is associated with large vertical perturbation pressure gradients.

Applying the anelastic approximation,  $\rho$  in Equation 1.3 is replaced with  $\bar{\rho}$  (alternatively, when applying the Boussinesq approximation,  $\rho$  is replaced with  $\rho_0 = \text{constant}$ ). Then, using the equation of state for moist air ( $p = \rho R_d T_v$ , where  $R_d$  is the specific gas constant for dry air and  $T_v$  is the virtual temperature), which is assumed to hold for the base state ( $\bar{p} = \bar{\rho} R_d \bar{T}_v$ ), and neglecting products of perturbation terms, the buoyancy acceleration may be expressed as

$$B = -\frac{\rho'}{\bar{\rho}} g \approx \left( \frac{T'_v}{\bar{T}_v} - \frac{p'}{\bar{p}} \right) g \quad (1.4)$$

The virtual temperature is given by

$$T_v = T \frac{1 + m_v/\varepsilon}{1 + m_v} \quad (1.5)$$

where  $T$  is the absolute temperature,  $m_v$  is the mixing ratio of water vapour (the ratio of the mass of vapour to the mass of dry air),  $\varepsilon = R_d/R_v$ , and  $R_v$  is the specific gas constant for water vapour. When hydrometeors are present and falling at their terminal velocity, they contribute a downward acceleration equal to  $m_h g$ , where  $m_h$  is the hydrometeor mixing ratio. Including this *hydrometeor loading*, the buoyancy is then

$$B = \left( \frac{T'_v}{\bar{T}_v} - \frac{p'}{\bar{p}} - m_h \right) g \quad (1.6)$$

The pressure perturbation term may be safely neglected for atmospheric convection (e.g. Emanuel 1994, p7). Thus, buoyancy increases with increasing (virtual) temperature perturbations but decreases with increasing hydrometeor loading.

### Parcel theory and its limitations

To understand the development of a convective cloud we consider a moist but unsaturated parcel of air lifted from the surface ( $z = 0$ ). We will neglect pressure perturbations

and the effects of hydrometeor loading, and assume that air is not exchanged between the parcel and the surrounding environment. These are the fundamental assumptions of *parcel theory*. If we further neglect the contribution of water vapour to the buoyancy, we may rewrite Equation 1.6 as

$$B = \frac{T_p - T_e}{T_e} g \quad (1.7)$$

where the subscripts ‘p’ and ‘e’ indicate values for the parcel and environment respectively. Thus, the parcel has positive buoyancy and will accelerate upward if it is warmer than the environment ( $T_p > T_e$ ) and has negative buoyancy and will accelerate downward if it is cooler than the environment ( $T_p < T_e$ ). If  $T_p = T_e$  the parcel is neutrally buoyant and will experience no net acceleration.

As the parcel is lifted from the surface, it cools due to adiabatic expansion at the *dry adiabatic lapse rate*

$$\Gamma_d \equiv -\frac{dT}{dz} = \frac{g}{c_{pd}} \quad (1.8)$$

where  $c_{pd}$  is the specific heat of dry air at constant pressure. By the Clausius–Clapeyron equation (e.g. Emanuel 1994, p116), this causes a reduction in the saturation water vapour mixing ratio  $m_v^*$ . The parcel mixing ratio meanwhile is conserved (since no water vapour enters or exits the parcel) resulting in an increase in its relative humidity  $\mathcal{H} = m_v/m_v^*$ . Eventually the parcel becomes saturated ( $\mathcal{H} = 100\%$ ) leading to condensation and cloud formation. The height at which this occurs is known as the *lifting condensation level* (LCL).

If the parcel continues to rise, the decrease in temperature associated with adiabatic expansion is partly compensated for by the release of latent heat during condensation. If all condensate remains within the parcel then the rate of cooling is given by the *reversible moist adiabatic lapse rate*

$$\Gamma_{rm} = \frac{1}{c_{pd} + c_{pl}m_t} \left[ g + \frac{\partial}{\partial z} (L_v m_v) \right] \quad (1.9)$$

where  $m_t = m_v + m_h$ ,  $c_{pl}$  is the specific heat of liquid water at constant pressure, and  $L_v$  is the latent heat of vapourisation. If on the other hand condensate is instantly removed from the parcel then it will cool at the *pseudoadiabatic lapse rate*

$$\Gamma_{ps} = \frac{1}{c_{pd} + c_{pl}m_v} \left[ g + \frac{\partial}{\partial z} (L_v m_v) \right] \quad (1.10)$$

Note that Equations 1.9 and 1.10 both neglect the effects of freezing of liquid water and sublimation of water vapour.

If at some height the parcel becomes warmer than its environment, it will begin to accelerate upwards due to buoyancy. This height is therefore known as the *level of free convection* (LFC). The parcel will then continue to rise until it reaches its *level of neutral buoyancy* (LNB) beyond which  $T_p < T_e$ . The kinetic energy that the parcel gains as it rises from its LFC to LNB is given by the integral of the buoyancy over this

depth; this quantity is called the convective available potential energy (CAPE):

$$\text{CAPE} = \int_{\text{LFC}}^{\text{LNB}} B dz \approx g \int_{\text{LFC}}^{\text{LNB}} \frac{T_p - T_e}{T_e} dz \quad (1.11)$$

It is easily shown that the maximum vertical velocity  $w_{\text{max}}$  is related to CAPE via the following expression

$$w_{\text{max}} = (2 \text{CAPE})^{\frac{1}{2}} \quad (1.12)$$

The total negative buoyancy that the parcel must overcome in order to reach the LFC is given by the convective inhibition CIN:

$$\text{CIN} = - \int_0^{\text{LFC}} B dz \approx -g \int_0^{\text{LFC}} \frac{T_p - T_e}{T_e} dz \quad (1.13)$$

Note that it is more accurate to compute CAPE and CIN using the virtual temperature (Doswell and Rasmussen 1994). Furthermore, the parcel need not start its ascent at the surface; the initial parcel conditions ( $p, T, m_v$ ) may be taken at any level and may additionally be averaged over a layer (e.g. 0–500 m).

It is important to realise that real convection differs from that described by parcel theory in a number of important ways. First, pressure perturbations are not negligible: a rising parcel of air is usually accompanied by positive  $p'$  above it and negative  $p'$  below it, giving a downward-directed perturbation pressure gradient acceleration which partly offsets the upward acceleration due to buoyancy. Second, *entrainment* of environmental air into a rising parcel (e.g. de Rooy *et al.* 2013) typically acts to reduce buoyancy, both directly through the incorporation of air with lower  $T_v$  and indirectly through evaporative cooling. The presence of hydrometeors also decreases  $B$  as previously discussed (Equation 1.6). Finally, compensating subsidence in the environment can modify both the buoyancy and perturbation pressure gradients thereby altering the net acceleration.

### Conserved variables

It is useful to define temperature variables which are conserved during the above-mentioned parcel processes. For unsaturated adiabatic ascent/descent, the potential temperature  $\theta$  is conserved. This is the temperature achieved by an air parcel when moved dry adiabatically to a reference pressure  $p_0 = 1000$  hPa. It is given by

$$\theta = T \left( \frac{p_0}{p_d} \right)^{R_d(1+m_v/\epsilon)/(c_{pd}+c_{pv}m_v)} \quad (1.14)$$

where  $p_d$  is the pressure of dry air and  $c_{pv}$  is specific heat of water vapour at constant pressure. Note that the dependence on  $m_v$  is typically neglected so that the exponent becomes simply  $R_d/c_{pd}$ . Another variable which is (very nearly) conserved for unsaturated adiabatic motions is the virtual potential temperature:

$$\theta_v = T_v \left( \frac{p_0}{p_d} \right)^{R_d/c_{pd}} \quad (1.15)$$

For saturated adiabatic ascent/descent,  $\theta$  and  $\theta_v$  are no longer conserved; however, in the absence of freezing, the equivalent potential temperature  $\theta_e$  is. This is the potential temperature that an air parcel would obtain if all its water vapour were to condense in an adiabatic process. It may be calculated as (Emanuel 1994, p120)

$$\theta_e = T \left( \frac{p_0}{p_d} \right)^{R_d/(c_{pd}+c_{pl}m_t)} \mathcal{H}^{-m_v R_v/(c_{pd}+c_{pl}m_t)} \exp \left[ \frac{L_v m_v}{(c_{pd} + c_{pl}m_t) T} \right] \quad (1.16)$$

Technically,  $\theta_e$  is only conserved for reversible moist adiabatic ascent/descent. In the pseudoadiabatic case, the appropriate variable is  $\theta_{ep}$  the pseudoequivalent potential temperature<sup>3</sup> (see Bolton 1980). However, for practical purposes the difference between  $\theta_e$  and  $\theta_{ep}$  is small and may be neglected. Henceforth, only  $\theta_e$  will be used. Similarly, the difference between  $\Gamma_{rm}$  and  $\Gamma_{ps}$  will be ignored and the generic symbol  $\Gamma_m$  will be used.

### Static stability

The behaviour of a parcel of air when it is displaced vertically depends on the *static stability* of the environment. This in turn is a function of the local environmental lapse rate  $\gamma \equiv \frac{\partial T}{\partial z}$ . If  $\gamma > \Gamma_d$ , buoyancy will act to accelerate the displaced parcel away from its initial position, irrespective of whether or not it is saturated. In this case, the lapse rate is said to be *absolutely unstable*. If on the other hand  $\gamma < \Gamma_m$ , the lapse rate is *absolutely stable* and buoyancy will act to return the parcel to its initial position. In fact, due to momentum conservation, the parcel overshoots this level and undergoes an oscillation of frequency  $N$ , the Brunt–Väisälä frequency. In an unsaturated environment, this is given by

$$N^2 = \frac{g}{\theta_v} \frac{\partial \theta_v}{\partial z} \quad (1.17)$$

while for a saturated environment we define a moist Brunt–Väisälä frequency  $N_m$  as (e.g. Markowski and Richardson 2010, p42)

$$N_m^2 = \frac{1}{1 + m_t} \left\{ \Gamma_m \frac{\partial}{\partial z} [(c_{pd} + c_{pl}m_t) \ln \theta_e] - (c_{pl}\Gamma_m \ln T + g) \frac{\partial m_t}{\partial z} \right\} \quad (1.18)$$

If  $\Gamma_m < \gamma < \Gamma_d$  the lapse rate is described as being *conditionally unstable*, since it is stable for unsaturated displacements but unstable for saturated displacements. The

<sup>3</sup>The pseudoequivalent potential temperature is related to the wet-bulb potential temperature  $\theta_w$  which is the potential temperature achieved by a parcel following saturated adiabatic ascent/descent to  $p_0$ . Typically, saturated adiabats (lines of constant  $\theta_{ep}$ ) on a tephigram are labelled with their  $\theta_w$  value.

lapse rate is said to be *neutral* when  $\gamma = \Gamma_d$  and *moist-neutral* when  $\gamma = \Gamma_m$ . Finally, when the environment is saturated and  $\gamma > \Gamma_m$  the lapse rate is *moist absolutely unstable* (Bryan and Fritsch 2000).

Note that these definitions refer to static stability with respect to infinitesimal parcel displacements. However, to assess the potential for free convection we consider finite displacements; i.e. the behaviour of a parcel of air lifted to its LFC. Beyond this, the parcel will continue to accelerate as long as  $B > 0$ , irrespective of the local value of  $\gamma$ .

### 1.2.2 Deep moist convection

Atmospheric moist convection (i.e. that which is accompanied by condensation and cloud formation) is broadly defined by its vertical extent. By *deep moist convection* (DMC) we typically mean that which spans a significant fraction of the depth of the troposphere, as opposed to *shallow* (moist) convection which is almost entirely contained within the atmospheric boundary layer. An alternative common definition of DMC is convection which is of sufficient depth to produce precipitation.

A necessary but not sufficient condition for DMC is the presence of CAPE in the environment. This requires two ingredients: a conditionally unstable lapse rate in the mid-troposphere, and sufficiently warm, moist air near the surface. As discussed by Doswell (1987), the former is typically supplied by synoptic-scale circulations while both large-scale advection and local surface fluxes contribute to the latter<sup>4</sup>. The third ingredient for DMC is a mechanism to lift parcels of air to their LFC (and, in doing so, overcome any CIN in the environment) so that convection can be initiated. This is typically associated with processes occurring at the mesoscale or storm-scale. Convective initiation (CI) is particularly favoured along low-level zones of horizontal wind convergence, such as fronts, drylines, and convective outflow boundaries. As well as allowing parcels to reach their LFC, the associated lifting acts to deepen the boundary layer which reduces CIN and the stabilising effects of entrainment. Other initiation mechanisms include forced orographic ascent, gravity waves, isentropic upglide, and ageostrophic circulations associated with upper-level jet streaks. Large-scale ascent associated with quasi-geostrophic processes (warm air advection, differential vorticity advection) can also contribute to CI both directly and through the erosion of CIN.

The life cycle of an individual deep convective cell was conceptualised by Byers and Braham (1948) as consisting of three main stages. During the initial “cumulus” stage, the cloud grows vertically and is characterised by a single *updraught* with compensating subsidence in the surrounding environment. Within the updraught, cloud drops and ice crystals grow at the expense of water vapour, eventually becoming large enough to fall out. This marks the onset of the “mature” stage. Hydrometeor loading, evaporation of rain, and melting/sublimation of snow, graupel, and hail (if present) result in a reduction in buoyancy eventually inducing a *downdraught*. This descends through the

<sup>4</sup>Note that in the case of *elevated* convection, the supply of warm, moist air comes from above the boundary layer and is thus not influenced by local surface fluxes

storm and, upon reaching the surface, spreads out laterally as a density current. The leading edge of this current is called the *convective outflow boundary* or *gust front* and is characterised by convergence and ascent which may initiate new convection. In the final “dissipating” stage, the advancing cold current cuts off the supply of warm, moist air to the storm resulting in the collapse of the updraught. As the remaining precipitation falls out, the downdraught too diminishes. Entrainment causes the lower portion of the cloud to gradually evaporate, while at upper levels the *anvil* (formed by divergence at the cloud top) may persist due to the low saturation mixing ratios at high altitudes. This entire process typically takes between 30 minutes and 1 hour.

### 1.2.3 Organisation of DMC

The above description pertains to *ordinary single cell* convection; however, this is just one of several possible *modes* of convective organisation. The mode that a developing storm adopts depends on a number of environmental factors including the CAPE (Kirkpatrick *et al.* 2011), LCL and LFC heights (McCaul and Cohen 2002), and mid-level relative humidity (James and Markowski 2010). However, of most importance is the *vertical wind shear* (VWS; Weisman and Klemp 1982). An increase in VWS has a number of important effects on a convective storm. First, it reduces the tendency for precipitation to fall through the updraught, thereby reducing the detrimental effects of hydrometeor loading and evaporative cooling on updraught buoyancy. It also increases the low-level storm relative flow which prevents the outflow from undercutting the updraught. This can additionally enhance convergence at the gust front, increasing the likelihood of new initiation there. Finally, strong VWS leads to the formation of vertical pressure gradients within the storm which can enhance updraught intensity and influence storm propagation.

Ordinary single-cell convection occurs in environments with weak VWS. As described above, it tends to be short lived due to the destructive effects of the precipitation on the updraught. Lifting at the gust front is relatively weak and does not initiate new cells in any organised manner. Cells typically move with the velocity of the environmental wind averaged over the cloud-bearing layer.

With intermediate shear, (ordinary) *multicell* convection can occur. In this case, the gust front repeatedly triggers new cell development, usually on a preferred flank of the storm, resulting in an organised *convective system* whose lifetime can significantly exceed that of the component cells. The movement of such a system consists of two distinct components: the *advection* of cells by the cloud layer-mean wind and *propagation* associated with the development of new cells. As will be discussed in the next section, quasi-stationary systems result when advection and propagation approximately cancel. Multicell storms can take on a wide variety of structures depending on the shear profile and other environmental factors (mainly CAPE), ranging from small-scale clusters consisting of just a handful of cells to expansive nearly unbroken lines of convection which can extend over hundreds of kilometres. The latter are referred to as *mesoscale*

*convective systems* (MCSs; e.g. Houze 2004). It is important to note that while the traditional description of multicell storms involves *self-organisation* via repeated initiation at the gust front, the same basic structures can be generated by external forcing mechanisms (e.g. lifting along a convergence line).

In environments with strong VWS, *supercell* convection can occur. This is characterised by a rotating updraught (mesocyclone), which is formed via the tilting and subsequent stretching of low-level horizontal vorticity associated with the wind shear. Unlikely ordinary convective cells in which updraughts are driven primarily by buoyancy, supercells are driven by both buoyancy and strong vertical perturbation pressure gradients. The latter develop both as a direct response to the updraught's rotation (nonlinear dynamic forcing) and via interactions between the updraught and VWS (linear dynamic forcing). The resulting vertical accelerations significantly enhance the low-level updraught and cause the storm motion to deviate from the cloud layer-mean wind. Due to their unique structure, supercells can remain in a quasi-steady state for many hours, during which time they may produce severe weather including large hail and tornadoes. For further information on these storms and their associated hazards, the reader is directed to Markowski and Richardson (2010).

## 1.3 Quasi-stationary convective systems

### 1.3.1 Definition and characteristics

As discussed in the Section 1.2.3, the motion of a multicellular convective system consists of two components: advection and propagation. When the propagation component acts in opposition to advection (i.e. new cells develop upstream of their predecessors) the system is said to be *back-building* (Bluestein and Jain 1985). A quasi-stationary system results when the two components almost exactly cancel so that the system velocity becomes very small; QSCSs may thus be thought of as a specific type of back-building multicell system. An alternative view of QSCSs is as systems in which the initiation of new cells occurs repeatedly in approximately the same geographical location. This is arguably a better definition since it emphasises the stationary aspect of the formation process. When CI is clearly tied to some surface topographical feature (e.g. a mountain), the system may be described as being *anchored* to that feature.

In radar imagery, the archetypal QSCS appears as a nearly unbroken line with embedded reflectivity/rain-rate maxima coincident with the cores of the component cells (shown schematically in Figure 1.1). New cells form at one end of the line and then move along it, decaying at the opposite end. The rainfall accumulation pattern thus also takes the form of a line, often with sharp gradients on either side. However, in reality, QSCSs show a great deal of variety in their structure, from small-scale clusters with little linear organisation (e.g. Schumacher and Johnson 2005, their Figure 10) to large MCSs containing multiple back-building elements (e.g. Luo *et al.* 2014, their Figure 3).

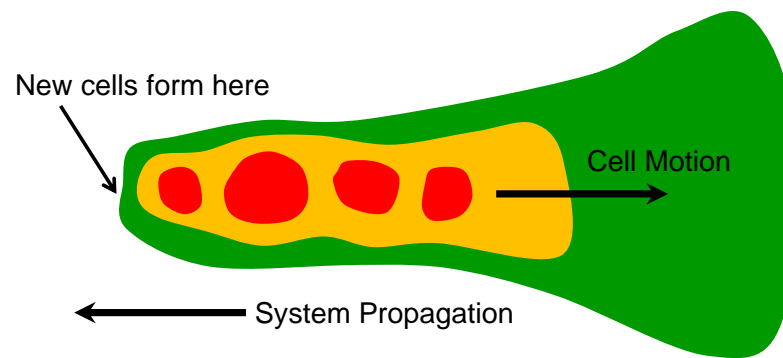


**Figure 1.1** Schematic diagram of the radar-observed structure an archetypal QSCS. Green, yellow, and red shading respectively indicate areas of low, moderate, and high reflectivity/rain rates. Adapted from Schumacher and Johnson (2005).

### 1.3.2 Role as flash-flood producers

The ability of QSCSs to produce extreme rainfall and flash flooding has been demonstrated in a large number of past studies. Table 1.1 provides a list of major flash flood events which have been attributed to these systems in the literature. Many other case studies have examined QSCSs which produced excessive rainfall that did not lead to serious flooding (e.g. Miller 1978; Seko *et al.* 1999; Kato and Goda 2001; Sun and Lee 2002; Lyman *et al.* 2005; Mayes and Winterton 2008; Sibley 2009; Mastrangelo *et al.* 2011; Zhang and Zhang 2012; Luo *et al.* 2014). Several climatologies of heavy precipitation events and flash floods have also highlighted QSCSs as a dominant mode of convective organisation giving rise to these extremes. In a widely cited study of flash floods over the conterminous United States during the period 1973–79, Maddox *et al.* (1979) noted that a characteristic common to many events was “convective storms and/or cells [which] repeatedly formed and moved over the same area”. More recently, Schumacher and Johnson (2005) examined 116 extreme rainfall events (those exceeding the 50 year recurrence interval amount for a location) in the area east of the Rocky Mountains (excluding Florida) between 1999 and 2001. They found that around two-thirds of these were caused by MCSs, of which 20% could be classified as “back-building/quasi-stationary (BB) systems”. An extended climatology for the period 1999–2003 showed that BB systems typically produced the highest 24 h rainfall accumulations of all MCSs and that the vast majority (92%) resulted in flash flooding (Schumacher and Johnson 2006).

### 1.3.3 Formation of QSCSs

In order for a QSCS to occur, local conditions must remain conducive to the development of deep convection for an extended period of time (several hours or longer). Thus there must be a continuous supply of CAPE (warm, moist air at low levels and conditionally unstable lapse rates aloft) and a persistent mechanism to lift air parcels to their LFC. Furthermore, for cells to repeatedly train over the same area, the wind

**Table 1.1** Examples of major flash floods which have been attributed to QSCSs in the literature.

Location	Date	Rainfall	Fatalities	Reference
Boscastle, SW England	16 August 2004	181 mm in 4h	0	Golding <i>et al.</i> (2005)
Vaison-La-Romaine, S France	22 September 1992	220 mm in 3h	35	Sénési <i>et al.</i> (1996)
Aude, S France	12–13 November 1999	485 mm in 18h	36	Ducrocq <i>et al.</i> (2008)
Gard, S France	8–9 September 2002	610 mm in 24h	25	Ducrocq <i>et al.</i> (2008)
Valencia, NE Spain	20 October 1982	>400 mm in 12h	40*	Romero <i>et al.</i> (2000)
Valencia, NE Spain	3–4 November 1987	>1000 mm in 36h	16*	Romero <i>et al.</i> (2000)
Catalonia, NE Spain	9–10 June 2000	223 mm in 24h	5	Martín <i>et al.</i> (2007)
Apulia, SE Italy	22 October 2005	160 mm in 6h	6	Miglietta and Regano (2008)
Železniki, W Slovenia	18 September 2007	303 mm in 24h	6	Rusjan <i>et al.</i> (2009)
Black Hills, South Dakota, USA	9 June 1972	380 mm in 6h	237	Maddox <i>et al.</i> (1978)
Big Thompson Canyon, Colorado, USA	31 July 1976	>300 mm in 4h	139	Maddox <i>et al.</i> (1978)
Johnstown, Pennsylvania, USA	19–20 July 1977	300 mm in 9h	77	Hoxit <i>et al.</i> (1978)
Minneapolis, Minnesota, USA	23 July 1987	254 mm in 24h	2	Schwartz <i>et al.</i> (1990)
Madison County, Virginia, USA	27 June 1995	>600 mm in 8h	3	Pontrelli <i>et al.</i> (1999)
Fort Collins, Colorado, USA	28 July 1997	135 mm in 6h	5	Petersen <i>et al.</i> (1999)
St. Louis, Missouri, USA	6–7 May 2000	>300 mm in 9h	2	Schumacher and Johnson (2008)
Nashville, Tennessee, USA	1–2 May 2010	345 mm 48h	11	Moore <i>et al.</i> (2012)
Dapto, New South Wales, Australia	18 February 1984	803 mm in 48h	0	Shepherd and Colquhoun (1985)
Korean Peninsula	26–27 July 1996	250 mm in 24h	86	Kim and Lee (2006)

\* Figures obtained from Barredo (2007).

direction should remain approximately constant during the lifetime of the system. Unsurprisingly, the most long-lived QSCSs (and largest associated rainfall totals) occur in very slowly evolving synoptic environments (e.g. Nuissier *et al.* 2008). As previously discussed, CAPE is usually supplied by the synoptic-scale circulation (although it may be augmented by local processes), while initiation mechanisms typically operate at the mesoscale or storm-scale. However, often the synoptic pattern determines what initiation mechanisms may operate. An obvious example is orographic triggering of convection which depends on the large-scale wind velocity and stability (see below). In such situations, the large and small scales are inextricably linked via the process of convective initiation. With this in mind, the following discussion of QSCS formation focuses on the processes by which cells may be repeatedly triggered in the same location and, where appropriate, links this to the large-scale flow.

Since the topography of the Earth's surface is fixed, lifting mechanisms associated with it can persist for as long as the evolution of the background flow allows. The most obvious CI process tied to topography is direct (mechanical) lifting of air moving along a sloped surface. Low-level flow impinging on a orographic barrier will tend to go over rather than around it if the Froude number  $Fr = U/Nh$  (where  $U$  is the cross-barrier wind speed and  $h$  is the mountain height) is greater than one. Assuming this condition is met and the barrier is sufficiently high for ascending air parcels to reach their LFC, convection can be triggered. If the flow remains steady, then a QSCS may develop. Systems formed via this mechanism are frequently the cause of flash floods in mountainous areas around the Mediterranean Sea, particularly during the Autumn when high sea-surface temperatures ensure a copious supply of warm, moist boundary layer air (e.g. Miglietta and Regano 2008, Pastor *et al.* 2010). Several major flash floods in the USA have also been shown to be associated with orographically forced QSCSs (Maddox *et al.* 1978; Petersen *et al.* 1999; Pontrelli *et al.* 1999). Two large-scale features are common to events in both locations: a low-level jet orientated approximately perpendicular to the triggering orography, and an approaching short-wave trough aloft (Lin *et al.* 2001). The former supplies potentially buoyant air to the storm, the latter reduces CIN via induced ascent, and both act to increase  $Fr$  (respectively, by increasing  $U$  and decreasing  $N$ ).

Orography can also trigger convection indirectly via its effects on the low-level wind field. For example, when air impinging on a mountain range is blocked it may be deflected, generating regions of convergence which provide a lifting mechanism. This process contributed to a extreme rain-producing QSCS on the island of Maui on 29 October 2000 (Lyman *et al.* 2005). Another indirect orographic triggering mechanism is elevated heating. This drives solenoidal circulations with upslope flow and convergence near the mountain peak (e.g. Banta 1990). Soderholm *et al.* (2014) showed that low-level flow directed along a mountain ridge is favourable to the formation of quasi-stationary storms (particularly when coupled with weak upper-level winds) because it prevents convective outflow from disrupting the thermally driven convergence. While this mechanism was shown to be important in producing heavy rainfall over the Black

Hills in South Dakota, USA, it has not, to my knowledge, been implicated in any flash flood events. However, other topographically generated thermal circulations have been. Specifically, Golding *et al.* (2005) showed that the ‘Boscastle’ storm, which caused severe flooding in southwest England on 16 August 2004, was initiated and maintained by convergence along a sea-breeze front<sup>5</sup>.

Quasi-stationary systems can also be triggered by processes not related to surface topography. One example is slow-moving or stationary synoptic fronts. In the USA, elevated convection occurring on the north (cold) side of an east–west orientated stationary front is frequently responsible for generating heavy rainfall. Moore *et al.* (2003) showed that in this situation, CI occurs when a strong low-level jet undergoes isentropic upglide along the sloping frontal surface, with subsequent echo training driven by cloud-layer winds aligned along the front. The same basic process has also been observed in association with cold domes left by previous convective activity (Zhang and Zhang 2012; Luo *et al.* 2014). It is important to note, however, that these systems do not necessarily feature a stationary initiation location and thus are not always QSCSs. As discussed by Junker *et al.* (1999), backwards propagation only occurs if the strongest low-level moisture flux convergence and instability remain near the western (upshear) end of the MCS. Non-stationary systems of this type featuring an adjoining region of stratiform precipitation were classed as “training line, adjoining stratiform (TL/AS)” MCSs by Schumacher and Johnson (2005). These were found to account for over 30 % of extreme rain-producing MCSs in the eastern US between 1999 and 2001.

All of the mechanisms discussed so far are associated with processes external to the resulting QSCS; however, in some cases back-building can be driven by internal processes. For example, where outflow produced by the storm acts in opposition to the background low-level flow, a stationary convergence zone can be generated along which cells may be repeatedly triggered. This was the mechanism by which the flash flood-producing storms in London, UK on 14 August 1975 (Miller 1978) and Johnstown, Pennsylvania, USA on 19–20 July 1975 (Hoxit *et al.* 1978) were maintained. In southern France, blocking of convective outflow by the Massif Central can lead to the development of QSCSs well upstream (to the south) of this mountain range; such was the case in Gard flash flood of 8–9 September 2002 (Ducrocq *et al.* 2008). Using idealised numerical simulations, Bresson *et al.* (2012) showed this configuration is favoured under weak flow which allows sufficient time for strong downdraughts to develop before cells reach the mountain slopes.

A less obvious internal mechanism for QSCS formation was identified by Schumacher and Johnson (2008) and investigated in detail by Schumacher (2009). This involves a series of convectively generated low-level gravity waves which trigger elevated CI in an isentropically ascending airstream near a mesoscale convective vortex. In the

---

<sup>5</sup>Via a similar mechanism, land breezes can lead to the formation of persistent convective cloud bands over and downwind of large lakes during cold-air outbreaks (e.g. Passarelli and Braham 1981; Steenburgh and Onton 2001). These cloud bands are technically a type of QSCS; however, they are typically quite shallow and produce snow rather than rain so are not associated with flash flooding.

cases examined, these waves were prevented from propagating away from the convective system by strong opposing flow and amplified by a reversal in the VWS profile.

Internal processes may also act to enhance externally forced QSCSs. For example, in an orographically triggered QSCS which caused catastrophic flooding in the Valencia region of Spain on 3–4 October 1987, a mesoscale area of low-pressure developing in response to latent heating in the system was found to strengthen the low-level inflow and moisture flux convergence thereby significantly increasing the precipitation totals (Romero *et al.* (2000)).

## 1.4 Thesis aims and structure

It is clear from the preceding discussion that, in recent decades, a great deal has been learnt about the mechanisms by which convective systems can become quasi-stationary and thereby produce extreme precipitation and flash flooding. However, the majority of existing research in this area has been based around events which occurred either in the United States or in Southern Europe (in particular, France, Spain, and Italy). Only a handful of studies have examined QSCSs in the UK and, of these, only two have investigated the physical processes in any detail (Miller 1978; Golding *et al.* 2005). Consequently, little is known about the frequency and regional distribution of these storms, and the mechanisms by which they commonly form. It is likely that QSCSs in the UK differ from those in the USA and Southern Europe where conditions are on average far more conducive to the formation of organised deep convection. Differences in both climate and topography will also significantly impact the external processes which can lead to repeated storm initiation in the same location. Research is thus needed into the climatology and formation mechanisms of QSCSs in the UK. It is also highly desirable to determine the predictability of these events and the ability of modern numerical weather prediction (NWP) models to simulate their initiation, organisation, and longevity.

With these considerations in mind, the following key questions were identified and used to guide the design of the present study:

1. How common are QSCSs in the UK and how does their occurrence vary geographically, seasonally, diurnally, and with the large-scale meteorological conditions?
2. What are the typical mechanisms by which QSCSs in the UK develop and how well are these understood?
3. How well are QSCSs represented in a high-resolution operational NWP model?

While a complete treatment of these is beyond the scope of this project, all three are addressed to some degree herein.

Chapter 2 first discusses the data sources used for this investigation. These include high-resolution rainfall observations from the UK radar network and convection-permitting simulations performed with the Met Office Unified Model (UM). The latter

can provide valuable insight into the physical mechanisms governing convective phenomena; however, such models have only recently become widely used in NWP. Part of the motivation for this work was the opportunity to utilise and provide verification of the UKV configuration of the UM which at the start of the project had only just become fully operational.

In Chapter 3, a method for automatically identifying long-duration convective rain events in the UK radar imagery is developed and applied to five years worth of data. The resulting events are then manually classified according to their organisational structure, with one of the categories being QSCSs. Subsequent analysis is designed to address question 1 above: first, the geospatial and temporal distributions of QSCSs are examined; then, the characteristics of the environments in which they form are explored using reanalysis data.

Chapter 4 next focuses on a specific event which occurred on 21 July 2010 over the UK Southwest Peninsula, a region identified as favourable for QSCSs in Chapter 3. This system showed remarkable similarity to the flash flood-producing Boscastle storm of 16 August 2004, but did not lead to flooding itself. An observation-based comparison of the two events is performed and used to identify the factors which distinguish high- and low-impact QSCSs. Simulations of the 2010 case are subsequently carried out using the UKV model. These are used to show that, like the Boscastle storm, this system was initiated and maintained by lifting along a quasi-stationary sea-breeze front. The sensitivity of the simulations to horizontal resolution is also explored.

Chapter 5 increases the focus further, exploring in detail the ways in which quasi-stationary sea-breeze fronts may form over a peninsula. Idealised simulations are employed for this, with a simple coastline geometry and imposed initial and boundary conditions. The sensitivities of sea breeze evolution to the ambient wind velocity, surface heating, stability profile, latitude, and surface roughness are explored. Particular attention is given to the case of shore-parallel flow which characterised both the Boscastle and 21 July 2010 cases but has received little attention in the sea-breeze literature.

Finally, Chapter 6 returns to the three questions above to drawn conclusions and suggest areas where further research is needed.

## Chapter 2

# Data and Models

### 2.1 The UK 1 km radar composite product

Meteorological radars provide information about the spatial distribution and intensity of precipitation within a limited range (typically a few hundred kilometres) of their location. Pulses of electromagnetic (microwave) radiation are transmitted into the atmosphere via an antenna which focuses them into a narrow beam. When the radiation encounters hydrometeors (and other *targets*), part of it is scattered back towards the radar which receives and amplifies the signal. Since the speed at which the radiation travels (the speed of light) is known, the distance to a target can be easily computed from the time between the transmitted and received signals. The amount of back-scattered radiation depends on the distribution (number and relative position) and characteristics (size, shape, orientation, and composition) of hydrometeors within the sampled volume. By making certain assumptions, the received power can be linked to a quantity called the radar reflectivity  $Z$  which is proportional to the sixth power of the mean drop diameter. This in turn can be converted to an estimate of the rain rate  $R$  using a ‘ $Z$ – $R$  relation’. These typically have the form

$$Z = AR^b \tag{2.1}$$

where  $A$  and  $b$  are constants which depend on the rain drop size distribution (e.g. Collier 1996, Chapter 3).

Most operational meteorological radars perform regular  $360^\circ$  scans at multiple elevation angles. In this way, the full three-dimensional evolution of precipitating cloud systems in the vicinity of the radar can be observed. However, for the purpose of forecasting and quantifying surface rainfall, typically only the lowest scan is used. More sophisticated radar systems (e.g. those with *Doppler* or *dual-polarisation* capabilities) can provide additional information about hydrometeors such as their shape and radial velocity. Information can also be gleaned from clear-air returns; for example, so-called reflectivity fine lines (which are primarily associated with scatter by flying insects; Wilson *et al.* 1994), can indicate the presence of boundary-layer convergence zones which

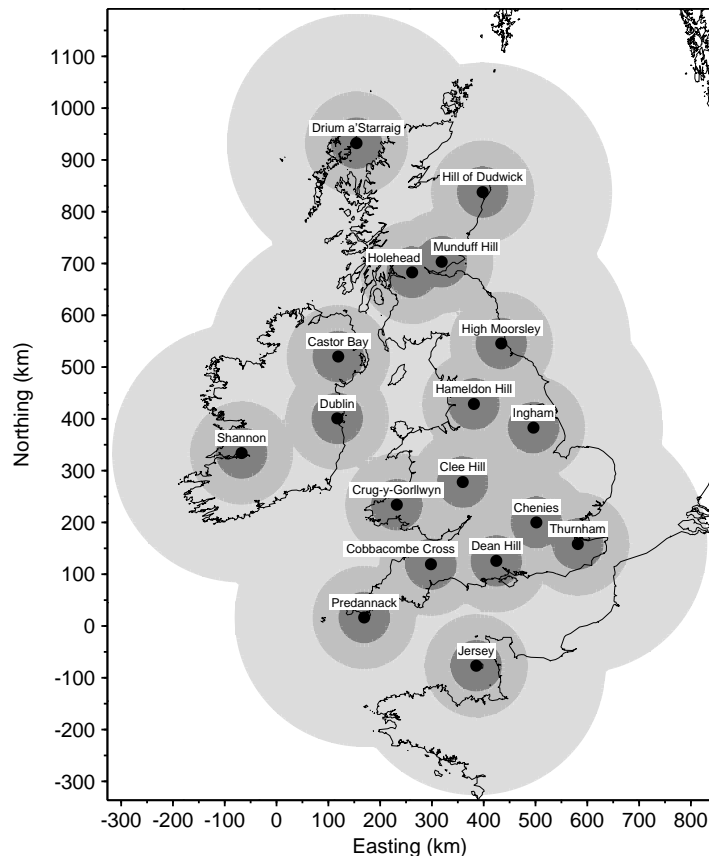


**Figure 2.1** Map showing the location of the 18 radars that provide coverage in the UK and Ireland. Grey shading from dark to light indicates radar ranges of 50, 100, and 250 km.

may later lead to convective initiation (Wilson and Schreiber 1986).

In the UK, a total of 18 C-band (5 cm wavelength) radars (15 operated by the UK Met Office, two by Met Éireann in the Republic of Ireland, and one by the State of Jersey) provide near-complete coverage of the country and surrounding waters at high spatial and temporal resolution (Figure 2.1). Specifically, reflectivity data from four or more elevations are obtained every five minutes with a horizontal spacing in polar coordinates ( $r, \phi$ ) of 600 m by  $1^\circ$  out to a range of around 250 km. Recently, the network has been upgraded so that all radars can measure Doppler velocities, and a further upgrade to dual-polarisation is ongoing at the time of writing. Neither of these measurements are used here so they will not be discussed further.

The product I have made use of is a 2-D composite of all the network radar reflectivity data converted to estimates of surface rain rate and interpolated to a 1 km Cartesian grid, which is available at the full 5 min time resolution. This will be referred to as the 1 km radar composite product (RCP1) although it is often still cited somewhat erroneously as ‘Nimrod data’ after the former Met Office radar processing and nowcasting system of the same name (Golding 1998). Data is available back to April 2004; however, due to processing changes, only those for the period 2008–2012 have been used in this work. The creation of the RCP1 has five key steps: initial quality control, adjustment for variations in the vertical profile of reflectivity (VPR), conversion from reflectivity

to rain rates, gauge-based adjustment, and compositing single-site data onto the 1 km grid. These are each discussed briefly below. For further details, the reader is referred to Harrison *et al.* (2012) and references therein.

Since 2005, all quality control procedures have been performed centrally at the Met Office headquarters in Exeter and applied to the data from each site in its original polar format. For every scan, the following corrections are made:

1. The mean noise as a function of range is estimated for each ray and subtracted from the returned power. Any cell whose value is within a specified number of standard deviations of the noise level is flagged as having no detectable precipitation.
2. A series of checks are used to remove spurious echoes associated with ground clutter, birds, insects, aircraft, ships, and interference from other emitters. These include comparison against a probability of precipitation diagnostic, computed at each cell based on infrared and visible satellite imagery.
3. Rays which are blocked by obstacles are flagged as unusable.
4. Following Gunn and East (1954), the attenuation  $A$  in dB at gate number  $n$  is computed as a function of the rain rate with the effects being cumulative with range:

$$A(n) = \sum_{i=1}^n 0.0044R_i^{1.17} \quad (2.2)$$

The correction is capped at a maximum of a factor of two increase in rain rate. Rather than convert from reflectivity to rain rate at this stage, the  $Z$ – $R$  relation (see below) is simply used to substitute  $Z$  for  $R$  in this equation.

The next step involves estimation of the surface reflectivity at each cell based on an assumed VPR. Corrections are required to account for (1) the increase in beam height with range, (2) enhanced reflectivities around the freezing level associated with melting snow (the ‘bright band’; Austin and Bemis 1950), and (3) low-level intensification of rainfall over orography associated with the seeder–feeder mechanism (Bergeron 1965). Idealised VPRs are constructed based on knowledge of the freezing-level, cloud-top height, local orography, wind velocity, humidity, and radar parameters (elevation angle and range). Meteorological quantities are estimated using data from the operational Met Office model, while cloud-top height is calculated using satellite-derived cloud-top temperatures and model-derived temperature profiles.

From the estimated surface reflectivity, the surface rain rate is computed using the  $Z$ – $R$  relation of Marshall and Palmer (1948):

$$Z = 200R^{1.6} \quad (2.3)$$

Real-time corrections are then applied to rain rates over the entire radar domain based on recent comparisons with rain gauges.

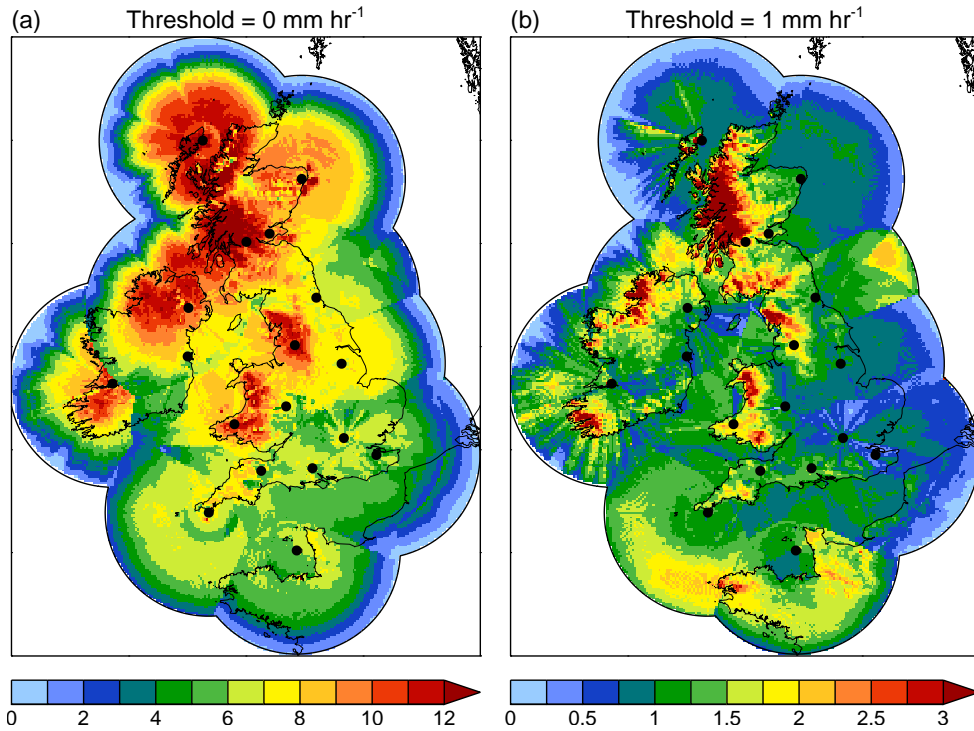


**Figure 2.2** Maps showing the frequency of occurrence (%) of rain rates greater than (a)  $0 \text{ mm h}^{-1}$  and (b)  $1 \text{ mm h}^{-1}$  in  $5 \times 5 \text{ km}$  grid boxes for 2008–2012. The radar sites are indicated by black circles.

The final step is interpolation of the polar-format data onto a regular 1 km grid; specifically, the Ordnance Survey National Grid (a Transverse Mercator projection with a true origin at  $49^\circ\text{N}$ ,  $2^\circ\text{W}$  and a false origin 400 km west and 100 km north of this). Prior to November 2007, interpolation was performed for each site individually, with grid spacings of 1, 2, and 5 km used out to ranges of 50, 100, and 250 km respectively. These were then interpolated onto the 1 km grid, using the highest resolution data available at every pixel. This method failed to use all the information contained in the polar data and resulted in step changes in apparent resolution at ranges of 50 and 100 km. Thus, a new method was devised which involves direct interpolation between the polar and Cartesian grids. Specifically, every polar cell within a specified maximum distance  $d_{\max}$  of a Cartesian pixel is given a weight  $w$  with a Gaussian dependence on distance  $d$ :

$$w(d) = e^{-\alpha(d/d_{\max})^2} \quad (2.4)$$

where  $\alpha$  is a specified constant. Note that  $d_{\max}$  increases with radar range to account for the increase in azimuthal spacing. At Cartesian pixels where data from more than one site is available, a quality index is used to choose between them. This is simply a function of the height of the lowest available (non-blocked) scan. Harrison *et al.* (2009) discuss this method further and demonstrate that it significantly reduces errors in hourly rainfall estimates with respect to rain gauge measurements.

Despite the various quality control measures discussed above, significant issues still

exist with the RCP1, as illustrated by the five-year (2008–2012) precipitation frequencies shown in Figure 2.2. First, when we consider the detection of any precipitation (Figure 2.2a), a strong decrease in frequency with radar range is apparent. This is a consequence of increasing beam height and scanning volume with range which respectively lead to more clouds being overshoot and a reduction in the signal-to-noise level. However, for a higher rain rate threshold, the frequencies actually increases with range at some sites, most notably Predannack and High Moorsley (Figure 2.2b). This may be due to inaccurate VPR corrections associated with errors in the elevation angle of these radars (Rob Thompson, personal communication); however, the true cause is currently unknown. Other features apparent in Figure 2.2 include sharp boundaries where data from the individual sites are stitched together (indicating differences in radar calibration) and ‘spokes’ of higher or lower frequency around some sites. The latter are likely associated with radial variations in the lowest usable elevation angle due to beam blockage. In addition to these climatological biases, individual scans can be affected by attenuation, clutter, anomalous propagation, and transmission failures which may lead to spurious echoes or missing data. Care must therefore be taken when interpreting data from the RCP1.

## 2.2 The Met Office Unified Model

The Unified Model (UM) is a suite of numerical modelling software developed by the UK Met Office for simulating the atmosphere and other Earth-system components on a range of space and time scales. For the present study, I have used version 7.3 of the UM, both in a standard operational configuration (Chapter 4) and idealised mode (Chapter 5). This section provides an overview of the model’s dynamical core (which represents resolved-scale processes) and subgrid physical parameterisation schemes. Details of the specific configurations used are reserved for the relevant chapters. For a complete treatment of the UM, the reader is referred to the model documentation papers available from the National Centre for Atmospheric Science Computer Modelling Services (NCAS–CMS) website (<http://cms.ncas.ac.uk/wiki/Docs/MetOfficeDocs>).

### 2.2.1 Dynamical core

The UM New Dynamics (Davies *et al.* 2005) solves the fully compressible, non-hydrostatic, deep-atmosphere dynamical equations in spherical polar coordinates  $(\lambda, \phi, r)$ , where  $\lambda$  is longitude,  $\phi$  is latitude,  $r = a + z$  is the distance to the Earth’s centre,  $a$  is the Earth’s radius (assumed constant), and  $z$  is the height above mean sea level. Prognostic variables are the three wind components  $(u, v, w)$ , potential temperature  $\theta$ , dry air density  $\rho_d$ , and mass mixing ratios for water vapour  $m_v$ , liquid water  $m_l$ , and ice  $m_i$ . Options exist to split the liquid and ice water into multiple variables (e.g. cloud and rain liquid water) and other tracers such as aerosols and chemical species may also be included. Collectively, these variables will be given the vector symbol  $\mathbf{m}$ . The gov-

erning equations—momentum equation, internal energy equation, transport equation, continuity equation, and equation of state—may be expressed as follows :

$$\frac{Du}{Dt} = 2\Omega \sin \phi v - 2\Omega \cos \phi w + \frac{uv \tan \phi}{r} - \frac{uw}{r} - \frac{c_{pd}\theta_v}{r \cos \phi} \frac{\partial \Pi}{\partial \lambda} + P_u \quad (2.5a)$$

$$\frac{Dv}{Dt} = 2\Omega \sin \phi u - \frac{u^2 \tan \phi}{r} - \frac{w}{r} - \frac{c_{pd}\theta_v}{r} \frac{\partial \Pi}{\partial \phi} + P_v \quad (2.5b)$$

$$\frac{Dw}{Dt} = 2\Omega \cos \phi u - \frac{(u^2 + v^2)}{r} - g - c_{pd}\theta_v \frac{\partial \Pi}{\partial r} + P_w \quad (2.5c)$$

$$\frac{D\theta}{Dt} = P_\theta \quad (2.6)$$

$$\frac{D\mathbf{m}}{Dt} = \mathbf{P}_m \quad (2.7)$$

$$\frac{\partial \rho_d}{\partial t} + \nabla \cdot (\rho_d \mathbf{u}) = 0 \quad (2.8)$$

$$\kappa \Pi \rho \theta_v = \frac{p}{c_{pd}}. \quad (2.9)$$

Here,  $\Omega$  is the Earth's angular speed of rotation,  $c_{pd}$  is the specific heat of dry air at constant pressure,  $\theta_v$  is the virtual potential temperature (Equation 1.15),  $\Pi = (p/p_0)^\kappa$  is the Exner pressure,  $p$  is pressure,  $p_0$  is the reference pressure,  $\kappa = R_d/c_{pd}$ ,  $R_d$  is the specific gas constant for dry air,  $g$  is the gravitational acceleration,  $\rho = \rho_d(1 + m_v + m_l + m_i)$  is the total air density, and the  $P$  terms represent tendencies from the various parameterisation schemes (Section 2.2.2). The material derivative (i.e. following fluid motion) is equal to the sum of the local rate of change and advection,  $D/Dt = \partial/\partial t + \mathbf{u} \cdot \nabla$ . In spherical polar coordinates, the gradient operator  $\nabla = \left( \frac{1}{r \cos \phi} \frac{\partial}{\partial \lambda}, \frac{1}{r} \frac{\partial}{\partial \phi}, \frac{\partial}{\partial r} \right)$ , hence

$$\frac{D}{Dt} = \frac{\partial}{\partial t} + \frac{u}{r \cos \phi} \frac{\partial}{\partial \lambda} + \frac{v}{r} \frac{\partial}{\partial \phi} + w \frac{\partial}{\partial r} \quad (2.10)$$

Equations 2.5–2.9 are discretised on a regular latitude–longitude grid ( $\Delta\lambda = \Delta\phi = \text{constant}$ ) in the horizontal with Arakawa C-grid staggering (Arakawa and Lamb 1977). In this configuration, the  $u$ - and  $v$ -components of the wind are held on grids staggered one half grid point in the  $\lambda$ - and  $\phi$ -directions respectively from the grid on which other model variables are stored. For limited-area model configurations, the pole of the grid is rotated such that the domain is approximately centred on the Equator. This is done to minimise latitudinal variations in the true zonal grid spacing  $\Delta x = \Delta\lambda r \cos \phi$  (since  $\frac{d}{d\phi} \Delta x = -\Delta\lambda r \sin \phi$ ). The true meridional grid spacing  $\Delta y = \Delta\phi r$  is constant and unchanged by the transformation.

In the vertical the model uses a terrain-following hybrid-height coordinate  $\eta$  which

varies from zero at  $z = h(x, y)$ , where  $h(x, y)$  is the height of the surface orography above  $r = a$ , to one at  $z = z_T$ , where  $z_T$  is the fixed height of the model lid. The true height is related to the hybrid height by the following equation

$$z = \begin{cases} \eta z_T + h \left(1 - \frac{\eta}{\eta_{\text{flat}}}\right)^2, & 0 \leq \eta < \eta_{\text{flat}} \\ \eta z_T, & \eta_{\text{flat}} \leq \eta < 1 \end{cases} \quad (2.11)$$

Thus, model levels follow the orography near the surface and gradually flatten out as  $\eta$  increases up to  $\eta_{\text{flat}}$ , beyond which they are completely level. The vertical grid spacing in  $\eta$  is chosen to be irregular, with more levels near to the surface in order to better-resolve the boundary layer where vertical gradients and fluxes are large. Specifically, a quadratic function is used with  $\eta$  at level number  $k$  given by  $\eta_k = (k/N)^2$  where  $N$  is the number of model levels. This is modified above a certain height to more rapidly increase the vertical grid spacing near the model top. Grid staggering is also applied following Charney and Phillips (1953):  $\theta$  and  $w$  are held on ‘ $\theta$ -levels’ which include the surface and model top, while  $u$ ,  $v$ ,  $\rho$ , and  $\Pi$  are held exactly halfway between these on ‘ $\rho$ -levels’.

Integration of the governing equations is performed using an off-centred, two time-level, semi-implicit scheme with semi-Lagrangian advection of all prognostic quantities excluding density for which an Eulerian treatment is used for mass conservation. This procedure leads to a three-dimensional, elliptic (Helmholtz) equation for the Exner pressure increment,  $\Pi' = \Pi^{n+1} - \Pi^n$  (superscripts indicate the time step), which is solved using a generalized conjugate residual (GCR) iterative solver (Eisenstat *et al.* 1983; Smolarkiewicz and Margolin 1994) with preconditioning to deal with the horizontal and vertical variations in resolution (Skamarock *et al.* 1997). The remaining variables at time level  $n + 1$  are then obtained through back-substitution with corrections applied where required to ensure conservation and monotonicity. For full details of the scheme, see UM Documentation Paper 15 (Staniforth *et al.* 2006).

It is worth noting that explicit horizontal diffusion is included in the UM dynamical core to account for unresolved mixing processes and prevent the accumulation of noise and energy at the grid scale. The latter is associated with three processes: the physical cascade of energy from larger to smaller scales, misrepresentation of nonlinear processes, and grid-scale forcing associated either with the specified surface boundary conditions (e.g. orography) or the parameterisation schemes which mostly operate on individual columns or grid points. A number of options exist for the diffusion operator but all incorporate eddy diffusivities  $K_\lambda$  and  $K_\phi$  which relate the amount of diffusion to horizontal gradients in the  $\lambda$  and  $\phi$  directions respectively. Vertical diffusion meanwhile is treated by a separate subgrid mixing scheme as described in the next section.

### 2.2.2 Parameterisation schemes

The UM includes a comprehensive set of parameterisation schemes to represent subgrid-scale processes across a wide range of resolutions. This section provides a brief overview

of those schemes that were active in one or more of the model configurations used herein (including runs that were not performed by me but provided initial and boundary condition data for my simulations). Schemes not discussed include those dealing with prognostic aerosols, river routing, and atmospheric chemistry.

### Cloud

The cloud scheme deals specifically with the condensation and evaporation of cloud liquid water associated with changes in grid-scale and subgrid-scale relative humidity. Other microphysical calculations associated with ice processes and rain formation and evaporation are handled by the so-called large-scale precipitation scheme (see below). At UM version 7.3, two cloud schemes were available: the diagnostic scheme of Smith (1990) and the PC2 (prognostic cloud fraction and condensate) scheme of Wilson *et al.* (2008). The latter was not used in my runs and is therefore not described here. Full details of the diagnostic schemes can be found in UM Documentation Paper 29 (Wilson and Morcrette 2010).

The amount of cloud liquid water condensed or evaporated is computed as the sum of two terms associated with the grid box–mean humidity and subgrid-scale fluctuations about this:

$$q_{\text{cl}} = Q_{\text{c}} + s, \quad (2.12)$$

where

$$Q_{\text{c}} = a_{\text{L}} (\bar{q}_{\text{T}} - q_{\text{v}}^* (\bar{T}_{\text{L}}, \bar{p})) \quad (2.13)$$

and

$$s = a_{\text{L}} (q'_{\text{T}} + \alpha T'_{\text{L}} + \beta p') \quad (2.14)$$

Here,  $q_{\text{T}} = q_{\text{v}} + q_{\text{cl}}$ , where  $q_{\text{v}}$  and  $q_{\text{cl}}$  are the water vapour content (specific humidity) and cloud liquid water content respectively,  $q_{\text{v}}^*$  is the saturation specific humidity,  $T_{\text{L}} = T - \frac{L_{\text{v}}}{c_{\text{pd}}} q_{\text{cl}}$ ,  $L_{\text{v}}$  is the latent heat of vapourisation,  $a_{\text{L}} = \left(1 + \alpha \frac{L_{\text{v}}}{c_{\text{pd}}}\right)$ ,  $\alpha = \frac{\partial q_{\text{v}}^*}{\partial T}$  at constant pressure,  $\beta = \frac{\partial q_{\text{v}}^*}{\partial p}$  at constant temperature, and overbars and primes represent grid box–mean values and fluctuations about these respectively. Note that the variables  $q_{\text{T}}$  and  $T_{\text{L}}$  are used because they are conserved during condensation and evaporation. A symmetric triangular probability density function (PDF) is assumed for  $s$  with a half-width  $b_s$  determined as

$$b_s = a_{\text{L}} q_{\text{v}}^* (\bar{T}_{\text{L}}, \bar{p}) (1 - \mathcal{H}_{\text{crit}}) \quad (2.15)$$

where  $\mathcal{H}_{\text{crit}} < 1$  is the critical relative humidity. This is the grid box–mean humidity at which saturation first occurs and accounts for the fact that the whole grid box does not need to be saturated for cloud formation to occur on subgrid-scales. In the model

configurations used herein,  $\mathcal{H}_{\text{crit}}$  is specified for each model level and decreases with height to account for the increase in vertical grid spacing and thus grid-box volume.

Due to the dependence of  $\alpha$  on  $T$ , Equation 2.15 must be solved iteratively. Once  $b_s$  is known,  $q_{\text{cl}}$  can be computed along with the new grid box-mean temperature and specific humidity. The fraction of the grid-box volume containing liquid cloud is easily obtained by integrating over the PDF of  $s$ . An ice cloud volume fraction is also diagnosed using the ice water content calculated in the large-scale precipitation scheme and the two are then combined to give the total cloud volume fraction.

Within a grid box, clouds are assumed to be uniformly distributed in the vertical, but not in the horizontal. The area cloud fraction, which is an important quantity in the radiation scheme (see below), is calculated by dividing the grid box into three layers, performing the cloud volume calculations for each, and then taking the maximum of these (i.e. assuming maximum overlap between clouds in the layers).

### Large-scale precipitation

The parameterisation of microphysical processes (excluding condensation and evaporation of cloud liquid water) is based on the mixed-phase, single-moment scheme of Wilson and Ballard (1999). My simulations all utilised the ‘3D’ version of this scheme, which is detailed in UM Documentation Paper 26 (Wilkinson *et al.* 2010). Generally, four classes of water are considered: vapour, liquid cloud drops, cloud ice/snow, and rain. In all configurations, the first three of these are represented as prognostic variables. At low resolutions (e.g. in the operational Global model), rain is treated diagnostically and thus falls out of a column in a single time step. However, at high resolutions (those with grid spacing less than about 4 km), it is represented as a prognostic (a mixing ratio  $m_r$ ) to allow for horizontal advection across grid boxes, which can be significant in strong low-level winds (e.g. Lean and Browning 2013). Typically, the ice variable is split by a diagnostic relationship into a large-ice category, ‘aggregates’, and a small ice category, ‘crystals’, which are treated separately by the scheme and then recombined. Options exist to treat both types as prognostic variables and to include an additional prognostic for ice in the form of graupel; however, neither of these were used in my runs.

The particle size distribution for each water quantity (excluding cloud liquid water)  $N(D)$ , where  $D$  is the particle diameter, is defined as a gamma function:

$$N(D) = N_0 D^\alpha e^{-\lambda D} \quad (2.16)$$

where  $N_0$ ,  $\lambda$ , and  $\alpha$  are respectively known as the intercept, slope, and shape parameters. The intercept parameter is assumed to be a simple function of  $\lambda$ :

$$N_0 = N_a \lambda^{N_b} \quad (2.17)$$

Constant values for  $N_a$ ,  $N_b$ , and  $\alpha$  are prescribed for each variable. The slope parameter is calculated from the mixing ratio of each prognostic quantity and from the flux of rain

when it is treated diagnostically. The size distribution of cloud water drops is calculated using a modified gamma distribution which is a function of liquid water content and the concentration of activated cloud nuclei. In my runs, the latter assumes constant values of 300 and 100 cm<sup>-3</sup> over land and sea grid points respectively; however, in more advanced versions of the scheme, it can be coupled to prognostic aerosol quantities.

The following microphysical processes (which lead to changes in the mixing ratio of one or more water classes within a grid box) are represented in the scheme:

- Sedimentation (fall) of ice and rain under gravity
- Heterogeneous and homogeneous nucleation of ice
- Deposition and sublimation of ice
- Aggregation of ice
- Collection of cloud droplets or rain by ice (riming)
- Melting of ice
- Evaporation of rain
- Collection of cloud droplets by rain (accretion)
- Autoconversion of cloud droplets to rain
- Settling (fall) of cloud droplets under gravity

These all require information about the subgrid distribution of the four variables. To this end, each model grid box is divided into eight ‘regions’ representing all possible combinations of the presence or absence of cloud liquid water, ice, and rain. The respective size of these regions depends on the volume fractions for each quantity and their overlap. The liquid water and ice cloud fractions are provided by the cloud scheme, together with the total cloud fraction, from which the mixed-phase cloud fraction can be computed. The rain fraction and its overlap with liquid, ice, and mixed phase cloud are calculated by the microphysics scheme. The specific humidity in each region must also be known. In regions with liquid cloud, the assumption of instantaneous condensation fixes it at its saturation value with respect to water; however, for the clear and ice-only portions of the grid box it has to be diagnosed based on a number of assumptions.

### Boundary layer

The UM uses the boundary-layer scheme of Lock *et al.* (2000) to parameterise subgrid-scale vertical mixing associated with atmospheric turbulence. Full details of this scheme can be found in UM Documentation Paper 24 (Lock 2007). For a conserved variable  $\chi$ , the (vertical) turbulent contribution to its rate of change is expressed as  $-\frac{1}{\rho} \frac{\partial}{\partial z} (\rho \overline{w' \chi'})$ , where primes indicate turbulent (subgrid-scale) fluctuations of a quantity and the over-bar indicates an ensemble average (the grid-box mean). This is computed for the horizontal momentum (wind components  $u$  and  $v$ ) and the following scalar variables which are approximately conserved under moist adiabatic ascent:

$$\theta_1 = T - \frac{L_v}{c_{pd}} q_l - \frac{L_s}{c_{pd}} q_i + \frac{g}{c_{pd}} z \quad (2.18)$$

$$q_t = q_v + q_l + q_i \quad (2.19)$$

where  $q_v$ ,  $q_l$ , and  $q_i$  are respectively the vapour, liquid, and ice water contents,  $L_s = L_v + L_f$  is the latent heat of sublimation, and  $L_f$  is the latent heat of freezing. The turbulent fluxes are parameterised as follows

$$\overline{w'\chi'} = -K_\chi \frac{\partial \chi}{\partial z} \quad (2.20)$$

where  $K_\chi$  is the eddy diffusivity appropriate to variable  $\chi$ . Separate diffusivities are calculated for momentum  $K_m$  and scalar variables  $K_h$ . For  $\chi = \theta_1$ , an additional ‘gradient adjustment’ term is included on the right-hand side of Equation 2.20 to allow for the maintenance of a well-mixed boundary layer when  $\frac{\partial \theta_1}{\partial z} \approx 0$ . Entrainment fluxes at the top of the boundary layer are also parameterised using an entrainment velocity following Lock (2001).

The first step in the scheme is diagnosis of the boundary-layer type based on the stability profile and the presence or absence of layer and/or cumulus cloud. The following seven classifications are used:

1. Stable boundary layer, with or without cloud
2. Decoupled stratocumulus over a stable boundary layer
3. Well-mixed boundary layer, possibly coupled to stratocumulus
4. Decoupled stratocumulus over a well-mixed boundary layer
5. Decoupled stratocumulus over cumulus
6. Cumulus-capped boundary layer
7. Shear-dominated unstable boundary layer

The eddy diffusivities at each level are then calculated as  $K_\chi = \max [K_\chi^L, K_\chi^{NL}]$  where  $K_\chi^L$  and  $K_\chi^{NL}$  are the diffusivities for local and non-local mixing respectively. Local mixing is computed using a first-order mixing-length closure:

$$K_m = \mathcal{L}_m^2 \left| \frac{\partial \mathbf{u}_H}{\partial z} \right| f_m(Ri) \quad (2.21)$$

$$K_h = \mathcal{L}_h \mathcal{L}_m \left| \frac{\partial \mathbf{u}_H}{\partial z} \right| f_h(Ri) \quad (2.22)$$

Here,  $\mathbf{u}_H = (u, v)$  is the horizontal velocity vector,  $\mathcal{L}_m$  and  $\mathcal{L}_h$  are the neutral mixing lengths for momentum and scalars respectively, and  $f_m$  and  $f_h$  are empirical stability functions which depend on the local Richardson number. These take on different forms for stable ( $Ri > 0$ ) and unstable ( $Ri < 0$ ) conditions. Non-local mixing occurs in un-

stable layers and is associated with two processes: surface heating and radiative and/or evaporative cooling at the top of stratocumulus cloud. These are represented using separate eddy diffusivities,  $K_\chi^{\text{sfc}}$  and  $K_\chi^{\text{sc}}$ , which depend on the magnitude of turbulence within the layer as a whole. Different vertical profiles of  $K_\chi^{\text{sfc}}$  and  $K_\chi^{\text{sc}}$  are defined for the different boundary-layer types. The total non-local eddy diffusivity is then given by  $K_\chi^{\text{NL}} = K_\chi^{\text{sfc}} + K_\chi^{\text{sc}}$ . For stable layers and above the boundary-layer top (i.e. in the free troposphere),  $K_\chi^{\text{NL}} = 0$  so only local mixing operates, while in decoupled stratocumulus layers, only  $K_\chi^{\text{sc}}$  is non-zero. In layers where cumulus convection is diagnosed,  $K_\chi$  is set to zero and mixing is performed by the model's convection scheme (see below), unless the latter is switched off (i.e. convection is being represented explicitly).

### Subgrid mixing at high resolution

Large-eddy models often represent 3-D turbulence using schemes based on the work of Smagorinsky (1963) and Lilly (1967). This type of scheme is also implemented in UM. Typically, it is only used in very high-resolution configurations (grid spacings of 500 m or less), although at slightly coarser resolutions (grid spacings around 1 km) it may be operated in the horizontal, with vertical mixing performed by the boundary-layer scheme; this is the case in the high-resolution operational models. It should be noted, however, that these choices are not definitive. Indeed, appropriate treatment of subgrid-scale mixing at these resolutions (the so-called grey-zone where the large eddies are partially resolved) is the subject of ongoing research.

The Smagorinsky scheme, as it is commonly called, calculates the eddy-diffusivities for momentum and scalars as follows:

$$K_m = \ell^2 S f_m(Ri) \quad (2.23)$$

$$K_h = \ell^2 S f_h(Ri) \quad (2.24)$$

Note the similarity to Equations 2.21 and 2.22. The stability functions  $f_m$  and  $f_h$  are simply those calculated in the boundary layer scheme. The mixing length  $\ell$  is a function of the horizontal grid length and is given by

$$\frac{1}{\ell^2} = \frac{1}{\ell_0^2} + \frac{1}{[k(z + z_0)]^2} \quad (2.25)$$

where  $\ell_0 = c_s \Delta x$ ,  $c_s$  is a specified constant,  $k$  is the von Kármán constant, and  $z_0$  is the roughness length. The second term on the right-hand side acts to reduce  $\ell$  close to the surface. The quantity  $S$  is computed as

$$S = \frac{\|S_{ij}\|}{\sqrt{2}} = \left( \frac{1}{2} \sum_{i,j=1,3} S_{ij}^2 \right)^{\frac{1}{2}} \quad (2.26)$$

where

$$S_{ij} = \frac{\partial u_i}{\partial x_j} + \frac{\partial u_j}{\partial x_i} \quad (2.27)$$

is the so-called rate-of-strain tensor. Note the use of tensor notation here:  $(u_1, u_2, u_3) = (u, v, w)$  and  $(x_1, x_2, x_3) = (x, y, z)$ .

If the Smagorinsky scheme is operated in the horizontal, the eddy diffusivities calculated from Equations 2.23 and 2.24 replace those used by the diffusion operator in the dynamical core (Section 2.2.1). Similarly, if the scheme is used for vertical mixing, the eddy diffusivities computed by the boundary layer scheme are replaced. Full details are provided in UM Documentation Paper 28 (Halliwell 2007).

### Surface exchange

In my runs, surface exchange calculations are performed using the Met Office Surface Exchange Scheme (MOSES) Version 2 (Essery *et al.* 2003; Best 2005). This is a tiling scheme, where subgrid-scale surface inhomogeneities are modeled explicitly by dividing each grid box into tiles with distinct properties. Nine tiles are used in the UM, five vegetated (broad-leaf trees, needle-leaf trees, temperate grass, tropical grass, and shrubs) and four non-vegetated (urban, inland water, bare soil, and ice). The surface temperature, short- and long-wave radiative fluxes, sensible, latent, and ground heat fluxes, canopy moisture, snow mass, and snow melting rate are calculated separately for each tile within a grid box. The grid box-mean values are then computed as a weighted average of these, where the weights are equal to the fractional coverage of each surface type prescribed from land-use datasets. Air temperature, humidity, wind speed, and precipitation above the surface and the temperature and moisture content of the four soil layers are assumed to be homogeneous within a grid box.

The surface fluxes of heat, moisture, and momentum are treated using Monin–Obukhov similarity theory (e.g. Foken 2006). Exchange coefficients for momentum and scalars are determined through an iterative procedure conditioned on the surface-layer wind shear and buoyancy flux. An important component of these calculations is the surface roughness length  $z_0$ . Over land, this is prescribed for each tile; however, at low horizontal resolutions, it is modified to take account of form drag based on subgrid-scale variations in orography. Over the sea,  $z_0$  is calculated using a modified version of the Charnock (1955) formula which describes the feedback between wind speed and surface drag via wind-driven waves. Sea-surface temperatures are prescribed and time-invariant in all of my runs.

### Radiation

Radiation in the UM is parameterised using the scheme of Edwards and Slingo (1996). This uses the two-stream approximation so only fluxes in the vertical direction are considered. Within each grid box, the fluxes of short-wave (solar) and long-wave (terrestrial) radiation are represented as the sum of upward and downward diffuse fluxes,

plus a direct flux in the shortwave. The short- and long-wave frequency ranges are divided into a set of distinct spectral bands whose properties are treated as independent of frequency with the exception of the gaseous absorption coefficients. These are then further subdivided into a set of quasi-monochromatic regions for which the gaseous absorption coefficients are treated as constant. Fluxes are computed for each of these regions taking into account gaseous and continuum absorption, absorption and scattering by aerosols, water drops and ice crystals, and Rayleigh scattering. Full details are provided in UM Documentation paper 23 (Edwards *et al.* 2004).

Radiation calculations are very computationally expensive and therefore they are not performed at every time step. The frequency of calls to the scheme typically increases with horizontal resolution to account for the more rapid evolution of the cloud field within a grid box. Non-radiation time steps use the most recent calculated fluxes, re-scaled to account for changes in solar zenith angle. At high resolutions, the cost is further reduced by performing calculations only at every other grid point in both the  $\lambda$ - and  $\phi$ -directions in a chessboard pattern, with intermediate values filled in through interpolation.

### Convection

At coarse resolutions (grid spacings greater than a few km), a convection parameterisation is employed to represent the subgrid-scale vertical transport of heat, moisture, and momentum by cumulus clouds. The UM uses the mass-flux scheme of Gregory and Rowntree (1990) but with numerous modifications (see UM Documentation Paper 27; Gregory *et al.* 2009). Surface-based shallow or deep convection is diagnosed by the boundary-layer scheme using a near surface-based, undilute parcel ascent. The distinction between shallow and deep convection depends on cloud depth and the (resolved-scale) vertical velocity around the 850 hPa level. Mid-level (elevated) convection is diagnosed by the scheme based on the presence of instability either above the boundary-layer top or above shallow/deep convection.

For each type of convection (shallow, deep, and mid-level), a cloud model is used to represent the bulk properties of an ensemble of convective plumes. This includes the effects of entrainment of environmental air and detrainment of cloudy air during ascent, and forced detrainment at cloud top. The transport of horizontal momentum and atmospheric tracers by the updraught is also treated. Precipitation is initiated when the cloud depth and condensed water reach specified thresholds. These thresholds differ over land and sea to represent differences in aerosol size distributions which affect the efficiency of the collision-coalescence process. Downdraughts are treated as saturated inverted entraining plumes in which negative buoyancy is maintained through evaporation and sublimation of falling precipitation and water loading. Transport of tracers by downdraughts is represented but momentum transport is not. For deep convection, the convective cloud area is made to increase with height above the freezing level to represent the radiative effect of anvils. The Convective Cloud for Radiation (CCRad)

scheme, which is used in the operational Global model configuration at Version 7.3, allows this anvil scheme to be applied to all convective-cloud types and represents the effect of vertically stacked convection (mid-level over deep/shallow).

The details of the cloud model differ for the different types of convection. One key difference is the closure used to specify the initial cloud-base mass flux. For deep and mid-level convection, a CAPE closure based on that of Fritsch and Chappell (1980) is used, where the convective mass flux acts to completely remove CAPE over a specified time scale. This time scale is set at 30 minutes but is reduced in the presence of strong grid-scale ascent (explicit convection) to prevent the occurrence of unrealistically large vertical velocities and excessive precipitation. For shallow convection, the scheme uses the closure of Grant (2001), where the cloud base mass flux is proportional to the mixed-layer convective velocity scale.

### Flow-blocking and gravity-wave drag

The effects of subgrid-scale orography on the flow in stable conditions are represented using the flow-blocking and gravity wave–drag scheme of Webster *et al.* (2003). The subgrid orography is described in terms of its amplitude, which is proportional to the standard deviation of the source orography in a grid box  $\sigma_h$ , and its anisotropy, which is described in terms of the squared gradients  $\delta_{xx} = (\partial h/\partial x)^2$ ,  $\delta_{xy} = (\partial h/\partial x)(\partial h/\partial y)$ , and  $\delta_{yy} = (\partial h/\partial y)^2$ . The scheme first defines the depth of the surface layer over which flow impinges on the subgrid orography as  $2.5\sigma_h$ . The components of the surface stress vector  $\boldsymbol{\tau} = (\tau_x \tau_y)$  are then computed as

$$\tau_x = \rho u_\tau N \hat{\kappa}^{-1} (\delta_{xx} \cos \chi + \delta_{xy} \sin \chi) \quad (2.28)$$

$$\tau_y = \rho u_\tau N \hat{\kappa}^{-1} (\delta_{xy} \cos \chi + \delta_{yy} \sin \chi) \quad (2.29)$$

where  $u_\tau$  is the wind velocity in the direction of the stress vector,  $N$  is the buoyancy frequency,  $\chi$  is the wind direction, and  $\hat{\kappa}$  is a specified wavenumber constant. Note that the variables in this calculation all represent vertical averages over the surface layer. The surface-layer Froude number is then used to partition this stress into gravity-wave and flow-blocking components. The flow-blocking drag  $\tau_{fb}$  is imposed uniformly across the surface layer (i.e.  $\tau_{fb}$  decreases linearly from its surface value to zero at  $2.5\sigma$ ), while the gravity-wave drag  $\tau_{gw}$  is launched at the top of the surface layer and carried upwards. At each level, a critical (saturation) stress  $\tau_{crit}$  is diagnosed and, if  $\tau_{gw} > \tau_{crit}$ ,  $\tau_{gw}$  is reduced to  $\tau_{crit}$ . The change in momentum at each level is then given by

$$\frac{\partial \mathbf{u}}{\partial t} = \frac{1}{\rho} \frac{\partial \boldsymbol{\tau}}{\partial z} \quad (2.30)$$

The Global configuration at UM Version 7.3 also includes a scheme (Scaife *et al.* 2002) to represent the drag associated with non-orographic gravity waves, which plays an important role in the circulation of the upper atmosphere. These waves originate

from dynamic motions associated with convection, frontogenesis, and jet streams; however, their spatial and temporal variability is poorly constrained by observations. Thus, the model uses a simplified tropospheric source which is independent of time and geographic location. The launch spectrum is specified close to the surface with an isotropic spectral density following Warner and McIntyre (2001). It then propagates upward, responding to variations in wind velocity and stability and the reduction in density, which respectively cause Doppler shifting and wave amplification. A standard dispersion relation is used but with Coriolis and non-hydrostatic effects neglected (the so-called mid-frequency approximation) so that wave reflection is not permitted. Momentum deposition then occurs through erosion of the spectrum where it exceeds a locally defined saturation spectrum.

For further details of the orographic and non-orographic gravity wave schemes see UM Documentation Papers 22 (Webster 2004) and 34 (Bushell *et al.* 2013) respectively.

## 2.3 Other data sources

This section describes those data that were used for more minor parts of my analysis; specifically, the European Centre for Medium-range Weather Forecasts (ECMWF) Interim Reanalysis (ERA-Interim), rain gauge measurements, and atmospheric soundings.

### 2.3.1 ERA-Interim

ERA-Interim represents the latest in a series of global reanalysis products produced by ECMWF. Reanalyses are gridded datasets representing the state of the atmosphere at regular intervals over a particular historical period (1979 to the present day in the case of ERA-Interim). They are produced using a data assimilation system which optimally combines observations with a previous model forecast in a physically consistent way. ERA-Interim uses four-dimensional variational (4DVAR) assimilation which is a generalisation of 3DVAR. The latter obtains an optimal analysis by minimising a cost function defined as the sum of the distance of the model state from a prior forecast (the background) and observations, weighted by their respective error covariances. In 3DVAR, observations are used simultaneously, but in 4DVAR, the assimilation is performed over a window (the *analysis cycle*) taking account of the temporal distribution of the observations. A 12 h analysis cycle is used for ERA-Interim, with separate procedures for upper-air and surface variables. The resulting analysis is then used to initialise a short-range model forecast which provides the background state for the next cycle. The model is release Cy31r2 of the ECMWF Integrated Forecasting System (IFS) which was run operationally from December 2006 to June 2007. It uses a spectral representation of the governing equations with a triangular truncation of T255 ( $\sim 79$  km on a reduced Gaussian grid), and a hybrid sigma–pressure vertical coordinate with 60 levels and a top at 0.1 hPa. For further details, the reader is directed to Dee *et al.* (2011) and references therein.

Both analysis and forecast data are included in ERA-Interim, but this study only uses the former. Specifically, in Chapter 3, six-hourly surface and upper-air fields are used to investigate the environments of QSCSs in the UK over the period 2008–2012.

### 2.3.2 UK rain gauges

The Met Office, in collaboration with the Environment Agency (EA) and other partners, operate a dense network of some 4,000 rain gauges across the UK, providing a mixture of monthly, daily, hourly, and sub-hourly measurements of precipitation. This work uses sub-hourly records from EA-operated tipping-bucket gauges to compare rainfall associated with two QSCSs over the UK Southwest Peninsula (Chapter 4). With these gauges, rainfall is collected via a funnel in a small bucket which, once filled, tips and electronically records the event. The capacity of the bucket at most sites is 0.2 mm. Care must be taken when interpreting measurements at the start of a precipitation event, when the initial tip may include rainfall from a previous event, and in the case of frozen precipitation which must melt before it can be logged. In very heavy rain events, under-reading can occur, both due to losses during the tipping process and locking of the bucket (Kelway 1975). Under-reading can also be caused by outsplash, evaporation from a partially filled bucket, and turbulent flow around the gauge (Strangeways 1996). Verification of rainfall amounts is performed on a daily to monthly timescale through comparison with co-located manually read ‘check-gauges’. If the difference exceeds 8 % of the check-gauge total, the tipping-bucket data is labelled as ‘suspect’. Further quality control is subsequently performed by the Met Office through comparison with nearby gauges, radar measurements, and other data sources.

### 2.3.3 Atmospheric soundings

Radiosondes are used across the globe to provide vertical profiles of air temperature, humidity, and winds for weather forecasts and atmospheric research. These soundings are typically performed twice a day at 0000 and 1200 UTC. Data from the majority of sites is available from the website of the University of Wyoming, USA (<http://weather.uwyo.edu/upperair/sounding.html>). In Chapter 4, data from one of these sites (Camborne in the southwest of England) are used to analyse and compare the environments of two QSCSs.

## Chapter 3

# A climatology of QSCSs in the UK

### 3.1 Introduction

#### 3.1.1 Background and motivation

As discussed in Chapter 1, QSCSs can produce very large amounts of rainfall over a period of several hours giving the potential for flash flooding. Accurately predicting the timing and location of these storms is therefore imperative to allow for the timely issuance of warnings. However, this remains a great challenge for NWP models, despite significant advances in resolution, subgrid physical-process parameterisations, and data-assimilation techniques. In part, this reflects the low intrinsic predictability (Lorenz 1969) of convective weather (Zhang *et al.* 2006; Melhauser and Zhang 2012). Convection-permitting ensemble simulations reveal rapid growth of small initial condition errors due to the nonlinearities inherent in moist processes, with an upscale transfer that ultimately leads to contamination of the mesoscale flow (e.g. Zhang *et al.* 2003; Zhang *et al.* 2007; Hohenegger and Schär 2007). Given these limitations, other sources of information must be sought to try to maximise forecast accuracy for high-impact convective weather. One approach is to use knowledge of past events and their environments to infer the likelihood of future events given information about the (generally more predictable) large-scale conditions. This is one purpose of an event climatology. Climatologies may also be used to better understand the physical processes controlling a particular phenomenon or (given a sufficiently long data record) assess changes in event frequencies and characteristics over time.

Climatologies of extreme-precipitation and flash-flood events have been produced for many different regions around the world (e.g. Maddox *et al.* 1979; Kodama and Barnes 1997; Hand *et al.* 2004; Ricard *et al.* 2012). Several of these studies have shown that QSCSs are one of the dominant modes of convective organisation which commonly produce large rainfall accumulations (e.g. Schumacher and Johnson 2005; Jessup and Colucci 2012). However, to my knowledge, no previous investigators have set out specifically to develop a climatology of quasi-stationary storms. Doing this for the UK was a key objective of my project. The purpose was two-fold. First, to establish

the main characteristics of QSCSs in the UK; their frequency, geographic distribution, and seasonal and diurnal variation. Second, to examine the environments of QSCSs and identify any unique characteristics that could be used to improve forecasts of these systems. The distinction between this work and previous studies is the focus on a particular mode of convective organisation that often leads to heavy rainfall and flash flooding, rather than the heavy rainfall/flooding itself.

### 3.1.2 Chapter aims and structure

The aim of this work chapter was to develop a climatology of quasi-stationary convective systems and their environments for the UK, in order to address the following questions:

1. How frequently do QSCSs occur in the UK?
2. How have past QSCSs been distributed geographically and are certain regions of the country more favourable for their occurrence than others?
3. How does the occurrence of QSCSs vary interannually, seasonally, and with the diurnal cycle?
4. Do certain large-scale conditions favour the occurrence of QSCSs generally and/or in particular geographic locations?
5. Are the environmental conditions associated with QSCSs significantly different from those that generally characterise UK convective episodes?

Development of a climatology that would address these questions required three things: a dataset in which QSCSs could be identified, a method to do this, and data to characterise the large-scale conditions in which the identified events formed. Early on in the project, it was decided that the identification method needed to be automated to allow for the efficient processing of multiple years of data. This chapter thus begins with a review of existing published techniques for the automatic identification, classification, and tracking of convective storms (Section 3.2). The chosen input dataset and development of the identification algorithm is then described in Section 3.3. Included in the latter is a method to distinguish between convective and stratiform precipitation features which was applied in isolation to produce a five-year climatology of convection in the UK. This is presented in Section 3.4 and compared to a similar dataset from Hand (2005). The full algorithm was then applied to the same five-year period and identified events were subjectively placed into one of six categories based on their organisational characteristics. This classification procedure and the event categories are described in Section 3.5. Subsequent analysis focused on QSCSs (one of the six categories) and is presented in Section 3.6. First, the geospatial and temporal distributions of these events are examined. Then, the large-scale and local environmental characteristics of QSCSs are analysed and compared to those for a simple climatology of summertime convective events over the southern UK. Finally, Section 3.7 summarises the findings of this chapter.

## 3.2 The automatic identification, classification, and tracking of convective storms

When dealing with large, dynamic datasets, manual analysis becomes prohibitively time-consuming and there is a need to automate the process. This can be challenging, particularly in the case of spatial grids because algorithms must mimic the highly evolved capabilities of the human visual system. In the atmospheric science community, the use of so-called *data-mining* algorithms has become widespread, driven by the need to extract useful information on meteorological phenomena from very large observational and model datasets. Convective storms represent one such phenomenon. In this case, algorithms are typically developed to meet one of the following objectives: (1) to create climatologies of convective storms, their associated hazards, and environments for statistical analysis or model verification; (2) to distinguish between convective and stratiform cloud/precipitation systems; or (3) to make short-range predictions (nowcasts) of the movement of observed convective storms. All of these require a method to *identify* convective storms; that is, to extract the subset of the input dataset(s) that define these features based on a number of criteria. The second additionally demands a scheme to *classify* identified precipitation systems according to certain unique characteristics. This may also be a requirement of climatological analyses if, for example, the focus is on one or more specific modes of convective organisation. The third objective also requires a method to *track* features across adjacent time frames and thus estimate their velocity. Tracking may also be applied in climatological studies if information on the lifecycle of storms is desired.

This section reviews published techniques for the automatic identification, classification, and tracking (ICT) of convective storms, beginning with a discussion of the datasets typically used in these algorithms.

### 3.2.1 Data sources

Any dataset that is to be used as input to an automatic identification algorithm must provide information that uniquely characterises the features of interest. In the case of convective storms, this information may relate to the cloud or precipitation structure, vertical velocities within updraughts, or the occurrence of lightning. Virtually all modern ICT algorithms use observations from remote-sensing platforms, typically either ground-based radar or satellites. The advantage of these datasets is that they provide coverage of a large area at high spatial and temporal resolution. A potential disadvantage is that the meteorological variables of interest are not measured directly, but inferred from quantities that can be measured (rain rates from radar reflectivity, cloud-top temperatures from infrared radiances, etc.). Thus, consideration must be given to whether processing is performed using the measured or derived variables. To avoid errors introduced in the computation of rain rate, most radar-based ICT algorithms use reflectivity data, while satellite-based methods typically use low brightness

temperatures as a proxy for high cloud tops. Consideration must also be given to the need for preprocessing of the image, either to mitigate measurement errors or prepare it for subsequent analysis (Lakshmanan 2012, Chapter 5).

The choice between radar and satellite data depends primarily on their respective coverage over the area of interest. Most of the Earth's surface is not covered by ground-based radar, therefore satellite measurements are the only option for identifying convective storms on a global or large regional scale. However, in some countries, national radar networks provide near complete coverage. The choice then depends on data resolution and quality, and the specific purposes of the algorithm. Radar data may be preferable at high latitudes due to parallax errors in satellite images, while satellite measurements may be better in areas of complex orography where blocking of radar beams can be severe. Some ICT algorithms use both data sources; for example, Hand (2005) created a climatology of convective showers over the UK using satellite imagery to distinguish between stratiform and convective cloud and radar measurements to identify areas of rainfall. Other data may also be incorporated; for example, the FLASH project (Price *et al.* 2011) used lightning observations from Very Low Frequency antennas across Europe to characterise flash flood-producing convective storms in the Mediterranean region.

It is worth noting that ICT algorithms may also be applied to high-resolution model data, either to investigate physical processes in convective systems (Tao *et al.* 1993b; Xu 1995) or to allow for feature-specific forecasting (Carley *et al.* 2011) and verification (Caine *et al.* 2013; McBeath *et al.* 2014). However, numerical models are only appropriate for climatologies if they have a very accurate representation of the phenomena of interest. Currently, this is not the case for convective storms.

### 3.2.2 Identification

One of the simplest methods of identifying convective storms is to choose an appropriate threshold value of the input data field so that pixels on one side of this value are part of a storm and the rest are not. Contiguous groups of pixels can then be clustered to form objects or regions which are given a unique label. Dixon and Wiener (1993) applied this method in their Thunderstorm Identification, Tracking, Analysis, and Nowcasting (TITAN) algorithm which was designed for use on three-dimensional radar measurements. A reflectivity threshold of 35 dBZ was used together with a minimum volume threshold of 50 km<sup>3</sup> to prevent subsequent tracking of noise or ground clutter and to limit the total number of identified storms. Similarly, Vila *et al.* (2008) applied a brightness temperature threshold of 235 K and a minimum area threshold of 2,400 km<sup>2</sup> to infrared satellite imagery to identify MCSs in their Forecasting and Tracking the evolution of Cloud Clusters (ForTraCC) algorithm.

Slight variations of the basic thresholding technique exist. For example, The Storm Cell Identification and Tracking (SCIT) algorithm introduced by Johnson *et al.* (1998) uses seven reflectivity thresholds, increasing the value from 30 to 60 dBZ in 5 dB intervals

and rejecting objects at lower thresholds that contain objects at a higher threshold. In this way, clusters and lines of storms are split into their component cells. Peak and Tag (1994) took a similar approach but only rejected objects at a lower threshold if they contained two or more objects at a higher threshold. Han *et al.* (2009) presented a series of improvements to the TITAN algorithm including the application of an erosion operator to mitigate the problem of false mergers, where two adjacent storms are treated as a single entity. In contrast, Baldwin *et al.* (2005) considered neighbouring objects part of the same rainfall system if they were within five pixels ( $\sim 20$  km) of each other.

More complicated methods of storm identification include the enhanced watershed transform introduced by Lakshmanan *et al.* (2009), and the  $K$ -Means clustering approach of Lakshmanan *et al.* (2003). Both of these avoid the need for global thresholds, instead allowing for the growth of regions around local maxima/minima. The latter additionally does not require that pixels within an object be contiguous, only that they are all “similar” as measured by a multi-parameter distance metric.

### 3.2.3 Classification

The purpose of a classification scheme is to place a set of objects into categories based upon their similarity to known classes or each other. Development such schemes involves first identifying object attributes which offer some level of discriminating power. These can then be formalised as a set of rules which form the basis of the algorithm. Testing and refinement of the classification rules may be performed using a training dataset. This consists of objects for which the classifications are already known, either based on manual analysis by a suitably qualified individual or application of an existing automated technique. However, in cases where misclassification can be readily identified, tuning may be performed through simple trial and error.

Classification of objects is sometimes implicit in the identification procedure. For example, the 35 dBZ reflectivity threshold used in the TITAN algorithm is sufficiently high that the identified features are predominantly convective. However, if the objective is to identify multiple meteorologically distinct features, a separate (explicit) classification scheme is required. One of the most common purposes of such a scheme is to distinguish between convective (C) and stratiform (S) precipitation systems. This is motivated by two issues. First, C and S systems produce distinct vertical profiles of latent heating which have important implications for global circulation and climate (e.g. Hartmann *et al.* 1984). While the heating cannot be directly measured, its vertical integral can be inferred from the precipitation field (e.g. Tao *et al.* 1993a). By partitioning observed rainfall into C and S components it is thus possible to estimate the full three-dimensional structure of heating. The second motivation relates to radar-based measurements of precipitation. It has been shown that C and S precipitation display distinct  $Z$ - $R$  relationships associated with differences in the underlying raindrop size distributions (e.g. Tokay and Short 1996; Ulbrich and Atlas 2002). Furthermore, computation of surface rain rates from reflectivity measurements aloft requires assumptions

about the vertical profile of reflectivity which differs in C and S systems (e.g. Kitchen *et al.* 1994). Knowledge of the precipitation type can therefore be used to improve rainfall retrievals.

Before discussing automated methods for distinguishing C and S precipitation, it is worth noting the physical definition of the two. These are based on the characteristic vertical velocity scales of C and S clouds (Houghton 1968; Houze 1997). Stratiform precipitation is associated with vertical air motions that are small compared to the fall velocity of ice crystals and snow ( $\sim 1\text{--}3\text{ m s}^{-1}$ ), while convective precipitation forms in stronger updrafts of  $\sim 1\text{--}10\text{ m s}^{-1}$ . Ideally, a C–S classification scheme would therefore use vertical-velocity measurements. This was the approach of Atlas *et al.* (2000). They applied a separation threshold of  $1\text{ m s}^{-1}$  to vertical-velocity data from aircraft penetrations of tropical clouds, and used simultaneous in-situ observations of drop-size distributions to derived unique  $Z$ – $R$  relationships for C and S precipitation. Of course, observations of vertical motion are not routinely available so for most purposes C–S classification must be based on other variables.

Numerous schemes have been presented which use either two- or three-dimensional radar reflectivity data. While these vary in their details and complexity, they are generally based on a number of well-defined differences in the horizontal and vertical structure of C and S precipitation systems, which in turn can be linked to the different characteristic vertical velocities. As discussed in Chapter 1, convective cells are characterised by an intense, narrow updraught where precipitation particles grow rapidly through accretion of cloud liquid water. This leads to a pronounced core of high reflectivity with strong horizontal gradients on its peripheries. In contrast, the large-scale, weak ascent in regions of stratiform precipitation gives rise to echoes that are quite horizontally homogeneous. Stratiform echoes also typically feature a layer of higher reflectivity around the freezing level known as the ‘bright band’, which is associated with changes in the optical properties of snow crystals as they begin to melt (Austin and Bemis 1950).

One widely cited method of C–S precipitation classification which uses only information about the horizontal echo structure is that of Steiner *et al.* (1995, hereinafter SHY95). In line with the preceding discussion, convective precipitation is identified by its high and peaked values of reflectivity. Specifically, pixels are classed as convective either if their reflectivity exceeds 40 dBZ or exceeds the average background reflectivity  $Z_{\text{bg}}$  (computed over non-zero echoes within an 11 km radius) by a certain amount. This amount is defined as a nonlinear function of  $Z_{\text{bg}}$ , with a lower difference threshold for high background reflectivities. All pixels within a certain radius of the convective cores (again, a function of  $Z_{\text{bg}}$ ) are also classified as convective and the remaining non-zero echoes are classified as stratiform. Using aircraft measurements, the authors demonstrated that their method provides classifications which are consistent with the definitions of C and S precipitation. Further validation was provided by Ulbrich and Atlas (2002) who found good agreement between the  $Z$ – $R$  relationships derived using the vertical velocity–based method of Atlas *et al.* (2000) and those of Yuter and Houze (1995) who used the SHY95 algorithm.

An alternative method to characterise the horizontal echo structure was presented by Baldwin *et al.* (2005). They used hourly accumulation data (derived from radar and rain gauges) to identify precipitation objects and fitted a gamma distribution to the rain histogram of each. This distribution is described by two parameters, called the shape and scale parameters, which respectively determine the skewness and the weight in the right-hand tail of the distribution (e.g. Wilks 2011). Through experimentation, the authors found that the scale parameter gave significant discriminating power, with stratiform rain objects characterised by lower values, indicative of fewer pixels with large rain amounts. This parameter thus acts in a similar way to the two criteria (intensity and peakedness) used by SHY95.

Other authors have used information on both the horizontal and vertical structure of radar echoes to distinguish C and S precipitation. For example, Biggerstaff and Listemaa (2000) extended the SHY95 algorithm with a series of checks based on the full three-dimensional reflectivity field. These were designed to deal with two main sources of error: classification of heavy stratiform rain as convective and classification of rain on the periphery of convective cores as stratiform. Pixels are reclassified if they fail to meet a number of criteria based on the horizontal and vertical gradients of reflectivity, and a modified version of the bright-band fraction defined by Rosenfeld *et al.* (1995). A similar technique is used to classify echoes observed by the precipitation radar on board the Tropical Rainfall Measuring Mission (TRMM) satellite (Awaka *et al.* 1997). Other schemes using 3-D reflectivity data include those of Anagnostou (2004) and Yang *et al.* (2013), who respectively used a neural network—a type of supervised learning algorithm—and a ‘fuzzy logic’ approach to perform their classifications.

A number of satellite-based classification schemes have also been developed (e.g. Adler and Negri 1988; Hong *et al.* 1999; Sui *et al.* 2007). One considered for the present study was that of Pankiewicz (1997). This used a neural network to analyse subdomains within Meteosat visible and infrared images and place each into one of four categories: clear sky, dynamic cloud, shallow convection, and deep convection. The algorithm was subsequently incorporated in the Met Office’s nowcasting system, GANDOLF (Pierce *et al.* 2000), and used by Hand (2005) in combination with data from the UK radar network to create a climatology of convective showers over the UK.

Some studies have taken the classification of cloud/precipitation systems beyond just C and S discrimination. Typically, this involves subdivision of convective features according to their organisational structure. This is motivated by the fact that the type and extent of hazardous weather associated with convective systems is often related to their mode of organisation (e.g. Gallus *et al.* 2008). Example studies include Baldwin *et al.* (2005) who considered just two convective classes, linear and cellular, and Gagne *et al.* (2009) who further subdivided these into six classes: isolated pulse, isolated strong, multicells, and leading-, trailing-, and parallel-stratiform linear systems. Since the mode of convective organisation is strongly dependent on certain environmental parameters (Section 1.2.3), some schemes use these, derived from observations or model data, to provide more meteorologically precise classifications (e.g. Lack and Fox 2012).

### 3.2.4 Tracking

So far, we have seen how convective storms may be automatically identified and classified based on their characteristics. Such schemes can be used to assess the spatial and temporal variability of storms as well as their physical characteristics. However, it is often desirable to understand how storms move and evolve during their lifetime. This necessitates the use of a tracking algorithm.

The fundamental step in any tracking scheme is the association of storms identified in the current time frame  $t_n$  with those identified in the previous time frame  $t_{n-1}$ . If an association is made, the storm at  $t_n$  inherits the label (and history) of the storm at  $t_{n-1}$ ; if not, then the storm at  $t_n$  is given a new label. This procedure is non-trivial because storms grow, decay, split, and merge. Typically, association is based on the proximity of storms or the degree of overlap between them. Other considerations include similarity in size and intensity and the age of the storm (i.e. the number of times in its track history). The occurrence of multiple suitable associations for a given storm indicates a split or merger. In the case of a split, multiple storms at  $t_n$  are associated with a single storm at  $t_{n-1}$ ; in the case of a merger, a single storm at  $t_n$  is associated with multiple storms at  $t_{n-1}$ . In either situation, careful consideration must be given to how the storm histories are propagated through the association.

For the original TITAN algorithm, Dixon and Wiener (1993) define a cost function as the sum over all object pairs of a weighted combination of the distance between the object centroids and the absolute difference in the cubed-root of their volume. This is minimised to provide a globally optimal association of all objects in the two frames. A maximum speed of  $60 \text{ km h}^{-1}$  is imposed to prevent association of storms over unrealistically large distances. However, the use of centroid displacement to determine storm motion means that this condition may be violated by sudden changes in storm shape, particularly for large storms. To mitigate this problem, Han *et al.* (2009) apply a dynamic maximum-speed constraint in their enhanced TITAN (ETITAN) algorithm which increases with storm area. Association is further improved through the use of an initial step where storms at  $t_{n-1}$  are projected forward based on their estimated motion and linked with storms at  $t_n$  if there is significant overlap between them. To determine storm motion, the authors employ the Tracking Radar Echoes by Correlation (TREC) algorithm of Rinehart and Garvey (1978), which computes a motion vector field for the entire radar scan based on cross-correlation of image subdomains at  $t_{n-1}$  and  $t_n$ . This technique has been widely used in nowcasting systems (e.g. Evans and Ducot 1994; Golding 1998) as it is accurate and can be implemented efficiently for large spatial grids using the Fast Fourier Transform (Lakshmanan 2012, Chapter 7).

Most other radar-based storm-tracking algorithms use some variation on the techniques described above. In the SCIT algorithm of Johnson *et al.* (1998), storms at  $t_{n-1}$  are projected forward and simply linked to the nearest storm at  $t_n$ . The motion vector in this case is computed using a linear least-squares fit of the storm's recent positions. Lakshmanan *et al.* (2009) also match projected storms at  $t_{n-1}$  with those at  $t_n$ ; however,

in their algorithm the matching is based on both distance and age, with longer-lived storms being favoured over younger ones. Motion estimates are again smoothed over time, in this case using a constant-acceleration Kalman filter (Kalman 1960). Finally, Lakshmanan and Smith (2010) combine aspects of the tracking algorithms of Dixon and Wiener (1993), Johnson *et al.* (1998), Han *et al.* (2009), and Lakshmanan *et al.* (2009) to devise a new method which is shown to outperform the others based on a series of objective criteria.

A number of tracking algorithms which use satellite data have also been developed. Many of these associate storms based on their degree of overlap, without any forward projection (e.g. Williams and Houze 1987; Boer and Ramanathan 1997; Mathon and Laurent 2001). Machado *et al.* (1998) demonstrate that this simple method performs comparably to more complex tracking algorithms provided the time step between frames is quite short (<3 h). This is because convective storms defined by their cloud shield are larger than those defined by the precipitation footprint seen by radar and less likely to undergo splitting and merging. However, as with radar-based storm tracking, other parameters may be incorporated to improve the association in cases of multiple overlapping storms (see Table 1 of Machado *et al.* 1998).

### 3.3 Data and methods

The objective of this work was to devise a method for the automatic identification of quasi-stationary convective systems in archived observational data. Such a method would have two basic requirements: (1) the ability to distinguish between convective and stratiform systems, and (2) the ability to isolate features showing limited movement over a period of several hours. These considerations motivated the choice of dataset. As noted in the previous section, satellite imagery and ground-based radar measurements are both suitable for the automatic identification, classification, and tracking of convective storms, and both are available over the UK at good spatial and temporal resolution. I originally considered using the neural-network algorithm of Pankiewicz (1997) to distinguish between convective and stratiform cloud in Meteosat imagery. However, Hand (2005) noted that it was unreliable at night due to the absence of the visible channel, and could not identify convection beneath thick upper-level cloud, including well-developed cumulonimbus anvils. Given these shortcomings, I opted to develop my own algorithm which would be applied to data from the UK 1 km radar composite product (RCP1). The high spatial resolution of these data means that the strong rainfall gradients characteristic of convection (Section 3.2.3) can be observed, while the short time step between images (5 mins) allows the movement of identified features to be determined with high accuracy (Section 3.2.4). Further details of the RCP1 are given in Section 2.1.

The first step in building my algorithm was selecting a method to identify rainfall objects within the radar images. I opted for a simple thresholding approach using an existing piece of code provided by Giovanni Leoncini (at the time, a researcher

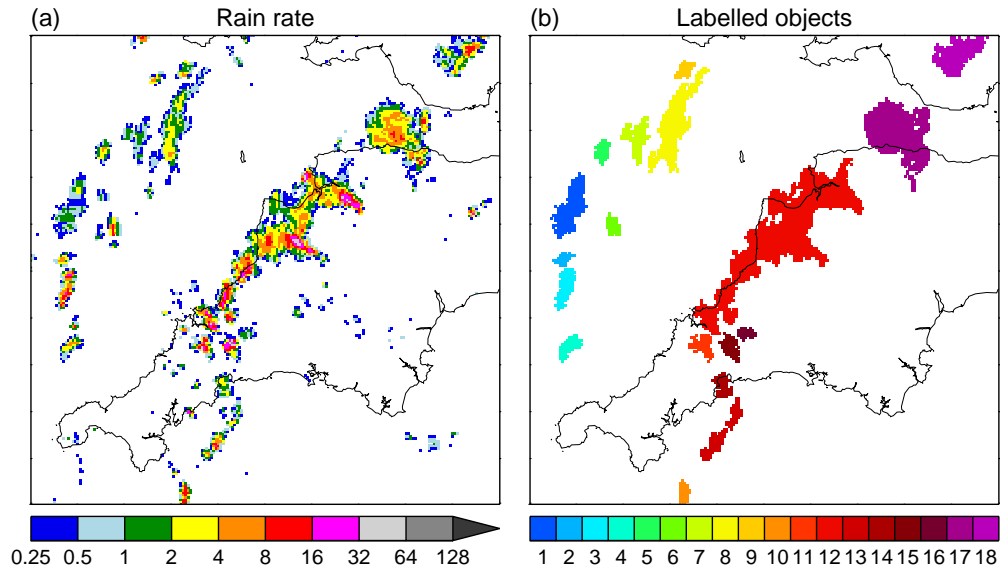


**Figure 3.1** Example of rainfall object identification and labelling. (a) Rain rate ( $\text{mm h}^{-1}$ ) over southwest England at 1200 UTC on 21/07/2010. (b) Objects (coloured by their label number) identified using the region growing code with  $R^* = 0.25 \text{ mm h}^{-1}$  and  $S_R^* = 25 \text{ km}^2$ .

with the MetOffice@Reading). This loops through a data array and labels contiguous pixels above a user-specified threshold as unique objects using the procedure of ‘region growing’. For every pixel that is above the threshold and not yet part of an object (region), a new object is initialised. The eight neighbours of that pixel are then examined and any which exceed the threshold are assigned to the current object. The neighbours of these pixels are also searched and the process continues recursively until the object is complete. The original algorithm was modified to include a minimum size criterion so that objects smaller than this are rejected. Thus, there are three key inputs: the rainfall data array (of size  $nx \times ny$ ), and the thresholds for rain rate  $R^*$  and object size  $S_R^*$ . The output of the algorithm is an  $nx \times ny$  array of the label number at every pixel (zero for pixels that are not part of an object) together with a list containing the size and centroid coordinates of every object.

Figure 3.1 demonstrates the application of this algorithm to a subdomain of an RCP1 image using the rain rate and size thresholds that were applied in the final algorithm (see Table 3.1). The choice of these parameters was largely dictated by the next consideration: isolating convective rainfall features.

Given that the RCP1 contains only 2-D measurements, many of the C–S discrimination methods discussed in Section 3.2.3 could not be used. The SHY95 algorithm would be suitable, although it would need tuning since it was originally developed using measurements of tropical rainfall on a 2 km grid. However, I opted instead for a novel approach based on work by Nigel Roberts at the MetOffice@Reading. The underlying principle is similar to that of SHY95 (and many other schemes): mature convective cells tend to produce high-intensity rainfall with large horizontal gradients in reflectivity/rain rate. Originally, the method was designed to be applied to square subdomains of a larger image; however, it was modified to allow for classification of individual rainfall

**Table 3.1** Thresholds for rainfall object identification and C–S classification.

Symbol	Meaning	Value	Considerations
$R^*$	Minimum rain rate ( $\text{mm h}^{-1}$ ) for object identification	0.25	Should be small enough that large rainfall gradients are within object
$S_R^*$	Minimum size ( $\text{km}^2$ ) for object identification	25	Should be large enough to exclude small areas of noise
$\Delta R^*$	Minimum $\Delta R_{\text{max}}$ ( $\text{mm h}^{-1}$ ) in object for C classification	1	Should be common in C rain but rare in S rain
$F^*$	Minimum fraction of object with $\Delta R_{\text{max}} \geq \Delta R^*$ for C classification	0.3	Should be large enough to exclude virtually all S rain

objects. The procedure is relatively straightforward. For every pixel within an object, the maximum difference  $\Delta R_{\text{max}}$  between its rain rate  $R$  and the rain rate of each of its eight neighbours is computed. Then, the fraction  $F$  of object pixels with  $\Delta R_{\text{max}} \geq \Delta R^*$  is found, where  $\Delta R^*$  is a threshold. If  $F \geq F^*$ , another threshold, then the object is labeled as convective. The use of a fraction rather than the object-maximum  $\Delta R_{\text{max}}$  is motivated by the fact that the latter would lead to incorrect classification of S rain containing even a single extreme-valued pixel, something which is quite common in the RCP1. For computational efficiency, the code to calculate  $\Delta R_{\text{max}}$  and  $F$  was added to the object-identification algorithm. Specifically,  $\Delta R_{\text{max}}$  at a given object pixel is computed during the neighbourhood search and the number of pixels with  $\Delta R_{\text{max}} \geq \Delta R^*$  is updated as the object is grown;  $F$  is then found by dividing this number by the total number of object pixels.

The classification scheme is demonstrated in Figures 3.2 and 3.3, again using the thresholds in the final algorithm (Table 3.1). These were selected through experimentation to try to maximise the correct identification of mature convective storms while minimising the incorrect labelling of stratiform rain as convective. Figure 3.2 shows a collection of showers over the Southwest Peninsula of England (the organised line over the west coast is the QSCS which is investigated in Chapter 4) while Figure 3.3 shows an area of frontal rain over western Scotland with a few showers to the southeast. We see that the more intense storms are classified as convective due to their stronger rainfall gradients while weaker cells and the frontal rain are classified as stratiform. Thus, the algorithm is not a true C–S precipitation classifier; rather, it isolates mature, deep convective storms from other forms of precipitation, including stratiform rain and lighter convective rain associated with shallow, growing, or decaying cells. However, this is perfectly adequate for the identification of QSCSs.

The second requirement of my algorithm is that it can identify quasi-stationary objects (QSOs). A number of approaches of varying complexity were considered, but the method ultimately applied was based on a simple premise: QSCSs produce quasi-continuous, heavy rainfall for a period of several hours, giving large accumulations.

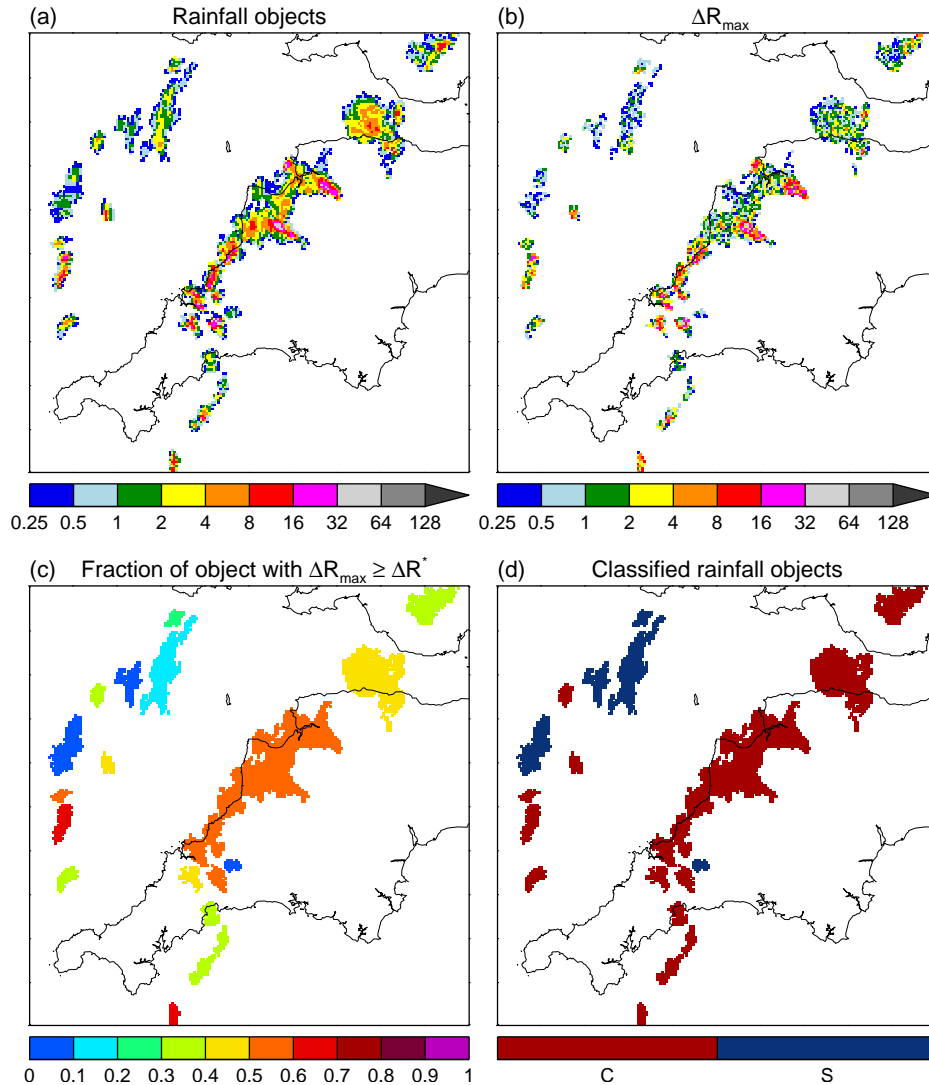


**Figure 3.2** Example of rainfall object classification. (a) Rain rate ( $\text{mm h}^{-1}$ ) for objects shown in Figure 3.1(b). (b) Neighbourhood-maximum pixel-to-pixel rain-rate difference  $\Delta R_{\max}$  ( $\text{mm h}^{-1}$ ) in objects. (c) Fraction of each object with  $\Delta R_{\max} \geq 1 \text{ mm h}^{-1}$ . (d) Object classifications obtained with  $F^* = 0.3$ .

Thus, accumulation objects were identified using a moderately high threshold (15 mm) and analysed to isolate those resulting from long-duration, quasi-continuous convective rainfall. The full procedure has the following steps:

1. Every  $\Delta T$  minutes, rainfall is accumulated over a period  $T$  by summing the rain rates in each frame and multiplying by the time step in hours. The accumulation from convective rain is also computed.
2. Accumulation objects are then identified using the region-growing code with thresholds for the minimum accumulation  $A^*$  and size  $S_A^*$ .
3. During the accumulation period, the first and last times ( $t_1$  and  $t_2$ , respectively) with  $R \geq R^*$  are stored at every grid point, together with the total number of times  $N_R$  for which  $R \geq R^*$ .

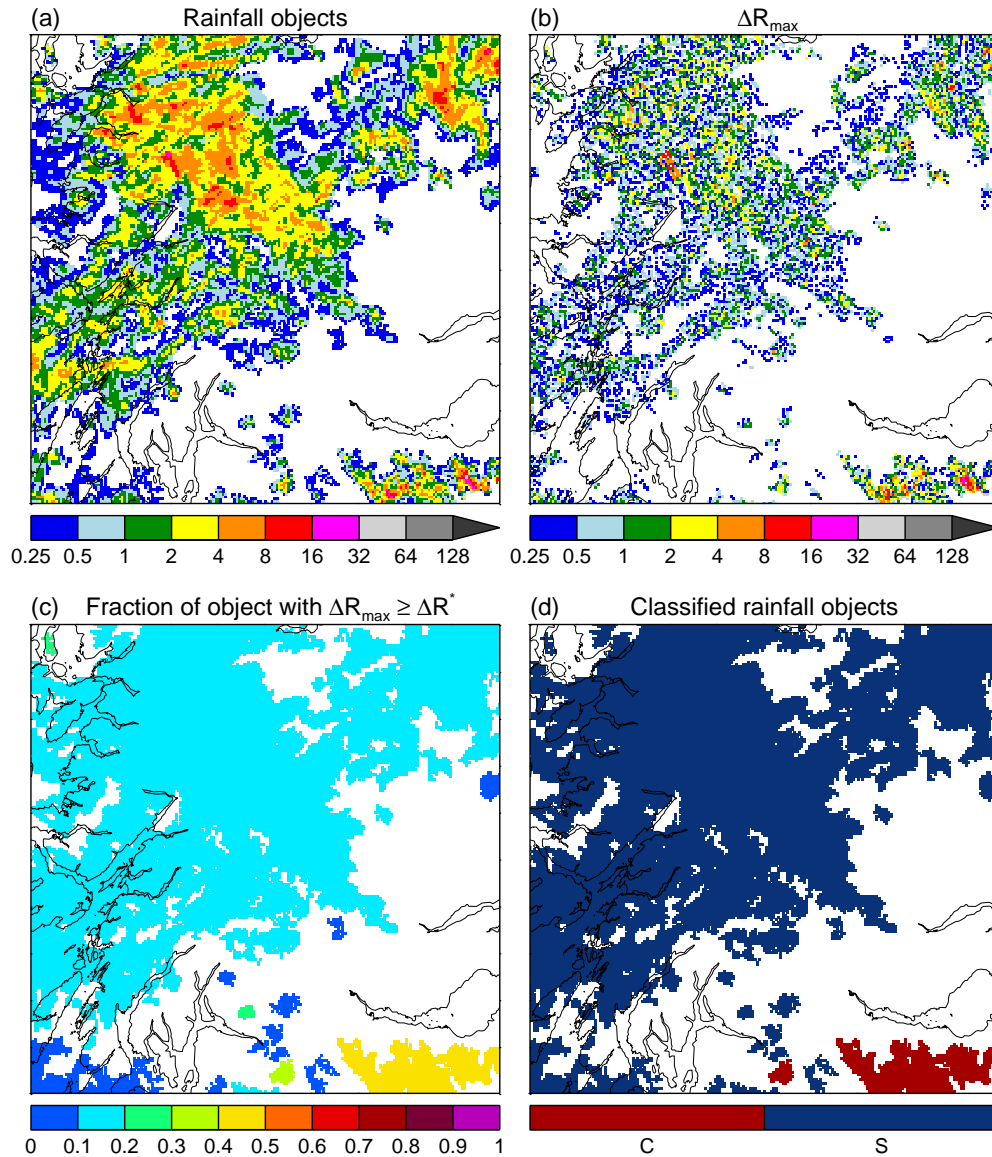


**Figure 3.3** As in Figure 3.2 but for over western Scotland at 1200 UTC on 21/07/2010.

4. From these the total rainfall duration  $T_R = N_R \times \Delta t$  (where  $\Delta t$  is the time step between images) and persistence ratio  $P_R = T_R / (t_2 - t_1)$  are computed. The latter quantity has a value between zero and one and provides a measure of how continuous the rainfall at a grid point was.
5. For each accumulation object, three fractions are computed:  $F_C$ , the fraction of the object-total accumulation due to convection,  $F_T$ , the fraction of the object area with  $T_R \geq T_R^*$ , and  $F_P$ , the fraction of the object area with  $P_R \geq P_R^*$ , where  $T_R^*$  and  $P_R^*$  are thresholds.
6. Accumulation objects for which  $F_C \geq F_C^*$ ,  $F_T \geq F_T^*$ , and  $F_P \geq F_P^*$  are then stored as candidate QSOs. The thresholds  $F_C^*$ ,  $F_T^*$ , and  $F_P^*$  are respectively used to ensure that the causative rainfall was mainly convective, long-duration, and quasi-continuous. For each candidate QSO, the grid points, label number, area,

duration, start and end time (defined respectively as the minimum  $t_1$  and maximum  $t_2$  within the object), and centroid coordinates are stored.

7. When a time is reached where no candidate QSOs can be found, the existing ones are examined and linked in time. This involves looping through the list of candidate QSOs and comparing all pairs of objects whose centroids are within a distance  $d_{\max}$ . Any objects which overlap both in space and time are linked. The links for each candidate QSO are represented by an ordered list containing that object's label and the labels of all the objects which it is linked to.
8. At the end of this procedure, the unique elements of the link array are identified and used to create a new set of candidate QSOs, consisting of the original objects linked temporally and spatially. For each of these, the object grid points, total size  $S$  (number of grid points), start and end time (defined respectively as the earliest start and latest end time of the component objects), and total duration  $D$  are computed, together with the centroid coordinates at every time. For times when there are multiple component objects, their centroids are averaged. Then, the maximum centroid movement in one time step  $d_{\text{step}}$  and the total centroid movement  $d_{\text{total}}$  (taken as the distance between the start and end positions) are computed.
9. To qualify as true QSOs, the resulting objects must meet a final set of criteria to ensure that they are (a) large enough ( $S \geq S^*$ ), (b) of sufficiently long-duration ( $D \geq D^*$ ), and (c) show little movement ( $d_{\text{step}} \leq d_{\text{step}}^*$  and  $d_{\text{total}} \leq d_{\text{total}}^*$ ).

The two main stages of this algorithm, the identification and linking of candidate QSOs, are illustrated in Figures 3.4 and 3.5 respectively, while Table 3.2 gives the values of the thresholds detailed above. These were again chosen largely through experimentation, though some were based more on simple reasoning. The thresholds used in the identification of candidate QSOs ( $T$ ,  $T_R^*$ ,  $P_R^*$ ,  $F_C^*$ ,  $F_T^*$ , and  $F_P^*$ ) were tuned by applying the algorithm to a training dataset consisting of a small number of manually identified QSCSs. This provided some confidence in the algorithm's hit rate (correct identifications), but did not illustrate the occurrence of false alarms (incorrect identifications). Subsequent application of the code to a larger dataset revealed that these were numerous, making up a majority of the identified events. It became apparent that, even with further tuning, the algorithm could not distinguish QSCSs from other long-duration heavy-rainfall events. To do this, one would need to infer either the existence of an approximately fixed initiation point or the cancellation of the advection and propagation components of system motion. While both approaches are feasible (see Chapter 6), it was decided due to time constraints that the algorithm would be applied as is to the full dataset, and QSCSs would subsequently be identified manually (Section 3.5).

The procedure described above identifies accumulation objects, each representing a unique long-duration convective rain event (LDCRE). For each of these, the following variables were stored:

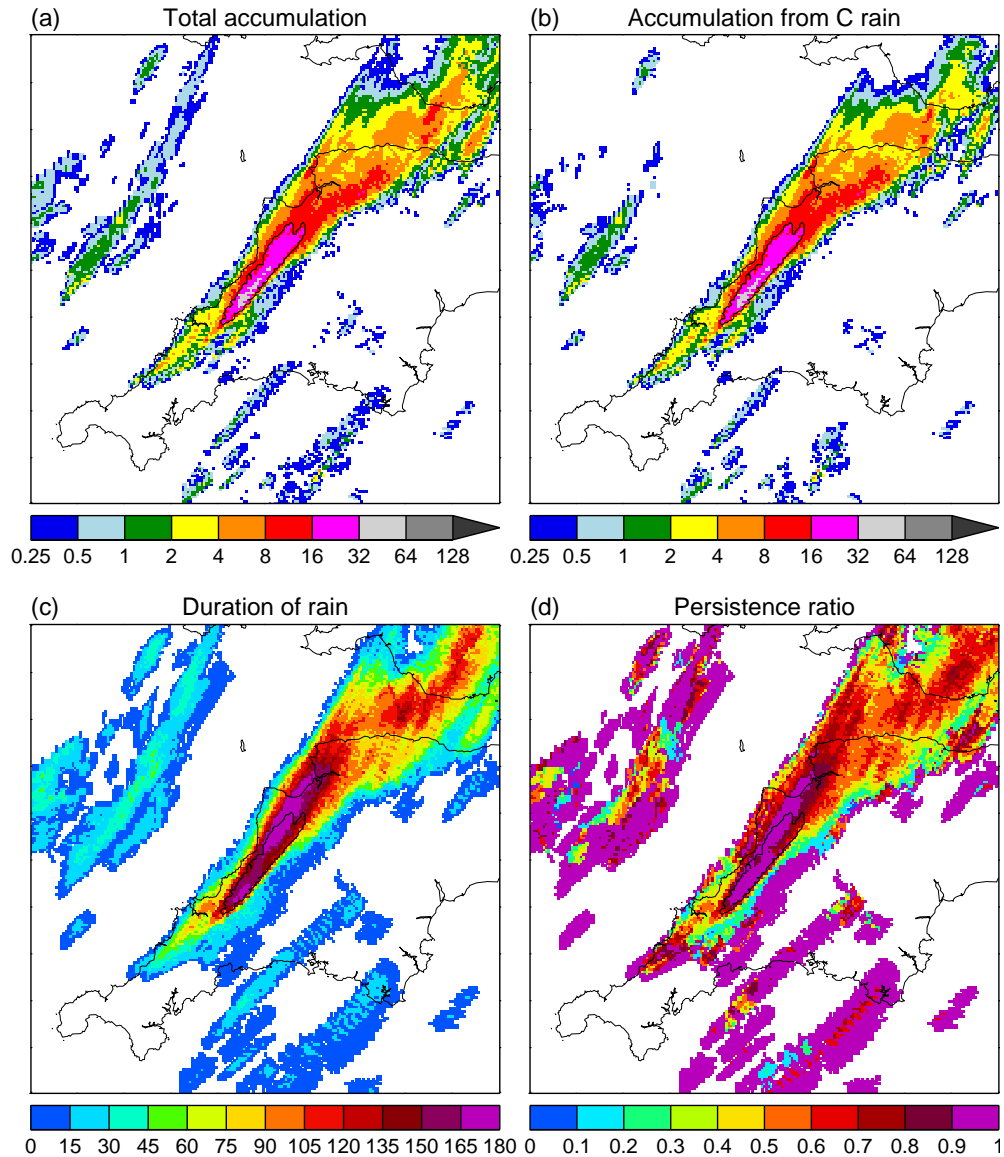


**Figure 3.4** Example of candidate quasi-stationary object identification. (a) Total accumulation (mm) over southwest England for 1200–1500 UTC on 21/07/2010. (b) Accumulation (mm) from convective rain. (c) Duration (mins) of rain with  $R \geq R^*$ . (d) Persistence ratio of rain with  $R \geq R^*$ . The black contour shows the accumulation object defined by  $A^* = 15$  mm and  $S_A^* = 25$  km<sup>2</sup>. For this object,  $F_C \geq F_C^*$ ,  $F_T \geq F_T^*$ , and  $F_P \geq F_P^*$  (see Table 3.2 for threshold values), so it is considered a candidate quasi-stationary object.

- Unique identifier
- Start time, end time, and total duration
- Number of pixels in the final accumulation object (equal to the area in km<sup>2</sup>)
- Parameters of an ellipse fitted to the accumulation object (centroid coordinates, major- and minor-axis lengths, and orientation)
- Accumulation maximum, 90<sup>th</sup> percentile, and average over the object pixels
- Time-averaged cell motion vector components and their standard deviations

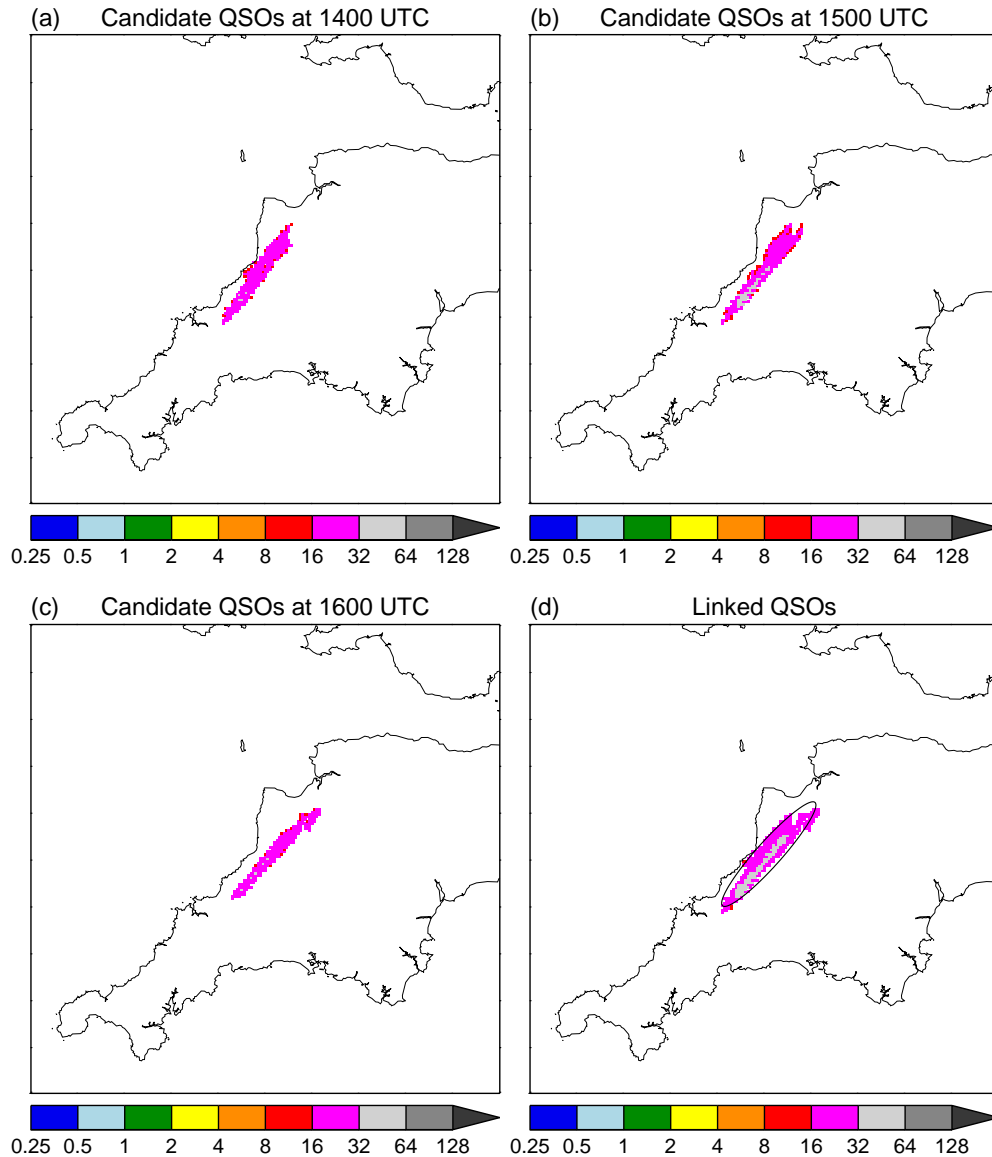


**Figure 3.5** Example of linking of candidate quasi-stationary objects. Accumulations (mm) for candidate QSOs over southwest England for the periods (a) 1100–1400 UTC, (b) 1200–1500 UTC, and (c) 1300–1600 UTC on 21/07/2010. (d) Total accumulation (mm) for the linked QSOs. The black contour in (d) shows the best-fit ellipse for the accumulation object.

The ellipse fitting was performed using a standard algorithm which computes the axes and orientation from the eigenvectors of the covariance matrix of the object pixel locations (e.g. Lakshmanan (2012), Chapter 6). The cell velocity, meanwhile, was estimated using the cross-correlation technique introduced in Section 3.2.4. For every time step in the event, the rain rate field is extracted over a  $201 \times 201$  km domain centred on the object centroid. For temporally adjacent frames  $F_1$  and  $F_2$ , the velocity is then estimated as follows:

1. Both frames are filtered using a Tukey window. This involves multiplying each

**Table 3.2** Thresholds for quasi-stationary object (QSO) identification.

Symbol	Meaning	Value	Considerations
$\Delta T$	Time step (mins) between accumulation periods	60	Objects in adjacent accumulation periods should overlap
$T$	Accumulation period (mins)	180	Should be long enough for moderately large accumulations
$A^*$	Minimum accumulation (mm) for object identification	15	Should be large enough to mainly identify intense and/or slow-moving systems
$S_A^*$	Minimum size (km <sup>2</sup> ) for object identification	25	Should be large enough to exclude small echoes associated with of noise
$T_R^*$	Minimum duration (mins) of $R \geq R^*$ in object for candidate QSO classification	120	Should be long enough to exclude short bursts of heavy rain
$P_R^*$	Minimum persistence ratio in object for candidate QSO classification	0.75	Rainfall should be quasi-continuous
$F_C^*$	Minimum fraction of object-total accumulation due to C rainfall for candidate QSO classification	0.6	The majority of rainfall should be from convection
$F_T^*$	Minimum fraction of object with $T_R \geq T_R^*$ for candidate QSO classification	0.5	Rainfall should be long-duration over at least half the object area
$F_P^*$	Minimum fraction of object with $P_R \geq P_R^*$ for candidate QSO classification	0.5	Rainfall should be quasi-continuous over at least half the object area
$d_{\max}$	Search radius (km) for linking of candidate QSOs	50	Objects associated with the same system should not move far between periods
$S^*$	Minimum size (km <sup>2</sup> ) for QSO classification	100	QSCSs should produce a larger area of high accumulations due to cell training
$D^*$	Minimum duration (mins) of $R \geq R^*$ for QSO classification	180	QSCSs can only be identified visually if they are stationary for several hours
$d_{\text{step}}^*$	Maximum centroid movement (km) in any $\Delta T$ for QSO classification	50	Movement of objects between periods should be minimal
$d_{\text{total}}^*$	Maximum start to end centroid movement (km) for QSO classification	50	Total movement of objects should be minimal

by a weight matrix given by  $\mathbf{W} = \mathbf{w} \cdot \mathbf{w}^T$  where

$$\mathbf{w} = \begin{cases} \frac{1}{2} \left\{ 1 + \cos \left[ \pi \left( \frac{2n}{\alpha(N-1)} - 1 \right) \right] \right\} & 0 \leq n \leq \frac{\alpha(N-1)}{2} \\ 1 & \frac{\alpha(N-1)}{2} \leq n \leq (N-1) \left( 1 - \frac{\alpha}{2} \right) \\ \frac{1}{2} \left\{ 1 + \cos \left[ \pi \left( \frac{2n}{\alpha(N-1)} - \frac{2}{\alpha} + 1 \right) \right] \right\} & (N-1) \left( 1 - \frac{\alpha}{2} \right) \leq n \leq N-1 \end{cases}$$

Here,  $n$  is vector index,  $N$  is the length of the vector, and  $\alpha$  is a parameter which determines the width of the central rectangular window where the weight equals one. I set  $\alpha = 0.5$ , so that rain rates maintain their original value in the inner  $101 \times 101$  grid-point area and taper to zero over the outer 50 grid points.

2. The normalised cross-correlation  $r$  of the two frames is then computed using the Digital Fourier Transform (DFT), specifically:

$$r = \mathcal{F}^{-1} \left( \frac{\mathcal{F}(F_1 - \bar{F}_1) \circ \mathcal{F}^*(F_2 - \bar{F}_2)}{\sigma_1 \sigma_2} \right)$$

where  $\mathcal{F}(x)$  is the DFT of  $x$ ,  $\mathcal{F}^{-1}(x)$  the inverse DFT,  $\mathcal{F}^*(x)$  the complex conjugate of the DFT,  $\bar{F}_i$  and  $\sigma_i$  are respectively the mean and standard deviation of the values in frame  $i$ , and  $\circ$  is the Hadamard (entry-wise) product. The DFTs are computed using Fast Fourier Transforms.

3. The location of the maximum in  $r$  gives the optimal displacement of the two frames which is converted to a velocity by dividing by the time step  $\Delta t$ .

This process is illustrated in Figure 3.6. Note that the filtering step is used to ensure that the maximum cross-correlation does not occur near the edges of the domain, giving an unrealistically large velocity estimate.

In addition to the variables listed above, an animation was produced for each event showing the evolution of the rain rate field over the  $201 \times 201$  km domain used in the velocity calculations. These were used to subjectively classify the events according to the organisational characteristics of the causative rainfall systems (Section 3.5).

### 3.4 A climatology of convective storms in the UK

As part of the development of my LDCRE identification algorithm, I tested the convection classification code in isolation. To do this, I followed the approach of Hand (2005, hereinafter H05) who developed a five-year (December 1999–November 2003) climatology of convective showers over the UK, subdivided by the season (MAM, JJA, SON, DJF), time of day (0000–0545, 0600–1145, 1200–1745, 1800–2345 UTC), and low-level wind direction (N, NE, E, SE, S, SW, W, NW). H05 used the neural network algorithm of Pankiewicz (1997) to identify regions of convective cloud in Meteosat imagery and the UK 5 km radar composite product to isolate precipitating pixels. Wind direction at  $\sim 900$  m was obtained from  $T + 9$  h forecasts from the Met Office mesoscale model,

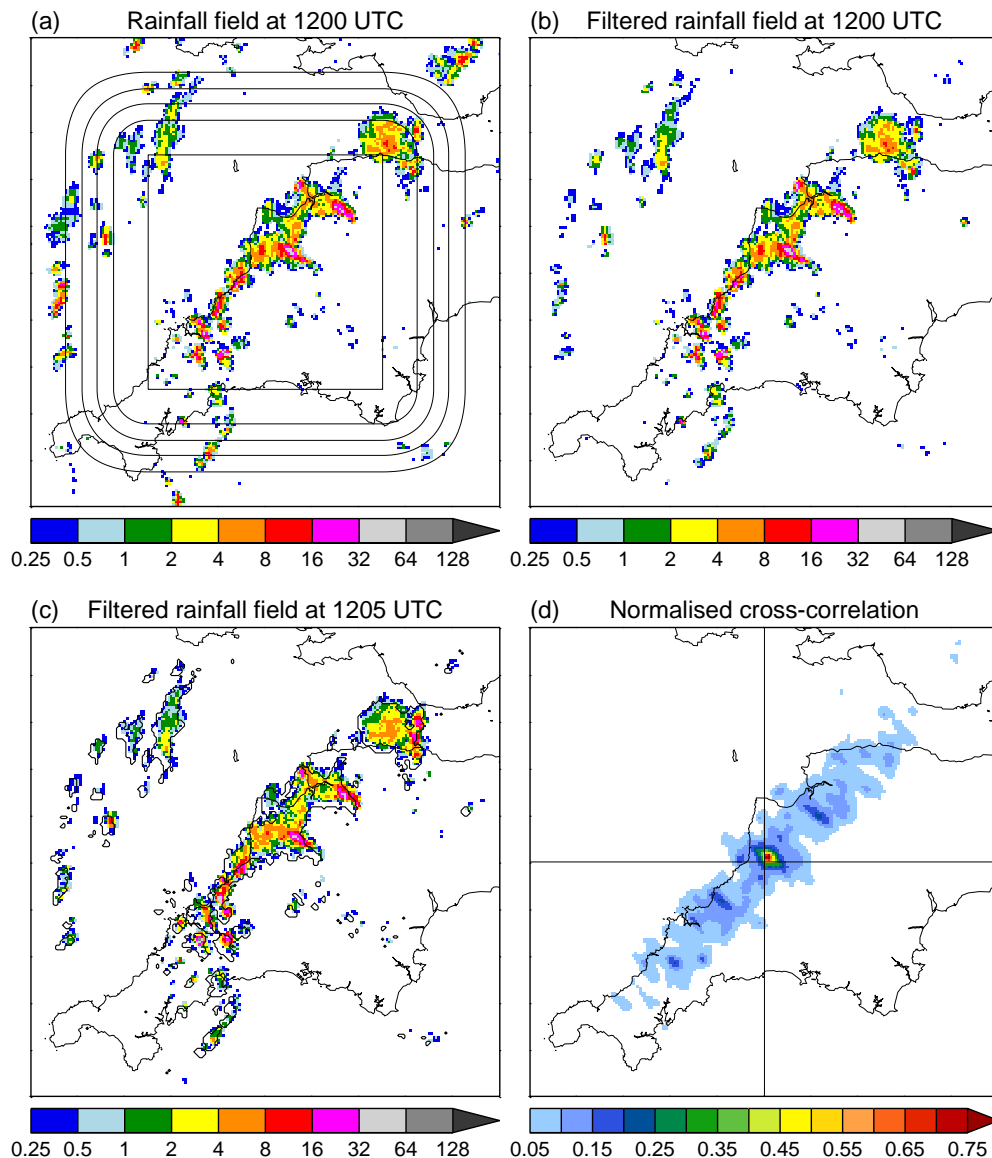


**Figure 3.6** Example of velocity estimation. (a) Rain rate ( $\text{mm h}^{-1}$ ) over southwest England at 1200 UTC on 21/07/2010. Black contours show the Tukey filter weights from 0.2 (outer) to 1 (inner) in intervals of 0.2. (b) Filtered rain rate field. (c) Filtered rain rate field at 1205 UTC. Black contours outline the filtered rain areas ( $R \geq 0.25 \text{ mm h}^{-1}$ ) at 1200 UTC. (d) Normalised cross-correlation matrix shifted  $(N - 1)/2 = 100$  points in the positive  $x$  and  $y$  directions. The maximum correlation is located at  $[2, 2]$  relative to the domain centre (the intersection of the thin vertical and horizontal black contours), indicating a velocity  $9.4 \text{ m s}^{-1}$  on a bearing of  $45^\circ$ .

verifying at 0300, 0900, 1500, and 2100 UTC. Winds less than  $5 \text{ m s}^{-1}$  were not assigned a direction, but placed in a separate ‘light wind’ category.

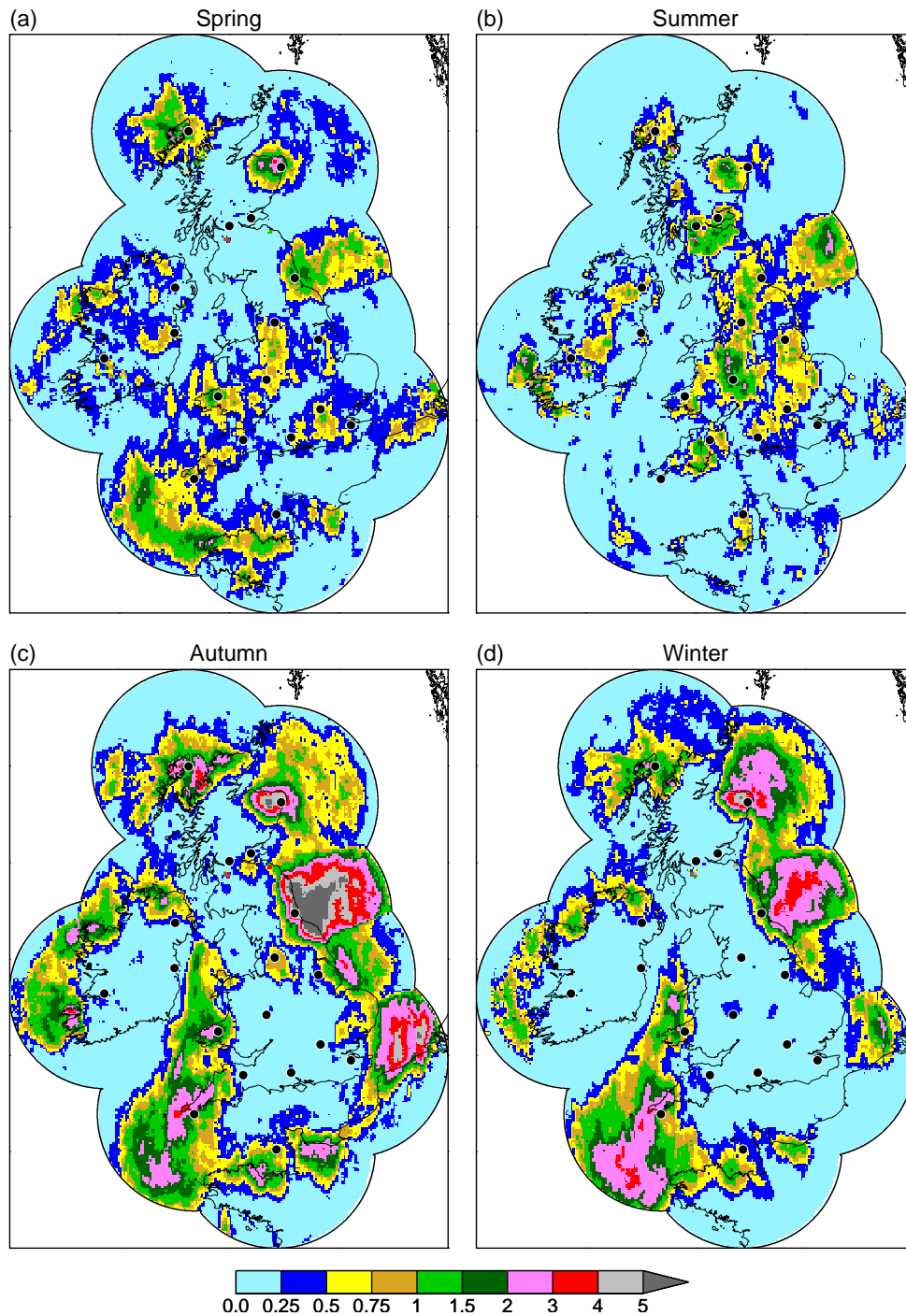
I also applied my convection code to five years-worth of data (January 2008–December 2012), but subdivided the resulting climatology only by season and wind direction to maintain reasonable sample sizes. Wind direction at 900 hPa was obtained from ERA-Interim analyses at 0000, 0600, 1200, and 1800 UTC. Values between these times were computed through linear interpolation of the velocity components (rather than assuming them to be constant as in H05). While convective precipitation was identified on

the full 1 km grid, frequencies were computed on a 5 km grid. Specifically, at a given time the convection count at each 5 km grid square was increased (by one) if *any* of the 25 1 km grid points within it were classified as convective. The frequency of convection for a particular wind direction and season was then computed by dividing the total convection count by the total number of occurrences of that wind direction during that season.

An updated version of the H05 climatology, covering December 1999–November 2006, was obtained and compared with my results. This revealed significant differences which can be related to the distinct nature of the two classification methods. While my algorithm isolates deep, mature convective storms with large rainfall gradients (Section 3.3), the H05 algorithm identifies *all* areas of convective rain, provided their cloud structures are not obscured by thick upper-level cloud. Therefore, the occurrence frequencies obtained by H05 are much higher than mine. Furthermore, H05 only presents results for the morning (0600–1145 UTC) and afternoon (1200–1745 UTC) periods because the neural-network classifier is unreliable at night when visible satellite images are not available. Thus, in the summer months, when there is a strong diurnal cycle of convection over land, my occurrence frequencies are likely to be further reduced relative to those of H05 due to the inclusion of the nighttime hours.

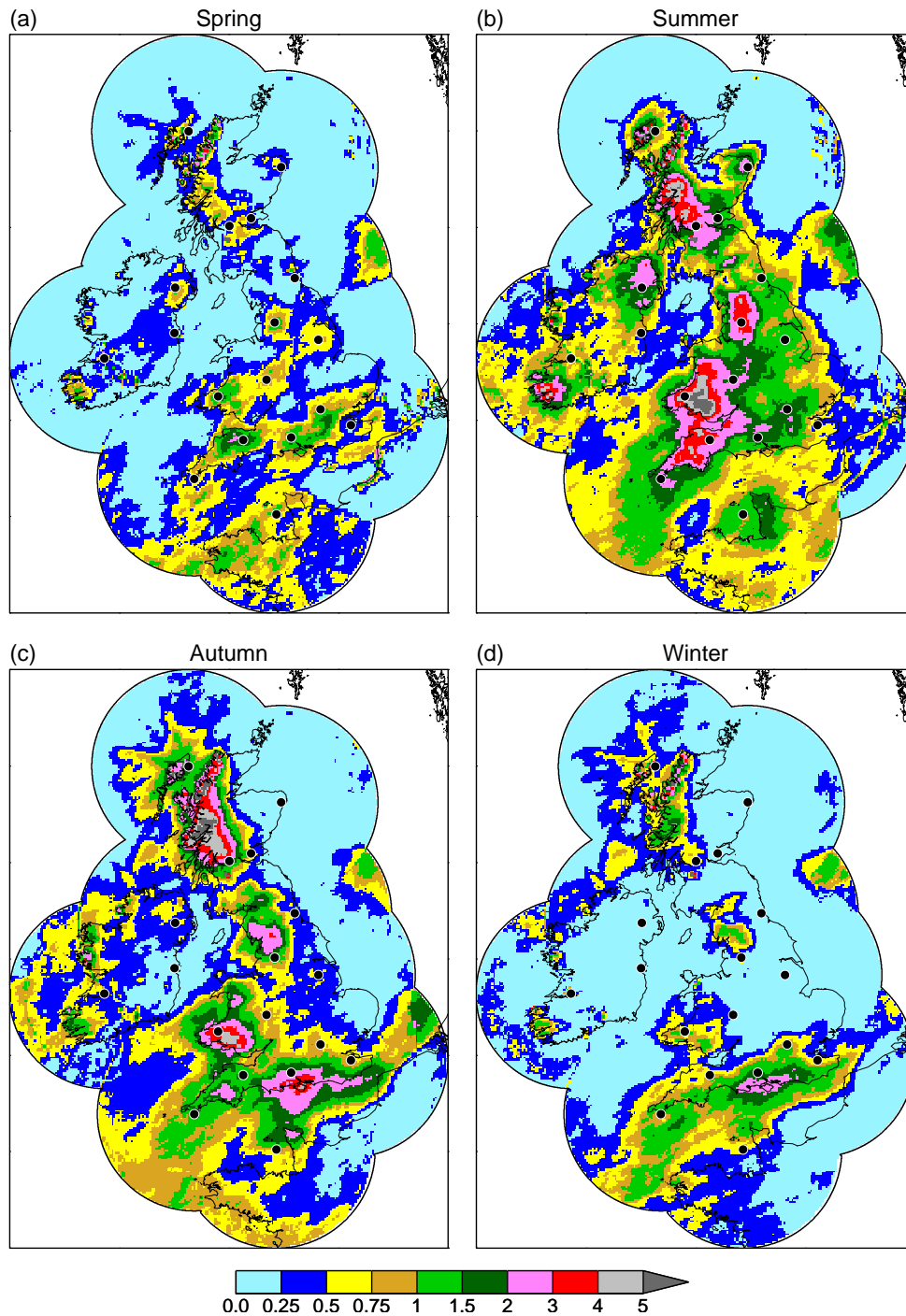
Let us first examine the spatial distribution of convection in the two climatologies for a subset of the wind directions. Figures 3.7 and 3.8 show maps of the percentage frequency of convection in each season for northerly and southwesterly wind directions respectively, while Figures 3.9 and 3.10 show equivalent images from the updated H05 climatology, but for the afternoon period only. The distributions of convection in my climatology look reasonable, with a number of recognised ‘hotspots’ showing up, including the peninsulas of southwest England and Wales under southwesterly flow during summer, the English Channel and south coast under southwesterly flow during autumn and winter, and the Irish Sea and east coast of England under northerly flow during Winter. There is also reasonable qualitative agreement with the H05 maps, although as previously noted, my frequencies are considerably lower. The most striking differences are during spring, suggesting that convection is common at this time of year but rarely strong enough to produce rainfall which exceeds my classification threshold. Similar differences can be observed over exposed coasts (e.g. northern Scotland and Ireland) under northerly flow during autumn and winter. In both cases, it is likely that instability is generally insufficient for deep convection due respectively to low insolation (compared to summer) and low sea surface temperatures (compared to farther south).

Figure 3.11 summarises the information from the map plots as histograms, showing the percentage frequencies of each wind direction, and of convection over both land and sea for each wind direction. This may be compared with Figure 3 of H05 (not reproduced here). The distribution of wind direction varies only slightly throughout the year, with SW, W, and NW together accounting for over 50 % in all seasons. Winds from the NE and E are more common during the spring, while southerly flow is more common during the summer and autumn. Convection occurs more frequently over land



**Figure 3.7** Maps showing the percentage frequency of convection in 5 km grid squares under northerly winds in (a) spring (MAM), (b) summer (JJA), (c) autumn (SON), and (d) winter (DJF). The maximum range of the radars is shown by the black contour and the individual radar sites are indicated with black circles.

during summer for all wind directions, and more frequently over the sea during winter except under southwesterly flow. Showers are also rarer under light winds and those from the eastern quadrant except over land in summer, and are notably more common over the sea under northerly and northwesterly flow during autumn and winter. These variations can largely be explained by consideration of the seasonal cycles of land and



**Figure 3.8** As in Figure 3.7 but for southwesterly winds.

sea surface temperatures and the characteristics of air masses that affect the UK. For example, in the autumn and (early) winter, northerly winds advect cold polar maritime air over relatively warm seas, while in the summer, cool returning polar maritime air in southwesterly flow can produce steep mid-level lapse rates above a strongly heated land surface; both situations give rise to large CAPE and the potential for heavy showers.

Figure 3.12 illustrates the diurnal and seasonal cycles of convection over the entire RCP1 domain. As one would expect, there is a strong diurnal cycle during the sum-

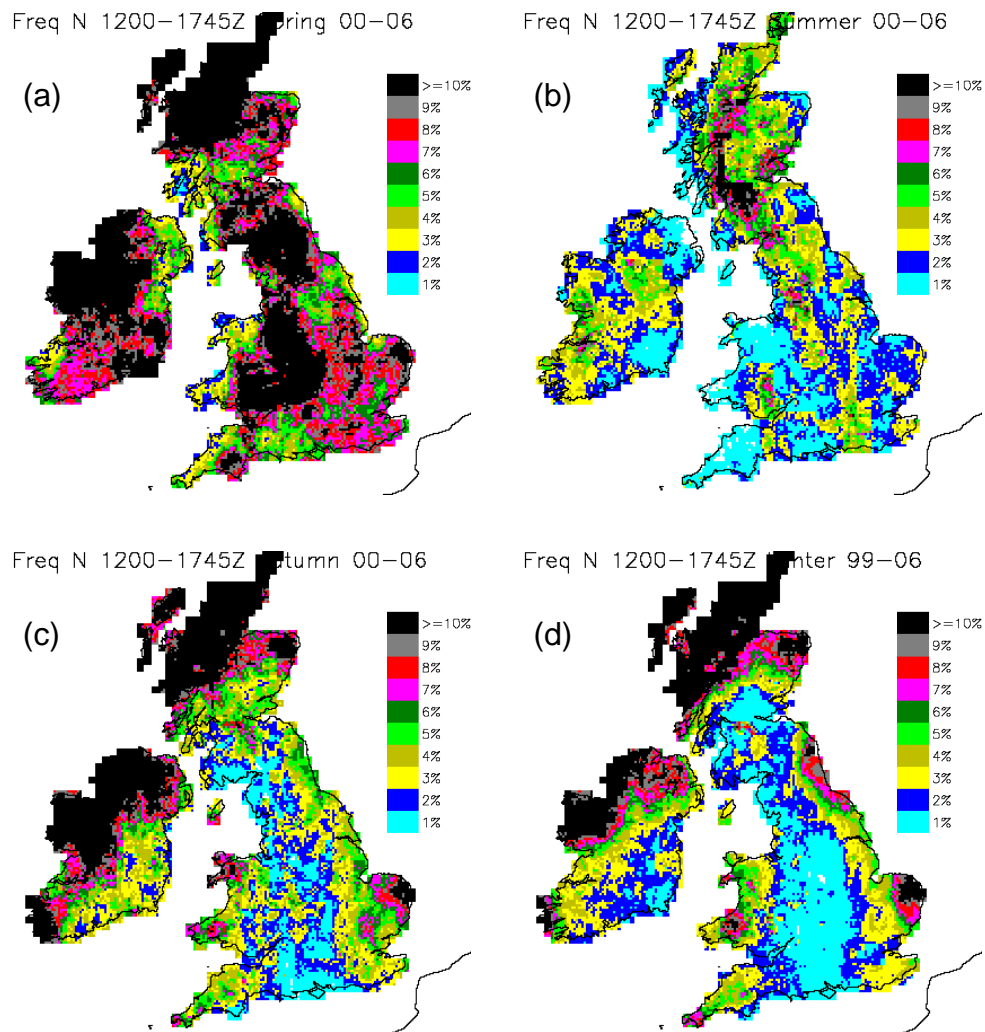


**Figure 3.9** As in Figure 3.7 but for the updated H05 climatology and only for afternoon periods (1200–1745 UTC). Courtesy of William H. Hand.

mer with the highest frequencies in July and August from 1100–1600 UTC. Between November and March there is no discernible diurnal cycle, indicating that the majority of storms during this period occur over the sea. There is very little activity at all during the first three months of the year due to low sea surface temperatures. A curious feature is the afternoon peak in convection in April which is stronger than those in both May and June. Examination of the seasonal cycles for each year (Figure 3.13) reveals quite large interannual variations on a monthly timescale, with the fraction of objects classified as convective varying by as much as 60 % of the five-year average. This indicates that a longer climatology would be required to determine whether the April peak in convection is a real feature of the average seasonal cycle.

The analysis above demonstrates that my classification algorithm is sufficiently accurate to capture the broad spatial and temporal variations of convection in the UK. However, it must be noted that it does produce some false alarms. In particular, heavy frontal and orographic rain is occasionally misclassified as convective. An example, is shown in Figure 3.14; the large area rain in the centre of the domain is associated with

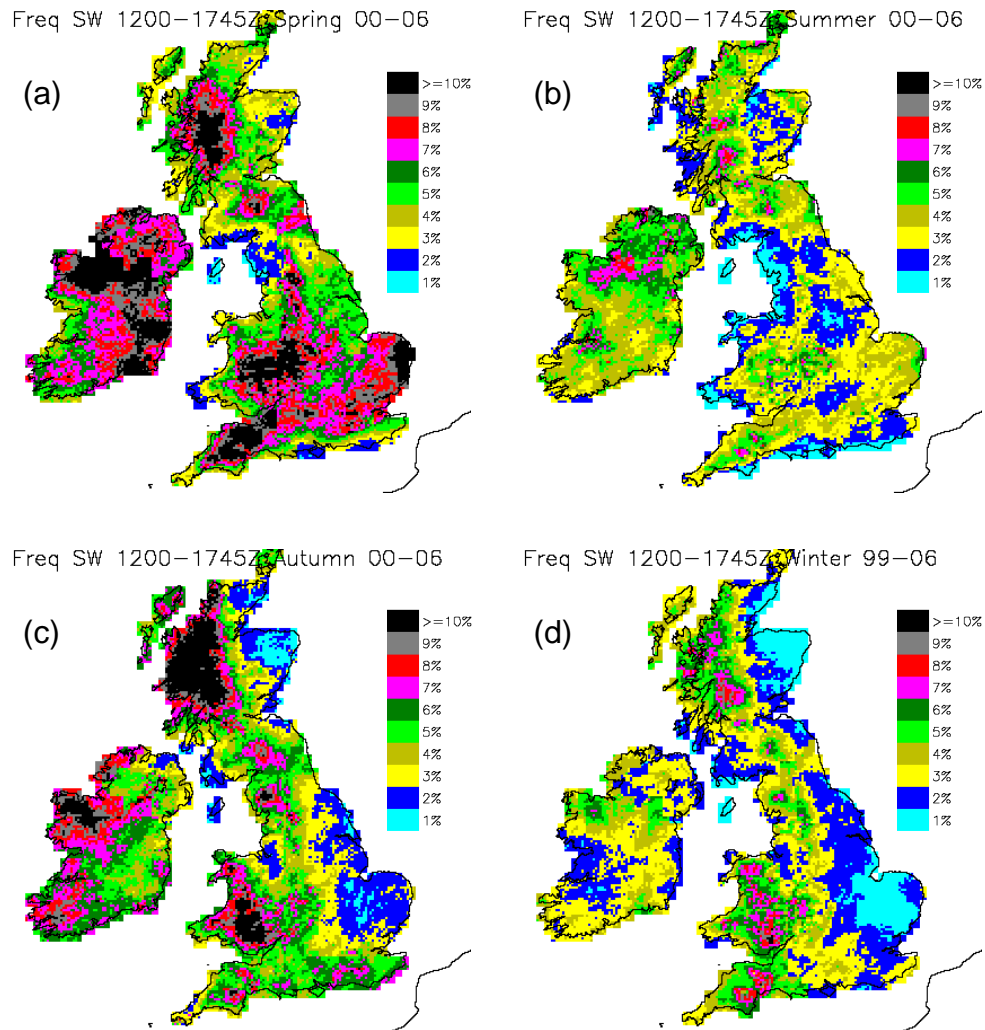


**Figure 3.10** As in Figure 3.9 but for southwesterly winds. Courtesy of William H. Hand.

an occluded front wrapping around a deep low pressure system, but is classified as convective by my algorithm. The scheme could no doubt be further developed to deal with these situations; however, this was deemed unnecessary for the present investigation. The small number of non-convective events identified by the LDCRE algorithm were rejected during the manual classification procedure which is described next.

### 3.5 Classification of identified events

In total during the 2008–2012 period, 525 LDCREs were identified by my algorithm. To isolate QSCSs and devise classifications for the remaining events, a painstaking manual analysis was performed using the radar animations produced for each case together with six-hourly Met Office surface analysis charts (obtained from [http://www.wetter3.de/Archiv/archiv\\_ukmet.html](http://www.wetter3.de/Archiv/archiv_ukmet.html)). A similar approach was used by Schumacher and Johnson (2005, hereinafter SJ05) and Jessup and Colucci (2012, hereinafter JC12) to classify convective systems associated with extreme rain and flash flooding (both in the USA)

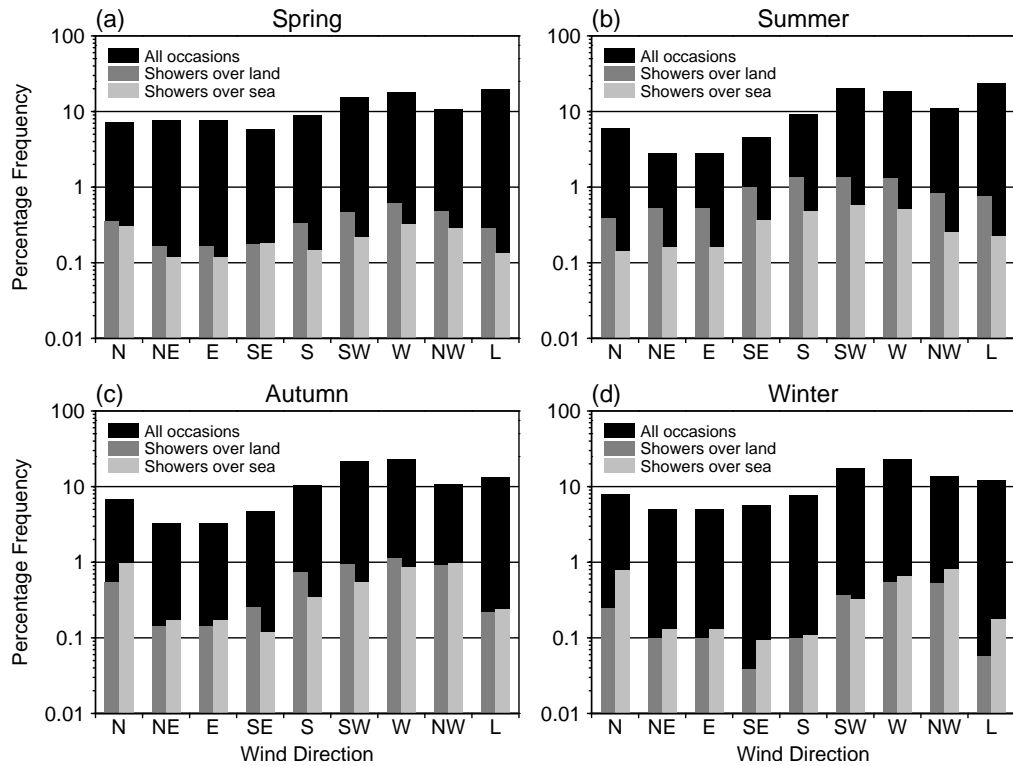


**Figure 3.11** Histograms showing the relative frequency (log scale) of winds for each of the eight cardinal compass points and ‘light winds’ (black bars), together with the frequency with which convection is observed over land (dark grey) and sea (light grey) under these wind directions, for (a) spring (MAM), (b) summer (JJA), (c) autumn (SON), and (d) winter (DJF).

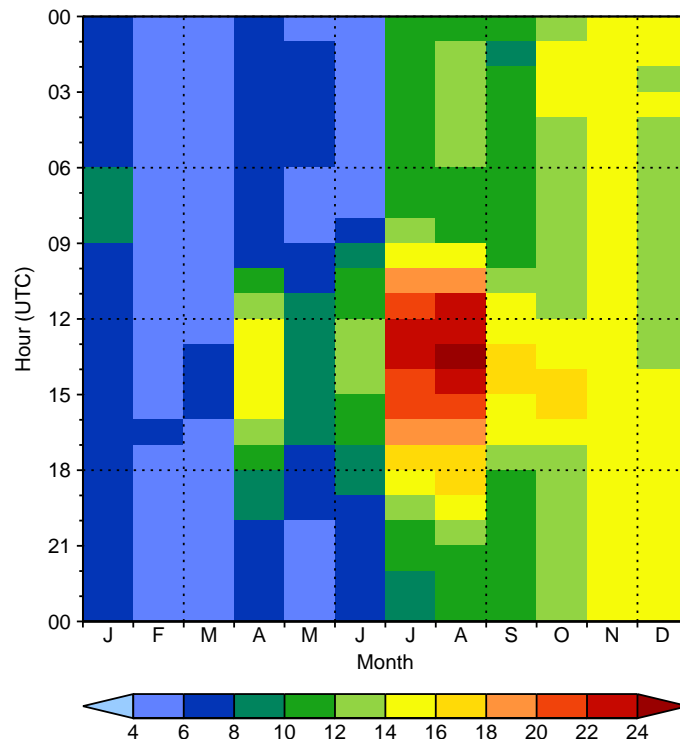


**Figure 3.12** Bivariate histogram showing the mean number of convective objects identified in the RCP1 domain as a function of month and hour.

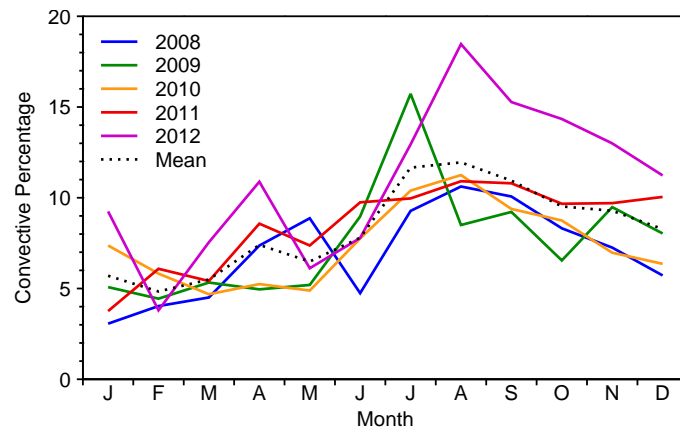


**Figure 3.13** Percentage of rainfall objects classified as convective as a function of month for each of the years in my climatology (solid coloured lines) and the five-year average (dotted black line).

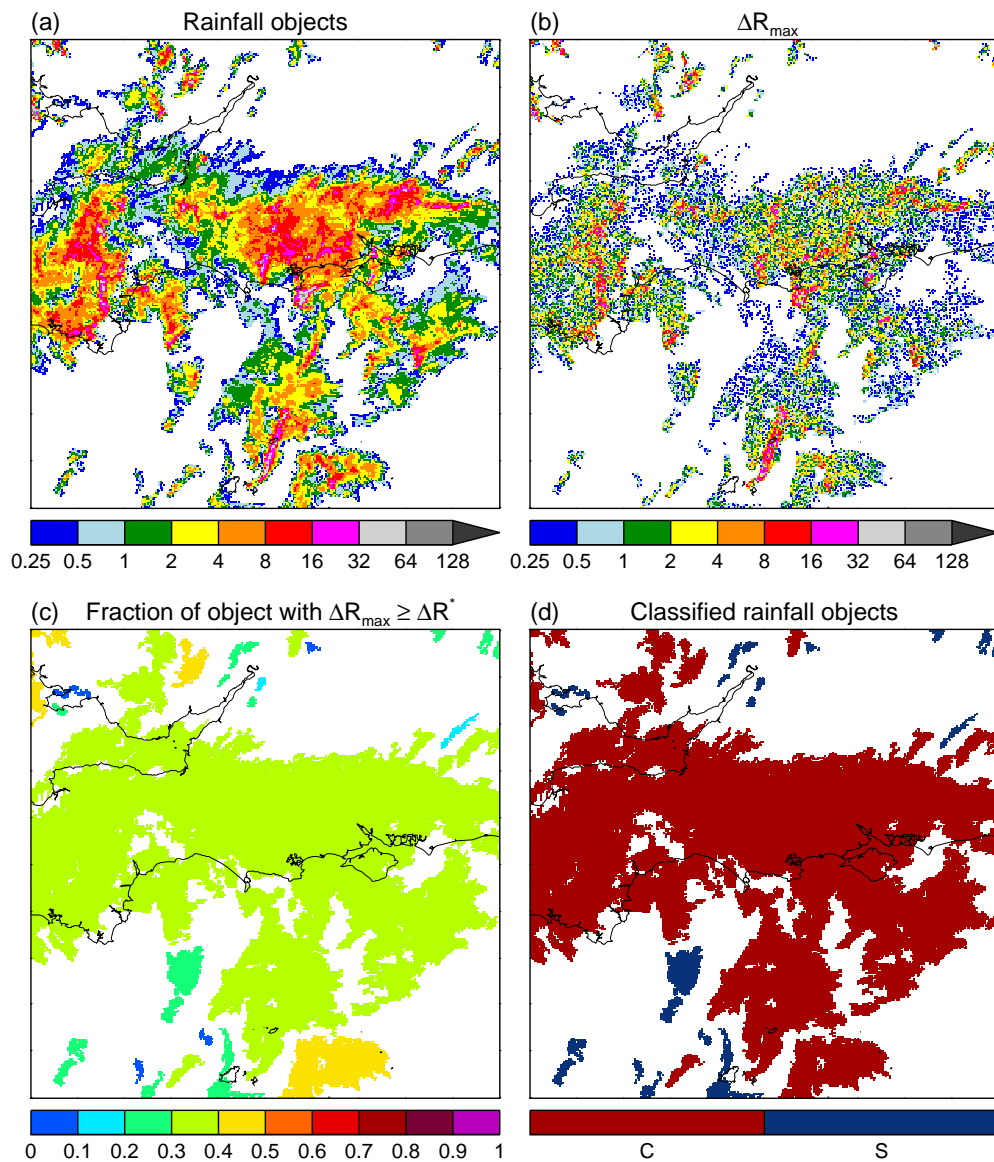


**Figure 3.14** As in Figure 3.2, but for southern England at 1630 UTC on 05/09/2008.

respectively. SJ05 first used two main classifications, synoptic and mesoscale (MCS), for all non-tropical systems (i.e. those not associated with tropical cyclones or their remnants). The distinction between these was based on the system size, its duration, and whether or not strong large-scale ascent was present. Synoptic events were then classified as either convective or non-convective, while events in the MCS category were placed into one of seven subcategories according to their organisational structure. JC12 followed a similar approach but used four primary categories of convective organisation—back-building, linear, multiple, and other/size—each of which had three or four subcategories describing the details of their structure, size, and/or movement.

In the present study, events were classified based on the structure and motion of the convective systems. After some iteration, I converged on the following six event types (values in parentheses give the number of events):

1. *Quasi-stationary systems* (88) – These were identified by the occurrence of training of convective cells with upstream development of new cells in approximately the same location. Most displayed the classic linear organisational structure, with multiple cells in different stages of their lifecycle; however, some were more cluster-like in appearance.
2. *Non-stationary training lines* (103) – These also displayed cell training associated with linear organisation, but did not feature a quasi-stationary initiation point. Often, they occurred along slow-moving fronts or other zones of horizontal convergence, with cells moving parallel to this feature.
3. *Near-stationary cells* (49) – In these events, the convective cells themselves were approximately stationary and either repeatedly developed in the same location, or dissipated very slowly. Unsurprisingly, such storms were generally associated with slack pressure gradients and thus weak flow.
4. *Rotational training* (24) – These systems were associated with the passage of a low-pressure centre and involved either training of cells or slow movement of a large convective cluster due to rotation of the steering-level winds. Storms initially moving in one direction would decelerate and then reverse direction as the low centre passed, often dissipating soon after.
5. *Unorganised training* (90) – In these events, closely packed but disorganised convective cells and systems would result in training that was usually just sufficient to meet the QSO criteria.
6. *Unstructured clusters* (67) – These events were the result of large and/or slow-moving convective clusters which did not display clear cellular characteristics and therefore could not be considered training events.

With the exception of quasi-stationary systems, these categories are quite different from those of SJ05 and JC12. This largely reflects differences in the typical organisational characteristics of convective systems in the UK and the USA. In many parts of the

USA, particularly the Great Plains, large values of CAPE (several thousand  $\text{J kg}^{-1}$ ) are frequently attained due a combination of factors including strong solar insolation, high boundary layer dewpoints associated with advection of moist air from the Gulf of Mexico, and steep mid-level lapse rates associated with elevated mixed layers. This strong instability often coincides with considerable wind shear, making conditions highly favourable to the development of organised MCSs. By comparison, in the UK, CAPE is rarely high enough for this degree of upscale growth so most convection occurs in the form of either isolated cells or small-scale mesoscale clusters and lines. It should be noted, however, that a few large MCSs were present in my climatology; most of these were placed in the non-stationary training line category.

Examples of each of the six event types are shown in Figure 3.15 with associated Met Office surface analyses provided in Figure 3.16. Figure 3.15a shows a long-lived ( $> 6$  h) nocturnal QSCS which occurred on 26 August 2012 in the so-called Cheshire Gap between the mountains of North Wales and the Pennines. In this system, new cells repeatedly formed over the sea and moved northwest-to-southeast through the line before gradually dissipating. Similar storms are frequently observed under northwesterly flow during autumn and winter and appear to be related to the upstream passage of air through the North Channel between Scotland and Northern Ireland (Browning *et al.* 1985). However, this is the only one in the present climatology suggesting that most may not be intense enough to meet my criteria for convective rain. Figure 3.15b shows a non-stationary training-line event over southeast England on 15 September 2009. This system formed in moist, northeasterly flow along a slow-moving occluded front (Figure 3.16b) and caused localised flooding and travel disruption in London (Young 2011). The event shown in Figure 3.15c, meanwhile, involved the formation and gradual dissipation of a small cluster of near-stationary intense convective cells over central Ireland under quiescent synoptic conditions (Figure 3.16c) on 30 May 2008. A rotational-training event which occurred during the early morning hours of 27 September 2012 is shown in Figure 3.15d. This was associated with a small low-pressure centre tracking slowly through the English Channel (Figure 3.16d). Twelve hours earlier, the same system was moving across southwest England (Figure 3.16e) bringing widespread showers which produced the small unorganised-training event in Figure 3.15e. Finally, Figure 3.15f provides an example of an unstructured cluster event: a moderately large “blob” of convective rain moving slowly across Northern Ireland on 15 June 2009.

Not all of the events were placed in one of these six categories. Almost a fifth (104) were rejected for one of the following reasons:

1. The causative rainfall was predominantly frontal (29);
2. The causative rainfall was predominantly orographic (25);
3. The event was the result of spurious radar echoes (22);
4. The radar data quality was too poor for the event to be classified (28).

Here, the terms frontal and orographic are used to indicate stratiform rainfall associated

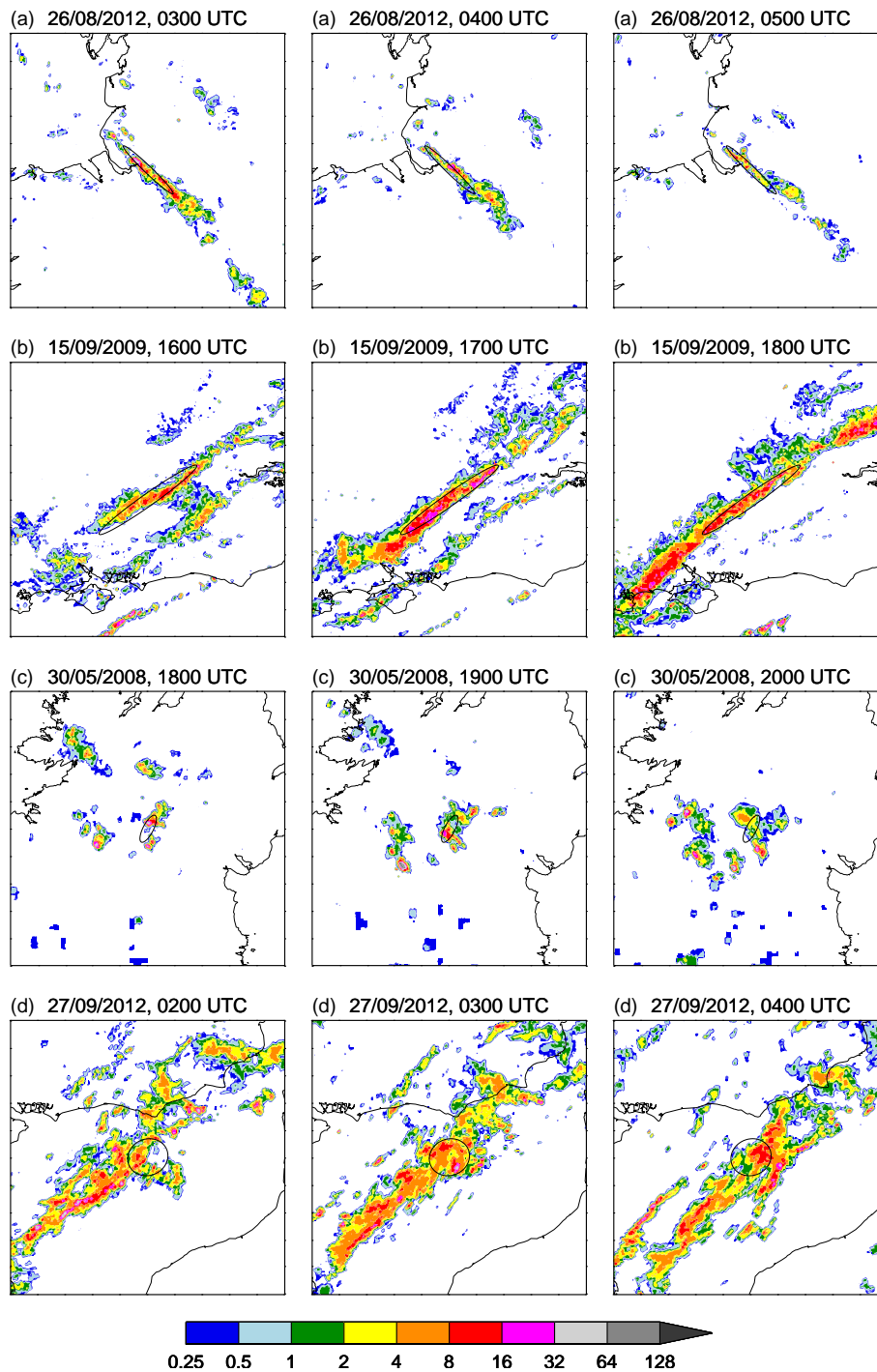


**Figure 3.15** Examples of the six event types: (a) a quasi-stationary system (b) a non-stationary training line, (c) near-stationary cells, (d) rotational training, (e) unorganised training, (f) an unstructured cluster. In each case, rain rates ( $\text{mm h}^{-1}$ ) are shown at hourly intervals over a 2 h period for a  $201 \times 201$  km box centred on the event centroid. Ellipses approximate the event accumulation areas.

with large-scale ascent in the vicinity of synoptic fronts and lifting by orography respectively. In most of the frontal events, embedded convection may have produced the heavy rainfall and associated strong gradients detected by the classification algorithm; however, very heavy stratiform rain can occur over orography due to the seeder-feeder

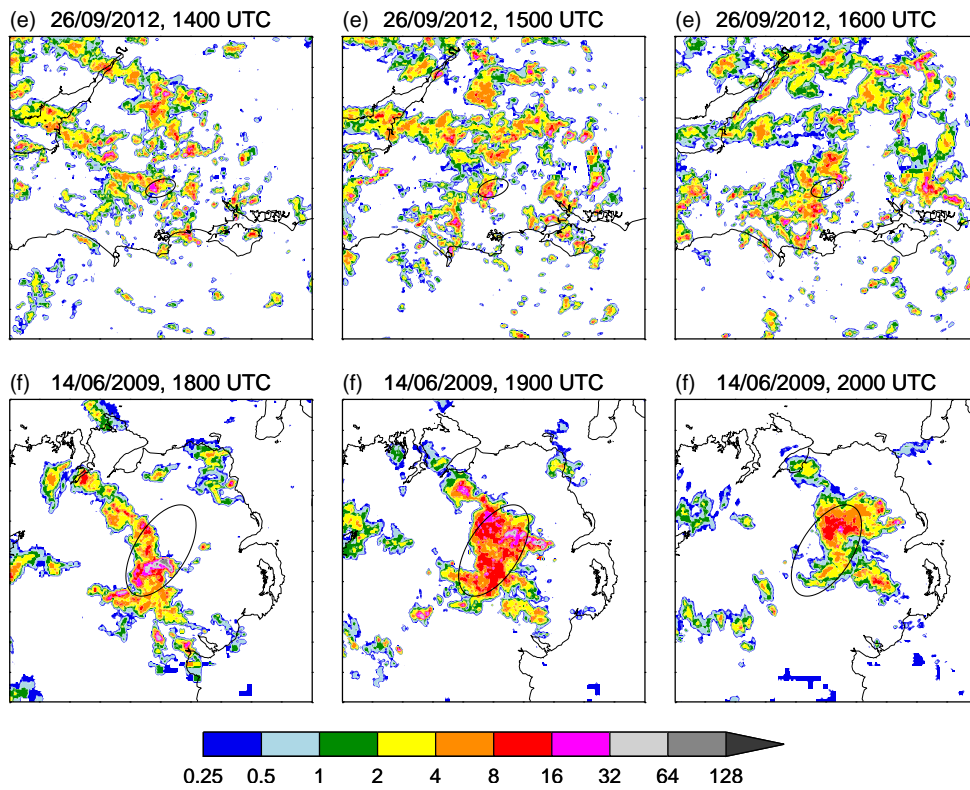


Figure 3.15 (Continued)

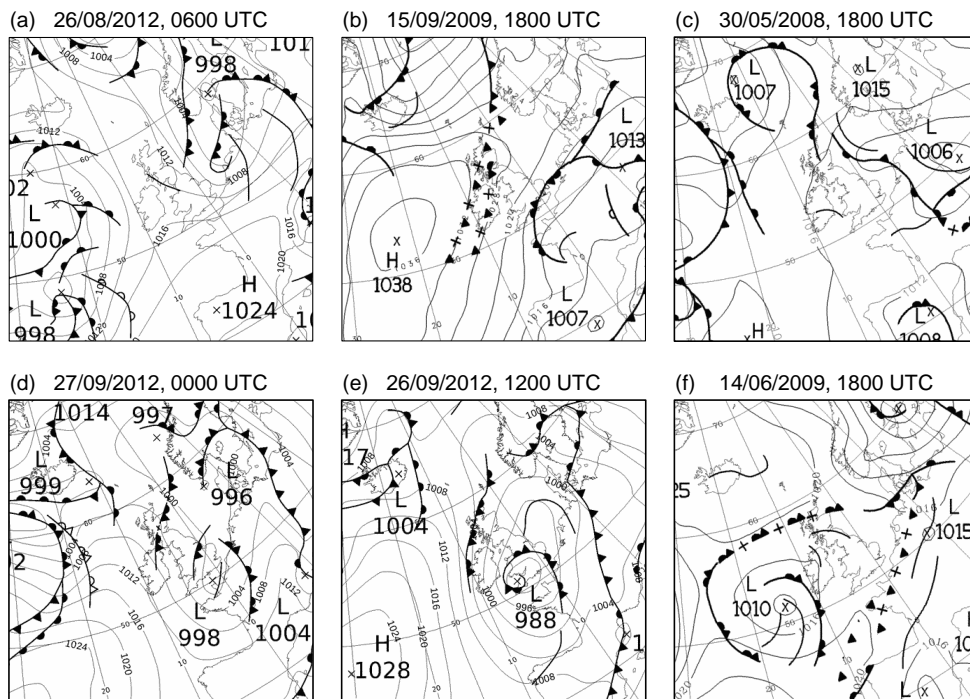


Figure 3.16 Met Office surface analysis charts for the times nearest to each of the events shown in Figure 3.15.

mechanism (Bergeron 1965) which is simulated in the calculation of surface rain rates for the RCP1 (see Section 2.1).

Examples of each of the four types of rejected event are provided in Figure 3.17. Figure 3.17a shows a large area of heavy rain associated with a warm front (not shown) moving across the UK Southwest Peninsula on the morning of 15 August 2012. The localised more intense areas of rainfall (possibly associated with embedded convection) meant that this system just met the threshold for convective classification. Figure 3.17b shows orographic precipitation occurring over the west coast of Scotland on 27 September 2011. Note how the higher rain rates occur mainly along the windward (southwest) slopes of the mountains; this is a consequence of the artificial orographic enhancement mentioned above. At around the same time as Figure 3.17a, persistent spurious echoes over the Isle of Anglesey, apparently produced by the Dublin radar, were identified as an event by my algorithm (Figure 3.17c). Finally, Figure 3.17d shows an event on 25 November 2010 associated with showers over the southern North Sea which could not be classified due to the low resolution of the data in this location at the time (apparently caused by the absence of data from the Thurnham radar in southeast England).

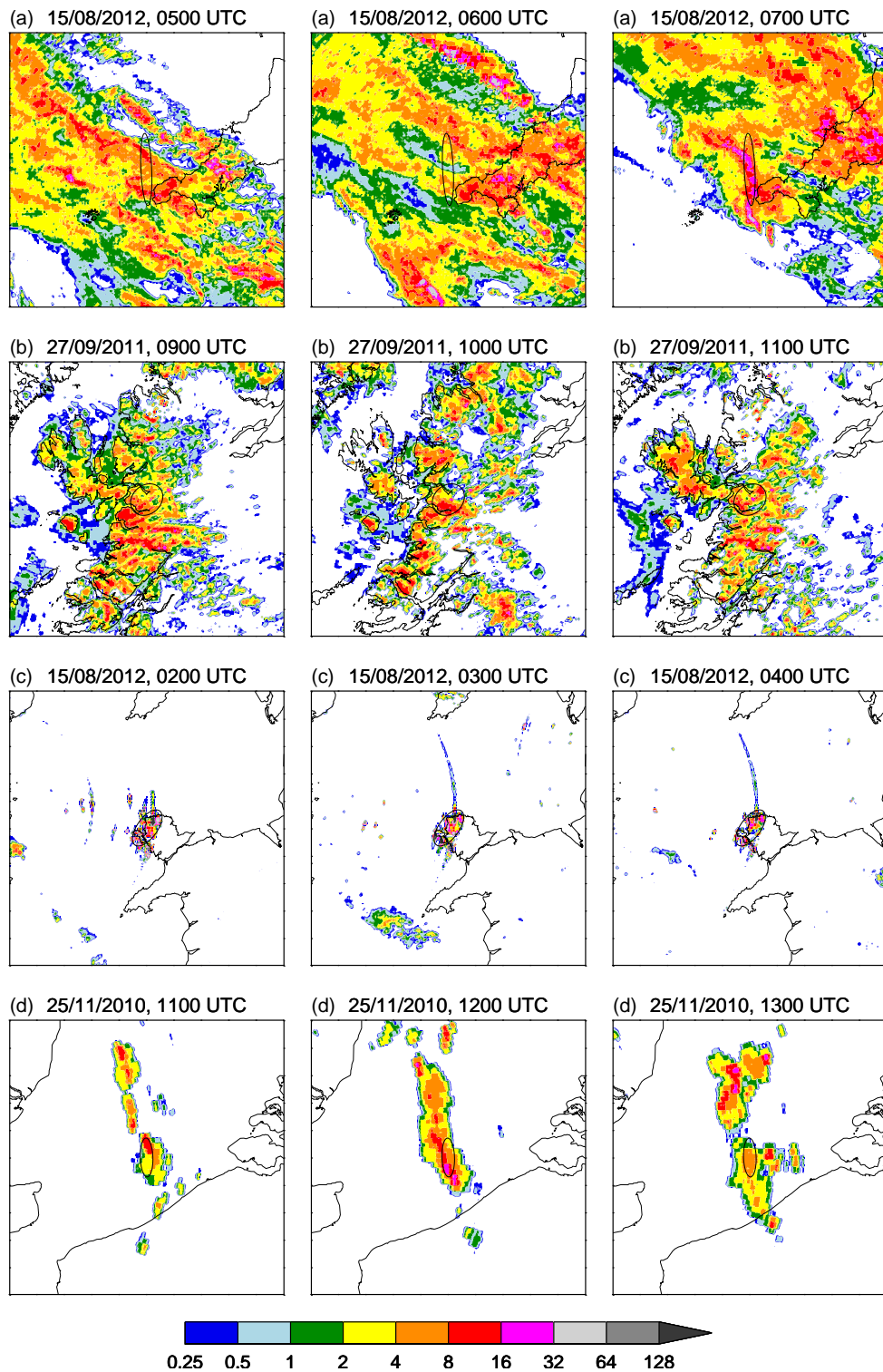
## 3.6 A climatology of QSCSs in the UK

This section investigates the characteristics of the 88 QSCSs in my climatology. The geospatial and temporal distribution of the events is first examined. Then, their environments are analysed and compared with those of other convective events using data from ERA-Interim.

### 3.6.1 Geospatial and temporal characteristics

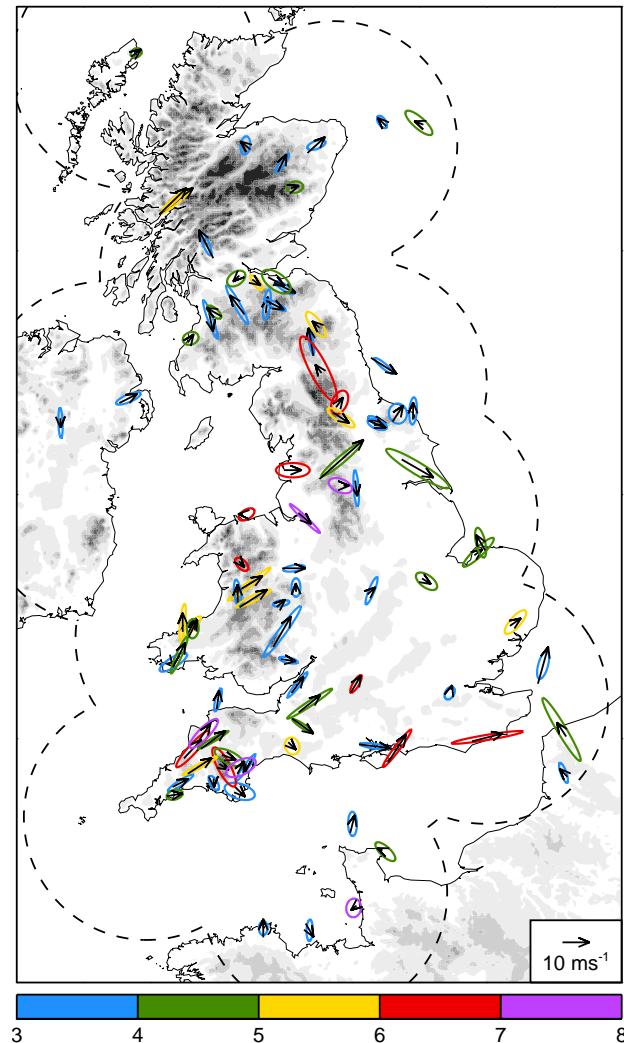
Figure 3.18 shows the location, best-fit ellipse, duration, and mean cell velocity for each of the 88 QSCSs in my climatology. The events are well distributed across the domain, but appear to be somewhat more common in the vicinity of complex orography and adjacent to coastlines. This suggests that most QSCSs in the UK are the result of forcing associated with surface topography. The English Southwest Peninsula in particular stands out, with a cluster of 13 events. As discussed in later chapters, many of these are likely associated with lifting along sea-breeze fronts, although the high terrain of Dartmoor may also be important in some cases. Other areas which seem favourable for QSCSs include the Cambrian Mountains in Wales, the Pennines in northern England, and the Southern Uplands in Scotland. Most events which occurred over the sea did so in close proximity to coastlines which further hints at the importance of surface topography, although it may also be a consequence of the decrease in radar data resolution with range.

It is worth considering how the geospatial distribution of QSCSs compares with that for convection in general. Figure 3.19 again shows the location of the identified events, but this time overlaid on data from my convection climatology; specifically, the convection frequencies for summer averaged over all wind directions. Perhaps unsurprisingly,



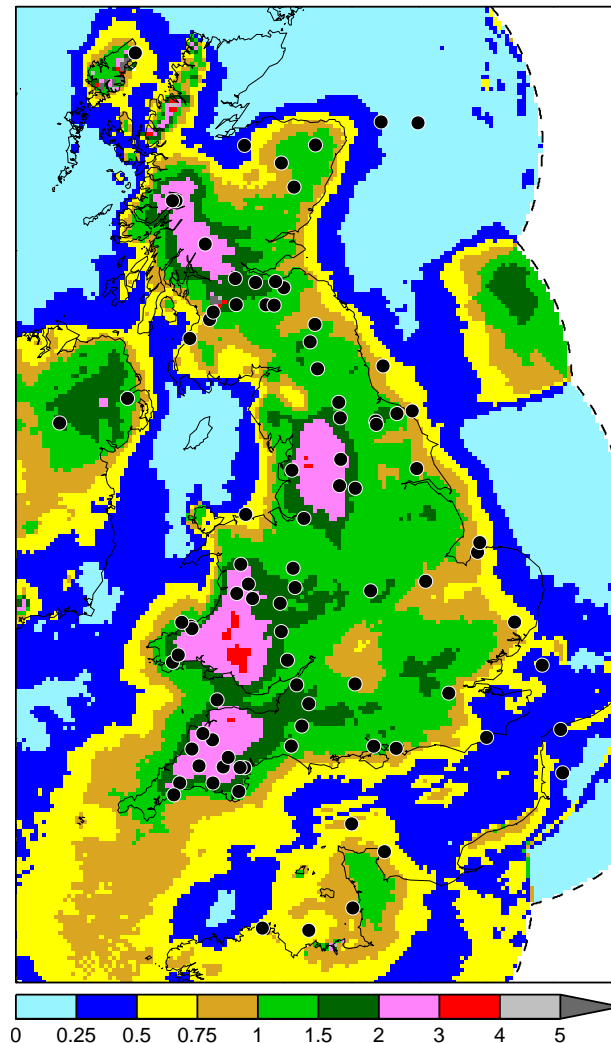
**Figure 3.17** As in Figure 3.15 but for the four types of rejected events: (a) frontal, (b) orographic, (c) spurious, and (d) low-quality.

QSCSs occur more commonly in areas where the frequency of convection is high. This does not contradict the previous hypothesis, but simply highlights the fact that, in general, surface topography plays an important role in the initiation of convective storms in the UK (Bennett *et al.* 2006).



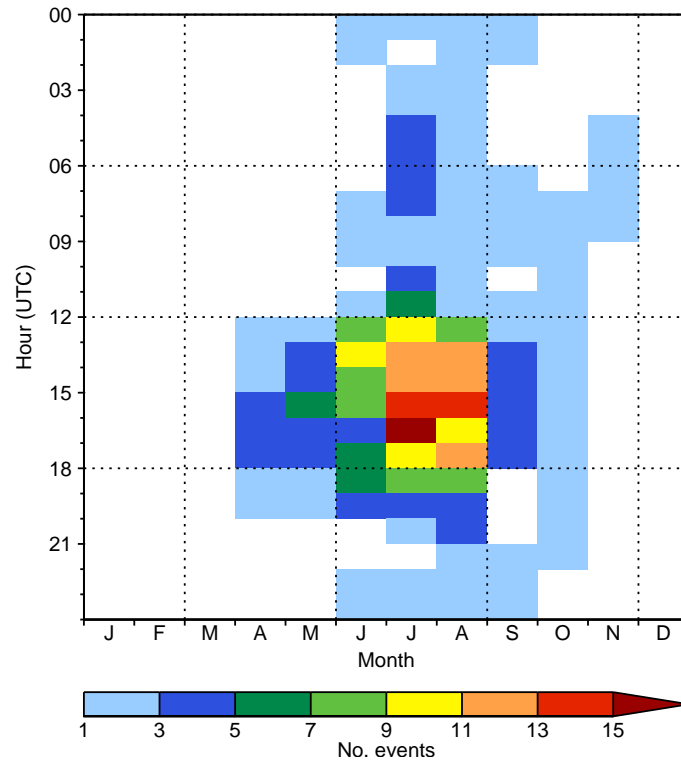
**Figure 3.18** Map showing the geographical distribution of the 88 QSCSs in my climatology. Ellipses approximate the accumulation area of each event, their colours indicate the duration in hours, and vectors show the time-averaged cell velocity. Orography height is shown in grey scale with a contour interval of 100 m up to 500 m. The dashed line encloses grid points which are within 150 km of a radar, excluding Shannon in southwest Ireland.

Figure 3.20 shows the seasonal and diurnal cycle of QSCSs as a bivariate histogram which may be compared directly with Figure 3.12. Over 75 % of the events occurred during the summer months and nearly half the total event hours were during summer afternoons (12–18 UTC). In July and August, the peak in QSCS frequency occurs slightly later in the day than that for convection in general. Similarly, Figure 3.21 shows that the majority of events start during the early afternoon (12–15 UTC) and end during the early evening hours (18–21 UTC). This suggests that the mechanisms which lead to repeated cell initiation operate more frequently or effectively in the latter part of the day, which would certainly be true of thermally driven circulations such as sea breezes. As with convection in general, there is a large degree of interannual variability on the monthly timescale (Figure 3.22), highlighting the need for a longer climatology to obtain robust statistics on the seasonal cycle of QSCSs.



**Figure 3.19** Map showing the percentage frequency of convection for all wind directions during summer (JJA) with black circles marking the centroids of the 88 QSCSs in my climatology.

An observation made during the event classification was that often, multiple QSCSs would occur on the same day. In fact, 45 of the 88 events (51%) occurred on the same calendar day as one or more other events. Figure 3.23 shows the spatial distribution of these events. There are three event pairs (on days 10, 11, and 18) which are almost exactly collocated (respectively, over western Scotland, southwest Wales, and northeast England). The first and last of these both represent a single convective system, suggesting a failure of the linking part of my algorithm (Section 3.3). However, the second is the result of distinct systems forming in the same location but at different times. This suggests that there is a persistent forcing mechanism acting in this location which is only intermittently strong enough to lead to convective initiation. A number of other closely spaced event pairs (on days 5, 7, 13, 15, 16, and 17) appear to be associated with the same forcing mechanism. For example, the systems over northeast England on day 16 both appear to be the result of repeated orographic triggering but over different peaks, while those over the Southwest Peninsula on day 15 are almost certainly



**Figure 3.20** Bivariate histogram showing the number of QSCSs identified as a function of month and hour. Note that for each event, the entire duration is considered; for example, an event which spanned the period 1200–1500 UTC contributes to the bins for 1200–1300, 1300–1400, and 1400–1500 UTC.

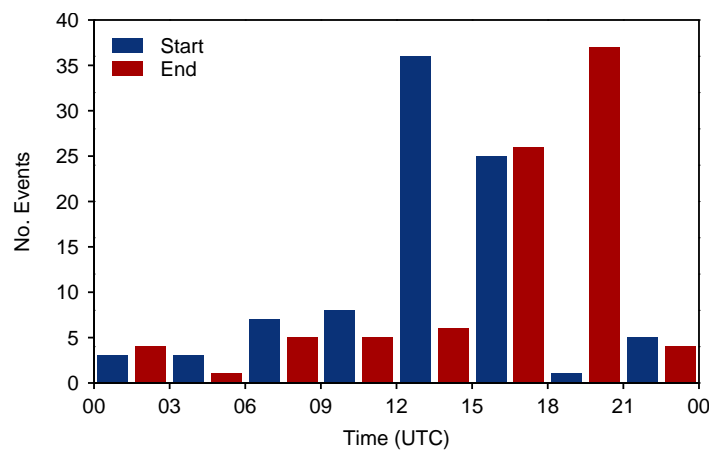


**Figure 3.21** Histogram showing the distributions of QSCS start (blue) and end (red) times. Note that an event which started at 1200 UTC contributes to the 1200–1500 UTC bin rather than the 0900–1200 UTC bin.

related to sea breezes. However, the majority (14) of the multi-event days in Figure 3.23 feature at least two systems which are spaced several hundred kilometres apart. This suggests that there may be certain large-scale meteorological conditions which favour the occurrence of quasi-stationary systems, a possibility which is explored next.

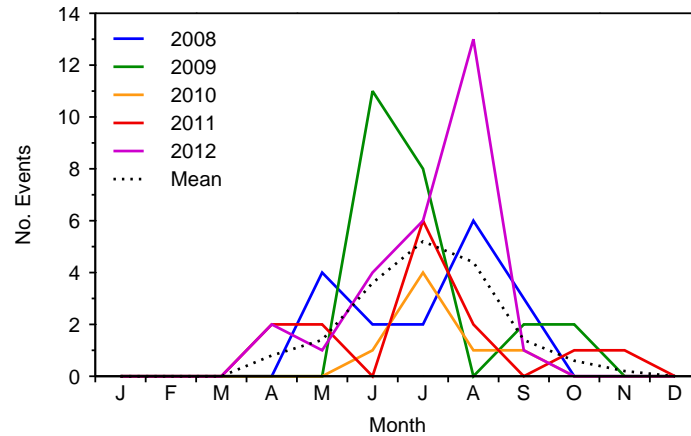


**Figure 3.22** Number of QSCSs identified as a function of month for each of the years in my climatology (solid coloured lines) and the five-year average (dotted black line).

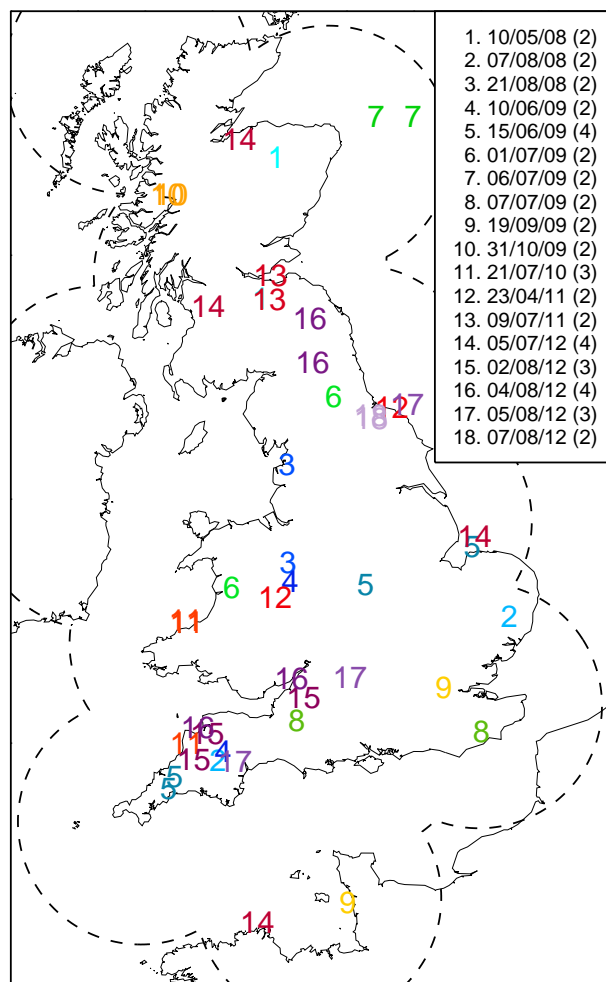


**Figure 3.23** Map showing the locations of events on 18 multi-event days. Dates are indicated by the numbers and colours, and are listed on the right-hand side with the number of events in parentheses. The dashed line encloses grid points which are within 150km of a radar, excluding Shannon in southwest Ireland.

### 3.6.2 Environmental characteristics

From a forecasting perspective, it is useful to know the background atmospheric conditions which characterise extreme events. A number of previous works (e.g. Maddox *et al.* 1979, Kodama and Barnes 1997, Ricard *et al.* 2012) have examined these conditions for heavy rain/flash flood-producing convective systems in various geographical locations. I have performed a similar piece of analysis for QSCSs in the UK using re-analysis data from ERA-Interim (Section 2.3.1). Specifically, I have used surface and pressure-level data from the 6-hourly analyses, valid at 0000, 0600, 1200, and 1800 UTC each day.

In a first step, figures were produced to summarise each event together with the synoptic-scale and local environment in which it formed. These consisted of three panels showing: (1) the rainfall accumulation from the RCP1 for a  $200 \times 200$  km area centred on the event centroid; (2) a chart of the 500 hPa geopotential height and mean-sea-level pressure over the UK and surrounding area; and (3) a vertical sounding (tephigram) taken in the vicinity of the event. The latter two were both produced using analysis data for the time closest to but before the event central time (the average of the start and end times) in order to best represent the conditions leading to QSCS formation. For the soundings, pseudoadiabatic parcel ascents were performed for each of the grid points in a  $3 \times 2$  box around the event centroid and the one with the highest CAPE was retained. If all six ascents had no CAPE, the one closest to the event centroid was selected. The initial parcel conditions were taken as the 2 m temperature and dewpoint temperature, and the surface pressure. Data on pressure levels above the surface (i.e. those with a pressure less than the surface pressure) were then used to define the environmental profile. The rationale for selecting the profile with the highest CAPE was to focus on the local conditions that were most favourable to deep convection. The amount of convective inhibition (CIN) is also important; however, this is often associated with sharp temperature inversions which are likely to be poorly represented in ERA-Interim due to the coarse vertical resolution (25–50 hPa).

The summary figures were examined and compared in an attempt to identify commonalities between the events. However, this in fact revealed great diversity in the conditions under which QSCSs form, as is illustrated by the examples in Figures 3.24 and 3.25. It can be seen that QSCSs may form in the vicinity of upper-level ridges, troughs, and cut-off lows, in slack and strong pressure gradients, and with a variety of vertical buoyancy, moisture, and wind profiles. One feature that did appear to be common to many events was a fairly unidirectional wind profile with weak to moderate speed shear. This is illustrated in Figure 3.26 which shows bivariate histograms of the wind speed and direction, rotated with respect to the estimated mean cell velocity (Section 3.3) as a function of pressure. One may also note from this figure that, on average, QSCSs move in the direction of the 700 hPa flow, but at a speed which better matches the flow at lower levels, around 875 hPa. This discrepancy is curious and may represent a systematic underestimation of convective cell speed.

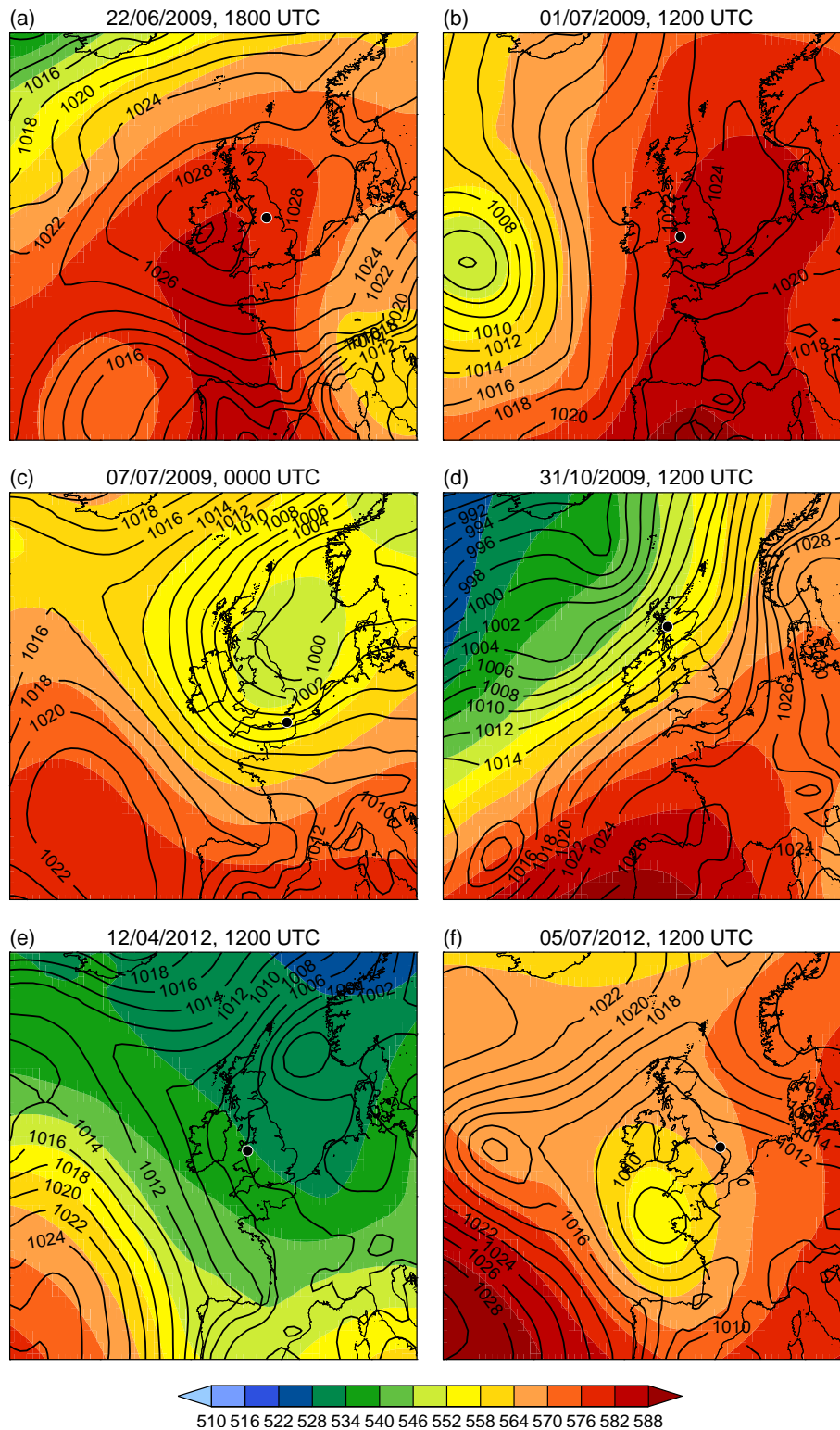


**Figure 3.24** ERA-Interim analyses of 500 hPa geopotential height (colour shading; dam) and mean-sea-level pressure (black contours; hPa) for six QSCSs. Black circles show the location of the event centroids.

The diversity in environmental conditions likely reflects the fact that most events are associated with distinct forcing mechanisms. Previous work (e.g. Tucker and Crook 2005, Kirshbaum and Durrant 2005, Metzger *et al.* 2014) has shown that the initia-

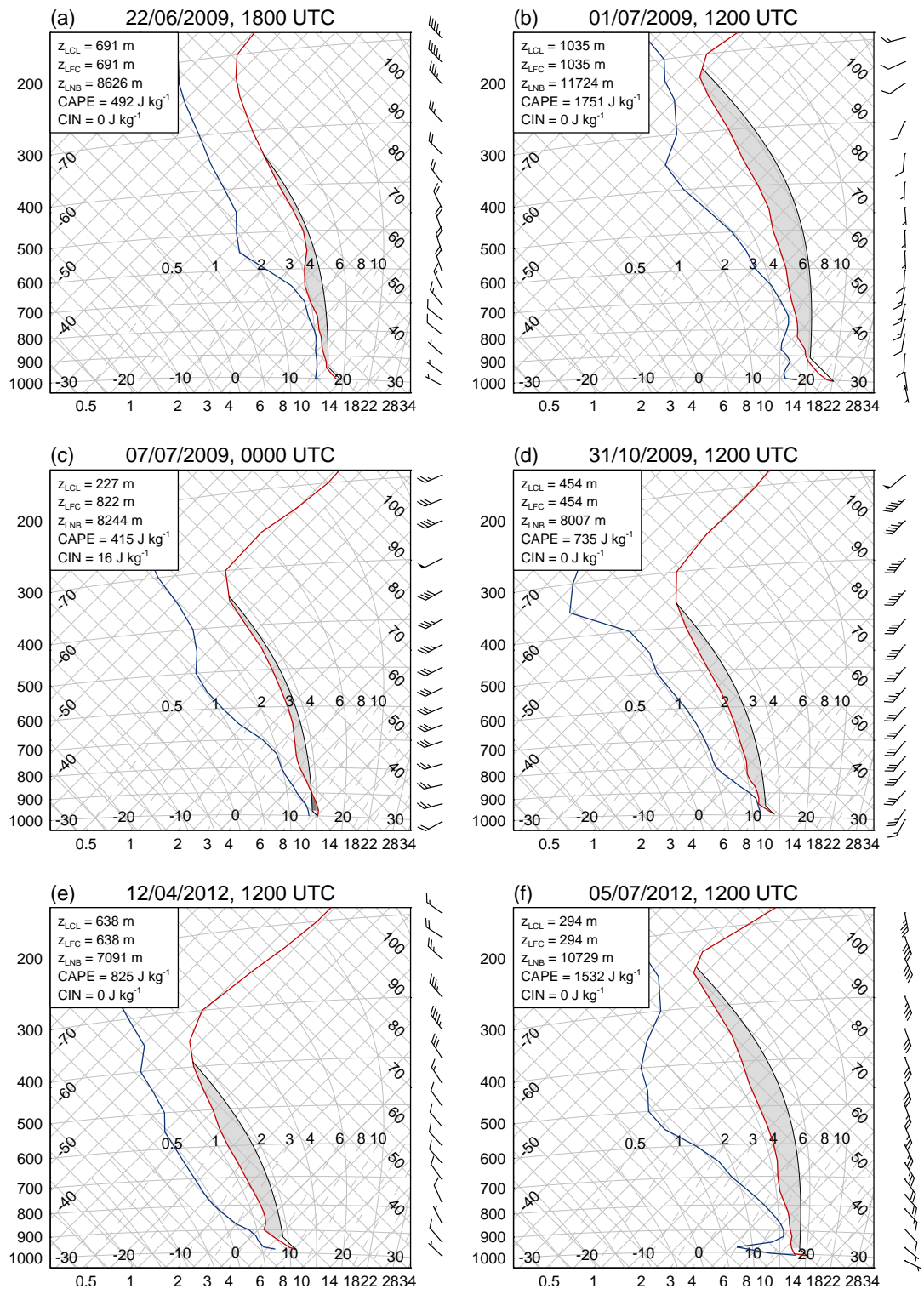


**Figure 3.25** Tephigrams for the same six QSCSs as in Figure 3.24. Red and blue lines show the temperature and dewpoint temperature profiles respectively. Black lines show surface-based pseudoadiabatic parcel ascents, with the resulting areas of positive and negative buoyancy shaded light and dark grey respectively. The heights of the LCL, LFC, and LNB, and the values of CAPE and CIN are given in top-left corner of each panel. The vertical wind profile is given in knots with half barbs, full barbs, and pennants indicating speeds of 5, 10, and 50 knots respectively.

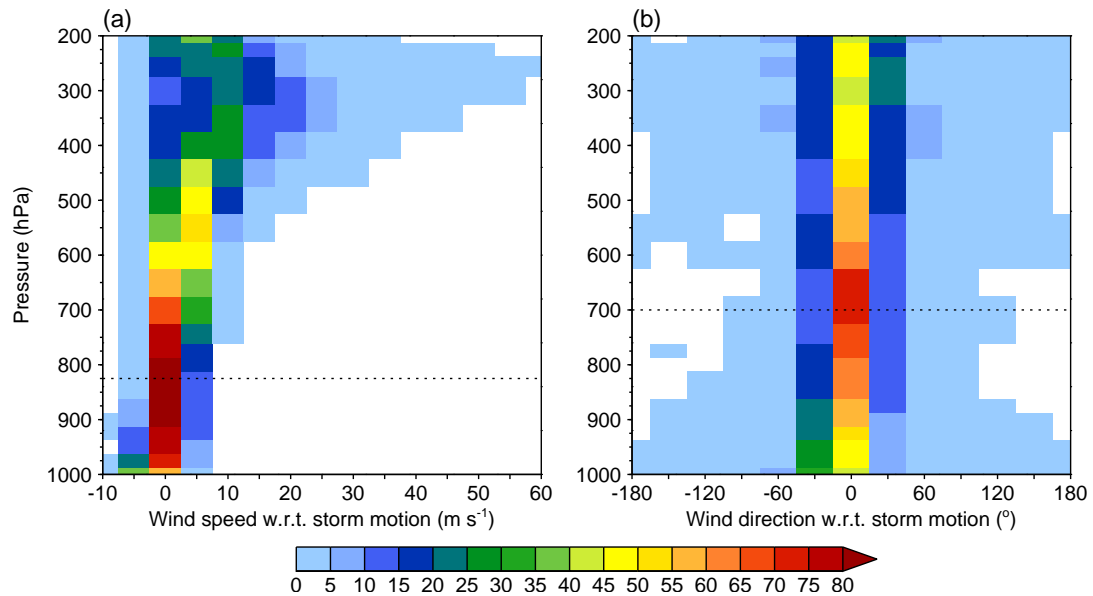


**Figure 3.26** Relative frequencies (%) for (a) wind speed and (b) wind direction with respect to storm motion as a function of pressure for QSCSs. Dotted lines indicate the level at which values best match the storm motion. Tick marks on the  $y$ -axis correspond to the ERA-Interim pressure levels.

tion locations and organisational characteristics of convection over complex orography vary greatly with wind speed, direction, vertical shear, and static stability. Similar sensitivities have also been noted for other convective systems associated with surface topography such as lake-effect precipitation bands (e.g. Laird *et al.* 2003). Thus, assuming that most QSCSs in the UK are linked to surface topography, we would expect events in different locations to occur under different environmental conditions. By the same argument, we would also expect events in roughly the same location to show clear similarities in their environmental conditions, provided they are associated with the same forcing mechanism. This appears to be true for southwest-to-northeast oriented QSCSs over the English Southwest Peninsula. Figures 3.27 and 3.28 show that the days on which these events occurred all featured an upper-level trough to the west of the UK with deep southwesterly flow and a deep layer of surface-based instability. Similar conditions were also present on the day of the Boscastle storm (see Chapter 4) and during a number of quasi-stationary cases observed during the Convective Precipitation Experiment (COPE) field campaign in summer 2013 (<https://www.ncas.ac.uk/index.php/en/cope-home>). The common initiation mechanism behind these events appears to be lifting along quasi-stationary sea-breeze fronts which are investigated in Chapter 5. It is likely that certain flow configurations may favour QSCSs in other parts of the country; however, the Southwest Peninsula is the only location showing a clear cluster of events with similar orientations (Figure 3.18). This is likely to be a consequence of the small sample size; a longer climatology and/or one including less-intense systems might highlight other favourable areas for the repeated initiation of convection under particular large-scale conditions.

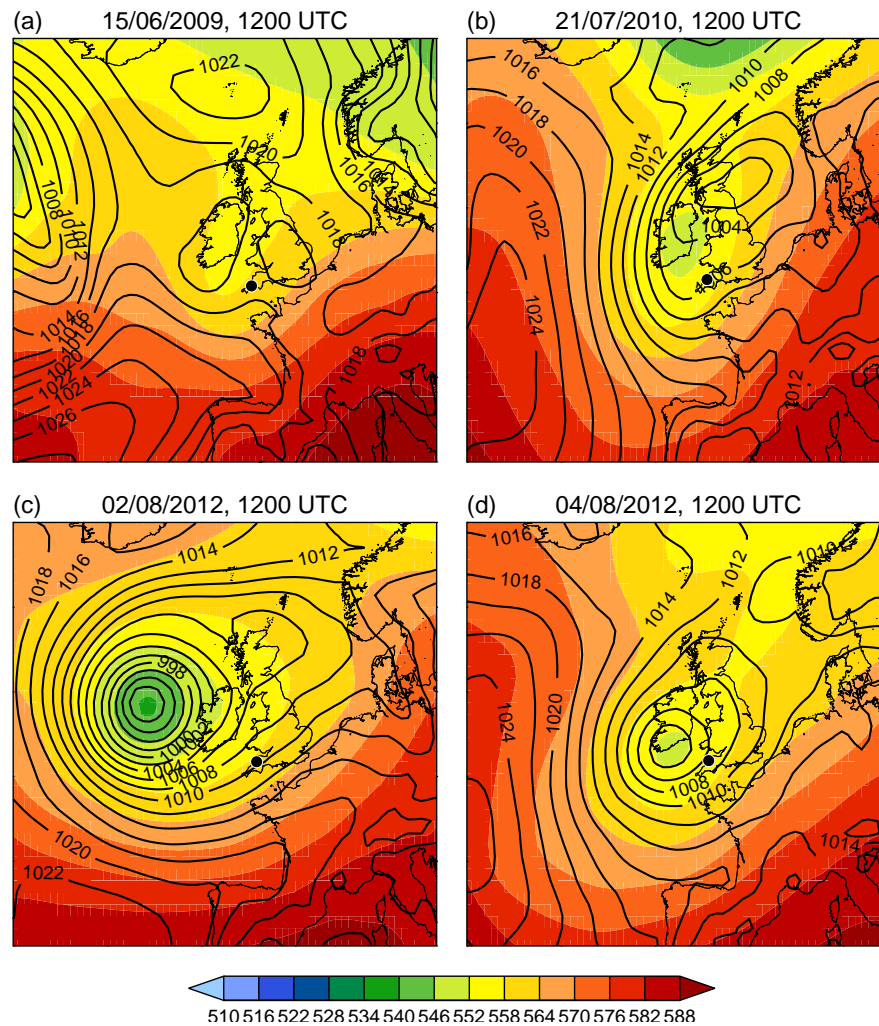


**Figure 3.27** As in Figure 3.24 but for four SW–NE oriented QSCSs which occurred over the UK Southwest Peninsula.

The next step in my analysis was to determine whether the environmental characteristics of QSCSs are in any way distinct from those that typify convective episodes in the UK. Unfortunately, no meteorological data was stored for the convection climatology presented in Section 3.4. Thus, a new climatology was created. To reduce computational expense, only the more active portions of the diurnal and seasonal cycle were considered; specifically, 1100–1700 UTC and June–September. Additionally, radar data was analysed only once every hour and for a portion of the RCP1 domain covering most of England and Wales (Figure 3.29). Within this domain, eight approximately equal-sized regions were defined based on the ERA-Interim grid boxes. On any given day, a region was defined as convective if at any time convective precipitation covered an area of at least  $500 \text{ km}^2$  within its boundaries. For 2008–2012, this resulted in 319 convective days (i.e. days with at least one convective region) and 1,203 convective regions. Data from the 1200 UTC ERA-Interim analysis was then extracted for each of the grid points within these convective regions (9,329 in total) and used to characterise the environments under which UK convection typically forms. For QSCSs, environment

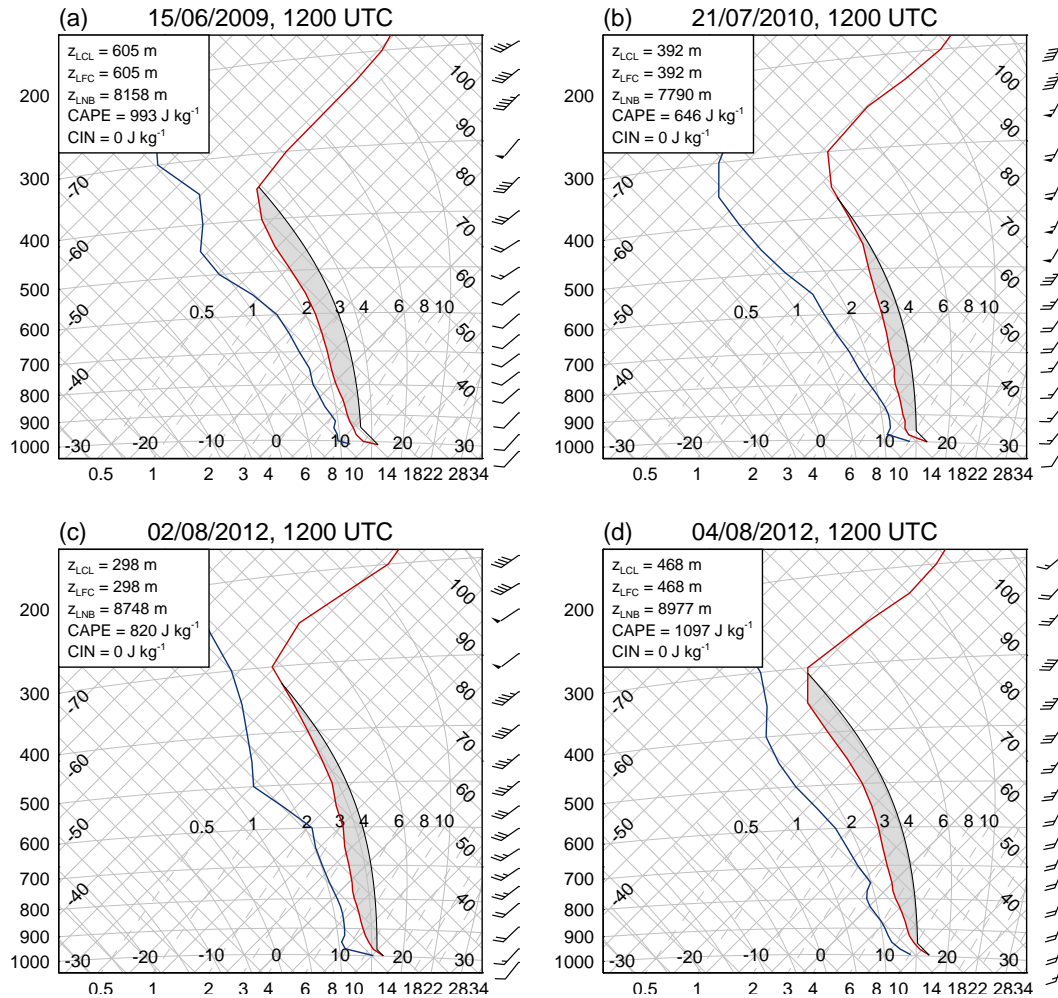


**Figure 3.28** As in Figure 3.25 but for four SW–NE oriented QSCSs which occurred over the UK Southwest Peninsula.

data was extracted for the  $3 \times 2$  grid points surrounding each event centroid at the analysis time closest to but preceding the event central time.

A variety of parameters were used to quantify and compare the environmental characteristics of convective episodes and QSCSs. The follow six are shown in Figure 3.30:

- CAPE, computed using a surface-based parcel ascent as described above.
- Precipitable water, computed as  $-\frac{1}{g} \int_{p_1}^{p_2} q dp$  where  $q$  is the specific humidity,  $p_1 = 1000$  hPa and  $p_2 = 150$  hPa.
- Steering-level (700 hPa) wind speed.
- Vertical speed shear, computed as the difference between the average wind speed in the 1000–700 hPa and 650–200 hPa layers.
- Magnitude of directional shear, computed as the absolute difference in the direction of the 1000–700 hPa and 650–200 hPa layer-averaged wind vectors.
- Magnitude of the change in 700 hPa wind direction during the 6 h following the event analysis time.

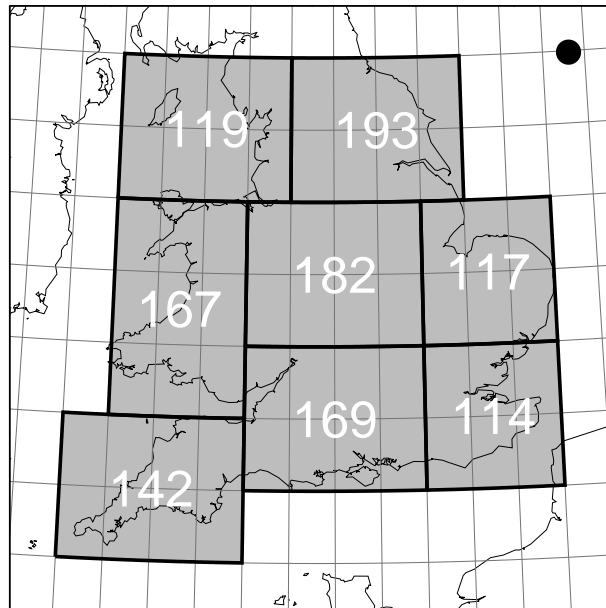


**Figure 3.29** Map showing the domain used for the convective environment climatology. The grey shaded area shows the eight regions with the number of convective days indicated for each. Dark grey lines mark the ERA-Interim grid boxes. The black circle in the top-right shows the minimum area ( $500 \text{ km}^2$ ) for a region to be classified as convective.

From Figure 3.30 we see that QSCS environments on average feature higher CAPE and weaker steering-level winds than those that typify afternoon summertime convection in the UK. Indeed, winds at all levels are weaker (not shown), giving rise to smaller values of speed shear. These differences are all found to be statistically significant at the 95 % test level using a standard difference of means test (Wilks 2011). It should be noted that the larger CAPE values in QSCS environments are associated with steeper mid-level lapse rates rather than higher surface  $\theta_e$  values (not shown). No significant difference exists between the distributions of precipitation water. In contrast to the suggestion above, QSCS environments are also characterised by larger directional shear on average. Furthermore, while one might expect the steering-level wind direction to evolve more slowly in QSCS environments (since cells must maintain a consistent trajectory), Figure 3.30 suggests the exact opposite. It can be noted, however, from Figure 3.31 that cases of large directional shear and changes in wind direction are mostly associated with light steering-level winds.

The presence of higher CAPE in QSCS environments is somewhat surprising. In conditions of weak steering level flow, large instability would favour the development of strong downdrafts in close proximity to the initiation point, potentially disrupting an external lifting mechanism. One might hypothesise that this characteristic is symptomatic, not of an environment which favours stationary convective systems, but those simply producing heavy precipitation (recall from Section 3.3 that LDCREs were identified using a threshold of 15 mm on 3 h rainfall accumulations). Previous studies (e.g. Fankhauser 1988, Kirkpatrick *et al.* 2011) have found no clear relationships between CAPE and surface rain rates or precipitation efficiency. Nevertheless, it is instructive

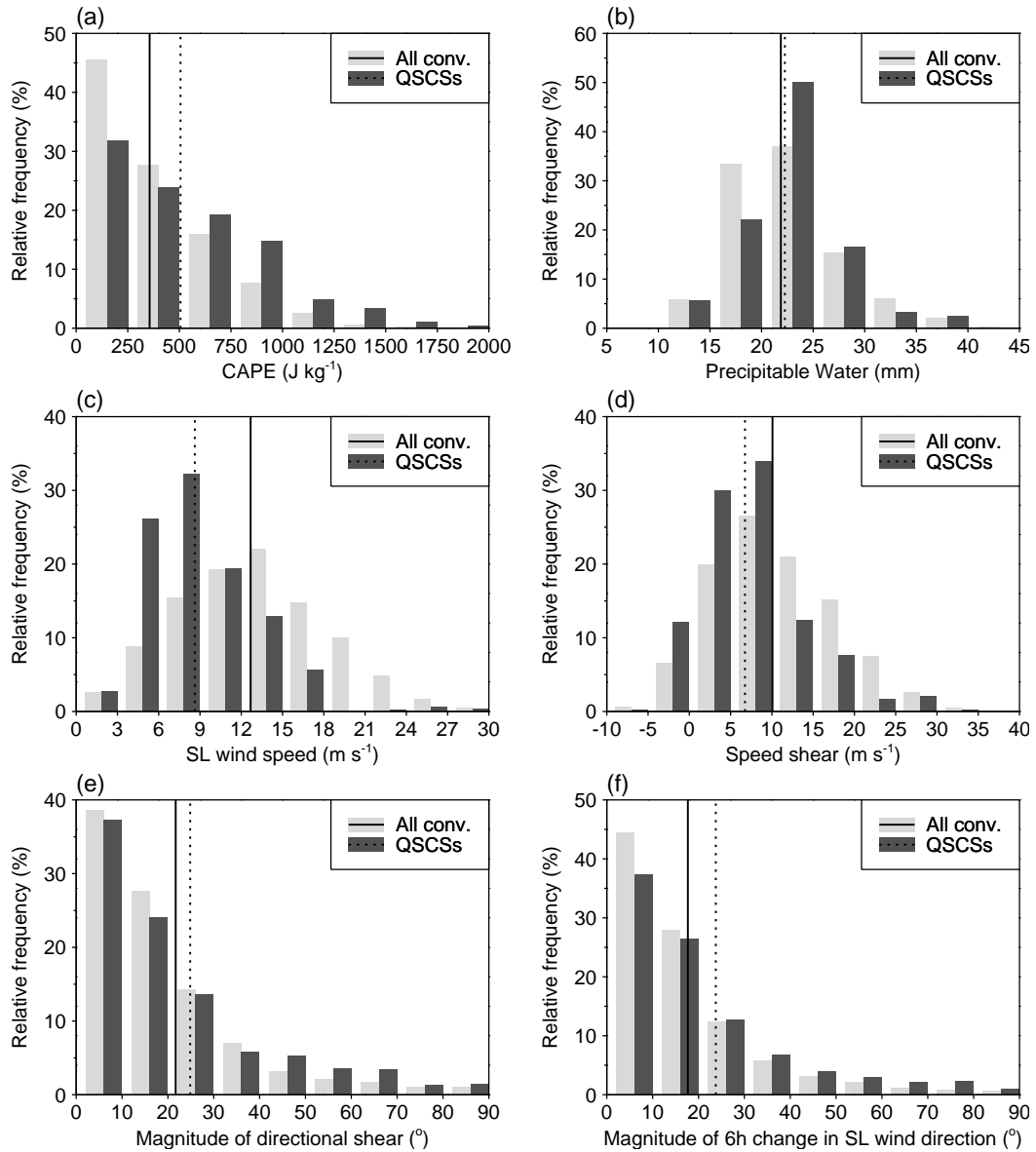


**Figure 3.30** Frequency distributions of six environmental parameters for all convection (light grey bars) and QSCSs (dark grey bars): (a) CAPE, (b) precipitable water, (c) steering-level (SL) wind speed, (d) speed shear, (e) the magnitude of directional shear, and (f) the magnitude of the 6 h change in SL wind direction. See text for definitions. Solid and dotted vertical lines show the distribution means for all convection and QSCSs respectively.

to consider whether the difference in CAPE distribution is unique to QSCSs or a feature of all events in my climatology. To this end, CAPE values were computed for the LDCREs in categories 2–6 (Section 3.5), again for a  $3 \times 2$  grid-point area around the event centroids, and compared to those for QSCSs and convection. Figure 3.32 shows that the distribution of CAPE for event types 2–6 is very similar to that for convection in general, although the former has somewhat higher frequencies at the extremes ( $\text{CAPE} < 250 \text{J kg}^{-1}$  and  $> 1000 \text{J kg}^{-1}$ ). We may thus conclude that higher values of CAPE are indeed favourable to the formation of QSCSs and not just symptomatic of heavy rainfall events. The reasons for this are not clear and require further investigation.

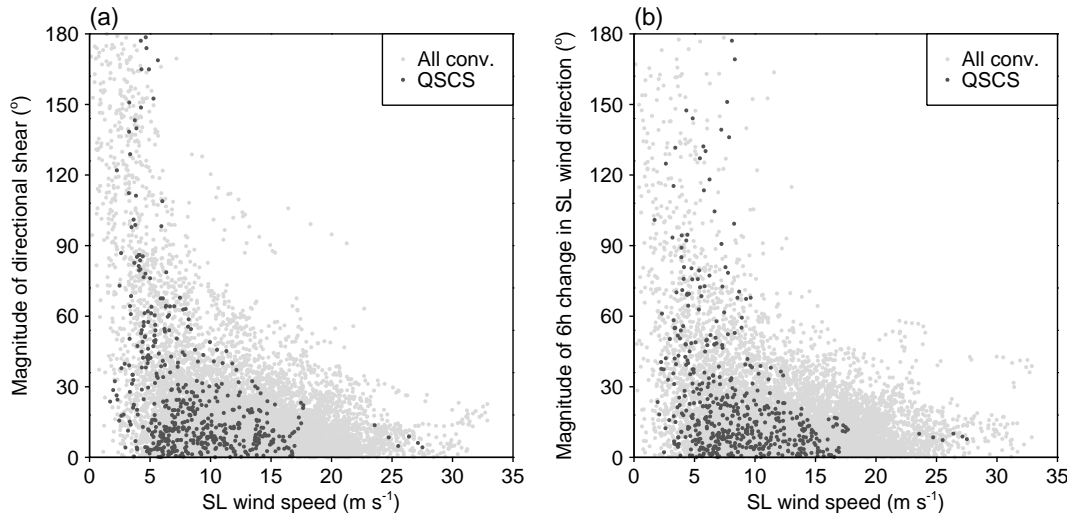


**Figure 3.31** Scatter graphs showing (a) the magnitude of directional shear and (b) the magnitude of the 6 h change in steering-level (SL) wind direction, both plotted as a function of the SL wind speed ( $\text{m s}^{-1}$ ) for all convection (light grey) and QSCSs (dark grey).

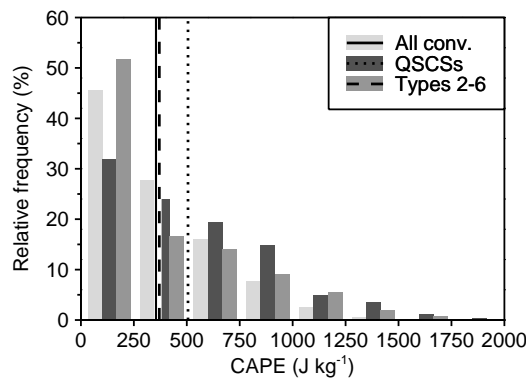


**Figure 3.32** Frequency distribution of CAPE for all convection (light grey bars), QSCSs (dark grey bars), and LDCRE types 2–6 (medium grey bars). Solid, dotted, and dashed vertical lines indicate the respective distribution means.

The presence of weaker winds in QSCS environments perhaps provides insight into the typical mechanisms by which these systems develop. Weak low-level winds reduce ventilation of heat at the surface and are thus favourable for the formation of thermally driven circulations (e.g. Banta 1990) which can initiate quasi-stationary systems (Golding *et al.* 2005; Soderholm *et al.* 2014). On the other hand, QSCSs formed through orographic or isentropic lifting typically occur in the presence of a low-level jet (e.g. Moore *et al.* 2003; Ducrocq *et al.* 2008). Meanwhile, for back-building systems where CI repeatedly occurs along a quasi-stationary portion of the storm’s outflow boundary, weak steering-level winds are required to prevent cells from being advected far downstream before they can develop a downdraught (e.g. Bresson *et al.* 2012). Thus, it may be that in the UK, QSCSs are more commonly associated with thermally driven circulations and internal mechanisms than direct lifting by orography or isentropic upglide. However, detailed analysis of many cases would be needed to confirm this hypothesis.

### 3.7 Summary, discussion, and conclusions

This chapter has explored the characteristics of QSCSs in the UK using a climatology derived from radar observations (the UK 1 km composite rainfall product) and meteorological reanalysis data (ERA-Interim). In order to create the climatology, three algorithms were developed: the first identified rainfall objects using the procedure of region growing with thresholds for rain rate and object size; the second classified rain rate objects as either convective or stratiform based on the fraction of pixels with large horizontal gradients in rain rate; the third identified long-duration convective rain events (LDCREs) using thresholds on the amount of rain, its duration, continuity, size, and the relative contribution of convective precipitation to the total accumulation.

The convective/stratiform classification algorithm was first run in isolation on five years (2008–2012) of data to produce a climatology of convective storms in the UK. This was compared with the results of Hand (2005) who used visible and infrared satellite imagery to distinguish between convective and stratiform cloud systems. My algorithm was able to identify many of the same spatial and temporal patterns in the occurrence of convection but produced lower relative frequencies due to its rejection of cells/systems which lack strong rainfall gradients. It was also noted that areas of intense frontal or orographic rain were occasionally misclassified as convective, although many of these likely contained areas of embedded convection.

The LDCRE identification algorithm was next applied to the same five-year dataset, resulting in a total of 525 events. Of these, 104 were rejected either for being associated with non-convective precipitation or spurious radar echoes, or due to poor radar data quality which would hinder further analysis. The remaining 419 events were placed into one of six categories based on the organisational characteristics of the causative rainfall as observed in radar animations. The first two categories, *quasi-stationary systems* (88 events) and *non-stationary training lines* (103 events), were both associated with the repeated movement of cells over the same area; however, only the first featured repeated initiation in approximately the same location. Examination of synoptic charts revealed that systems in the second category were often associated with flow approximately parallel to a slow-moving air-mass boundary or shear zone. Events in the third category, *near-stationary cells* (49 events), formed under quiescent conditions and featured either the repeated development or slow growth and decay of convective cells in the same location with virtually no lateral movement. In the fourth category, *rotational training systems* (24 events), the long rainfall duration was a consequence of changes in cell/system velocity associated with the passage of a low pressure centre. Events in the *disorganised training* category (90 events), again featured the repeated passage of cells over the same location but in the absence of any clear linear organisation. Finally, the sixth category, *unstructured clusters* (67 events), contained events associated with large and/or slow-moving convective systems showing little or no cellular structure.

Further analysis of the climatology focused on the 88 QSCSs. First, their geospatial and temporal characteristics were explored. The events were widely distributed across

the country, but appeared to be more common in the vicinity of coastlines and areas of complex orography. This suggests that many QSCSs in the UK are initiated and maintained by topographic forcing, either directly via mechanical lifting by orography or indirectly via induced circulations. Previous work (e.g. Hand 2005, Bennett *et al.* 2006) has demonstrated that, in general, topography plays a major role in CI in the UK, and numerous case studies from around the world have highlighted its role in the formation of flash flood-producing QSCSs (e.g. Maddox *et al.* 1978, Golding 2005, Ducrocq *et al.* 2008). However, as discussed in Chapter 1, some QSCSs develop in the absence of stationary surface forcing and are instead associated with processes internal to the convective system such as outflow boundaries (e.g. Miller 1978) and diabatically generated gravity waves (Schumacher 2009). Furthermore, upper-level forcing may play a role in the formation and maintenance of some quasi-stationary systems. Diagnosis of the relative contribution of these various mechanisms to QSCSs in the UK would require a detailed analysis of each case in the climatology, something which is outside the scope of this work.

The seasonal and diurnal cycles of QSCS occurrence were found to be similar to those of convection in general, with the highest frequencies being during the afternoon hours in late summer, although, there is significant interannual variability. Interestingly, over half the events (51%) occurred on the same day as another event. In some cases, systems formed in close proximity and appeared to be associated with the same initiation mechanism, but often they were widely separated. This suggested a causative link between the large-scale circulation pattern and the occurrence of QSCSs, a possibility which was explored using six-hourly analyses from the ERA-Interim dataset. However, examination of the 500 hPa geopotential height and mean-sea-level pressure fields for each event revealed great diversity in the synoptic conditions under which QSCSs may form. Similar, diversity was also observed in vertical profiles of temperature, dewpoint, and wind velocity taken in the vicinity of each system.

This finding contrasts with previous studies of extreme-precipitation and flash-flood events (e.g. Maddox *et al.* 1979, Nuissier *et al.* 2008) which have identified, for particular regions, a number of distinct circulation patterns under which these events typically take place. One explanation for this difference is that the ingredients for extreme rainfall are more specific than those for QSCSs. Both require mechanisms to sustain precipitation in one location for multiple hours, but for extreme accumulations and flash flooding the precipitation must also be very intense. In the absence of significant local surface evaporation, this necessitates large horizontal fluxes of water vapour which, in most midlatitude locations, places hard constraints on the wind direction and thus the large-scale circulation pattern. For example, in southern France, flash flooding almost always occur in the presence of a strong southerly low-level jet which advects warm, moist air inland from the Mediterranean Sea. This, in turn, is typically only present when there is an upper-level trough or cut-off low over Spain (Nuissier *et al.* 2008). By comparison, QSCSs only require enough water vapour to be sustained for their lifetimes, here defined to be as short as 3 h. Thus, it is hypothesised that, *provided conditions are favourable to*

*convection, a QSCS is possible wherever lifting can be sustained for a period of several hours.* Whether or not a given QSCS leads to extreme rainfall depends on the intensity of the rain (the amount of moisture available) and the stationarity of the system.

While the occurrence of QSCSs somewhere within the UK does not appear to be particularly sensitive to the large-scale circulation pattern, the exact location where these systems form is likely to depend strongly on the ambient flow, at least in cases where initiation is tied to surface topography. It was found that systems aligned along the Southwest Peninsula all occurred in the presence of unidirectionally sheared south-westerly flow and a deep layer of instability associated with an upper-level trough to the west of the UK. As will be discussed in later chapters, this flow configuration appears to favour the formation of quasi-stationary sea-breeze fronts which provide a mechanism for the repeated initiation of convective cells. Thus, the large-scale flow offers at least some predictive power for QSCSs in this part of the UK. It seems highly probable that the same would be true for stationary systems in other locations; however, this could not be assessed from the five-year climatology examined here.

The final part of my analysis involved a comparison between the environments proximate to QSCSs and those that typify afternoon summertime convection in the UK. To quantify the latter, another climatology of convection was produced, focusing on the southern UK which was divided into eight approximately equal-sized regions. On a given day, a region was classified as convective if, at any time between 1100 and 1700 UTC, convective precipitation covered a significant area (at least 500 km<sup>2</sup>) within it. Environment data (again taken from ERA-Interim analyses) was then stored for all grid points within these convective regions and compared with those for a  $3 \times 2$  box around each QSCS centroid. This analysis revealed that, on average, the environments in which QSCSs form feature significantly higher CAPE and lower wind speeds, with associated weaker vertical speed shear. It was also found that QSCS environments typically feature larger amounts of directional shear and experience larger temporal changes in the direction of the steering-level flow. However, both of the latter characteristics appear to be associated with the predominance of weak and variable winds. No significant differences were found in the amount of precipitable water. Further investigation is needed to understand why higher instability and weaker flow might favour the occurrence of stationary systems. However, it should be noted that over 50 % of the QSCS profiles featured CAPE less than 500 J kg<sup>-1</sup> and over 30 % had 700 hPa wind speeds exceeding 10 m s<sup>-1</sup>. Thus, as previously observed, these systems can form in a wide variety of environmental conditions.

## Chapter 4

# Case study of a QSCS over the UK Southwest Peninsula

### 4.1 Introduction

#### 4.1.1 Background and motivation

The previous chapter demonstrated that QSCSs may occur almost anywhere in the UK, but are somewhat more common in regions of significant topographic forcing. One area that stood out in particular was the Southwest Peninsula of England (Figure 4.1). Most of the systems identified in this region were orientated approximately southwest-to-northeast (i.e. along the peninsula) and occurred under conditions of unidirectional southwesterly flow and deep instability. This was also true of another QSCS which has become one of the most widely known severe weather events in the country: the Boscastle storm of 16 August 2004. This system formed along and just inland of the west coast of the Southwest Peninsula and remained stationary for several hours, resulting in rainfall totals which exceeded 200 mm over a narrow swath of land (Burt 2005). The steep and rocky local catchments rapidly channelled this water downstream, leading to devastating flooding in the coastal settlements of Boscastle and Crackington Haven (see Figure 4.1 for locations). Amazingly, given the rapid onset and severity of the flooding, there were no fatalities but the damage to local homes and businesses was severe.

Golding *et al.* (2005, hereinafter GCM05) investigated the Boscastle case using observations and numerical simulations with a high-resolution ( $\Delta x = 1$  km) version of the Met Office Unified Model (UM). They found that deep convection was initiated and maintained by a persistent, narrow convergence line which developed along the coastline during the day. Based on sensitivity tests, the authors concluded that this convergence line was “a sea-breeze front whose position was determined by a subtle balance between the gradient wind direction, retardation and backing of the wind over land, and differential heating”. They also suggested that the modest instability in this

---

A slightly abridged version of this work has been published in the Quarterly Journal of Royal Meteorological Society (Warren *et al.*, 2014).

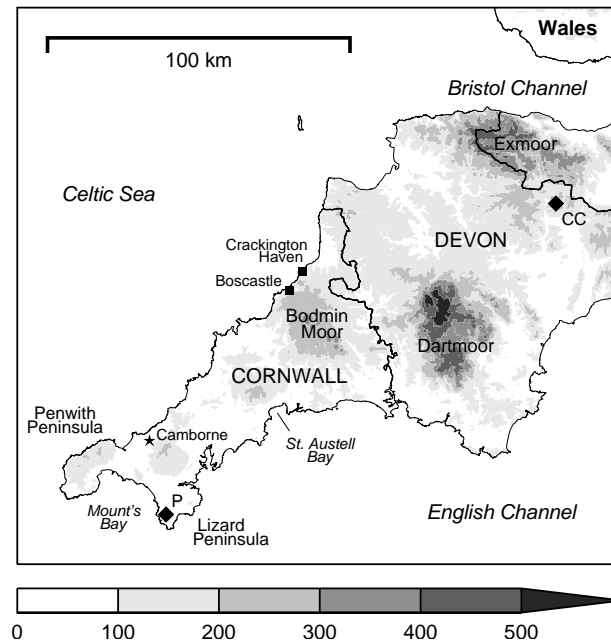


**Figure 4.1** Map of the UK Southwest Peninsula showing orography height (grey shading; m) and locations mentioned in the text. Diamonds show the locations of the two weather radars which provide coverage for this region: Predannack (P) and Cobbacombe Cross (CC).

case favoured “closely packed storms with weak downdraughts that did not distort the coastal convergence line”. The extreme intensity of the rainfall, which may have briefly exceeded  $500 \text{ mm hr}^{-1}$  (Burt 2005), was linked to high tropospheric humidity, sustained by large-scale ascent, which promoted unusually high precipitation efficiencies.

None of the Southwest Peninsula QSCSs in my climatology produced rainfall comparable in intensity or amount to that seen in the Boscastle event. However, one was remarkably similar in terms of its location and structure. It occurred on 21 July 2010 and produced maximum rain accumulations of around 50 mm in 3 hours, with no reports of flooding. This case provides an excellent opportunity to investigate the factors which distinguish severe (i.e. flash flood-producing) and non-severe QSCSs, without the complications associated with comparing events in different geographical locations. It also allows me to build on the work of GCM05, first, by examining a wider range of factors which might influence the formation and maintenance of QSCSs over the Southwest Peninsula, and second, by exploring the potential benefits of very high-resolution ( $\Delta x < 1 \text{ km}$ ) numerical simulations for forecasting this type of convective system.

#### 4.1.2 Chapter aims and structure

For this chapter, I set out to answer the following questions related to the 21 July 2010 QSCS:

1. What were the characteristics of the event in terms of the synoptic environment, storm evolution, and rainfall intensity and distribution?

2. Why was this event so much less severe than the Boscastle case?
3. What were the mechanisms responsible for the repeated initiation of convective cells and were these the same as in the Boscastle case?
4. How well is the QSCS represented in a high-resolution NWP model?
5. Does the representation improve with increasing horizontal resolution?

The first two of these are addressed in Section 4.2 through examination of large-scale model analyses and observations for both the 2010 and Boscastle cases. The latter three demanded the use of a high-resolution operational forecasting model, specifically, the UK Variable-resolution (UKV) configuration of the UM. Section 4.3 describes this model and details the various simulations performed. Modelling results are then presented in Section 4.4. First, output from a control run is examined and its accuracy assessed through comparison with radar observations. The mechanisms by which the QSCS was initiated and maintained are then explored using this run and a series of sensitivity experiments designed to isolate the role of specific processes. Finally, the impact of enhanced horizontal resolution and other changes in model setup (specifically, time step and subgrid-mixing parametrization) are considered. A summary of my findings is provided in Section 4.5.

## 4.2 Observational analysis

This section examines the 21 July 2010 event in terms of the evolution of the large-scale flow, the life cycle of the convective system, and the resulting precipitation distribution. A comparison is then made with the Boscastle case to determine the factors that made the latter so much more severe.

### 4.2.1 Synoptic setting

The synoptic situation over the British Isles at 0600 UTC on 21 July 2010 was characterised by a slow-moving low-pressure system at the surface and a cut-off low at upper-levels (Figure 4.2a). The centre of the surface low was located over the north-east coast of England, while a secondary, weaker circulation centre was present over southeast Ireland. The Met Office surface analysis for this time (available online at [http://www.wetter3.de/Archiv/archiv\\_ukmet.html](http://www.wetter3.de/Archiv/archiv_ukmet.html)) shows a cold front over the east coast of England, a warm front running northeast from the main low centre to Norway, and a trough line extending south from the secondary circulation centre. Over the Southwest Peninsula, the surface flow was from the southwest and thus roughly parallel to the western coastline. Quasi-geostrophic forcing in the region was minimal, with weak cold air advection and cyclonic vorticity advection aloft, and the peninsula was not positioned under any favourable regions for ascent associated with upper-level jet streaks (not shown). As the day progressed, the surface cyclone and associated cut-off low aloft moved very slowly northeastward. This resulted in veering winds with time

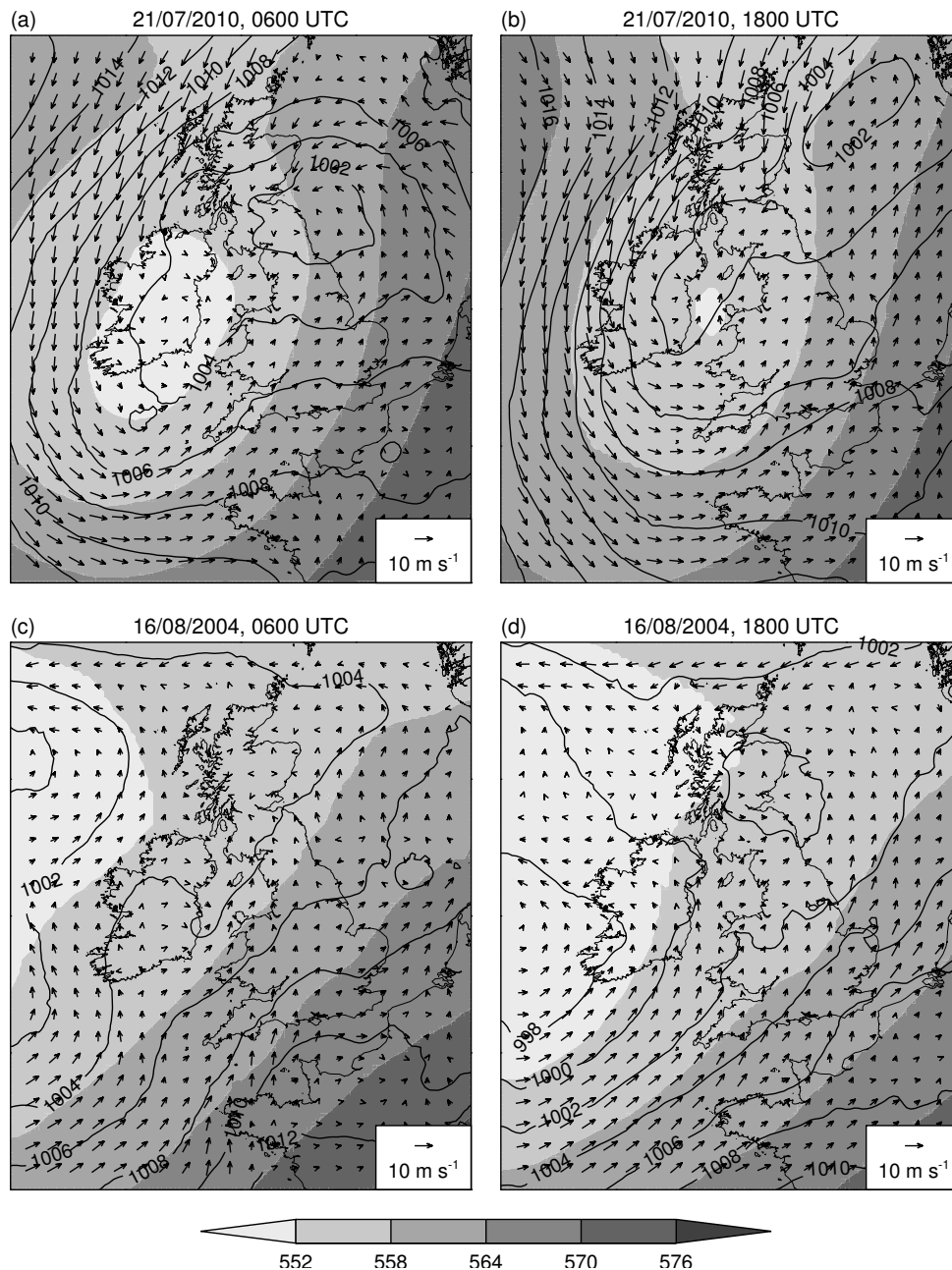


**Figure 4.2** Unified Model 12 km grid-length analyses for 0600 and 1800 UTC on (a),(b) 21 July 2010 and (c),(d) 16 August 2004 showing 500 hPa geopotential height (colour shading; dam), mean-sea-level pressure (black contours; hPa) and 10 m wind vectors.

over the Southwest Peninsula such that by 1800 UTC (Figure 4.2b), the surface flow over the west coast was approximately zonal.

The radiosonde ascent from Camborne, Cornwall (see Figure 4.1 for location) at 1200 UTC on 21 July 2010 is shown as a tephigram in Figure 4.3a. The atmosphere at this time was characterised by an absolutely unstable surface layer, moist, conditionally unstable air below a weak temperature inversion at 700 hPa, and drier, absolutely stable air aloft. A surface-based pseudoadiabatic parcel ascent gives CAPE of  $483 \text{ J kg}^{-1}$  and no CIN, with the LCL and LFC at 938 hPa (590 m) and the LNB at 453 hPa (6.3 km). Note

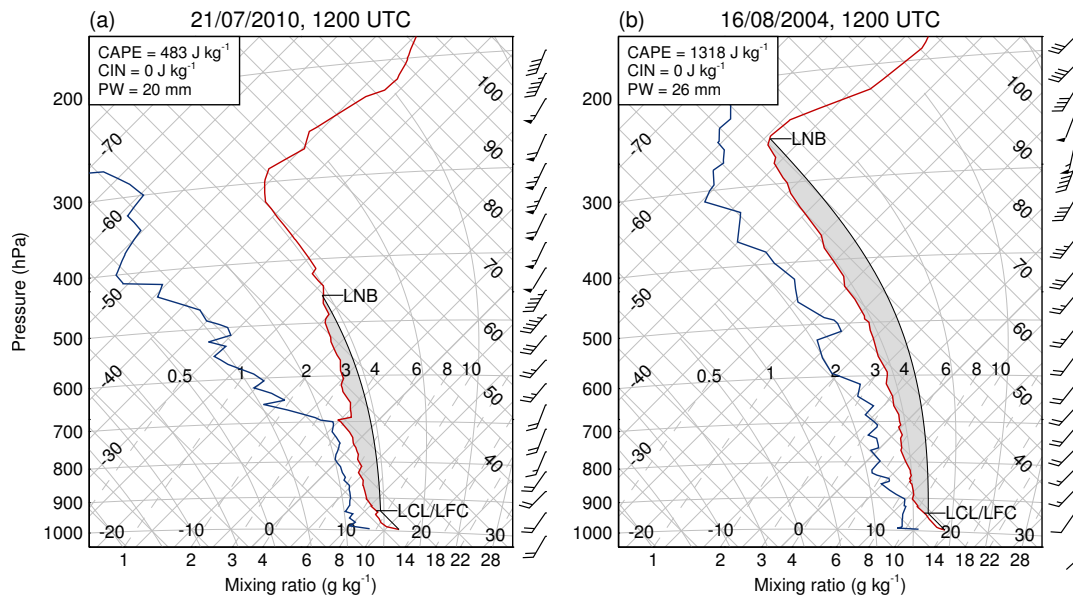


**Figure 4.3** Tephigrams showing the 1200 UTC radiosonde ascents from Camborne on (a) 21 July 2010 and (b) 16 August 2004. Red and blue lines show the temperature and dewpoint temperature profiles respectively. Black lines shows surface-based pseudo-adiabatic parcel ascents with the LCL, LFC, and LNB indicated and the resulting CAPE distribution shaded grey. Values for CAPE, CIN, and precipitable water (PW) are given in the top left corner of each panel. Wind barbs show speed in knots with half barbs, full barbs, and pennants indicating 5, 10, and 50 knots respectively.

that, due to relatively high temperature and humidity at the surface, the surface-based parcel is the most unstable in the sounding; a parcel initialised with the mixed-layer properties over the lowest 100 m has CAPE of only  $122 \text{ J kg}^{-1}$  and an LNB at 576 hPa (4.5 km), though again negligible CIN. Thus, we would expect convection to readily develop but remain rather shallow, with cloud tops generally below 6 km. The wind profile in Figure 4.3a shows southwesterly flow over the depth of the troposphere, with a density-weighted cloud layer-mean wind speed of  $12 \text{ m s}^{-1}$ . The slight unidirectional shear in the cloud layer may have reduced the potential for downdraughts to suppress the convective updraughts (Section 1.2.3).

#### 4.2.2 Storm evolution and rainfall accumulations

In the moist, conditionally unstable flow over southwest England, convection readily developed during the morning of 21 July. High-resolution visible satellite imagery from Meteosat Second Generation (not shown) reveals the development of shallow cumuli over much of the Southwest Peninsula between 0700 and 0800 UTC. These clouds rapidly deepened and organised into bands (cloud streets) parallel to the prevailing southwesterly flow. Surface rainfall data from the UK 1 km radar composite product (Section 2.1) show that between 0830 and 1000 UTC, numerous precipitating cells formed over the peninsula, in particular along and just inland of the west coast (Figure 4.4a). These cells tracked northeast at a speed of around  $11 \text{ m s}^{-1}$ , consistent with the calculated cloud layer-mean wind. Over the next two hours, the cells increased in size

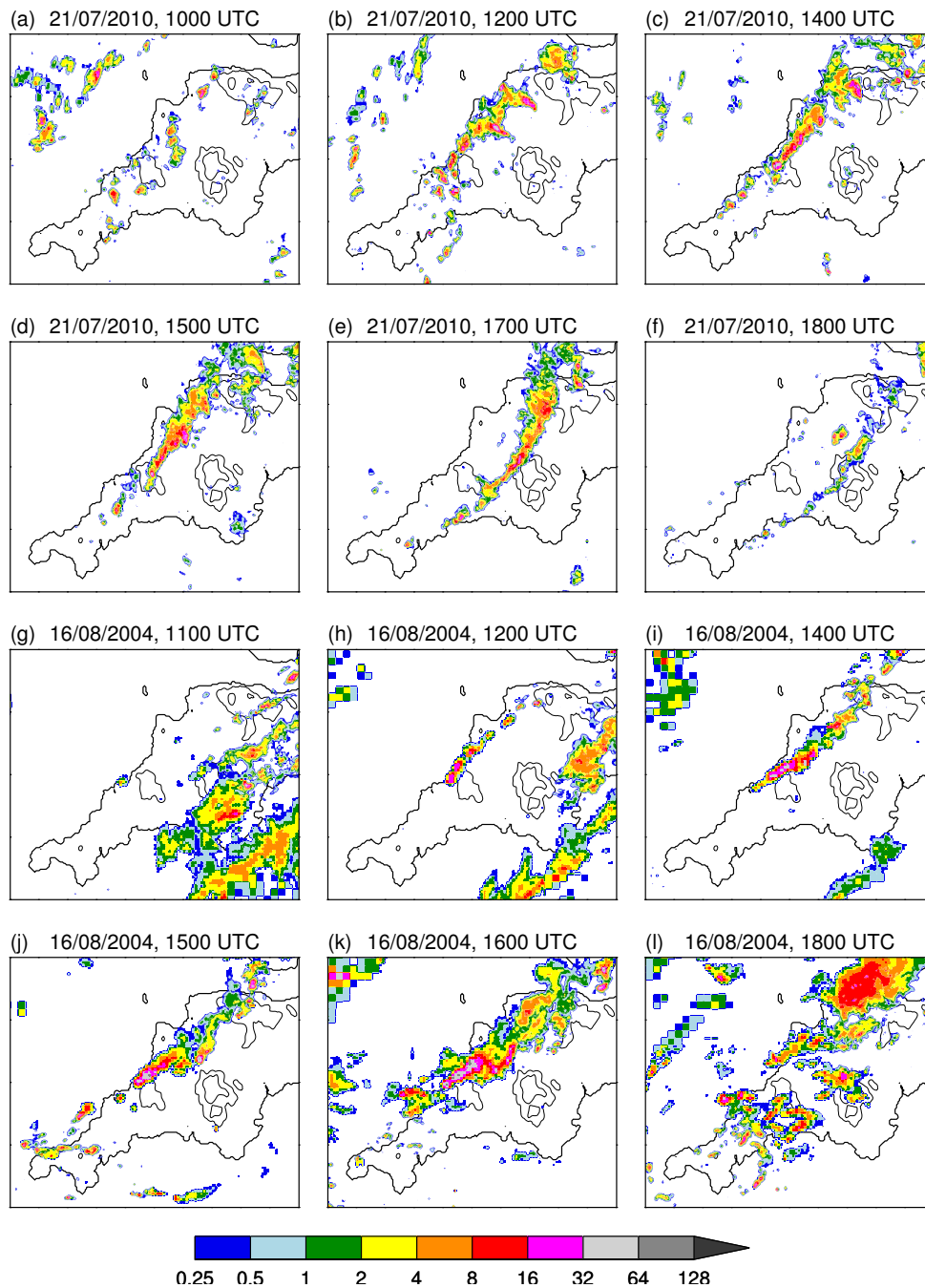


**Figure 4.4** Radar-derived surface rain rates (colour shading;  $\text{mm h}^{-1}$ ) over the Southwest Peninsula at various times on (a)–(f) 21 July 2010 and (g)–(l) 16 August 2004. Orography height is contoured every 200 m. For both dates, the radar data have a grid spacing of 1 km; however, prior to 2007 the interpolation method used to produce the composite caused the apparent resolution to degrade with distance (see Section 2.1 for details).

and coverage, forming an almost continuous line of precipitation along the coastline (Figure 4.4b). The rainfall intensity also increased; around 1049 UTC, the tipping bucket rain gauge at Boscastle briefly recorded rain rates exceeding  $150 \text{ mm h}^{-1}$ .

Following this, the line remained quasi-stationary for around 2 h, showing only slight inland movement between 1200 and 1300 UTC. At 1400 UTC (Figure 4.4c), the system was composed of two distinct areas: the main convective line extending from Bodmin

Moor into Exmoor, and a collection of more isolated cells located farther southwest. Animations of the rainfall field show that these cells did not merge with the main line but drifted to the west of it and dissipated. The cells that made up the main line appear to have initiated farther east, along the centre-line of the peninsula. These rapidly intensified as they joined with the main line over Bodmin Moor, then continued northeast, weakening as they approached Exmoor and the Bristol Channel. Several of the more intense cells experienced a sudden eastward acceleration as they approached the northeast end of the convective line (two such cells can be seen protruding from the main line in Figure 4.4b). This was likely associated with new initiation occurring along outflow boundaries produced by the storm. Maximum cloud top heights (derived from Meteosat Second Generation imagery; not shown) were around 5.5 km at the northeast end of the line, consistent with the parcel analysis in Section 4.2.1.

After 1400 UTC, the convective line began to move inland, starting at its southwest end with the movement gradually spreading northeast (Figure 4.4d). The model simulations to be presented in Section 4.4 indicate that this movement was due to veering low-level winds associated with the gradual eastward progression of the surface cyclone (Figure 4.2a–b). By 1700 UTC (Figure 4.4e), the line had moved away from the west coast, and extended in an arc from St. Austell Bay to Exmoor. Over the next hour, the system rapidly weakened (Figure 4.4f), eventually dissipating around 1900 UTC.

Figure 4.5a shows rain-gauge and radar-derived accumulations between 1200 and 1500 UTC (i.e. the period for which the most intense portion of the line was stationary) over part of the Southwest Peninsula’s west coast. Typical for a quasi-stationary storm, the precipitation area forms an elongated streak along the direction of cell motion, with sharp rainfall gradients either side (particularly, in this case, on the east side). Peak accumulations of around 50 mm occurred on the northwest slopes of Bodmin Moor; not an insignificant amount of rainfall for a 3 h period, particularly over such fast-response catchments. However, there were no reports of flooding and the effect of the rain on river levels was “unremarkable” (Maggie Summerfield, Environment Agency, personal communication). There was a rapid rise in the level of the River Otter shortly after 1500 UTC noted at the Canworthy Water flood warning station (indicated with a star in Figure 4.5a), but the level attained happens many times a year. The lack of a significant hydrological response can be explained by the distribution of the heaviest rain across river catchments. Figure 4.5a reveals that the highest accumulations occurred close to the headwaters of several rivers, thereby spreading the runoff across multiple drainage basins. In contrast, in the Boscastle case, the heaviest rain fell to the west of the high ground, over just a handful of small coastal catchments (Figure 4.5b).

### 4.2.3 Comparison with the Boscastle case

Figures 4.2–4.5 provide a comparison of the 21 July 2010 and Boscastle cases in terms of the large-scale and local environmental conditions, the evolution of the convective systems, and the resulting precipitation accumulations. In this section, the main simi-

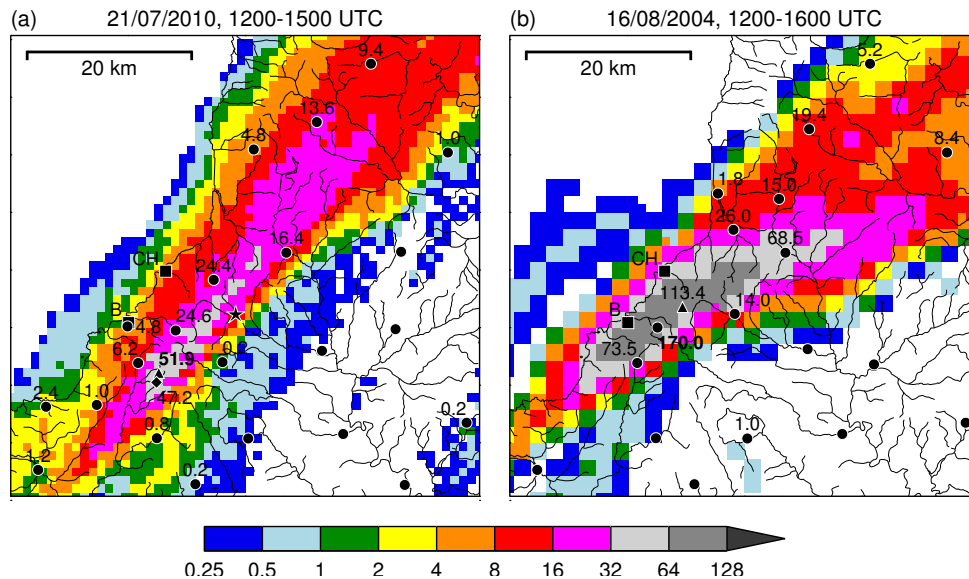


**Figure 4.5** Radar-derived rainfall accumulations (colour shading; mm) over a portion of the Southwest Peninsula for (a) 1200–1500 UTC on 21 July 2010 and (b) 1200–1600 UTC on 16 August 2004. Note that while both images have the same gridded resolution ( $\Delta x = 1$  km), the pixels are generally larger ( $2 \times 2$  km) in (b) due to a change in the interpolation method used to create the radar composite (Section 2.1). Thin black contours denote rivers from the Ordnance Survey GR dataset (obtained from <http://www.sharegeo.ac.uk/handle/10672/85>). Triangles indicate the maximum radar-derived accumulation in each case, while circles indicate accumulations measured by Environment Agency tipping-bucket rain gauges. The highest accumulations in each event are labelled in bold. The value of 170.0 mm in (b) is based on the corrected Lesnewth rain-gauge record from Burt (2005). In (a), the diamond indicates the accumulation from the Met Office day (0900–0900 UTC) recording gauge at Lower Moor and the star shows the location of the Environment Agency’s Canworthy Water flood-warning station.

larities and differences between the two cases are discussed. For a detailed description of the Boscastle case see Burt (2005), GCM05, and Golding (2005).

On 16 August 2004, a slow-moving weakly baroclinic low-pressure system was again affecting the UK; however, this system was positioned around 1000 km farther west than the one on 21 July 2010 (Figure 4.2c–d). Despite this difference, winds over the Southwest Peninsula were again southwesterly over the depth of the free troposphere, with weak unidirectional shear (Figure 4.3b). However, the large-scale evolution on 16 August 2004 did not act to significantly turn the wind with time; Figure 4.6 shows that deep, southwesterly flow was maintained throughout the day, whereas on 21 July 2010 the wind veered by around  $45^\circ$  in the lowest 4 km between 0600 and 1800 UTC. The 1200 UTC Camborne sounding on 16 August 2004 (Figure 4.3b) shows an approximately moist-neutral temperature profile with high humidity throughout the troposphere. GCM05 suggested that this deep moist layer was the result of large-scale ascent associated with an upper-level jet streak (not shown). The surface-based parcel ascent in this case has a much deeper layer of instability extending up to the tropopause at 250 hPa, with CAPE of  $1318 \text{ J kg}^{-1}$ . Note that this value is considerably larger than that quoted by GCM05 ( $170 \text{ J kg}^{-1}$ ) which was calculated using a 500 m mixed-layer parcel.

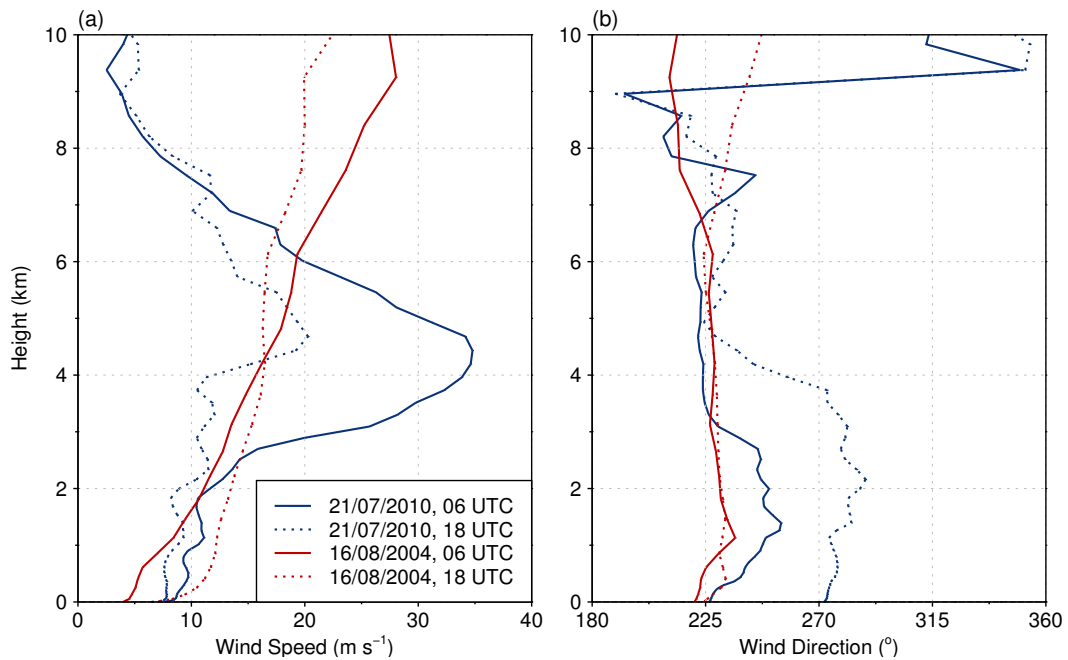


**Figure 4.6** Horizontally averaged vertical profiles of (a) wind speed and (b) wind direction (clockwise from north) computed for a  $4 \times 4$  grid-point box just southwest of the Southwest Peninsula from UM 12 km grid-length analyses valid at 0600 (solid) and 1800 UTC (dotted) on 21 July 2010 (blue) and 16 August 2004 (red).

Figure 4.4 provides a comparison of the evolution of the 21 July 2010 and Boscastle QSCSs. The similarity in the location and structure of the two systems is striking; however, there are several important differences. First, in the Boscastle case, convection initiated later, with the first precipitating cells along the west coast of the peninsula appearing around 1100 UTC. This suggests that CIN was initially too high and/or lifting was too weak for parcels to reach their LFC, giving a longer period for instability to grow through surface heating. Second, the rain rates in the convective cores of the Boscastle system were considerably higher. Comparing the soundings in Figure 4.3, we note several features of the environment which may have favoured more intense precipitation on 16 August 2004:

1. Higher specific humidity throughout the troposphere. This indicates the presence of more water vapour available for condensation and precipitation formation (26 mm of precipitable water compared with 20 mm in the 2010 case).
2. Higher relative humidity at mid-levels. This will have reduced the detrimental effects of entrainment on cloud liquid water content (and buoyancy) favouring higher precipitation efficiencies.
3. Higher CAPE. This will have favoured stronger updraughts, with an associated increase in the vertical flux of water vapour and thus the rate of cloud water production.<sup>1</sup>

<sup>1</sup>Kirkpatrick *et al.* (2011) found no significant linear correlation between CAPE and rain intensity in their simulations of supercell storms; however, a relationship may exist for less-organised systems.

4. Deeper cloud layers both above and below the freezing level. This may have simultaneously increased both warm-rain and ice-phase precipitation formation allowing for a more efficient collection of cloud droplets.

Despite high low-level humidity and reduced potential for precipitation evaporation, the intense rainfall in the Boscastle case appears to have resulted in rapid downdraught formation, giving rise to bowing segments in the convective line to the northeast of Bodmin Moor (visible in Figure 4.4i,j,k). The final important difference between the two cases was that the Boscastle storm remained stationary for a longer period of time. As previously noted, the 2010 system began to move inland after 1400 UTC. In contrast, the Boscastle storm remained in place until 1630 UTC when it was swept northeast by a separate area of convection (visible southwest of the main line in Figure 4.4k). This difference appears to be related to the persistence of deep southwesterly flow in the Boscastle case, compared to veering flow in the 2010 case (Figure 4.6).

The result of these differences was a far more extreme rainfall event on 16 August 2004. While radar-derived totals for the Boscastle storm reached just over 110 mm between 1200 and 1600 UTC, corrected data from the Environment Agency's tipping-bucket rain gauge at Lesnewth (Burt 2005) shows an accumulation of 170 mm for this period (Figure 4.5b). This underestimation by the radar does not appear to have occurred on 21 July 2010; the total for the rainfall day (0900 UTC, 21 July–0900 UTC, 22 July) at the Met Office Lower Moor gauge (indicated by the diamond in Figure 4.5a) agrees well with the nearby radar maximum. The difference in radar–gauge agreement between the two cases may be related to changes in the processing of radar data between 2004 and 2010 (Harrison *et al.* 2009). Another possibility is that attenuation effects were more severe in the Boscastle case due to the higher rain rates. However, as suggested by Golding (2005) the discrepancy may simply reflect the different sampling characteristics of the two instruments.

To further illustrate the differences in precipitation between the two cases, Figure 4.7 compares rain-rate and accumulation time series for the radar grid point with highest accumulation on 21 July 2010 with those for the Lesnewth gauge on 16 August 2004. This illustrates the relative impact of higher rain rates and longer rain duration in the Boscastle case. Extrapolation of the 2010 data suggests that had the storm persisted as long as the Boscastle QSCS, peak accumulations would have reached around 90 mm. This equates to roughly 30% of the difference between the two events. Meanwhile, average rain rates in the Boscastle case were around  $30 \text{ mm hr}^{-1}$  higher than in the 2010 case ( $47 \text{ mm h}^{-1}$  compared to  $16 \text{ mm h}^{-1}$ ). Of course, we cannot know how intense the convective system on 21 July 2010 would have become had it remained stationary for longer. In the Boscastle case, the heaviest rain occurred after 1430 UTC, with over half the total (around 100 mm) falling in the 50 minutes from 1455 to 1545 UTC.

In summary, it may be noted that while the 21 July 2010 QSCS showed clear similarities to the Boscastle QSCS of 16 August 2004, differences in the intensity, duration, and distribution of precipitation gave rise to very different impacts, with no recorded

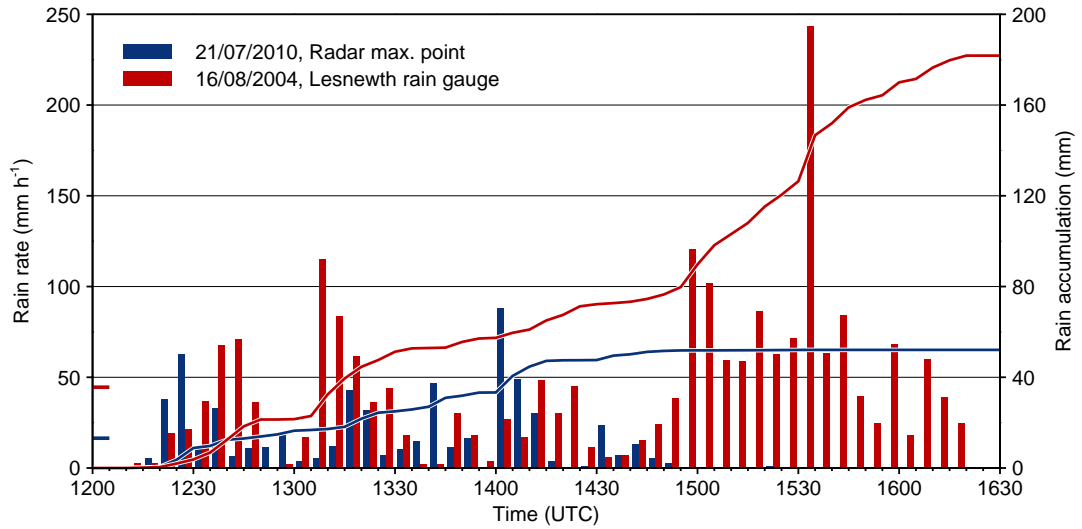


**Figure 4.7** Time series of rain rate (bars) and rain accumulation (lines) for the point of maximum radar-derived rainfall accumulation on 21 July 2010 (blue) and for the Environment Agency’s tipping bucket rain gauge at Lesnewth, Cornwall on 16 August 2004 (red). A heuristic correction has been applied to the Lesnewth data to account for under-reading during periods of intense rainfall; see Burt (2005) for details. The horizontal lines on the  $y$ -axis show the time-averaged rain rates for each case computed over values  $\geq 0.2 \text{ mm h}^{-1}$  (the resolution of the tipping-bucket gauge).

flooding in the former case and a devastating flash flood in the latter. Both events were characterised by deep southwesterly flow, which, as shown in Chapter 3, appears to favour the formation of QSCSs over the Southwest Peninsula. However, it is clear that subtle differences in the properties of this flow, as well as its evolution over time, can dramatically alter the severity of convective systems which develop.

### 4.3 Numerical model and experiment design

In order to explore the processes by which the 21 July 2010 QSCS formed, a series of high-resolution numerical simulations were performed with the UM. This section describes the model configuration and simulation strategy.

#### 4.3.1 The UKV model

The UKV model is a limited-area, variable-resolution configuration of the UM. It was developed to improve the resolution of forecasts over the UK without the need for an intermediate-resolution model to properly treat boundary condition data from the 12 km grid-length North Atlantic European (NAE) model (Tang *et al.* 2013). The UKV horizontal domain consists of three sections: a coarse-resolution ( $\Delta x = 4 \text{ km}$ ) outer frame, a fine-resolution ( $\Delta x = 1.5 \text{ km}$ ) inner domain, and a variable-resolution transition area in-between (Figure 4.8). In the vertical, the model has 70 levels with a top at 40 km. At UM Version 7.3, the operational UKV was run at 0300, 0900, 1500 and 2100 UTC each day, with initial and boundary conditions provided by an NAE run initialised 3 h earlier. A data assimilation cycle operated from  $T - 2 \text{ h}$  to  $T + 1 \text{ h}$  (where

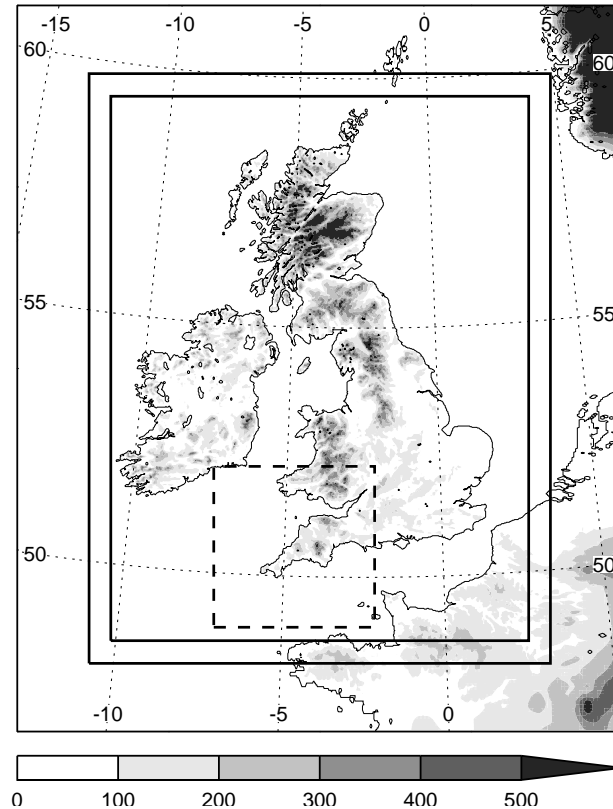


**Figure 4.8** UKV model domain and orography height (grey shading; m). The inner and outer solid boxes show the limits of constant-resolution interior domain and the variable-resolution transition zone respectively. The dashed box shows the domain used in the simulations presented herein. Dotted lines show true latitude and longitude.

$T$  is the forecast run time) which included assimilation of surface- and satellite-derived 3-D cloud fractions (Renshaw and Francis 2011) and radar-derived surface rain rates (Jones and Macpherson 1997).

A key feature of the UKV model is that it treats convection explicitly, i.e. without the use of a parametrization scheme. Since numerical models can only accurately represent processes larger than several grid lengths, individual convective cells (and in particular, their updraughts and downdraughts) are still significantly under-resolved with 1.5 km grid spacing. In the UKV model this leads to a number of biases including delayed convective initiation, and cells which are too large, intense, and circular (Halliwell *et al.* 2013; McBeath *et al.* 2014; Hanley *et al.* 2014). To truly capture the turbulent nature of deep moist convection, one must apply large-eddy simulation (LES) techniques and use grid lengths of 100 m or less (Bryan *et al.* 2003). Despite this,  $O(1\text{ km})$  grid length configurations of the UM have been shown to provide substantial benefit in quantitative precipitation forecasting (QPF) for convective situations in the UK compared to lower-resolution configurations with parametrized convection (e.g. Roberts and Lean 2008, Lean *et al.* 2008).

### 4.3.2 Simulation strategy

Simulations of the 21 July 2010 QSCS have been carried out using the UKV configuration of the UM at Version 7.3. Note that at the time of the event, the Met Office was actually running a later version (7.6); however, this was not available for the present investigation. The 0400 UTC operational UKV analysis (the output of the model's 3 h data assimilation cycle) was used as initial conditions (ICs) while lateral boundary conditions (LBCs) were provided by the 0000 UTC NAE model forecast. In addition to a control simulation, a number of sensitivity tests were carried out in order to isolate the mechanisms responsible for the repeated initiation of convective cells along the peninsula coastline. These are discussed in detail in Section 4.4.2. A run with 500 m grid spacing was also performed and is described in Section 4.4.3. In each case, the model was integrated forward for 15 h (to 1900 UTC).

In order to reduce computational expense and prevent undesirable feedbacks on the large-scale flow in the sensitivity runs, all simulations were performed on a smaller domain nested within the full UKV model but with the same resolution ( $\Delta x = 1.5$  km). This domain, shown by the dashed box in Figure 4.8, consists of  $240 \times 240$  grid points which correspond exactly to points on the UKV model grid (to eliminate the need for interpolation of the initial analysis). A single run of the full UKV model was used to provide LBCs for the nested domain at half-hourly intervals. Comparison between the output of the full UKV run and the control run (not shown) revealed only slight differences in storm evolution and precipitation accumulations.

It should be noted that the 1.5 km configuration used for the present study had a different treatment of subgrid vertical mixing from the operational UKV model. The latter uses the standard boundary-layer scheme which includes both local and non-local mixing while my configuration used the Smagorinsky-type scheme (Section 2.2.2). This setting may not be optimal at 1.5 km grid spacing; however, it has been used successfully in even-coarser-resolution studies of convection by Holloway *et al.* (2012). For my purposes, it allowed for a cleaner comparison with the 500 m run, which by default uses the Smagorinsky scheme. Sensitivity to the mixing scheme in the present case is examined in Section 4.4.4.

## 4.4 Simulation results

This section presents results from the various simulations of the 21 July 2010 QSCS. Model data are presented on the rotated pole grid used in UK limited area configurations of the UM. Where a direct comparison between model and radar data is required, the latter are bilinearly interpolated to the model grid.

### 4.4.1 Control simulation

Figure 4.9 shows the evolution of the surface precipitation field in the control simulation. This can be directly compared with the observed evolution shown in Figure

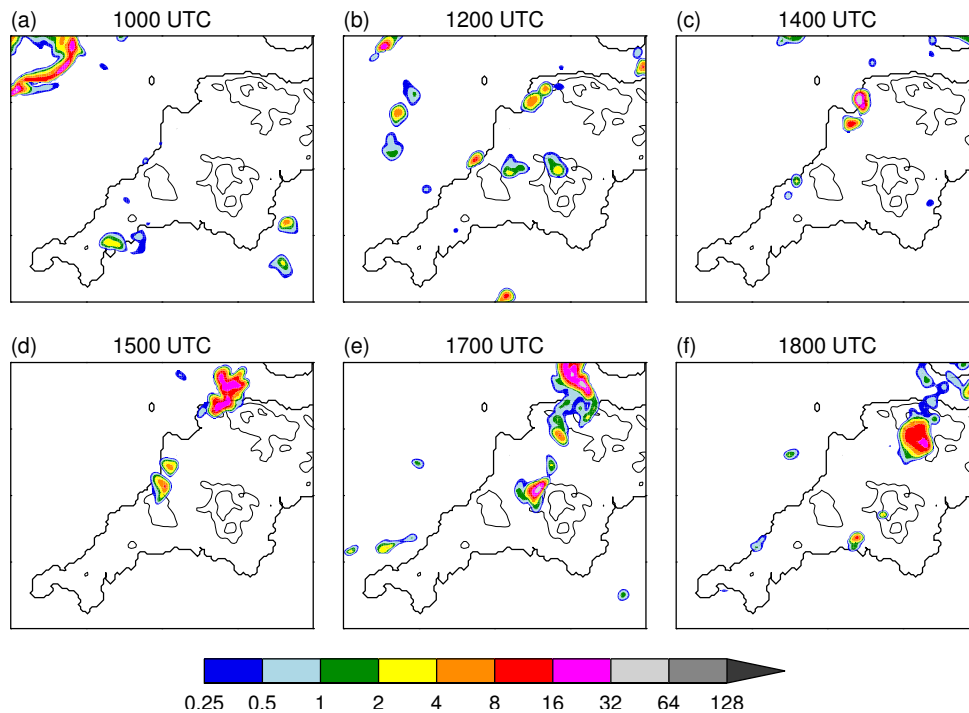


**Figure 4.9** Evolution of surface rain rates (colour shading;  $\text{mm h}^{-1}$ ) in the control simulation. Model orography is contoured every 200 m. The times shown match those for the radar images in Figure 4a–f.

4.4. The model appears to have captured the repeated development of convective cells along the west coast of the peninsula during the late morning and early afternoon, and their subsequent inland propagation. However, there are some notable deficiencies in its representation of both the timing and structure of the storm system. These are further illustrated in subsequent figures which compare the observed and simulated accumulations (Figure 4.10), system evolution (Figure 4.11), and rain rates (Figure 4.12).

We first note that the model initiates convection late, with the first precipitating cell appearing at 1000 UTC, over an hour later than observed in the radar imagery (Figure 4.11). The length of time (and thus the distance) between successive cells is also greater in the model. Consequently, the storm system fails to achieve the continuous, linear structure seen in the radar images. The cells themselves are smoother than those observed and too large, particularly during the mature stage of their evolution (Figure 4.9). Furthermore, they evolve too slowly in terms of the intensity of rainfall they produce (Figure 4.11). As noted in Section 4.2.2, the observed cells developed rapidly and produced heavy precipitation over Bodmin Moor where they joined the main convective line. As they approached the northeast end of the line in Devon, they generally weakened and became less organised (Figure 4.4a–f). By contrast, the modelled cells produce only light rainfall over Bodmin Moor and do not peak in intensity until they reach North Devon (Figure 4.9). Beyond this, they continue to grow laterally and weaken only slightly as they move across the Bristol Channel into Wales.

The net effect of these differences on the accumulated rainfall is shown in Figure 4.10. For the 9 h period considered, the accumulation pattern associated with the

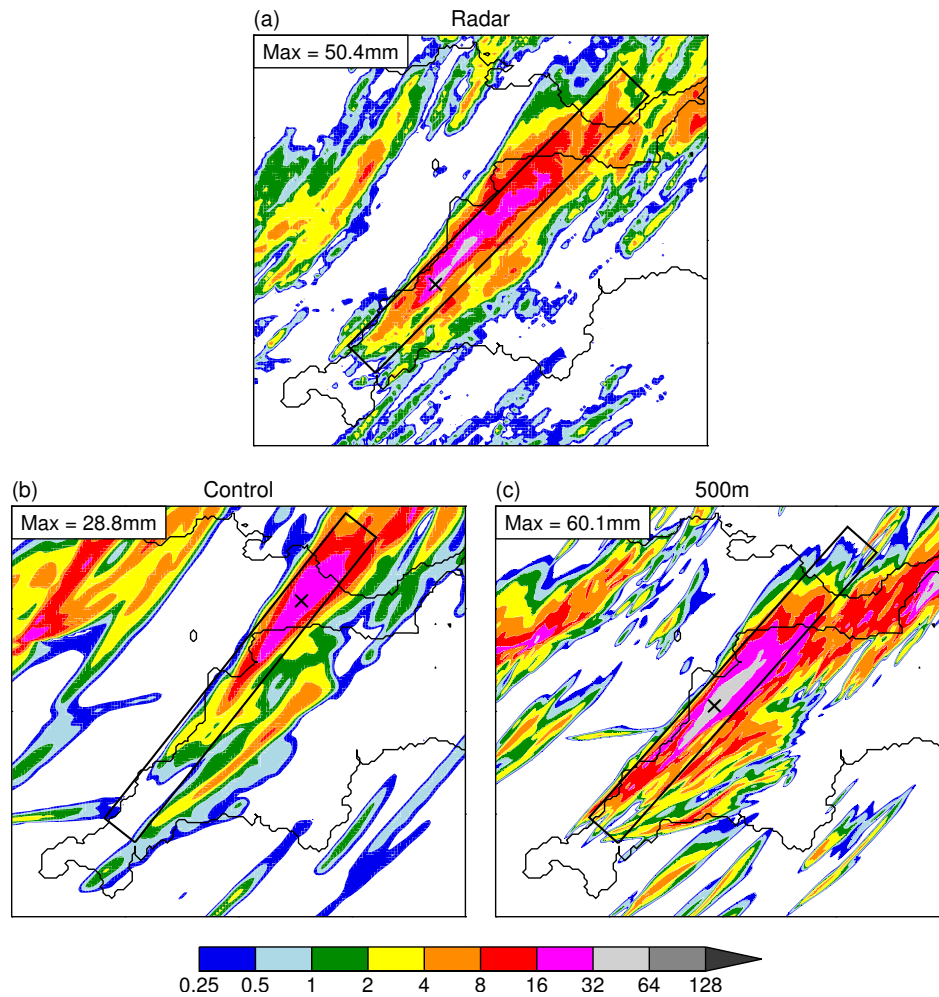


**Figure 4.10** Rain accumulations (colour shading; mm) from (a) the radar composite (interpolated to the 1.5 km model grid), (b) the control simulation, and (c) the 500 m grid-length simulation for the period 0900–1800 UTC. Crosses mark the point of maximum accumulation with the corresponding values given in the top left corner of each panel. Boxes show the area used to produce the Hovmöller plots in Figure 4.11. These all originate at the same point, are 200 km long and 20 km wide, and are orientated such that they pass through the point of maximum accumulation.

QSCS is fairly well captured; however, the maximum is less by almost a factor of two and shifted around 100 km to the northeast (Figure 4.11). This shift is primarily due to the slower development of the simulated cells, which also results in reduced along-line accumulation gradients on the upstream (southwest) side of the precipitation maximum. We might expect the difference in maximum accumulation to be greater given the wide spacing between successive cells in the model; however, this appears to have been at least partly compensated for by overly intense precipitation in the convective cores. Indeed, Figure 4.12 reveals that the simulation has a substantial positive bias in rain rates when compared to the radar observations. This becomes more pronounced if we consider only those grid points with large accumulations. In general, too little rainfall occurs at rates less than around  $10 \text{ mm h}^{-1}$  and too much occurs at rates between 10 and  $30 \text{ mm h}^{-1}$ .

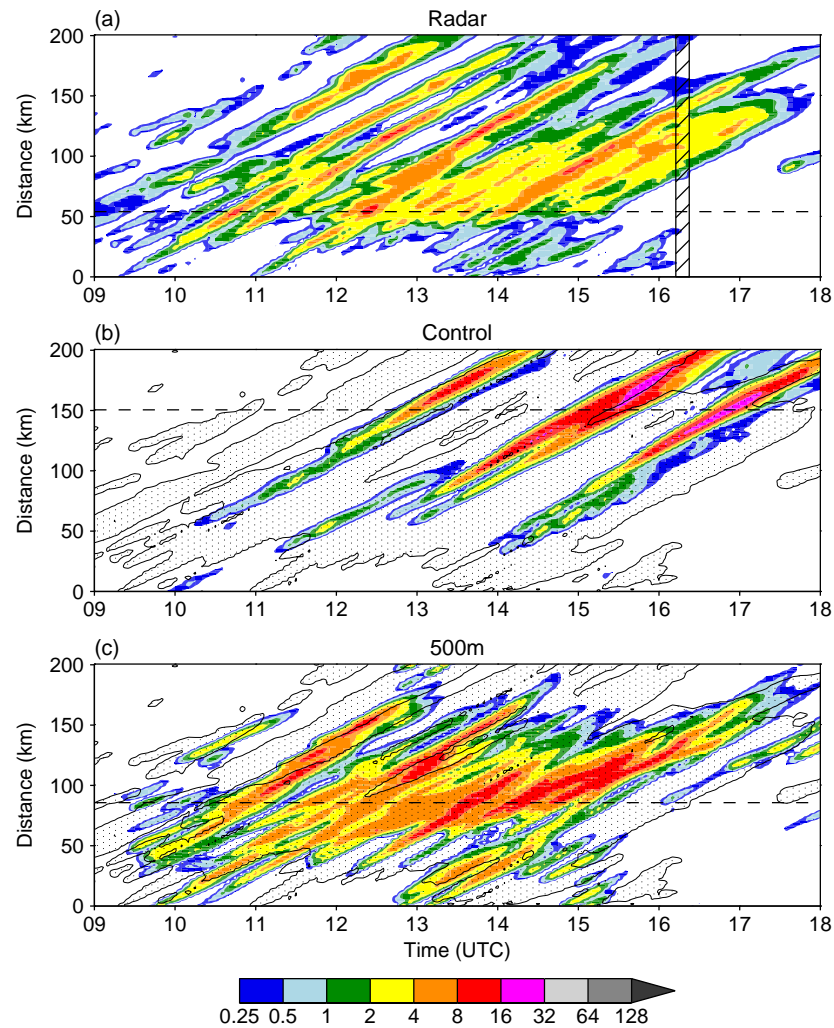


**Figure 4.11** Hovmöller plots of rain rate (colour shading;  $\text{mm h}^{-1}$ ) at 5minute temporal resolution between 0900 and 1800 UTC on 21 July 2010 from (a) the radar composite, (b) the control simulation, and (c) the 500 m grid-length simulation. These were computed along the long axes of the boxes shown in Figure 4.10 with values averaged over the short axes (20 km width) and smoothed using a 5 km boxcar moving average. Dashed horizontal lines show the location of the maximum rainfall accumulation in each case. No radar data were available for 1615 and 1620 UTC so values have been linearly interpolated in time for this period (hatched in (a)). The stippling in (b) and (c) shows the rain area in (a) for comparison.

Clearly there are some significant deficiencies in the control simulation’s representation of the 21 July 2010 QSCS. Some of these may be due to inadequate horizontal resolution, a possibility which is explored in Section 4.4.3. However, a comprehensive investigation of all model biases is outside the scope of this work. Much research is ongoing into the ability of high-resolution configurations of the UM (and other operational models) to accurately forecast convective precipitation. Here, it is noted that, while the simulation is far from perfect, it successfully captures the key process for QSCS development: the repeated generation of convective cells in roughly the same location. Let us therefore turn our attention to the initiation mechanism.

Based on the findings of GCM05, we would anticipate that lifting along a boundary-

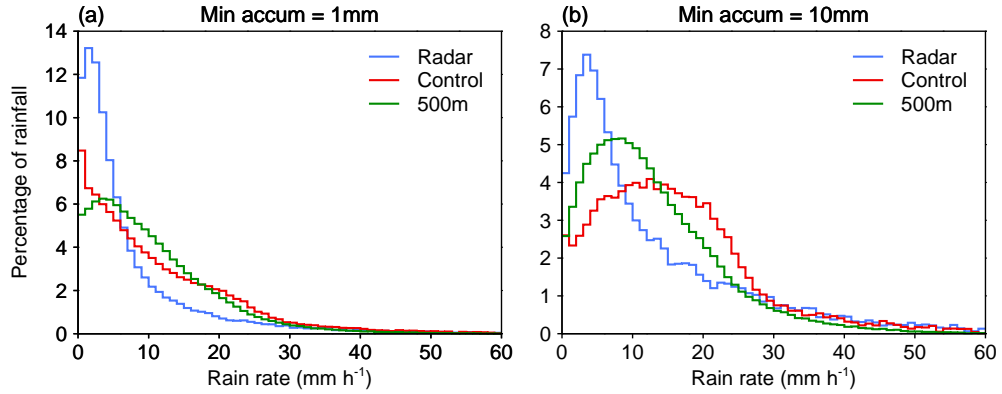


**Figure 4.12** Histograms showing the percentage contribution of rainfall rates (in  $1 \text{ mm h}^{-1}$  bins up to  $60 \text{ mm h}^{-1}$ ) to grid points with rainfall accumulations (a)  $\geq 1 \text{ mm}$  and (b)  $\geq 10 \text{ mm}$ . These were computed over the full simulation domain and period (0400–1900 UTC). Data are shown for the radar (blue), control simulation (red), and 500 m grid-length simulation (green). Before processing, the radar data were bilinearly interpolated to the simulation grid, and the 500 m data were smoothed to the control-simulation resolution using a  $3 \times 3$  boxcar moving average.

layer convergence line was responsible for the repeated initiation of convection in the present case. An examination of the 10 m horizontal divergence field from the control simulation (Figure 4.13) confirms this to be the case. Over the course of the morning, areas of strong convergence (divergence  $< 0.001 \text{ s}^{-1}$ ) develop along portions of the west coast of the peninsula (Figure 4.13a,b). These gradually expand and join up, forming a quasi-continuous line by the early afternoon (Figure 4.13c) which subsequently moves inland (Figure 4.13d). The inland movement of the line after 1400 UTC appears to be due to gradual veering of the background flow associated with the eastward progression of the surface low-pressure system, as seen in observations. Figure 4.13 shows that convective cells repeatedly develop and track along the northwest side of the convergence line and remain bound to it as it moves inland. Vertical cross-sections taken perpendicular to the coastline (Figure 4.14a) reveal that the low-level convergence is associated with an overturning circulation, approximately 1.5 km in depth, superimposed on the background wind field, with vertical velocities up to  $1 \text{ m s}^{-1}$ . At particular times and locations along the line, this lifting was clearly sufficient for parcels to reach their LFC, initiating deep convection. The resulting cells were then advected northeast, parallel to the convergence line, which continued to supply them with moist, potentially buoyant air (Figure 4.15a).

From Figure 4.13 it can be seen that the convergence line is associated with a change in wind direction from southerly/south-southwesterly on the southeast (land) side to southwesterly/west-southwesterly on the northwest (sea) side. One might speculate that this results from frictional backing of the flow over land; however, in some locations the wind just offshore clearly veers towards the land. This veering is particularly pronounced at 1400 UTC (Figure 4.14c) at the southwest end of the coastline where it creates a stream of divergent flow emanating from the northern tip of the Penwith Peninsula (a feature that was also present in the simulations of GCM05; their Figure 12). These

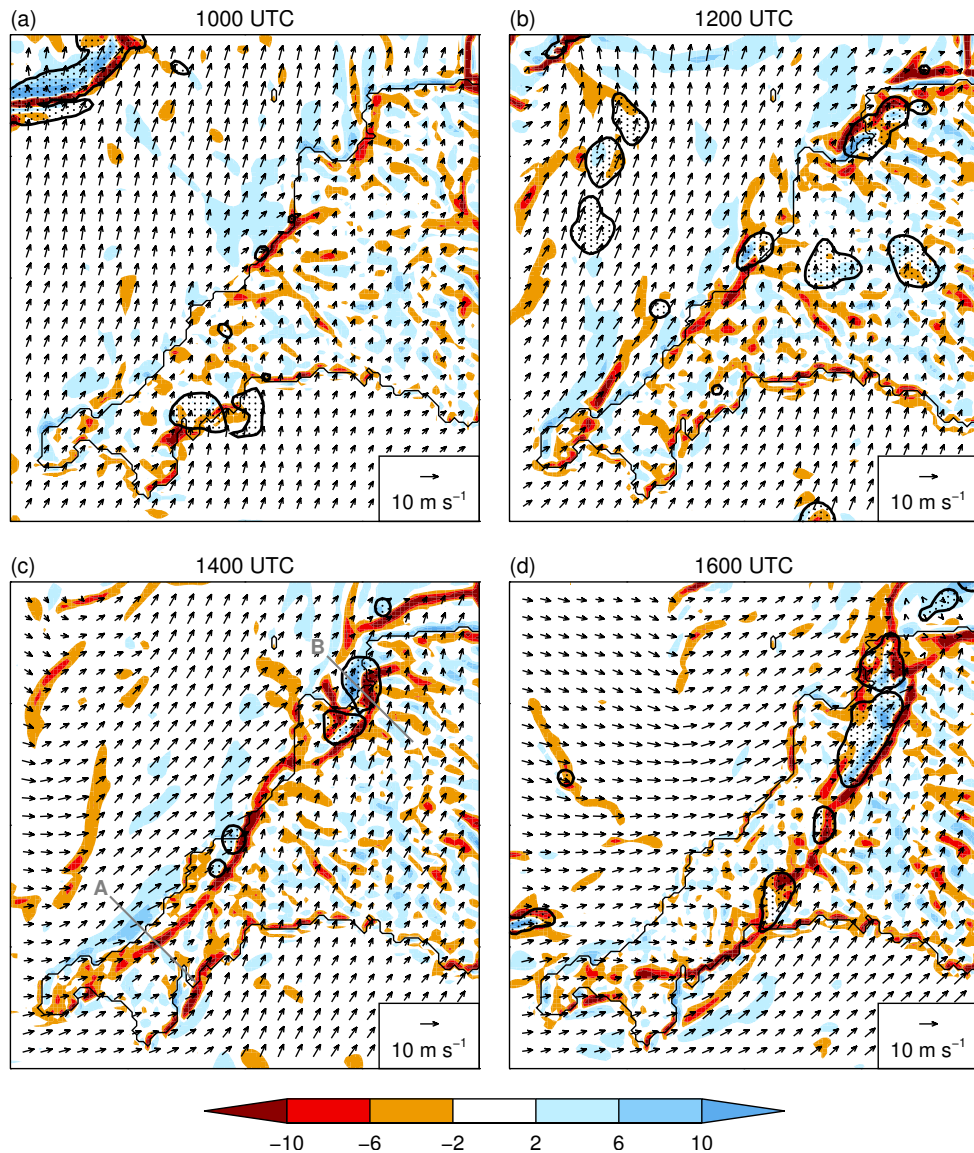


**Figure 4.13** Divergence (colour shading;  $10^{-4} \text{ s}^{-1}$ ) and wind vectors at 10 m, and surface rain rates greater than  $1 \text{ mm h}^{-1}$  (black contours with stippling) in the control simulation at (a) 1000, (b) 1200, (c) 1400, and (d) 1600 UTC. Lines ‘A’ and ‘B’ in (c) indicate the locations of the cross sections in Figures 4.14 and 4.15 respectively.

observations are consistent with the idea of the convergence line as a sea-breeze front: higher temperatures over land result in a pressure gradient acceleration directed from sea to land which drives onshore flow with convergence and ascent at its leading edge (see Chapter 5 for a more thorough discussion of the sea-breeze system). To verify this hypothesis and determine the relative importance of the land–sea temperature contrast and frictional effects (as well as other potential influences), a series of sensitivity tests were performed. These are the subject of the next section.

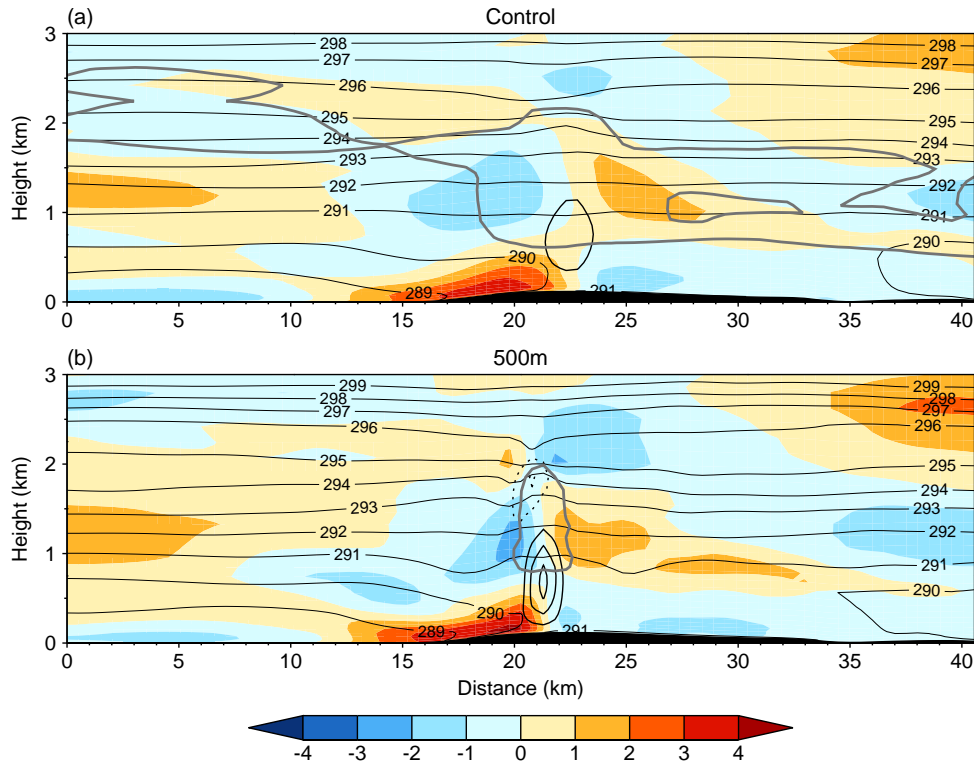


**Figure 4.14** Vertical cross sections taken northwest to southeast along the line ‘A’ shown in Figures 4.13c and 4.21c for (a) the control simulation and (b) the 500 m grid-length simulation at 1400 UTC. Variables plotted are the along-section perturbation wind velocity (colour shading;  $\text{m s}^{-1}$ ), potential temperature (thin black contours; K), vertical velocity (thick black contours, solid and dotted for positive and negative values respectively;  $0.5 \text{ m s}^{-1}$  intervals), and cloud outline (thick grey contours; total cloud water  $q_c = q_l + q_i = 0.01 \text{ g kg}^{-1}$ ). Note that the perturbation wind velocity is computed with respect to the section-mean at each level. The aspect ratio of the sections is 4:1.

#### 4.4.2 Sensitivity tests

To investigate the origins of the simulated convergence line, I have considered four factors which are known to generate and modulate regions of boundary-layer convergence: differential surface heating, differential surface roughness, orography, and convective outflow. For the Boscastle case, GCM05 found that a positive land–sea temperature difference was critical to the formation of the convergence line, suggesting that the latter was a sea-breeze front. Orography, meanwhile, was shown to slightly modulate the precise location of the line and the resulting distribution of precipitation. The authors also suggested the importance of frictional backing of the flow over land in creating an offshore flow component which balanced the sea breeze, maintaining the convergence line in place, and storm-generated outflow in distorting the convergence line at its northeast end. However, these factors were never formally addressed through sensitivity tests. Leoncini *et al.* (2013) also performed simulations of the Boscastle case using a 1 km grid-length version of the UM, including a run without the land–sea roughness contrast. In contrast to GCM05, they concluded that this was only a modulating factor in the formation of the convergence line.

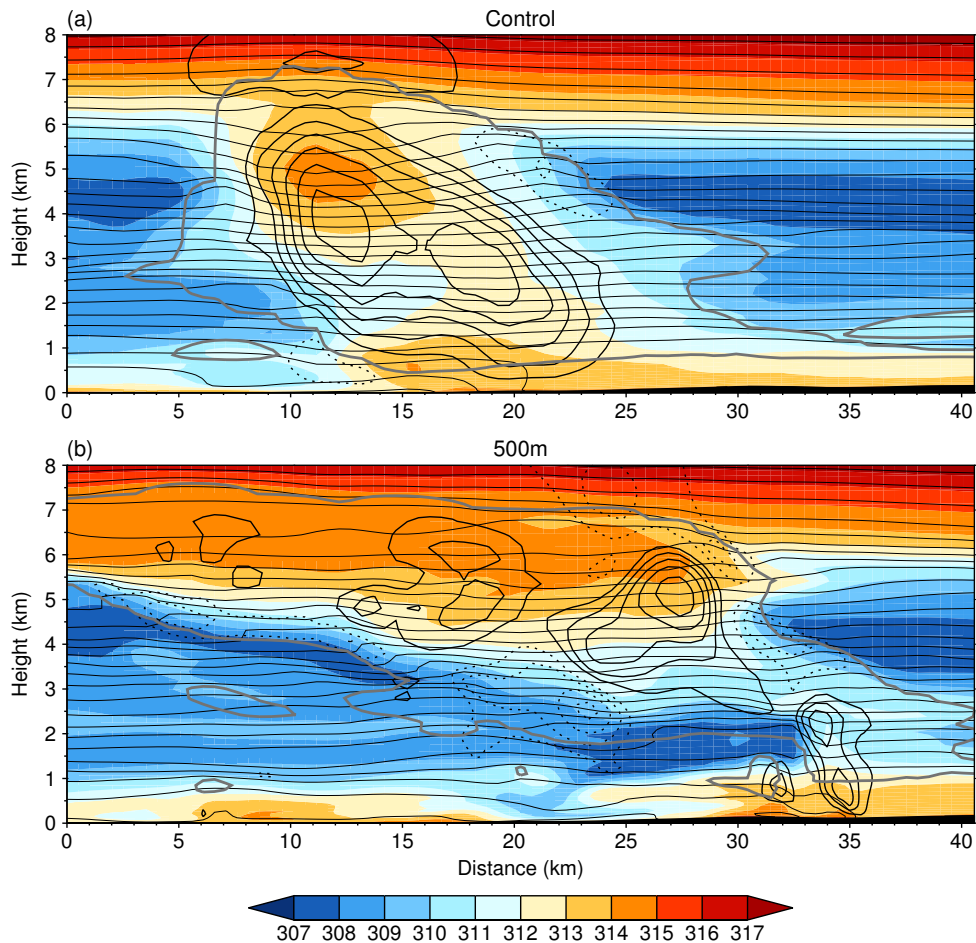


**Figure 4.15** Vertical cross sections taken northwest to southeast along the line ‘B’ shown in Figures 4.13c and 4.21c for (a) the control simulation and (b) the 500 m grid-length simulation at 1400 UTC. Variables plotted are the equivalent potential temperature  $\theta_e$  (colour shading; K), potential temperature (thin black contours; 1 K intervals), vertical velocity (thick black contours, solid and dotted for positive and negative values respectively;  $0.5 \text{ m s}^{-1}$  intervals), and cloud outline (thick grey contours; total cloud water  $q_c = q_l + q_i = 0.01 \text{ g kg}^{-1}$ ). The aspect ratio of the sections is 2:1.

Table 4.1 details how each of the sensitivity tests in the present investigation was carried out. Note that the method employed here to remove the land–sea temperature contrast is different from that in GCM05. Specifically, they fixed the land surface temperature and fluxes to values typical of nearby sea points whereas I have simply decreased the model’s solar constant. This reduces insolation of the land surface which limits the surface sensible heat flux, resulting in lower boundary-layer air temperatures. Sea surface temperatures, on the other hand, are fixed to climatological values, so fluxes and temperatures over sea points are not directly affected. As will be shown, the result is that the low-level land–sea air temperature difference remains negative throughout the simulation. While my approach is less direct than that of GCM05, it had the advantage of being very simple to implement in the model.

Figure 4.16 shows the impact of each sensitivity test on the low-level wind and divergence fields at 1400 UTC (c.f. Figure 4.13c). Surface precipitation is also shown;

**Table 4.1** Details of the sensitivity tests performed.

Name	Factor under investigation	Method
WEAKSUN	Differential surface heating	Solar constant reduced to $400 \text{ W m}^{-2}$
SAMEROUGH	Differential surface roughness	Roughness length for momentum over land and sea fixed to $4 \times 10^{-5} \text{ m}$
NOOROG	Orography	Land height over Southwest Peninsula set to 1 m
NOOUTFLOW	Convective outflow	Latent cooling due to evaporation of rain and melting of snow switched off

however, it is important to note that slight changes in the instantaneous position and size of the convective cells cannot be considered indicative of a systematic response to a particular change in model setup. The WEAKSUN run (Figure 4.16a) immediately stands out due to the complete disappearance of the coastal convergence line. Consistent with this, the region of divergent flow emanating from the Penwith Peninsula is no longer present and the winds along much of the coastline have a reduced westerly component. This confirms the hypothesis that the veering flow offshore is a response to differential heating of the land and sea, and thus part of a sea-breeze circulation.

In contrast, the impact of the other sensitivity tests is relatively minor. As one would expect, reducing the land roughness (Figure 4.16b) results in higher wind speeds and veering (or rather, reduced frictional backing) of the flow over land. These two changes have counteracting effects on the convergence line: faster winds enhance convergence with the onshore flow along the west coast, while clockwise turning of the wind reduces it. The net effect appears to be small. Thus, contrary to the conclusions of GCM05 but in agreement with Leoncini *et al.* (2013), frictional effects over land are not necessary for the development of this type of quasi-stationary convergence line. In agreement with both of these studies, flattening the orography also has a minor influence on the convergence line, although it does of course reduce small-scale variations in the divergence field over land (Figure 4.16c).

In the control simulation, convective outflow is apparent as localised areas of strong divergence coinciding with precipitating cells (Figure 4.13; see also the descending area of low- $\theta_e$  air on the left (northwest) side of the storm in Figure 4.15). These features are clearly absent in the NOOUTFLOW run (Figure 4.16d), but this again has little impact on the convergence line. Animations of the divergence field for the control run reveal that convective outflow may have locally enhanced and distorted the convergence line; however, it was too weak to substantially influence the evolution of the line or the associated convection. As noted in Section 4.2.2, in reality, several cells at the northeast end of the line showed a sudden eastward movement, presumably associated with propagating cold pools. The failure of the control simulation to capture this perhaps relates to the wide spacing between convective cells. This will have allowed

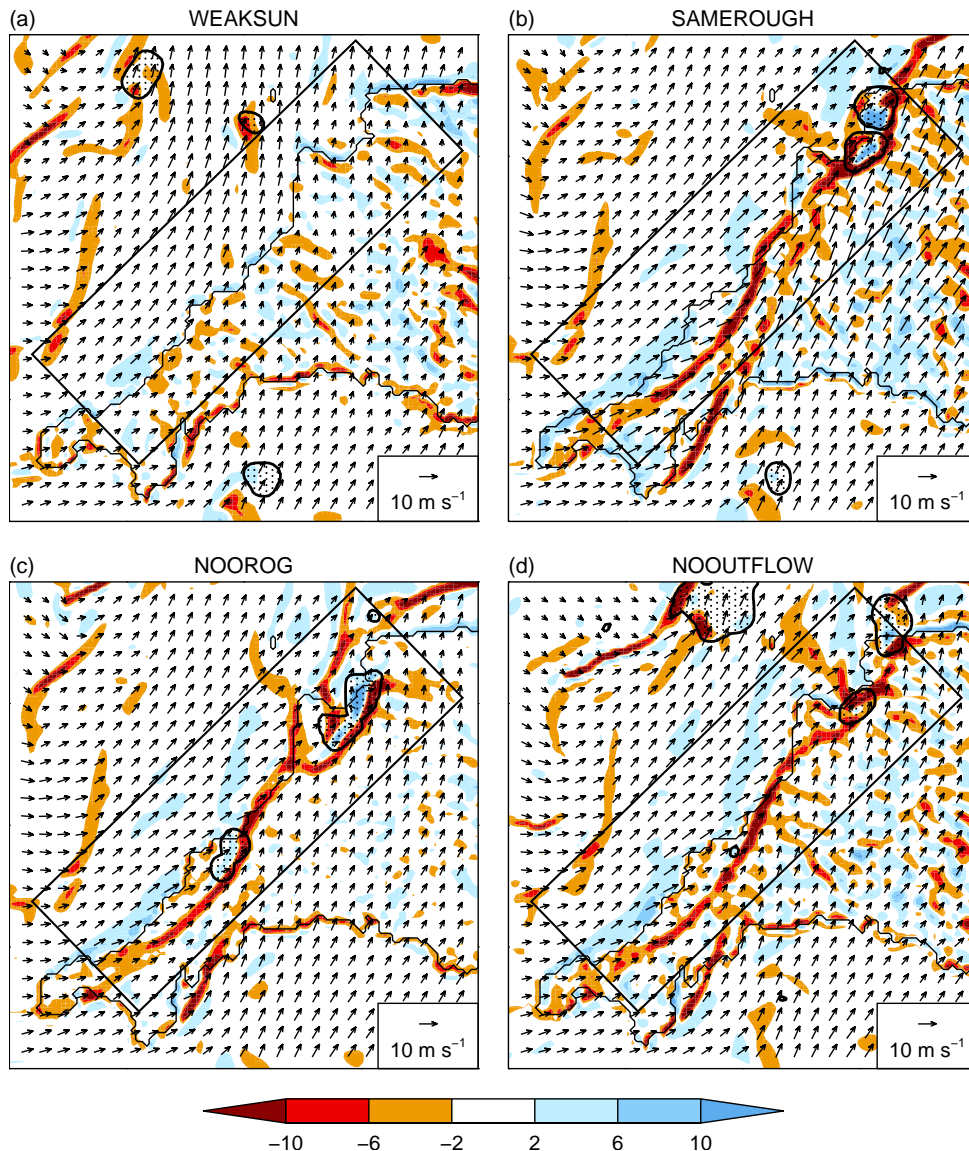


**Figure 4.16** As in Figure 4.13 but for each of the sensitivity runs at 1400 UTC: (a) WEAKSUN, (b) SAMEROUGH, (c) NOOROG, and (d) NOOUTFLOW. Black boxes show the area used to compute the time series in Figures 4.17 and 4.22.

outflow to spread out in both the along-line and cross-line directions, whereas in reality, adjacent cold pools may have merged, restricting motion to only the cross-line direction. Note that in the NOOUTFLOW run, other areas of convection within the simulation domain are quite strongly affected by the absence of latent cooling. In particular, intensification of a system to the northwest of the peninsula alters the low-level flow here giving rise to the convergence lines and precipitation area visible at the northern edge of Figure 4.16d. However, these features do not appear to influence the convection over the peninsula.

Figure 4.17 summarises the evolution of each simulation in terms of a number of key variables: mean land surface heat flux,  $\overline{H}_{\text{land}}$ , difference between the mean land and sea temperatures at 1.5 m,  $\Delta\overline{T} = \overline{T}_{\text{land}} - \overline{T}_{\text{sea}}$ , mean 10 m wind speed and direction over land and sea points, number of grid points with ‘strong’ 10 m wind convergence

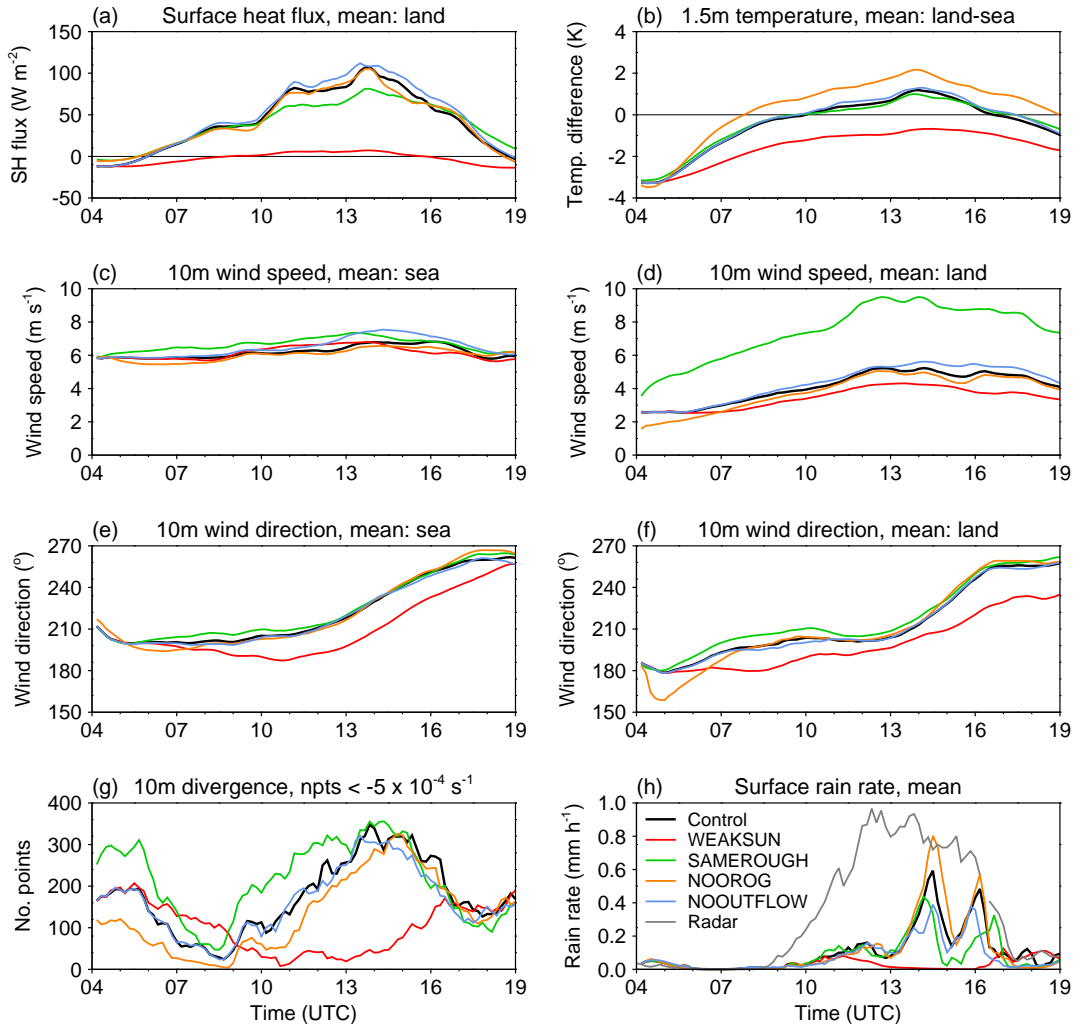


**Figure 4.17** Time series from the control run (black) and each of the sensitivity runs—WEAKSUN (red), SAMEROUGH (green), NOOROG (yellow) and NOOUTFLOW (blue)—computed over the box shown in Figure 4.16: (a) surface heat flux averaged over land points; (b) difference in 1.5 m temperature averaged over land and sea points; (c) 10 m wind speed averaged over sea points; (d) 10 m wind speed averaged over land points; (e) 10 m wind direction averaged over sea points; (f) 10 m wind direction averaged over land points; (g) number of points with 10 m wind divergence less than  $-5 \times 10^{-4} \text{ s}^{-1}$ ; (h) mean surface rain rate. In (h), rain rates from the radar data (interpolated to the model grid) are also shown (grey). All data are plotted with a time resolution of 10 minutes.

(divergence less than  $-5 \times 10^{-4} \text{ s}^{-1}$ ), and mean surface rain rate. To focus attention on the area of interest, each of these has been computed over the box shown in Figure 4.16. As we would expect,  $\overline{H}_{\text{land}}$  and  $\Delta\overline{T}$  (Figure 4.17a, b) follow the diurnal cycle, increasing during the morning and early afternoon, peaking around 1400 UTC, and then decreasing again thereafter. However, in the WEAKSUN run,  $\overline{H}_{\text{land}}$  is dramatically reduced and consequentially  $\Delta\overline{T}$  remains negative throughout the day. Some localised areas of positive land–sea temperature difference do occur (not shown), but on average the low-level air over this part of the peninsula remains cooler than that over the sea. Note that the higher values of  $\Delta\overline{T}$  in the NOOROG run are purely a result of increased near-surface temperatures associated with the lower land elevation.

The low-level wind shows gradual veering during the afternoon (Figure 4.17e,f), partly in response to the evolution of the large-scale flow, but also due to the thermal pressure gradient associated with positive  $\Delta\bar{T}$ . The absence of the latter effect in the WEAKSUN run is evident, with a reduced westerly wind component over both land and sea during most of the day.

Regions of strong convergence exist at the start of the simulations due to land breezes, with cool air descending down the hills of the peninsula and moving out across the sea. These are stronger in the SAMEROUGH run and weaker in the NOOROG run due respectively to faster and slower flow off the land (Figure 4.17d). The land breezes decay during the subsequent hours as insolation warms the land, reversing the thermal pressure gradient; however, this process is retarded in the WEAKSUN run. In the other simulations, regions of strong convergence again start to form after 0830 UTC, associated with the development of the sea-breeze circulation. These are slightly stronger in the SAMEROUGH simulation due to faster winds over land. Convergence peaks between 1330 and 1500 UTC, coincident with the development of heavy precipitation (Figure 4.17h), and decays thereafter as the line moves inland and out of the box. In contrast, in the WEAKSUN run, convergence remains weak, increasing only slightly between 1400 and 1600 UTC with the passage of a transient feature associated with the base of the surface pressure trough (visible to the west of the peninsula in Figure 4.13c). Consequently, no heavy convective precipitation develops in this simulation (Figure 4.17h).

#### 4.4.3 500 m grid-length simulation

In Section 4.4.1, it was noted that the control simulation shows a number of deficiencies in its representation of the 21 July 2010 QSCS. These include late initiation of convection, cells that are too large, intense, and widely spaced, and slow convective evolution. It has also been noted that even with 1.5 km grid spacing, convective storms remain significantly under-resolved. One might therefore anticipate that increasing the resolution would improve the model's representation of this event. To test this hypothesis, a simulation with a horizontal grid length of 500 m was performed using a standard research configuration of the UM. Compared to the 1.5 km control simulation, the only difference in model physics is higher values in the profile of critical relative humidity, which is used by the cloud scheme to diagnose condensation and evaporation (see Section 2.2.2).

The same domain, nested within the full UKV model, was used in this simulation but with triple the horizontal resolution ( $720 \times 720$  grid points). The vertical grid was not altered. Orography and other ancillary data were initially kept at the same resolution and bilinearly interpolated to the 500 m grid. However, this concentrated the curvature of the orography field at the original (UKV model) grid points (Figure 4.18), resulting in spurious regions of low-level convergence and divergence when the simulation was run (not shown). The latter effect can be understood by noting that the horizontal velocity field for a near-surface flow of uniform speed  $U$  moving parallel to

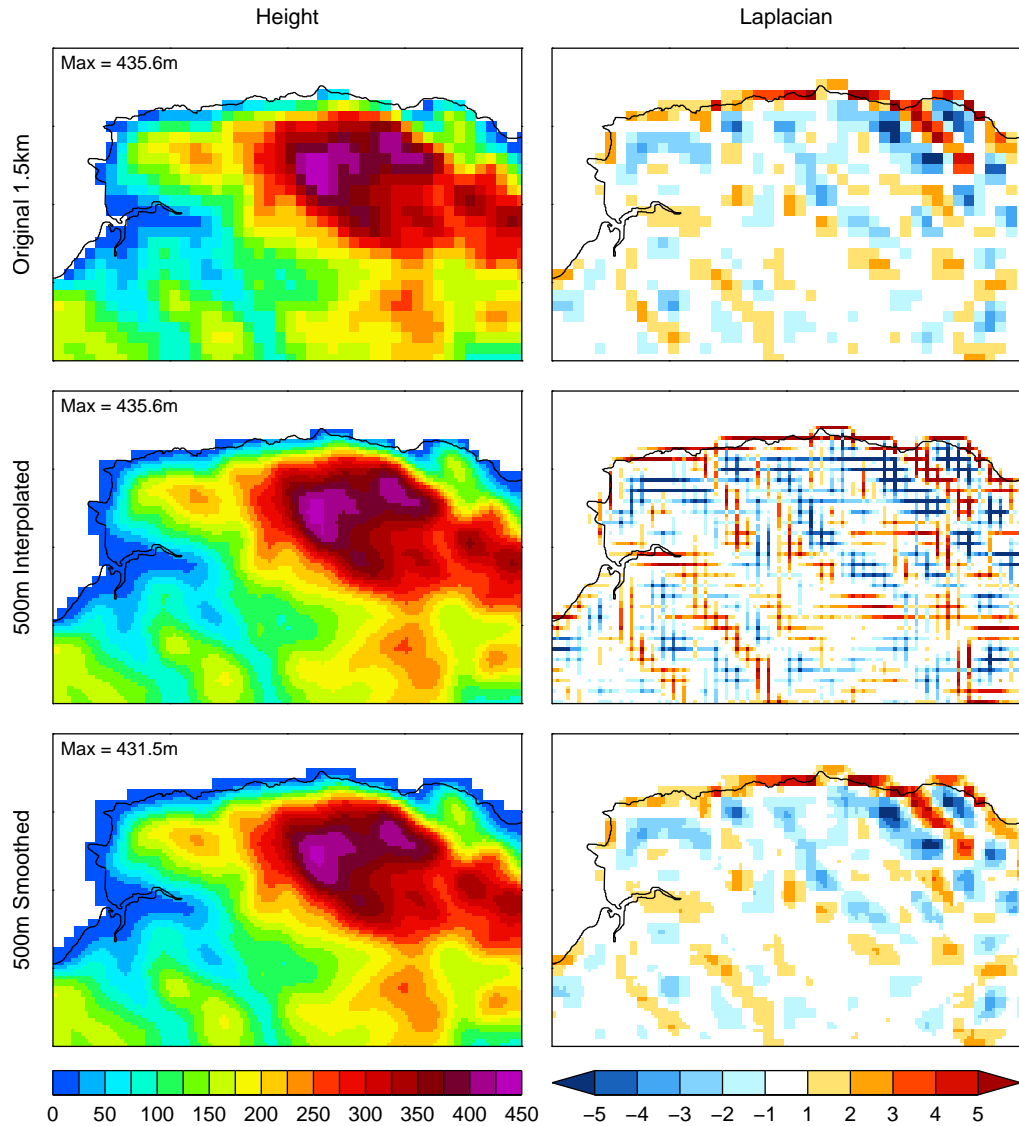


**Figure 4.18** Illustration of the issues with bilinearly interpolating data to a higher resolution. The orography height (m) and its Laplacian ( $10^{-5} \text{ m}^{-1}$ ) over North Devon are shown in the left and right columns respectively. The top row shows these quantities in the UKV model. Bilinear interpolation of the UKV orography data to the 500 m grid results in a smooth height field but concentrates the curvature at the original grid mid-points (middle row). This issue can be alleviated by smoothing, in this case using a  $3 \times 3$  boxcar moving average (bottom row). However, this results in expansion of the land area and a slight reduction in the amplitude of local maxima and minima.

the lower boundary is proportional to the slope of the orography height  $h(x, y)$ :

$$\mathbf{u}_H = U \nabla_H h$$

Here,  $\mathbf{u}_H = (u, v)$  and  $\nabla_H = \left( \frac{\partial}{\partial x}, \frac{\partial}{\partial y} \right)$ . It is then easily seen that the horizontal divergence is proportional to the second derivative (curvature) of the height field:

$$\nabla_H \cdot \mathbf{u}_H = U \nabla_H^2 h$$

To alleviate this problem, the interpolated orography data was smoothed using a  $3 \times 3$

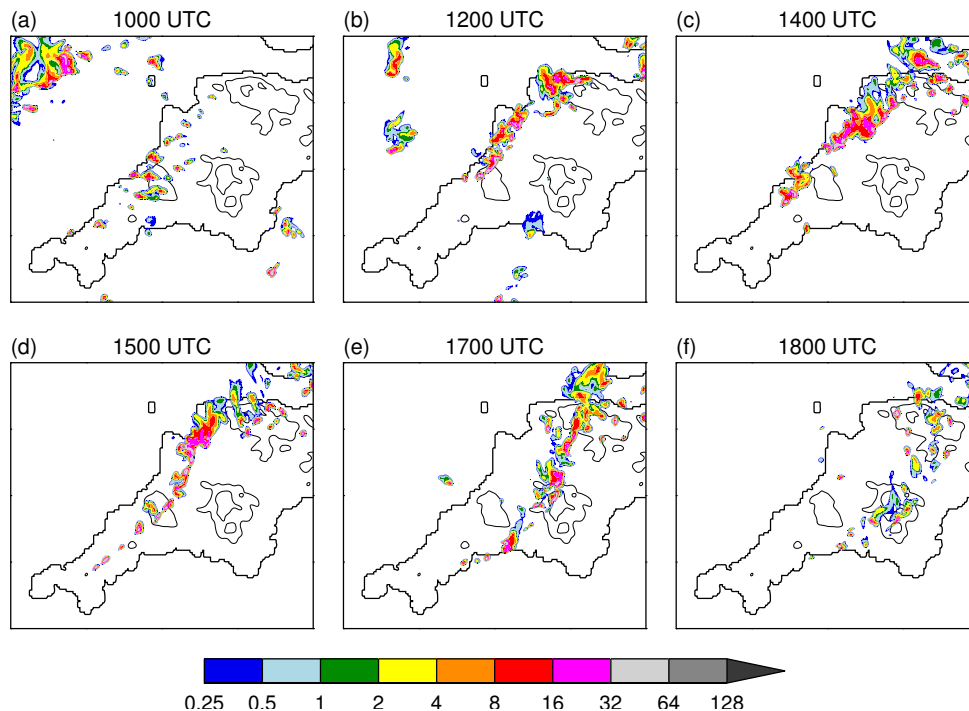


**Figure 4.19** As in Figure 4.9 but for the 500 m grid-length simulation.

boxcar moving average (Figure 4.18). It may be noted that the interpolation and smoothing procedures both lead to a very slight lateral expansion of the land surface and reduction in the maximum orography height; however, these changes does not appear to influence the results.

Figure 4.19 shows the evolution of the surface rain rate field in the 500 m simulation and may be compared directly with Figures 4.4 and 4.9. A comparison between this run, the control simulation, and radar observations is also provided in Figures 4.10–4.12. These plots reveal a significant improvement in the representation of the precipitation system when grid spacing is reduced from 1.5 km to 500 m. Cells are more numerous, more closely packed, and have enhanced fine-scale detail (Figure 4.19), giving a system structure which more closely resembles that seen in observations. They also develop (produce heavy precipitation) more rapidly (Figure 4.11) and show evidence of stronger convective outflow at the northeast end of the line where (as in observations) eastward bowing segments are observed. Indeed, the cross-sections in Figure 4.15 show stronger mid-level downdraughts in the 500 m run with low- $\theta_e$  air descending from around 2 km to the surface and spreading laterally. This surge of cool air appears to drive the sea-breeze convergence line farther inland (to  $x = 35$  km as opposed to  $x = 20$  km in the control run) and create a secondary region of low-level ascent along the gust front (around  $x = 32$  km). Peak rain rates in the 500 m run are still too high (Figures 4.19), but, when aggregated to the 1.5 km grid, the data shows a reduced bias compared to the control run (Figure 4.12). Together, these changes lead to a vastly improved representation of the rainfall accumulation pattern (Figure 4.10), although the maximum is overestimated by around 10 mm (20 %).

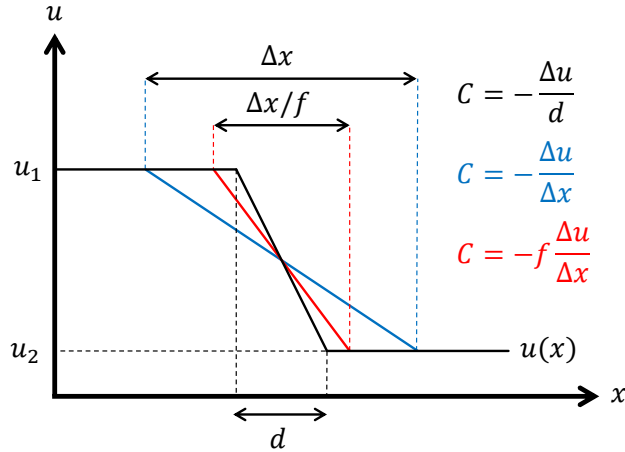


**Figure 4.20** Schematic showing how a reduction in horizontal grid spacing can lead to improved representation of convergence zones. The black line shows a change in wind speed  $\Delta u = u_2 - u_1$  occurring over a distance  $d$ . Blue and red lines show the representation of this feature on model grids with grid length  $\Delta x$  and  $\Delta x/f$  respectively.

Many of these changes in the precipitation field can be linked to an improved representation of the convergence line and its associated lifting. Consider a simple 2-D incompressible flow characterised by low-level convergence where the wind changes linearly from  $u_1$  to  $u_2$  ( $u_1 > u_2$ ) over a distance<sup>2</sup>  $d$  (Figure 4.20). If the convergence occurs uniformly over a depth  $D$  then, ignoring variations in density and assuming no flux through the lower boundary, the vertical velocity at height  $D$  is given by  $w = DC$ , where  $C = -\Delta u/d$  is the horizontal convergence and  $\Delta u = u_2 - u_1$ . Represented by finite differences on a model grid of length  $\Delta x > d$ , the horizontal convergence is equal to  $-\Delta u/\Delta x$ . If we decrease the grid spacing by a factor  $f > 1$  and the new grid spacing  $\Delta x/f \geq d$  then it is easily seen that both the convergence and vertical velocity will be  $f$  times larger (Figure 4.20). Figures 4.21 and 4.14 reveal that the convergence line is indeed narrower and more intense in the 500 m compared to the control simulation, with stronger rising motion along it. This enhanced lifting allows near-surface air parcels to more readily reach their level of free convection, promoting earlier and more frequent initiation of deep convection along the line. Observations of boundary layer convergence zones (e.g. Wilson and Schreiber 1986; Wilson *et al.* 1992) suggest that in reality  $d$  is between 0.5 and 5 km. It is therefore not surprising that the 1.5 km model fails to adequately resolve the convergence line in this case, particularly when we consider the additional smoothing generated by numerical diffusion and the model’s subgrid mixing scheme (which acts to increase the effective  $\Delta x$ ).

Figure 4.22 summarises the differences in evolution between the 500 m and control runs in an almost identical manner to Figure 4.17, the only change being that in this case, mean convergence is shown in place of the number of ‘strong’ convergence points. Figure 4.22a reveals a notable change in  $\overline{H}_{\text{land}}$ , with values between 0800 and 1300 UTC being 30–40  $\text{W m}^{-2}$  higher in the 500 m run. This results in slightly higher temperatures

<sup>2</sup>This distance may be thought of as the width of the convergence zone. It is controlled by dynamic pressure forces which act to decelerate the opposing flows (e.g. Markowski and Richardson 2010).

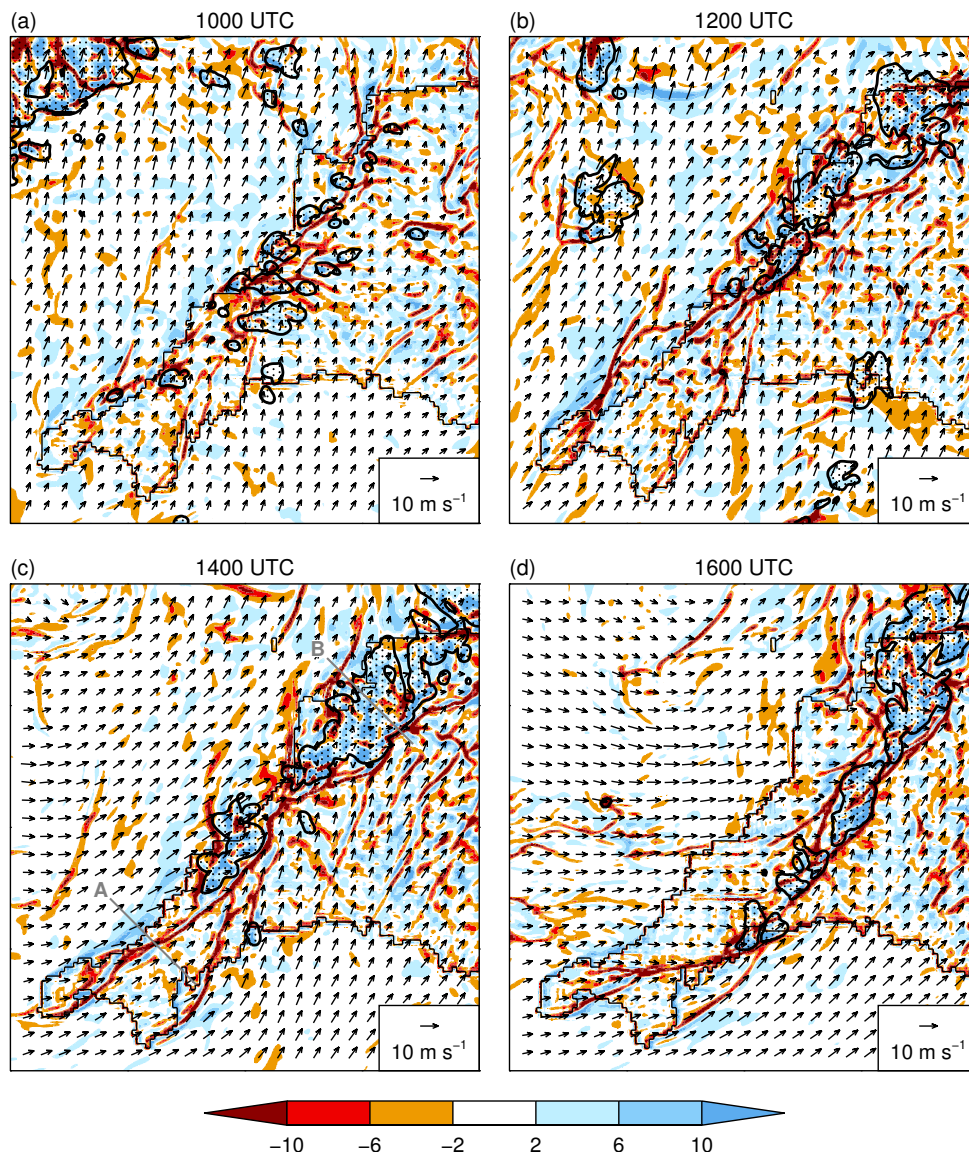


**Figure 4.21** As in Figure 4.13 but for the 500 m grid-length simulation.

over land and thus an increased  $\Delta\bar{T}$  during this period (4.22b). The enhanced heat flux is a consequence of reduced cloud cover in the 500 m simulation (presumably associated with the higher values of critical relative humidity) which acts to increase the downwelling shortwave radiation and surface temperatures (not shown). This in turn drives a slightly stronger onshore (i.e. more westerly) flow during the middle of the day (Figure 4.22e). Comparison of the modelled cloud field with satellite imagery (not shown) demonstrates that cloud cover is too extensive in the control run. In the late afternoon,  $\Delta\bar{T}$  is smaller in the 500 m run than in the control run due to lower temperatures over land associated with more expansive convective cold pools (c.f. Figures 4.9 and 4.21). These are also responsible for the weaker and more westerly winds seen over land throughout the afternoon (Figure 4.22d,f). The most dramatic changes, however, are seen in the convergence and precipitation fields. Throughout the simulation, but especially from 0900–1600 UTC convergence is enhanced in the 500 m run (Figure 4.22g).

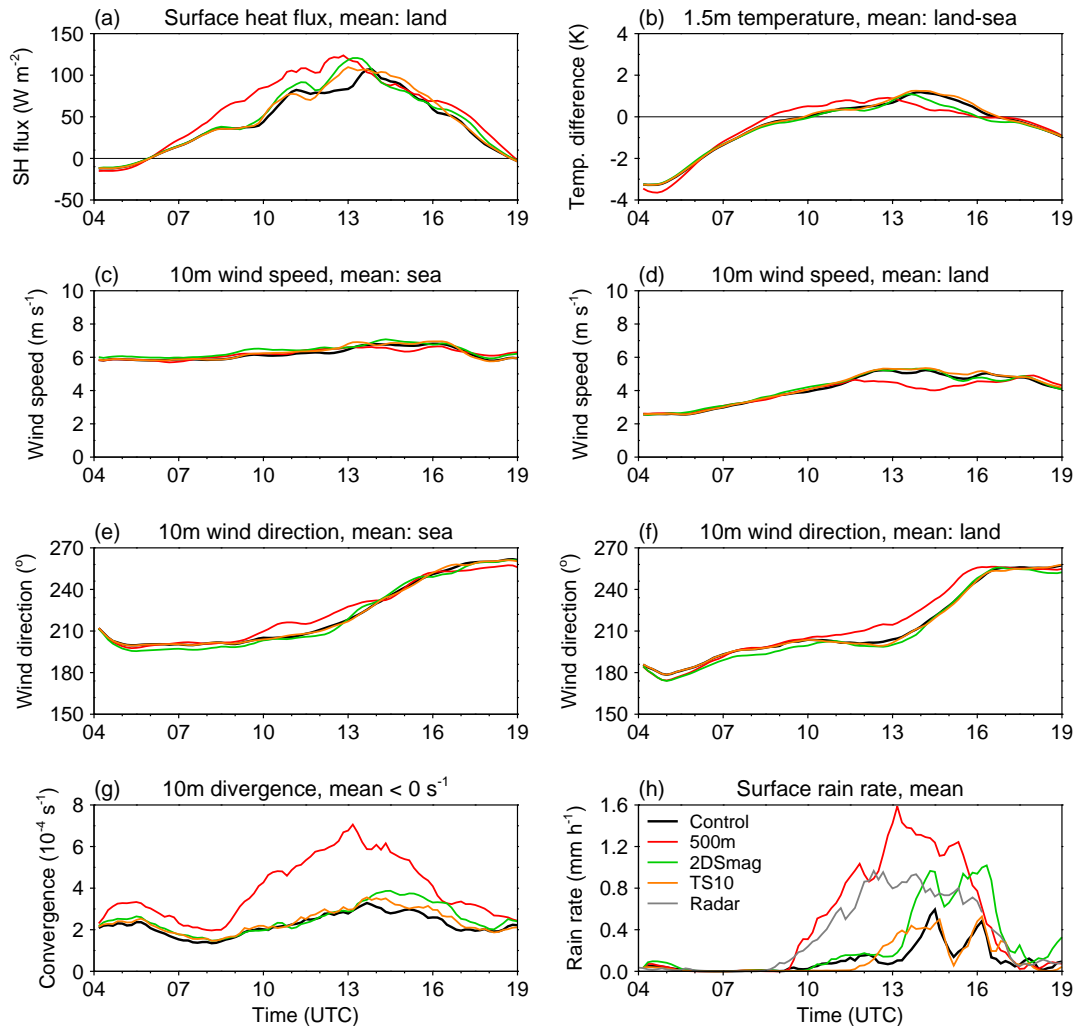


**Figure 4.22** As in Figure 4.17 but comparing the control simulation (black) with the 500 m (red), 2DSmag (green), and TS10 (yellow) runs. Here, (g) shows the mean 10 m wind convergence (i.e. the mean over all points with negative divergence).

The rapid increase in values around 0900 UTC (associated with the development of the sea breeze) is shortly followed by the onset of heavy precipitation (Figure 4.22h). As previously noted, when compared to the radar observations, the 500 m run shows vast improvements in the timing and rate of convective development, although it overdoes the area-averaged rainfall intensity.

#### 4.4.4 Other runs

To further explore the sensitivity of this case to model configuration, two additional experiments were performed. In the first, the standard boundary-layer scheme was used in place of the Smagorinsky scheme for vertical mixing (Section 2.2.2). As discussed in Section 4.3.2, the former is the default option in the UKV configuration, but the latter was used here to provide a cleaner comparison with the 500 m run for which the Smagorinsky scheme is standard. All other settings were kept the same as in the control simulation. The evolution of this run (labelled 2DSmag, since Smagorinsky mixing only

operates in the horizontal) is shown in Figure 4.22. The most pronounced difference from the control run is in the rainfall intensity during the afternoon which at times is around a factor of two greater. This is in part due to a better representation of the system structure, particularly during the late afternoon, with more numerous and closely packed cells along the convergence line (not shown). The maximum rainfall accumulation is also notably increased (to 74.0 mm for 0900–1800 UTC) but is still displaced around 100 km to the northeast of the observed maximum (not shown). Thus, use of the boundary-layer scheme for vertical mixing improves the representation of this QSCS, but far less dramatically than trebling the horizontal resolution.

The second additional run was performed following a suggestion by Dr Todd Lane of Melbourne University during the presentation of this work at a conference. Recall from Chapter 2 that the UM uses a semi-Lagrangian advection scheme with semi-implicit time differencing. This allows it to run with considerably longer time steps than those permitted by Eulerian and explicit schemes at the same resolution. However, this means that fast processes, some of which may be important in deep convection, are damped. Dr Lane hypothesised that part of the improvement seen in the present case when going from 1.5 km to 500 m grid spacing might be a consequence of the reduced time step rather than the higher horizontal resolution. To test this, a run was performed with 1.5 km grid length but a 10 s time step as in the 500 m run. In order to isolate the role of the time step, an additional change was required in the Smagorinsky mixing scheme. This is because there is a numerical stability-based constraint on the diffusion coefficient  $K$  which is a function of the time step:

$$\frac{K\Delta t}{r^2\Delta\phi^2} \leq \frac{1}{8}$$

where  $\Delta t$  is the time step,  $\Delta\phi$  is the angular horizontal grid spacing, and  $r$  is the radius of the Earth. In the model, the maximum value of the diffusion coefficient  $K_{\max}$  is defined as:

$$K_{\max} = F \frac{r^2\Delta\phi^2}{8\Delta t}$$

where  $F$  is a parameter between 0 and 1. In the UKV model,  $F = 0.25$ . To preserve  $K_{\max}$  with  $\Delta t$  reduced by a factor of five,  $F$  must be also be reduced by a factor of five; thus,  $F = 0.05$  was used. As can be seen from Figure 4.22, this run (labeled TS10) shows very little difference from the control simulation except for a slightly more delayed and rapid development of convection along the convergence line. Further analysis (not shown) reveals that the representation of the precipitation pattern is slightly degraded; however, overall there appears to be little sensitivity to the change in time step. This supports my previous conclusion that a reduction in horizontal grid length vastly improves the simulation of this case.

## 4.5 Summary, discussion, and conclusions

This chapter has presented an analysis of a QSCS which occurred over the UK Southwest Peninsula on 21 July 2010 and showed remarkable similarity to the flash flood-producing Boscastle storm of 16 August 2004. In both events, convective cells repeatedly developed and moved along and just inland of the peninsula's west coast, producing intense precipitation over a narrow swath of land. However, maximum rainfall accumulations were approximately four times smaller in the 2010 case and no flooding was recorded. This difference was related to three factors: the intensity of the rainfall, the duration of the convective systems, and the distribution of the rainfall across drainage basins. In the Boscastle case average rain rates were around three times higher than those in the 2010 case. A comparison of soundings for the two cases suggests a more favourable environment for intense precipitation on 16 August 2004, with greater precipitable water, higher mid-level relative humidity, a deeper layer of instability, and higher CAPE. The Boscastle storm also remained quasi-stationary for around 90 minutes longer than the 2010 storm due to slower evolution of the wind field; in the latter case, veering low-level flow caused the convective system to move inland several hours before it dissipated. Finally, slight differences in the location of the two storms meant that in the Boscastle case the heaviest rainfall was distributed over fewer river catchments, further enhancing the hydrological response. At the synoptic scale, both events were characterised by a slow-moving, weakly baroclinic cyclone; however, in the 2010 case this feature was over the UK while in the Boscastle case it was centred around 1000 km farther west. Despite this difference, both situations gave rise to deep southwesterly flow over the Southwest Peninsula which appears to be highly favourable for the development of the QSCSs in this region. Clearly the persistence of this flow configuration plays a critical role in determining the stationarity of such systems when they do develop and thus the associated flood risk.

Numerical simulations of the 21 July 2010 event were performed using a 1.5 km grid-length configuration of the Met Office Unified Model. A control simulation successfully captured the repeated development of convective cells along the coastline, but failed to accurately represent the narrow, linear structure of the storm system. The model also showed a substantial positive bias in instantaneous rain rates and underestimated maximum accumulations by around a factor of two. Despite these issues, the simulation was able to reveal that, as in the Boscastle case, convective initiation was maintained by lifting along a quasi-stationary boundary-layer convergence line. Sensitivity tests were performed to determine the mechanisms controlling this feature. In agreement with the findings of GCM05 for the Boscastle case, the convergence line was shown to be the result of a balance between the background flow and a sea-breeze along the west coast. However, in contrast to a hypothesis put forward by GCM05, frictional turning of the wind over land was not found to be necessary for this process to occur. Furthermore, the effects of convective outflow and the orography of the Southwest Peninsula were not significant in the 2010 case.

To investigate the impact of enhanced horizontal resolution on the modelled QSCS, a simulation with 500 m grid spacing was performed. This showed marked improvements in the timing of convective initiation, the structure of the convective system, and the rainfall intensity. Critical to the improvements in storm initiation and structure was an increase in the strength of the convergence line, which allowed low-level air parcels to more readily reach their LFC. This change can be attributed directly to an improved representation of sharp horizontal wind gradients which, due to their small scale, are likely under-resolved with 1.5 km grid spacing. Slight improvements in the simulated convective system were also observed when the UM boundary-layer scheme was used to represent subgrid-scale vertical mixing rather than a Smagorinsky-type scheme; however, no significant changes were observed when a reduced time step was used in the 1.5 km configuration. The latter result confirms that it is the change in resolution rather than time step which results in the improved accuracy of the 500 m run.

This final finding is important as it suggests that in situations where boundary-layer convergence is the dominant mechanism of convective initiation, the highest resolutions currently used operationally may still be insufficient for quantitative precipitation forecasting. Barthlott *et al.* (2010) reached a similar conclusion based on simulations of a convergence line–forced thunderstorm observed during the Convective and Orographically induced Precipitation Study (COPS; Wulfmeyer *et al.* 2008). They used the German Weather Service’s COSMO–DE model with horizontal grid lengths of 2.8 and 1 km. Both runs failed to predict the storm because simulated updraughts along the convergence line were too weak for parcels to overcome CIN. Significant improvements in forecasting convection and its associated hazards are anticipated in the next decade, with the introduction of convective-scale ensemble prediction systems (e.g. Clark *et al.* 2012) and continuing advances in the assimilation of high-resolution remotely sensed observations (e.g. Renshaw and Francis 2011). However, in certain meteorological situations, improved prediction might only be achieved with the use of even higher resolutions ( $\Delta x < 1$  km). Of course, the computational requirements for such configurations are vast, and in the near future, resources may be better spent on other modelling developments, such as those mentioned above.

Returning to the issue of QSCSs, this study and GCM05 highlight the potential significance of quasi-stationary sea-breeze fronts as a mechanism by which convection may be repeatedly initiated in one area. The basic ingredients for such a feature—a positive land–sea temperature difference and an offshore-directed ambient wind component—are no doubt quite common; however, the balance between the two is delicate, as evidenced in the present case by the sudden inland movement of the convergence line following a subtle shift in the background flow. Based on a synthesis of many previous numerical investigations of sea breezes, Crosman and Horel (2010) suggested that an offshore geostrophic wind greater than  $4\text{--}8\text{ m s}^{-1}$  but less than  $6\text{--}10\text{ m s}^{-1}$  could cause a sea-breeze front to stall at the coastline. However, in the present case, the offshore wind component was only around  $1\text{--}2\text{ m s}^{-1}$ . This discrepancy may be related to the relatively small land–sea temperature difference ( $1\text{--}2^\circ\text{C}$ ), but also to the existence of a strong along-

shore wind component. Historically, the along-shore component of the ambient wind has been considered of secondary importance to the cross-shore component which strongly modulates the ability of the sea breeze to move inland or even form (Crosman and Horel 2010). However, this may in part be because the majority of numerical investigations of these interactions have considered infinite coastlines, either through the use of two-dimensional models or three-dimensional models with periodic boundary conditions in the along-shore direction. It is hypothesised here that in the case of a peninsula with strong along-shore flow, the sea-breeze circulation will be weaker (at least near the upstream end of the coastline) because the offshore air is being continually replenished and therefore is always only beginning to adjust to the thermally driven pressure gradient. Thus, for a given land–sea temperature contrast, a weaker offshore-directed background wind component may be required to balance the sea breeze and create a quasi-stationary convergence line. This hypothesis is explored in detail in the next chapter.

## Chapter 5

# Idealised simulations of peninsula sea breezes

### 5.1 Introduction

#### 5.1.1 Background and motivation

So far, I have examined the general characteristics of QSCSs in the UK (Chapter 3) and looked in detail at a particular case (4). In this chapter, I will investigate a specific mechanism by which these systems may form; namely, lifting along a quasi-stationary sea-breeze front.

The sea breeze has been the subject of countless studies and its role in convective initiation has long been recognised (Byers and Rodebush 1948). However, to my knowledge, only in the Boscastle case study of Golding *et al.* (2005) has it been implicated in the formation of a flash flood-producing storm. Those authors argued that a balance between the ambient wind and the sea breeze at low levels resulted in a quasi-stationary convergence line (the sea-breeze front) that provided lift for the repeated triggering of convection. In the last chapter, a very similar QSCS, which occurred on 21 July 2010, was analysed and found to also be the result of this mechanism.

The stalling of a sea-breeze front in the presence of opposing synoptic-scale flow has been noted before in a number of observational and numerical studies (e.g. Bechtold *et al.* 1991, Grisogono *et al.* 1998). In general, it has been found that a seaward cross-shore wind of between 4 and 10 m s<sup>-1</sup> is necessary for this to occur (Crosman and Horel 2010). However, in the Boscastle and 21 July 2010 cases, the flow was almost parallel to the coastline with only a slight cross-shore component of around 1–2 m s<sup>-1</sup>. It is hypothesised that this discrepancy reflects the fact that for flow along a peninsula the land–sea temperature contrast is a function of distance from the upstream coastline. Near the tip of the peninsula, where this contrast is small, the sea breeze may be too weak to propagate inland and/or balanced by a slight offshore ambient wind. The purpose of this chapter is to test this hypothesis and gain a more general understanding of the evolution and characteristics of the sea-breeze system over a peninsula.

Observations and simulations of real cases are not ideal for this type of investigation due to the inherent complexity of the real atmosphere and the forcing which drives its circulations. Thus, idealised numerical simulations are employed, in which the dimensionality of a problem is reduced by holding some parameters fixed and simplifying the variation of others. In this way, the role of specific processes and parameters can be more easily isolated. Of particular interest to the present investigation is the sensitivity of the sea breeze to two variables: the land–sea temperature difference and the background wind velocity. This has been the subject of many previous numerical studies (see Crosman and Horel 2010 for a review); however, virtually all of these have considered a coastline which is effectively infinite, either through the use of a 2-D model or a 3-D model with periodic boundary conditions in the along-shore direction. The novelty of the present work thus derives from the use of a finite-length coastline (peninsula).

### 5.1.2 Chapter aims and structure

In this chapter, I will use idealised numerical simulations of sea breezes over a simple peninsula to address the following questions:

1. How do sea breezes evolve over a peninsula under different wind directions?
2. How does the behaviour change with wind speed and land–sea temperature contrast?
3. How sensitive is the evolution to other factors such as stability, surface roughness, and latitude?
4. Under what conditions do quasi-stationary sea-breeze fronts form?
5. Can we predict the evolution of the sea breeze using scaling laws?

The rest of the chapter is organised as follows. Section 5.2 provides a brief introduction to the sea-breeze system, with particular focus on how external factors modify the inland movement of the sea breeze. Section 5.3 then describes the design of the numerical simulations. Results are presented in Section 5.4. First, the evolution of the sea breeze in the absence of ambient flow is considered, including its sensitivity to the land surface heat flux (which determines the land–sea temperature difference) and other relevant parameters. Substantial attention is then given to the rarely studied case of along-shore flow. Next, a method for predicting the inland movement of the sea breeze is developed and tested. The remaining results are concerned with (1) the more well-studied situation of purely cross-shore flow, (2) intermediate flow directions, and (3) the effect of using slightly more realistic coastlines. Conclusions are drawn in Section 5.5.

## 5.2 The sea-breeze system

The sea breeze forms in coastal regions around the world in response to differential heating of adjacent land and sea surfaces. Its ubiquity and well-defined characteristics have made it one of the most well studied phenomena in mesoscale meteorology. Academic writings on the sea breeze date back to Ancient Greece (Simpson 1994), and it remains a topic of active research today; a quick search on Google Scholar reveals almost 600 articles with ‘sea breeze’ in the title published since the year 2000. This section provides a brief overview of the structure and life cycle of the sea breeze, as well as its interactions with the background meteorological environment. For further details, the reader is directed to the reviews by Abbs and Physick (1992), Simpson (1994), Miller *et al.* (2003), and Crosman and Horel (2010).

### 5.2.1 Structure and life cycle

Following Miller *et al.* (2003), let us define the sea-breeze system (SBS) as the collective of components shown in Figure 5.1. The primary feature is a mesoscale cell (the sea-breeze circulation; SBC), with onshore flow near the surface, a compensating return current (RC) aloft, and rising and sinking motion over the land and sea respectively. The archetypal sea breeze forms on a clear summer’s day in the absence of background flow. However, provided that the air over land is warmer than that over the sea and the cross-shore component of the ambient wind is not ‘too strong’ (see Section 5.2.2), a sea breeze can occur.

Over the course of the day, inland temperatures increase in response to surface insolation, causing the air to expand. Meanwhile, due to the high heat capacity of water, temperatures over the sea remain approximately constant. This sets up a horizontal pressure gradient between the land and sea via the process of hydrostatic adjustment, in which sound waves play an important role (Tijm and van Delden 1999). In response to the thermal pressure gradient force (PGF), marine air then begins to move inland as a gravity/density current (the sea-breeze gravity current; SBG).

The leading edge of the marine air is referred to as the sea-breeze front (SBF) and is characterised by convergence and ascent. This gives the SBG a raised head (the sea-breeze head; SBH) which can be twice the depth of the main current (typically a few hundred metres to a kilometre). Behind this, Kelvin–Helmholtz billows (KHBs) may develop along the upper boundary of the SBG, resulting in mixing between the marine and continental air. This generates a drag force on the SBG which may slow its inland progression during the early afternoon (e.g. Sha *et al.* 1991). The lower portion of the SBG is also slowed by surface friction giving rise to an overhanging ‘nose’ at the SBF.

As the marine air moves inland, it is heated from below, resulting in the formation of a convective internal boundary layer (CIBL) which grows in depth with inland distance. A temperature gradient thus develops within the SBG causing the entire current to accelerate. Robinson *et al.* (2013) point out that this behavior is quite different from that of classical gravity currents (those resulting from the instantaneous introduction of

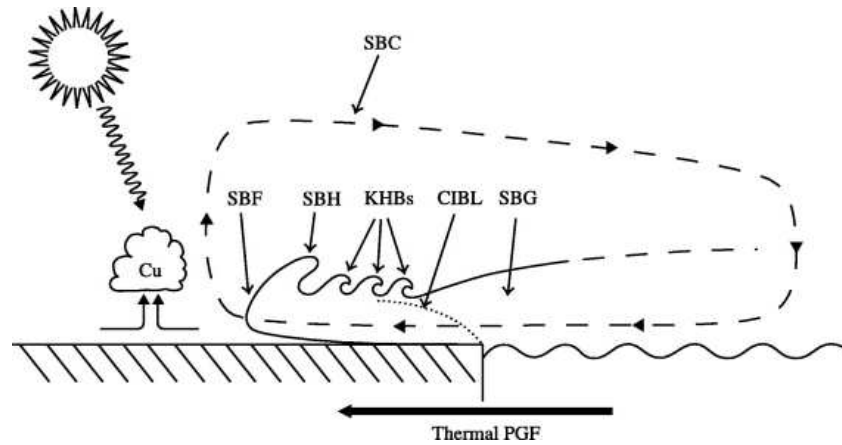


**Figure 5.1** Schematic showing the components of the sea-breeze system (SBS). See text for details. From Miller *et al.* (2003).

a density discontinuity), where accelerations are concentrated at the current head. The propagation of the SBG is also influenced by the Coriolis force which causes the wind to rotate clockwise with time in the Northern Hemisphere and anticlockwise with time in the Southern Hemisphere.

As surface insolation diminishes, the KHBs decay, surface drag is reduced, and the temperature gradient across the SBF increases due to reduced heating of the marine air. In response to these changes, the sea breeze may undergo a notable acceleration during the late afternoon and early evening (Simpson *et al.* 1977; Tijnj *et al.* 1999). Momentum and the temperature gradients within the SBG can continue to drive the SBF inland for several hours after sunset. Interactions between the sea breeze and a nocturnal temperature inversion may subsequently cause the SBH to separate from the feeder flow behind it and move inland as a cut-off vortex or undular bore (Sha *et al.* 1993; Simpson 1994).

### 5.2.2 External controls on sea-breeze evolution

The precise evolution of the SBS varies depending on the meteorological environment in which it develops and the characteristics of the land surface. Most relevant to the present investigation are those factors which influence  $U_{sb}$ , the rate at which the sea breeze propagates inland. Two are considered of primary importance: the magnitude of the land-sea temperature difference  $\Delta T$  and the strength and direction of the shore-perpendicular ambient wind  $U_{\perp}$ . The former depends on the land surface sensible heat flux  $H$ , the period of heating (day length), and the boundary-layer depth. It is fairly obvious that a larger  $\Delta T$  will drive a stronger sea breeze. However, the relationship is nonlinear, with scaling analyses suggesting that  $U_{sb}$  increases with the square- or cube-root of  $H$  (e.g. Segal *et al.* 1997; Steyn 2003; Antonelli and Rotunno 2007). This reflects the fact that an increase in surface heat flux also increases the boundary-layer depth and acts to weaken the thermal gradient via turbulent frontolysis (Abbs and Physick 1992).

The effects of the background wind on sea breeze propagation are somewhat more complicated. A weak to moderate offshore wind acts to enhance the low-level temperature gradient through convergent frontogenesis. This drives a stronger SBG which further increases the temperature gradient creating a positive feedback. The inland penetration of the SBF is also reduced and vertical velocities at the front are enhanced, making this a favourable situation for convective initiation. However, if the background wind is too strong, the SBF is prevented from ever reaching the coastline causing the entire circulation to remain over the sea (Arritt 1993). The maximum sea breeze intensity (largest vertical velocities) occurs when the flow in the SBG exactly cancels the background wind so that the sea breeze remains stationary along the coastline (Bechtold *et al.* 1991). Based on many previous studies, Crosman and Horel (2010) suggested that this ‘critical’ wind speed lies in the range 4–10 m s<sup>-1</sup>. The opposite effects are observed during onshore ambient flow. Divergent frontolysis acts to reduce the horizontal temperature gradient creating a weaker sea breeze whose passage may be hard to identify in observations. Wind speeds of just a few metres per second are sufficient to prevent the formation of a well defined SBF (Arritt 1993).

As previously noted, the shore-parallel component of the background wind  $U_{\parallel}$  is thought to have little influence on  $U_{sb}$  (Crosman and Horel 2010). This is certainly true for long stretches of coastlines where  $\Delta T$  is approximately constant in the along-shore direction. However, as we shall see, the magnitude of  $U_{\parallel}$  is critical to sea breeze behavior near the upstream edge of a peninsula where strong gradients in  $\Delta T$  exist.

Other factors which have been found to influence the inland propagation of the SBF include atmospheric stability, latitude, coastline curvature, inland orography, and interactions with external meteorological phenomena such as convective outflow boundaries. Strong near-surface stratification acts to damp the SBC by suppressing ascent at the SBF (e.g. Estoque 1962; Arritt 1993), but also decreases the depth of the mixed layer over land resulting in a larger  $\Delta T$ . Scaling analyses mostly suggest a weak inverse dependence of  $U_{sb}$  on the Brunt Väisälä frequency  $N$  (Steyn 1998; Tijn 1999; Porson *et al.* 2007b). As one moves poleward, the Coriolis force increases resulting in greater turning of the onshore flow with time; thus,  $U_{sb}$  is typically found to have an inverse dependence on latitude (Tijn 1999; Steyn 2003). Convex coastlines enhance the sea breeze through convergence of the onshore flow, while concave coastlines have the opposite effect (McPherson 1970). Furthermore, the presence of small-scale bays and peninsulas can lead to along-shore variations in  $U_{sb}$ . In regions of coastal orography, thermally driven upslope flows may act in concert with the sea breeze causing it to propagate more rapidly; however, very steep slopes will act to block its inland penetration (e.g. Barthlott and Kirshbaum 2013). Finally, the SBF may undergo acceleration or deceleration due to interactions with other sea breezes (or lake/river/inland breezes), convective outflow boundaries, horizontal convective rolls, boundary layer thermals, synoptic-scale fronts, and urban heat islands (Zhong *et al.* 1991; Yoshikado 1992; Atkins *et al.* 1995; Brümmer *et al.* 1995; Kingsmill 1995; Ogawa *et al.* 2003; Fovell 2005).

### 5.3 Numerical model and experiment design

To investigate the formation of quasi-stationary SBFs over a peninsula, a large number of simulations were performed using the idealised configuration of the UM at Version 7.3. This uses the same dynamical core and parameterisation schemes as the standard UM, but allows for the specification of simplified initial and boundary conditions as well as prescribed forcing for certain variables within the simulation domain. It has been used to investigate a variety of atmospheric processes and phenomena including banded frontal clouds (Gray and Dacre 2008), moisture transport in midlatitude cyclones (Boutle *et al.* 2011), valley wind systems (Schmidli *et al.* 2011), and sting jets (Baker *et al.* 2014). Full details of the idealised UM are given in UM Documentation Paper 33 (Davies *et al.* 2007).

The simulation domain used herein is shown in Figure 5.2. It consists of  $600 \times 300$  grid points with a flat  $400 \times 100$  grid-point strip of land in the centre of the domain, 100 grid points from each lateral boundary. The angular grid length  $\Delta\phi = 0.009^\circ$ , which corresponds to  $\Delta x = 1$  km. A flat Earth (Cartesian geometry) is assumed so that there is no latitudinal variation in this value. The land and sea surface roughness lengths are prescribed as 0.1 m and  $2 \times 10^{-4}$  m respectively. The former was chosen to be representative of the Southwest Peninsula (based on values specified in the UKV model) while the latter is a widely quoted value from Wiernga (1993). An  $f$ -plane approximation is used so that  $\phi$  is assumed constant ( $50^\circ\text{N}$ ) across the domain. The UKV model vertical level set is used (see Section 4.3.1) with Rayleigh damping applied above 10 km to reduce spurious reflection of waves off the rigid model lid. Within the damping layer, variables  $\chi = (u, v, \theta, m_{\text{vap}})$  are relaxed back to a reference profile (that of the initial conditions; see below) through the addition of the following term to the model's prognostic equations (Section 2.2.1):

$$\frac{\partial \chi}{\partial t}^{\text{damp}} = \begin{cases} \frac{1}{\tau_D} \left[ \exp\left(\frac{z-z_D}{h_D}\right) - 1 \right] (\chi - \chi_{\text{ref}}) & z > z_D \\ 0 & z \leq z_D \end{cases} \quad (5.1)$$

Here,  $z_D$  is the base of the damping layer, and  $\tau_D$  and  $h_D$  are time and height scales specified respectively as 1000 s and 10 km.

Fixed lateral boundary conditions are used: the solution evolves freely within the interior  $584 \times 284$  grid points while the outermost five grid points retain their initial values throughout the simulation. Between these regions is a blending zone, three grid points in width, where variables are linearly interpolated to smooth the transition from interior to exterior values. However, significant discontinuities can still occur along the boundaries in the presence of strong flow perturbations and/or interior forcing. This motivated the use of an island rather than a peninsula: the 100 sea grid points around the land mass keep the prescribed land surface heating (described below) well removed from the boundaries. The circulations which develop in response to this heating do ultimately impact at least one lateral boundary giving rise to spurious vertical motions;

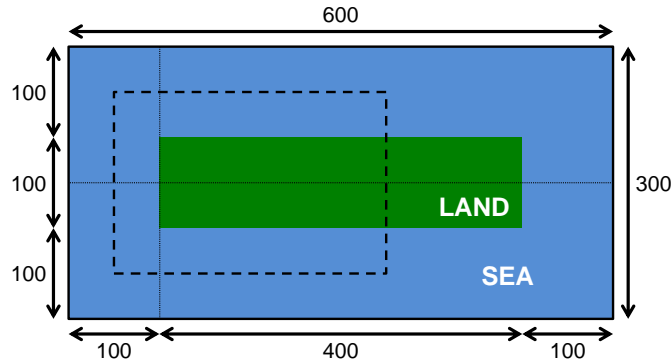


**Figure 5.2** Schematic showing the simulation domain. Lengths are given in grid points (approximately equal to km). The intersection of the thin dotted lines indicates the origin  $(x, y) = (0, 0)$ . The dashed box shows the subdomain for which results are presented. This is  $300 \times 200$  grid points in size and extends from  $(-50, -100)$  to  $(250, 100)$ .

however, these do not significantly influence the interior solution. This was confirmed through sensitivity tests performed on a larger domain with 50 additional sea grid points in each direction (not shown).

All the simulations to be presented were dry: no moisture was included in the initial conditions and surface latent heat fluxes were set to zero. The initial pressure profile was specified to be in hydrostatic balance, with a surface value of 1000 hPa. The initial potential temperature profile was specified as a rough approximation to those observed during the 21 July 2010 and Boscastle QSCS events over the UK Southwest Peninsula (Figure 5.3). It consists of three layers of constant static stability: a neutral boundary layer ( $\frac{\partial\theta}{\partial z} = 0 \text{ K km}^{-1}$  for  $z < 1 \text{ km}$ ), a stable free troposphere ( $\frac{\partial\theta}{\partial z} = 5 \text{ K km}^{-1}$  for  $1 < z < 10 \text{ km}$ ), and a stratosphere ( $\frac{\partial\theta}{\partial z} = 15 \text{ K km}^{-1}$  for  $z > 10 \text{ km}$ ). The surface potential temperature is set at 288.15 K (15°C). One might commonly associate marine boundary layers with a stable near-surface stratification; indeed, this has been the configuration used in most numerical studies of the SBS (Crosman and Horel 2010). However, if the stratification is not too strong, vertical wind shear associated with surface friction drives turbulence which acts to mix out gradients in potential temperature. A neutral boundary layer may also develop due to buoyancy-driven turbulence when cold air is advected over a relatively warm sea. Both mixing processes were likely active in the returning polar-maritime flow which characterised the 21 July 2010 and Boscastle cases. The 1200 UTC soundings from Camborne (see Figure 4.1 for location) on both days show approximately neutral boundary layers, although these are shallower than 1 km (Figure 5.3). The profiles may have been modified slightly during the short passage of the air over land to reach Camborne; however, model-derived soundings taken upstream of the peninsula feature similar mixed layers (not shown). The sensitivity of sea-breeze evolution to both the depth of the mixed layer and stability of the free troposphere is explored in the simulations.

To generate a background flow in my simulations, geostrophic momentum forcing was applied. This represents the effect of a uniform pressure gradient on the wind and involves the addition of the following terms in the  $u$ - and  $v$ -momentum equations:

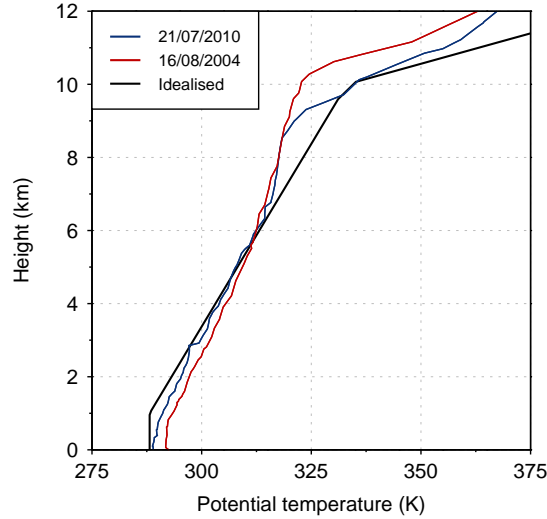


**Figure 5.3** Potential temperature profiles derived from the Camborne soundings at 1200 UTC on 21 July 2010 (blue) and 16 August 2004 (red), and the idealised profile used in the present simulations (black).

$$\frac{\partial u^{\text{geo}}}{\partial t} = -2\Omega \sin \phi v_g \quad (5.2)$$

$$\frac{\partial v^{\text{geo}}}{\partial t} = -2\Omega \sin \phi u_g \quad (5.3)$$

where,  $u_g$  and  $v_g$  are prescribed geostrophic wind components. To minimise spin-up at the inflow boundaries, it was desirable to have wind profiles which were well adjusted to the sea surface roughness. These were obtained using a 10day run on a  $100 \times 100$  grid point bi-periodic all-sea domain with an initially uniform zonal wind of strength  $U_g$  and geostrophic momentum forcing  $(u_g, v_g) = (U_g, 0)$ . This ‘spin-up simulation’ had to be performed for each of the geostrophic wind speeds  $U_g$  used herein, as well as for non-zero-flow cases where the latitude, mixed-layer depth, and stability of the free-troposphere were varied from their control values (see below). Figure 5.4 shows the adjusted zonal and meridional wind profiles obtained for a westerly flow of  $5 \text{ m s}^{-1}$ . These are very similar in appearance to the classic ‘Ekman Spiral’ (e.g. Stull 1988, p210) which is not surprising since the assumptions used to derive the latter (a steady-state, horizontally homogeneous, barotropic flow under neutral stability) are all met here; the only difference is that the eddy diffusivity is not a constant in the UM.

The standard idealised UM contains an option to specify diurnally varying surface sensible and latent heat fluxes over the sea. For the present simulations, the code was modified to include an identical option for land points. The time-dependent surface sensible heat flux  $H(t)$  is prescribed as

$$H = H_{\text{max}} F^{1.5} \quad (5.4)$$

where

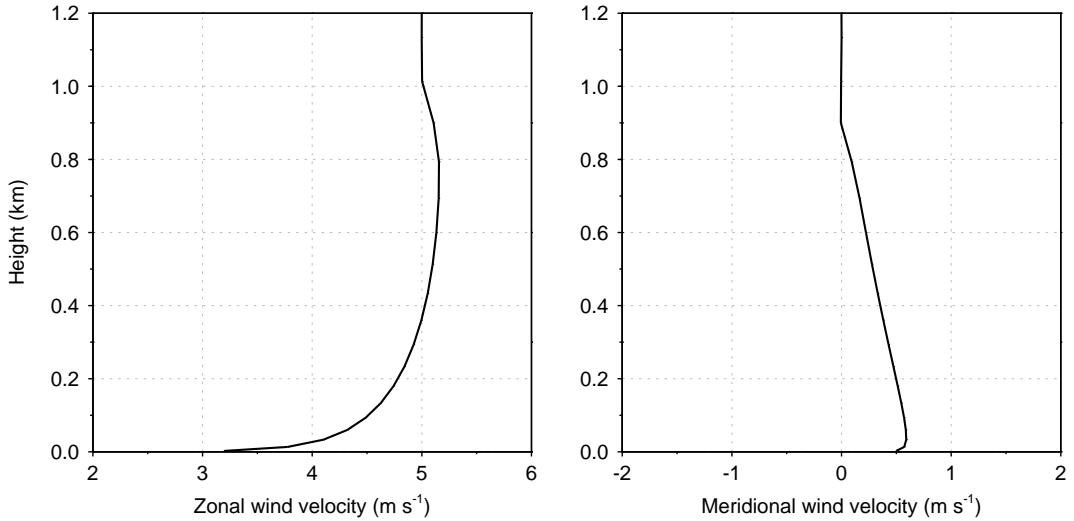


**Figure 5.4** Domain- and time-averaged vertical profiles of (a) zonal and (b) meridional wind velocity in the lowest 1.2 km for the final 24 h of a 10 day spin-up simulation with an initially constant zonal flow of  $5 \text{ m s}^{-1}$  and geostrophic momentum forcing.

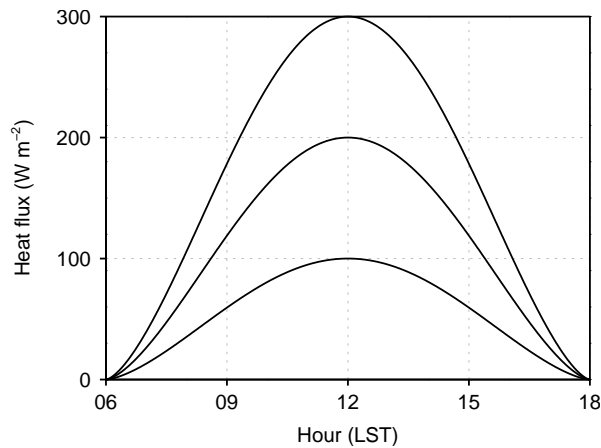


**Figure 5.5** Specified land surface heat fluxes as a function of time (LST = Local Solar Time) for the three values of  $H_{\max}$  used herein.

$$F = \max \left\{ \cos \left[ \pi \left( \frac{t_{\max} - t}{L} \right) \right], 0 \right\}, \quad (5.5)$$

$H_{\max}$  is the maximum heat flux which occurs at time  $t_{\max}$ , and  $L$  is the day length. I have specified  $L$  as 12 h with  $t_{\max}$  occurring at  $t_0 + 18$  h where  $t_0$  is the run start time. This gives 12 h of spin-up, during which time the flow is able to adjust to surface friction over land. The heating is then applied from  $t_1 = t_0 + 12$  to  $t_2 = t_0 + 24$  h after which the simulation is stopped. Three values of  $H_{\max}$  are used: 100, 200, and  $300 \text{ W m}^{-2}$ . The diurnal cycle of  $H$  for each of these cases is shown in Figure 5.5. In this figure and hereinafter, times are described in terms of Local Solar Time (LST) where  $t_{\max} = 1200 \text{ LST}$  and ‘sunrise’ and ‘sunset’ occur at 0600 and 1800 LST respectively.

The use of prescribed surface fluxes necessitated a modification to the parameterisation of surface drag in the boundary-layer scheme. In the standard scheme, the drag

**Table 5.1** Variable parameters and their values. Asterisks indicate the default values. Wind directions are taken anticlockwise from due east so that  $0^\circ$  indicates westerly flow.

Parameter (units)	Symbol	Values
Geostrophic wind speed ( $\text{m s}^{-1}$ )	$U_g$	0, 1, 2, 2.5, 3, 4, 5, 6, 7.5, 10
Geostrophic wind direction ( $^\circ$ )	$\psi_g$	-45, 0, 15, 30, 45, 90
Maximum heat flux ( $\text{W m}^{-2}$ )	$H_{\max}$	100, 200*, 300
Peninsula width (km)	$W$	50, 100*
Latitude ( $^\circ$ )	$\phi$	30, 50*, 70
Mixed-layer depth (km)	$h_{\text{ml}}$	0.5, 1*, 1.5
Stability of the free troposphere ( $\text{K km}^{-1}$ )	$\gamma_{\text{ft}}$	2.5, 5*, 7.5
Land surface roughness length (m)	$z_0$	0.01, 0.1*, 1

coefficient  $C_D$  is a function of the surface buoyancy flux  $F_B$  which itself depends on the difference in temperature between the surface and the first model level. In the present simulations,  $F_B$  was instead determined using the specified sensible heat flux as follows:

$$F_B = \frac{gH}{T_1 c_{\text{pd}}} \quad (5.6)$$

where  $T_1$  is the temperature at the first model level.

Table 5.1 summarises all the variable parameters used in the simulations. The main focus of this study is on the case of along-peninsula (westerly) flow and the sensitivity of sea-breeze evolution to  $U_g$  and  $H_{\max}$ . However, these sensitivities are also explored for cross-peninsula (southerly) flow, while the behavior under other wind directions is considered briefly. The effects of changing the remaining parameters (in isolation) within realistic bounds are examined in a number of sensitivity tests.

Before exploring the results of the simulations, it is important to consider what processes are neglected. First, since the surface heat flux is prescribed, it does not respond to changes in near-surface wind speed or stability associated with the sea breeze, or modifications to the other model parameters (e.g. the roughness length). The passage of an SBF is always accompanied by lower temperatures which act to enhance  $H$  by increasing the surface-layer temperature gradient. With no background flow, wind speed obviously increases behind the front which enhances  $H$  through ventilation; however, in the presence of an ambient wind, the sign and magnitude of the change in wind speed will depend on the relative direction and magnitude of the two flows. Feedbacks can also occur through cloud formation which obviously cannot occur in these simulations. If the daytime convective boundary layer over land is cloud-topped, insolation is reduced leading to a smaller land–sea temperature difference and weaker sea breeze. If deep convection develops, its outflow may interact with and disrupt the inland propagation of the SBF. As demonstrated in Chapter 4, temporal variations in the ambient wind can also strongly impact sea breeze evolution; however, here the flow is assumed to be steady. Finally, it must be noted that the structure of the sea breeze in these simulations is

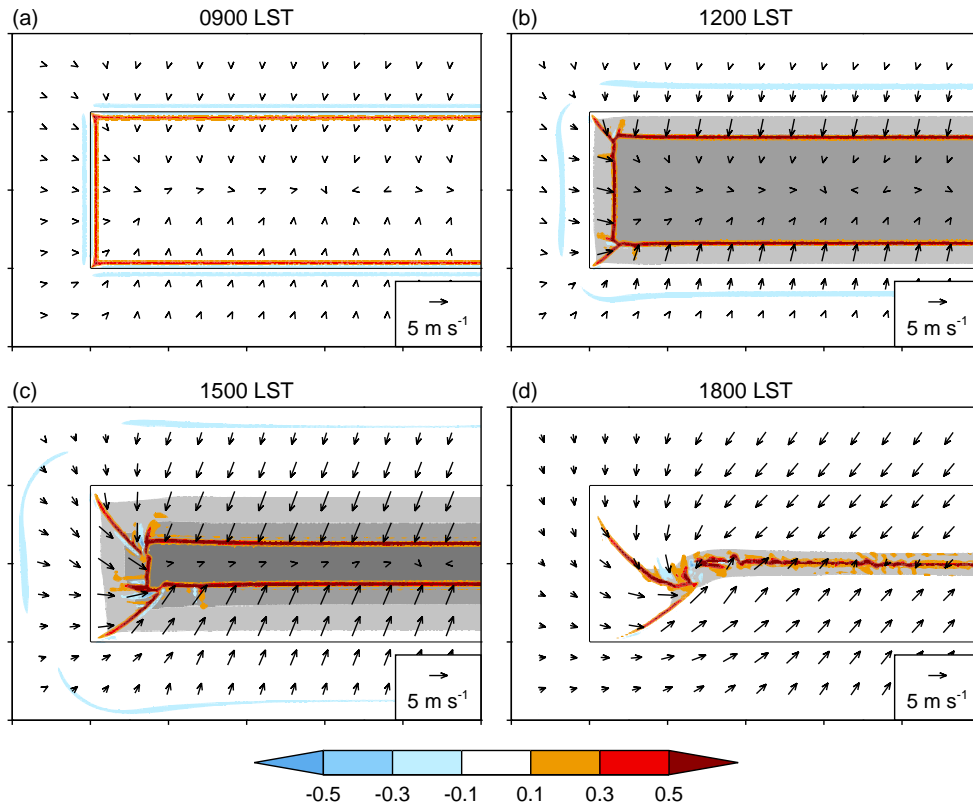
greatly simplified by the use of straight coastlines and a homogeneous, flat land surface. Real coastlines are far more complex, with many small-scale bays and peninsulas that add structure to the SBF and cause along-shore variations in its rate of movement (see for example Figure 4.4). They may also feature significant orography which can block the inland propagation of the sea breeze and generate upslope flows that interact with it (e.g. Barthlott and Kirshbaum 2013).

## 5.4 Simulation results

In the following sections, the results of the idealised simulations are analysed. We will first consider the sea breeze in the absence of a background flow (Section 5.4.1), as this is the easiest situation to understand, before moving on to examine the case of along-peninsula flow (Section 5.4.2). In Section 5.4.3, a method is developed to predict the behavior of SBFs in these two cases based on existing scaling laws. The remaining sections briefly consider cross-peninsula flow (Section 5.4.4), other wind directions (Section 5.4.5), and the role of coastline geometry (Section 5.4.6).

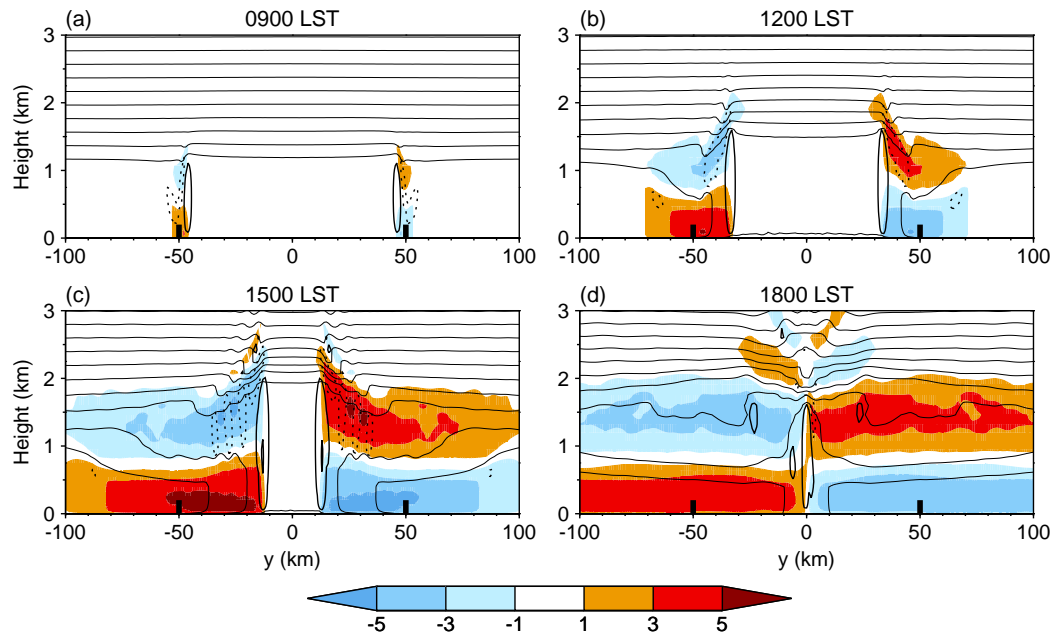
### 5.4.1 No background flow

Figure 5.6 shows the evolution of a simulation with zero initial flow and a maximum heat flux of  $200 \text{ W m}^{-2}$ . At 0900 LST, 3 h into the heating cycle, the developing SBC is visible along the entire coastline as a vertical-velocity couplet, with rising motion just inland and sinking motion just offshore (Figure 5.6a). As the land–sea temperature difference grows, the circulation strengthens and expands in the horizontal: the SBF propagates inland while the region of descent moves farther offshore. By 1200 LST (Figure 5.6b), an onshore flow is clearly visible at low levels, with maximum velocities of around  $5 \text{ m s}^{-1}$  behind the front. Note that this flow is not perpendicular to the shoreline, but rotated slightly clockwise due to the Coriolis force. The degree of rotation grows with time, or rather with distance travelled by the air, such that by the end of the simulation (Figure 5.6d), the wind vectors are angled at approximately  $45^\circ$  with respect to the coast. The flow between the SBF and the coast is quite uniform, presumably due to the temperature gradient which develops within the SBG as it propagates inland (Figure 5.6c). As the SBFs move inland, lines of ascent develop downstream of the corners of the peninsula associated with convergence between the north-/south- and west-coast SBGs. Eventually, the north- and south-coast SBFs collide forming a zone of strong convergence and ascent along the centre of the peninsula (Figure 5.6d). This remains approximately stationary and develops fine-scale structure through horizontal shear instability (e.g. Markowski and Richardson 2010, Chapter 3). Farther west, a region of strong rotation develops at the ‘triple point’ where the north-, south-, and west-coast SBFs meet. This feature is reminiscent of the mesoscale vortices which form in winter over the Great Lakes of North America in association with land breezes (e.g. Forbes and Merritt 1984; Niziol *et al.* 1995).



**Figure 5.6** Evolution of the no-flow case ( $U_g = 0$ ) with  $H_{\max} = 200 \text{ W m}^{-2}$ . Variables shown are the vertical velocity at 600 m (colour shading;  $\text{m s}^{-1}$ ), potential temperature perturbation at 5 m (grey shading; 1 K intervals starting at 1 K), and wind velocity at 50 m (vectors). Tick marks on the axes are shown every 50 km.

Figure 5.7 shows the vertical structure of the north- and south-coast sea breezes, away from the west coast, as they evolve. Both the SBG and RC are clearly seen in the meridional wind field, as is their lateral expansion with time. Once mature, the SBG has a depth of around 700 m in its middle section but extends to around 900 m at the current head. A similar feature is apparent at the trailing edge of the SBG coincident with a local minimum in the vertical-velocity field (the offshore region of descent seen in Figure 5.14). This appears to be due to ‘slumping’ of the cool marine air, similar to that seen in fluid tank ‘lock-release’ density current experiments. The RC also slopes up towards the SBF, but, at 1–1.5 km in vertical extent, is deeper than the SBG. Consistent with this, the horizontal flow in the RC is weaker than that in the SBG. The ascending branches of the circulation grow vertically as the daytime convective boundary layer develops, reaching a maximum depth of around 2 km at 1500 LST. As they impinge on the stable free troposphere, gravity waves are triggered, visible in both the vertical velocity and potential temperature fields. By 1800 LST (Figure 5.7d), the circulation extends beyond the domain shown and in fact impinges on the lateral boundaries of the simulation domain (not shown). Since the flow there is fixed (at zero in this case), the horizontal extent of the circulation is effectively limited. As a consequence, strong descent occurs just within the boundary zone. However, as noted in Section 5.4, this does not significantly impact the interior portion of the circulation.



**Figure 5.7** Vertical cross sections taken at  $x = 200$  km for each of the times shown in Figure 5.6. Variables shown are the meridional wind velocity (colour shading;  $\text{m s}^{-1}$ ), potential temperature (thin contours; 1 K intervals), and vertical velocity (thick contours, solid and dotted for positive and negative values respectively;  $-0.1, 0.1, \text{ and } 1 \text{ m s}^{-1}$ ). Thick black markers on the  $x$ -axis show the location of the coastlines.

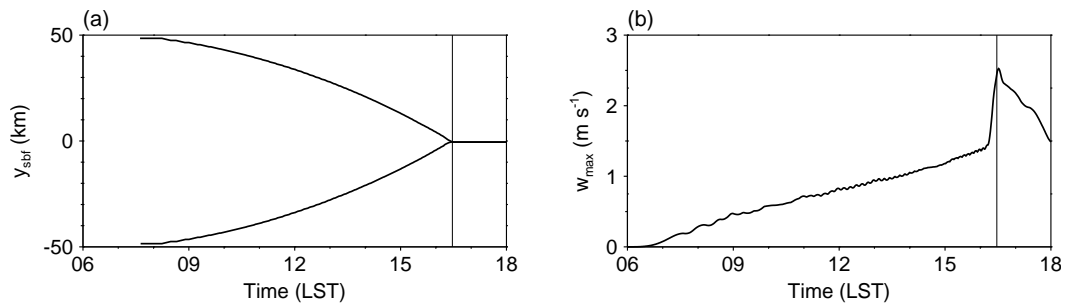


**Figure 5.8** Time series of (a) SBF positions  $y_{\text{sbf}}$  and (b) maximum vertical velocity  $w_{\text{max}}$ , both calculated at  $x = 200$  km. Thin vertical lines indicate the time at which the north- and south-coast sea breezes collide. The data have a time resolution of 1 min but have been smoothed using a 15 min moving average. The oscillations in  $w_{\text{max}}$  (which are significantly larger in amplitude without the smoothing) appear to be a consequence of representing the continuous movement of the SBF on a discontinuous model grid; the period of each half wave corresponds to the time over which the SBF moves one grid point.

Figure 5.8 summarises the evolution of the north- and south-coast sea breezes in terms of two variables measured at the same location as the cross sections ( $x = 200$  km): the SBF positions  $y_{\text{sbf}}$  and the maximum vertical velocity  $w_{\text{max}}$  at 600 m. The former were identified as points where the vertical velocity (again at 600 m) exceeded two standard deviations of the mean between  $y = -50$  and  $50$  km. Acceleration of the onshore flow with time can clearly be seen in the curved SBF trajectories, as can the associated increase in maximum vertical velocity (due to strengthening convergence at the front). The collision of the two fronts is accompanied by a sudden increase in  $w_{\text{max}}$ ,

after which values remain high ( $\geq 1 \text{ m s}^{-1}$ ) but gradually decrease.

Before investigating the evolution of the SBS in along-peninsula flow, let us consider the sensitivity of the no-flow case to some of the model parameters listed in Table 5.1; specifically, the maximum heat flux  $H_{\text{max}}$ , latitude  $\phi$ , mixed-layer depth  $h_{\text{ml}}$ , stability of the free troposphere  $\gamma_{\text{ft}}$ , and land surface roughness length  $z_0$ . A series of runs were performed where each of these was either increased or decreased in isolation. The results are summarised in Figures 5.9 and 5.10. Figure 5.9 shows cross sections at  $x = 200 \text{ km}$  and 1500 LST for each run, which may be compared directly with Figure 5.7c. Figure 5.10 shows time series of  $y_{\text{sbf}}$  (as in Figure 5.8) and area-integrated updraught mass flux (UMF), both at  $x = 200 \text{ km}$ . Mass flux is used instead of maximum vertical velocity as it gives a better measure of the overall strength of the SBC. It is interesting to note that unlike  $w_{\text{max}}$ , UMF does not increase at the time of sea breeze collision.

All of the parameters have a noticeable effect on the sea-breeze system; however, only  $H_{\text{max}}$  significantly influences the rate at which the SBFs propagate inland. With a higher heat flux the land–sea temperature contrast increases more rapidly and attains a higher maximum, leading to a stronger and deeper SBC with increased mass flux at the SBFs. Latitude influences the rate of turning of the wind via the Coriolis force; hence changes in sea-breeze characteristics due to a change in  $\phi$  become more pronounced over time. At a lower latitude, the wind turns less and therefore the shore-perpendicular component of the onshore flow is slightly stronger (Figure 5.9c). Consequently, the vertical velocities and mass flux are slightly higher and the SBFs collide slightly earlier. A change to the mixed-layer depth or free-tropospheric stability unsurprisingly affects the vertical extent of the circulation, with a deeper SBC when  $h_{\text{ml}}$  is higher and  $\gamma_{\text{ft}}$  is lower. The horizontal flow shows little sensitivity to these parameters; however, the vertical velocities and mass flux are impacted via the increased/decreased depth over which convergence occurs. Finally, as the land surface roughness is increased, the SBG velocities decrease, reducing the rate of SBF propagation and the mass flux, albeit by a fairly small amount.

Two important conclusions can be drawn from the results presented in this section. First, the idealised UM configuration produces a sea-breeze system that evolves in a manner consistent with previous observations and numerical simulations. Second, the movement of the SBFs is largely insensitive to many of the model parameters, with the exception of the maximum heat flux. Let us now move on to examine sea-breeze evolution in the presence of along-peninsula flow.

## 5.4.2 Along-peninsula background flow

### Temperature evolution

The control simulation for along-peninsula flow ( $\psi_{\text{g}} = 0^\circ$ ) has a geostrophic wind speed of  $5 \text{ m s}^{-1}$  and a maximum heat flux of  $200 \text{ W m}^{-2}$ . Before examining the SBS, let us consider the evolution of the low-level temperature field in this case. This is shown for  $y = 0$  (i.e. along the centre of the peninsula) in Figure 5.11. With non-zero flow,

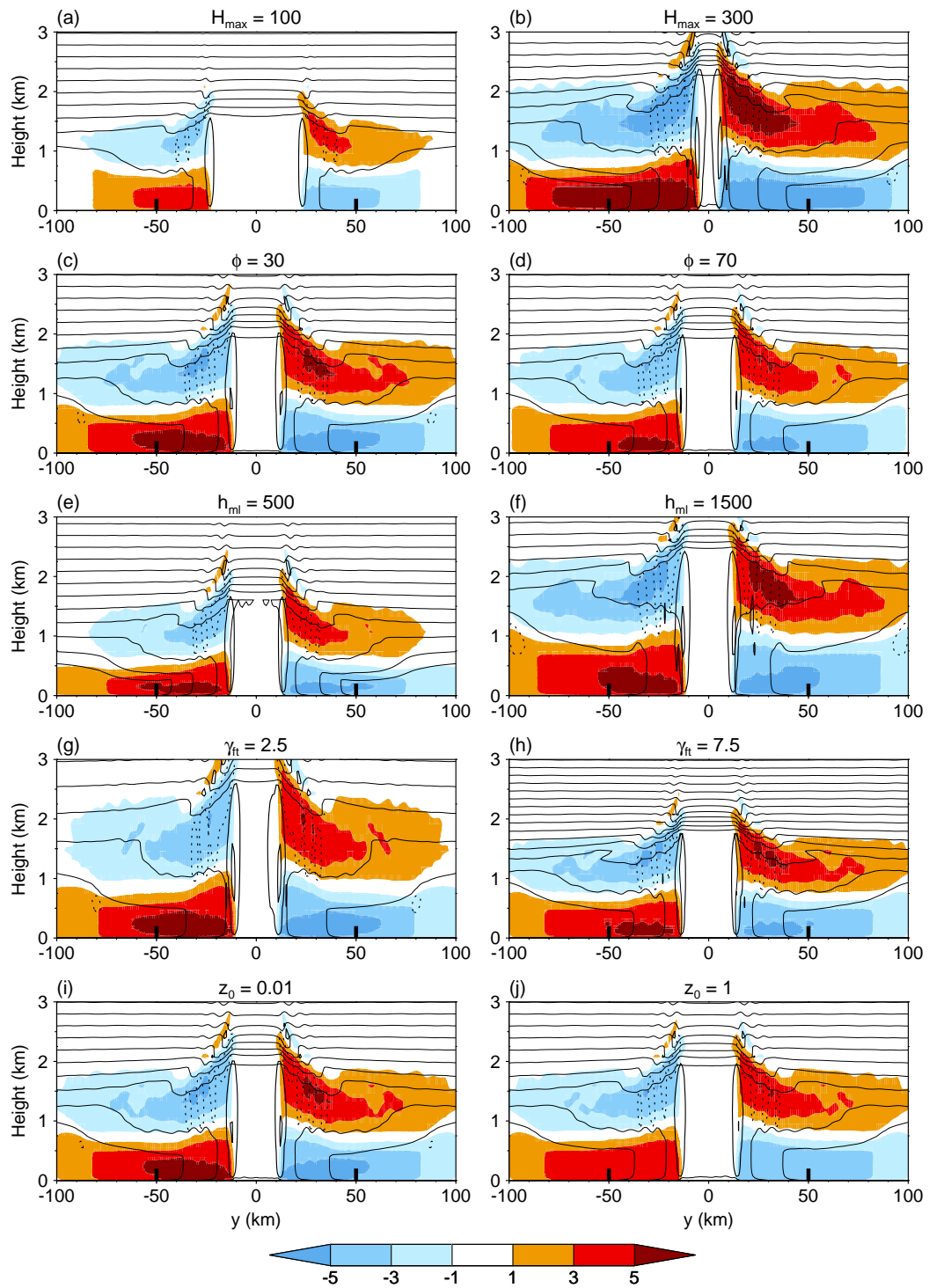


**Figure 5.9** As in Figure 5.7 but for each of the sensitivity runs at 1500 LST.

the low-level temperature becomes a function of both time of day and the distance travelled over land (as seen behind the SBFs in the no-wind case). As air moves along the peninsula, it accumulates heat resulting in a west-to-east temperature gradient whose horizontal extent and strength varies with the diurnal cycle of surface heating. Specifically, the gradient reaches peak intensity shortly after 1200 LST (the time of maximum surface heat flux), while its horizontal extent increases approximately linearly

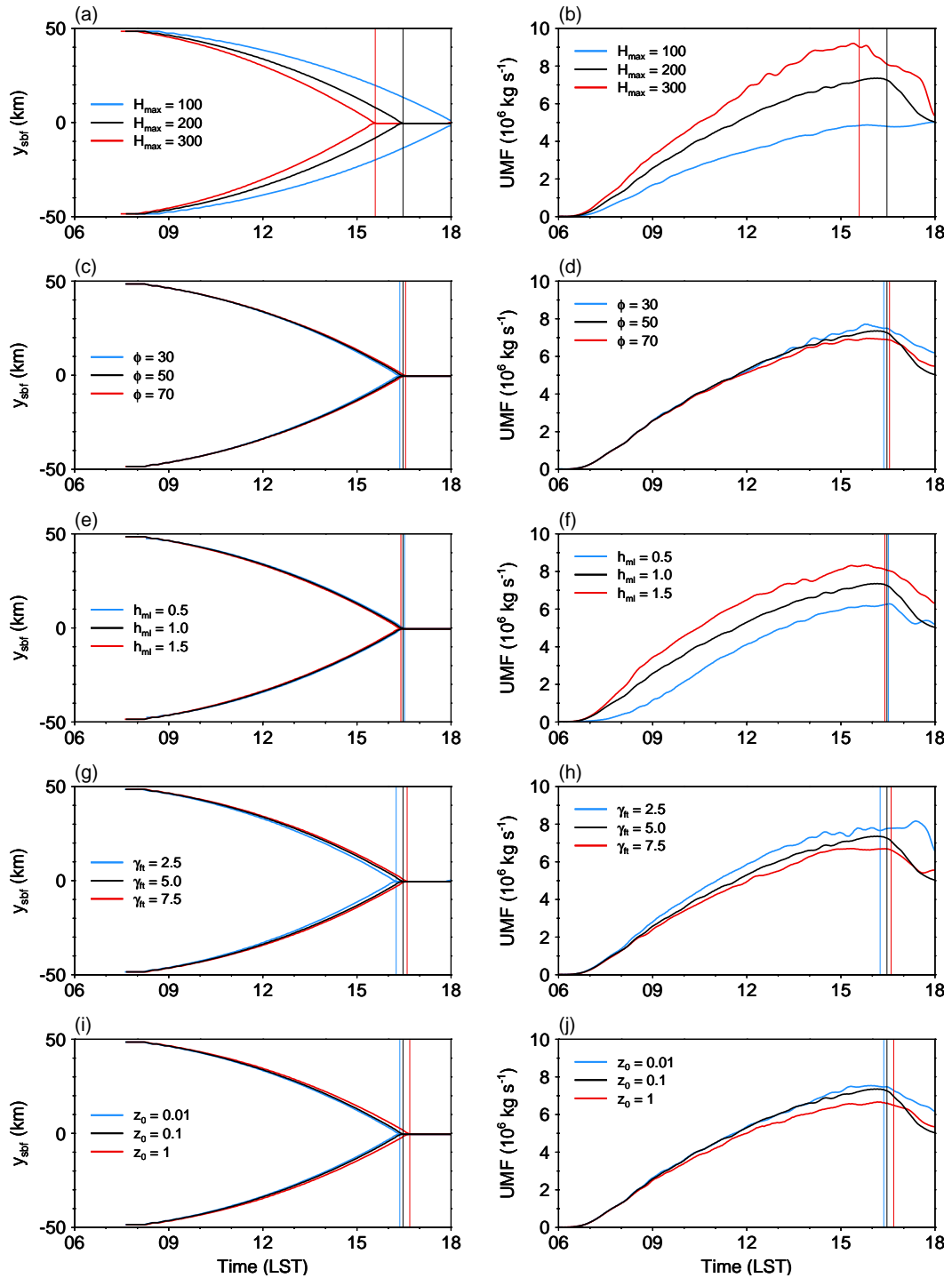


**Figure 5.10** Time series of (left) SBF positions  $y_{\text{sbf}}$  and (right) area-integrated updraught mass flux (UMF) at  $x = 200 \text{ km}$  for the control simulation (black lines) and each of the sensitivity tests (red and blue lines for increased and decreased parameter values respectively). Thin vertical lines indicate the time at which the north- and south-coast sea breezes collide. The data have a time resolution of 1 min but have been smoothed using a 15 min moving average.

throughout the day (Figure 5.11a). The eastern boundary of this ‘adjustment zone’ (AZ) marks the point beyond which the residence time over land exceeds the time since heating commenced (0600 LST); hence, the temperature farther downstream is constant

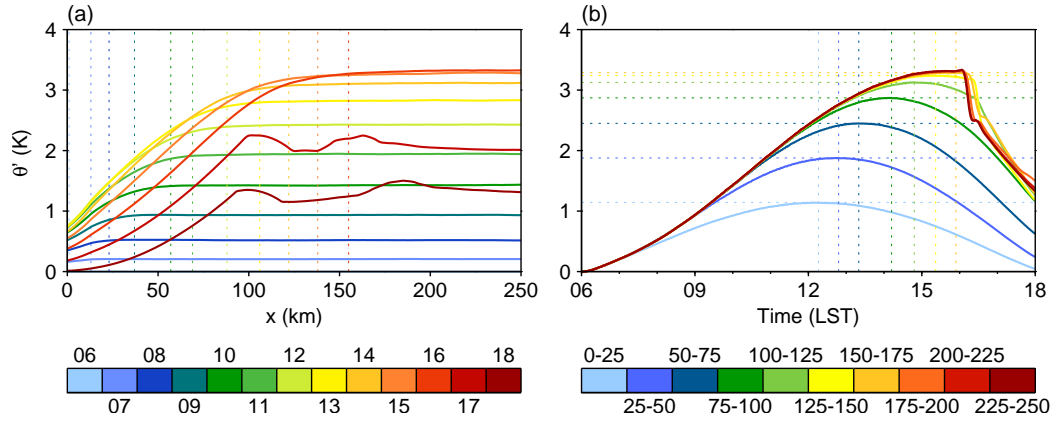


**Figure 5.11** Evolution of potential temperature perturbation (with respect to the initial value)  $\theta'$  on the lowest model level along  $y = 0$  for the along-peninsula flow simulation with  $U_g = 5 \text{ m s}^{-1}$  and  $H_{\text{max}} = 200 \text{ W m}^{-2}$ . In (a),  $\theta'$  is plotted as a function of  $x$  with different coloured lines for each hour from 0600 to 1800 LST. The data have been smoothed using a 25point moving average. Dotted vertical lines mark the approximate end of the adjustment zone, taken as the first point beyond which  $\partial\theta'/\partial x < 0.005 \text{ K km}^{-1}$ . These are not shown for 1700 and 1800 LST. In (b),  $\theta'$  is averaged in  $x$  using 25 km bins and plotted as a function of time with different coloured lines for each bin. Dotted lines indicate the maximum temperature and the time at which it occurs. These are not shown for the final three bins.

in  $x$  (at a particular time). We may also note from Figure 5.11b that the amplitude of the diurnal variation in temperature and the time at which the maximum temperature occur both increase with downstream distance, the latter approximately linearly and the former nonlinearly (at a decreasing rate). Shortly after 1600 LST, the diurnal evolution is disrupted by the collision of the north- and south-coast sea breezes.

To understand this behaviour, consider the rate of change of temperature following the flow as it traverses the peninsula. In the absence of diabatic heating, this is simply given by the vertical convergence of the turbulent temperature flux:

$$\frac{dT}{dt} = -\frac{\partial}{\partial z} (\overline{w'T'}) \quad (5.7)$$

If we assume that the heat input at the surface is distributed uniformly within a layer of constant depth  $h$  and density  $\rho$ , then we can write

$$\frac{dT}{dt} = \frac{H}{\rho c_{pd} h} \quad (5.8)$$

Integration of this equation from time  $t_i$  where  $T(t_i) = T_i$  to time  $t$  gives

$$T(t) = T_i + \frac{1}{\rho c_{pd} h} \int_{t_i}^t H dt \quad (5.9)$$

Thus, the temperature of the layer depends on the time-integrated surface heat flux. When there is no flow, this integration is simply performed from the start of the diurnal cycle  $t_i = t_1$  (0600 LST); however, with a non-zero wind, the heat flux must be integrated *along the path travelled over land*. If we assume a constant wind speed  $U$  then the perturbation temperature  $T' = T - T_i$  (equivalent to the land–sea temperature difference

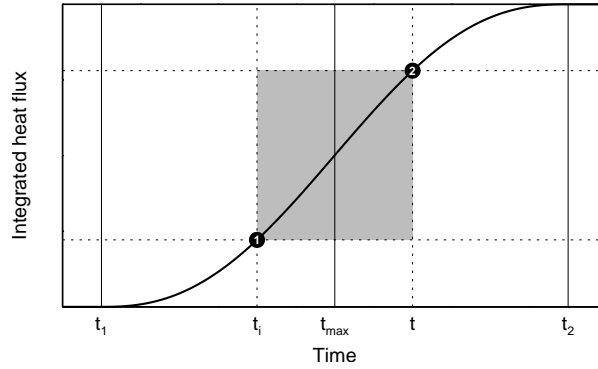


**Figure 5.12** Integrated heat flux as a function of time, computed numerically from Equation 5.4 using a time step of 60 s. The grey-shaded area, dotted lines, and numbered black circles illustrate the calculation of  $\hat{H}$  for a particular time  $t$  and downstream distance  $x = U(t - t_1)$ . See text for details.

when there is zero heat flux at the sea surface) at a downstream point  $x$  and time  $t$  will be given by

$$T'(x, t) = \frac{1}{\rho c_{pd} h} \int_{t_1}^t H dt \quad (5.10)$$

where  $t_1 = t - x/U$  is the time at which the air crossed the western edge of the peninsula ( $x = 0$ ).

The equation for heat flux in the idealised UM (Equation 5.4) cannot be integrated analytically; however, insight can be gained by examining the shape of the curve obtained through numerical integration. This is shown in Figure 5.12. The grey box, defined by the position of Points 1 and 2 on the curve, has width and height equal to  $\Delta t = x/U$  and  $\hat{H} = \int_{t_1}^t H dt$  respectively. It is clear that  $\hat{H}$  (and thus  $T'$ ) is proportional to both  $\Delta t$  and  $t$  but the relationship is nonlinear. If at a particular time (fixed  $t$ ) we move downstream, Point 1 will shift left along the curve, increasing  $\hat{H}$ , up until  $t_1 = t_1$ , after which  $\hat{H}$  becomes constant in  $x$ . This represents the end of the AZ which we will designate as  $x^* = U(t - t_1)$ . If instead we move forward in time at a fixed location (fixed  $\Delta t$ ), both points will move to the right causing  $\hat{H}$  to increase for  $t < t_{\max} + \frac{1}{2}\Delta t$  and decrease for  $t > t_{\max} + \frac{1}{2}\Delta t$ . The maximum  $\hat{H}$  and maximum perturbation temperature  $T'_{\max}$  thus occur when  $t = t_{\max} + \frac{1}{2}\Delta t$  (i.e. when the grey box is centred on  $t_{\max}$ ).  $T'_{\max}$  will increase nonlinearly (at a decreasing rate) as we move downstream (increase the width of the box); however, the time at which it occurs increases linearly with  $x$ . The absolute maximum temperature that can be achieved occurs when  $t = t_2$  and  $x \geq x^*$ .

In Figure 5.13,  $\hat{H}$  is plotted as a function of  $x$  and  $t$  in the same manner as  $\theta'$  in Figure 5.11. In the calculation, the wind speed was set as  $U = 0.855U_g$  for reasons that will be discussed later. Comparison of Figures 5.11 and 5.13 reveals that the simulated low-level temperature field evolves in a manner which is quite consistent with the simple theoretical considerations above. However,  $\theta'$  increases very rapidly in the first few km of the peninsula and peaks earlier in the day at all downstream

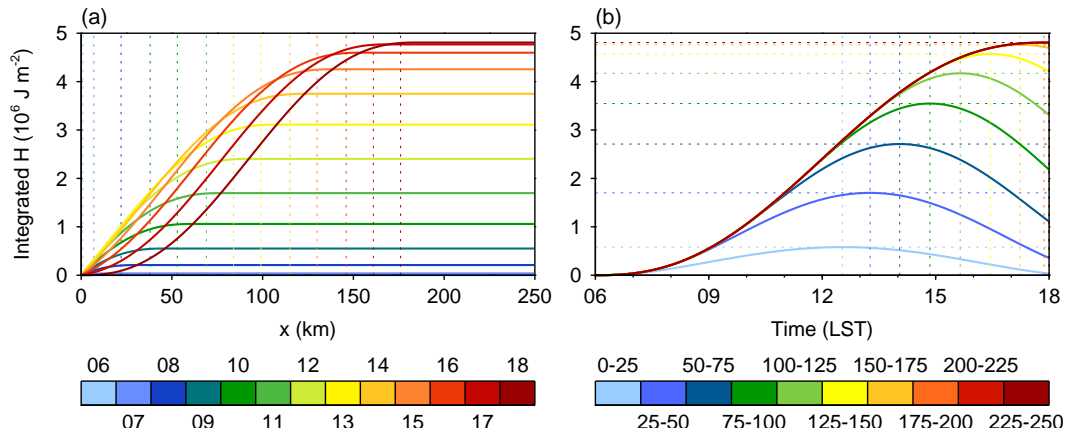


**Figure 5.13** As in Figure 5.11 but for the integrated heat flux  $\hat{H}$  computed numerically using a time step of 60 s and  $U = 0.855U_g$ . In this case, the end of the AZ was identified as the first point beyond which  $\partial\hat{H}/\partial x < 5 \times 10^3 \text{ J m}^{-2} \text{ km}^{-1}$ .

locations than  $\hat{H}$  alone would suggest. It is also non-zero at  $x = 0$ , although this may be associated with pressure rather than temperature perturbations (recall that  $\theta$  is a function of both  $T$  and  $p$ ). These discrepancies demonstrate that the assumptions made in deriving Equation 5.10 (uniform heating in a layer of constant thickness and density) are not valid. A large part of the error probably relates to the development of an internal boundary layer which causes  $h$  to increase with  $x$  in a similar manner as  $T'$  (e.g. Garrat 1992, p188). However, as will be shown,  $\hat{H}$  is a useful quantity for predicting the evolution of the SBS.

### Sea-breeze evolution

Let us now move on to consider how the SBS develops in the along-peninsula-flow case, which is illustrated by Figure 5.14. We first note that slight acceleration and veering (or rather reduced frictional backing) of the low-level flow occurs in the AZ in response to the west-to-east temperature gradient there. This may be thought of as the west-coast SBG, dramatically weakened (compared to the no-wind case) by the strong onshore flow. The north- and south-coast sea breezes are also clearly modified in this case. Specifically, their strength varies with distance downstream of the west coast in a manner consistent with the temperature perturbations over land. Thus, the meridional perturbation flow increases with  $x$  in the AZ but is approximately constant beyond  $x^*$ . As a result, the SBFs are angled (from northwest to southeast on the north coast and southwest to northeast on the south coast) up to  $x^*$  but orientated west to east thereafter. Another noteworthy feature, not observed in the no-flow case, is horizontal convective rolls (HCRs) which are visible as elongated updraughts and downdraughts ahead of the SBFs during the afternoon (Figure 5.14c). These are a common feature of unstable boundary layers in vertically sheared flow (e.g. Markowski and Richardson 2010), although they are likely under-resolved here.

Some notable asymmetries exist between the two sea breezes. First, the south-coast

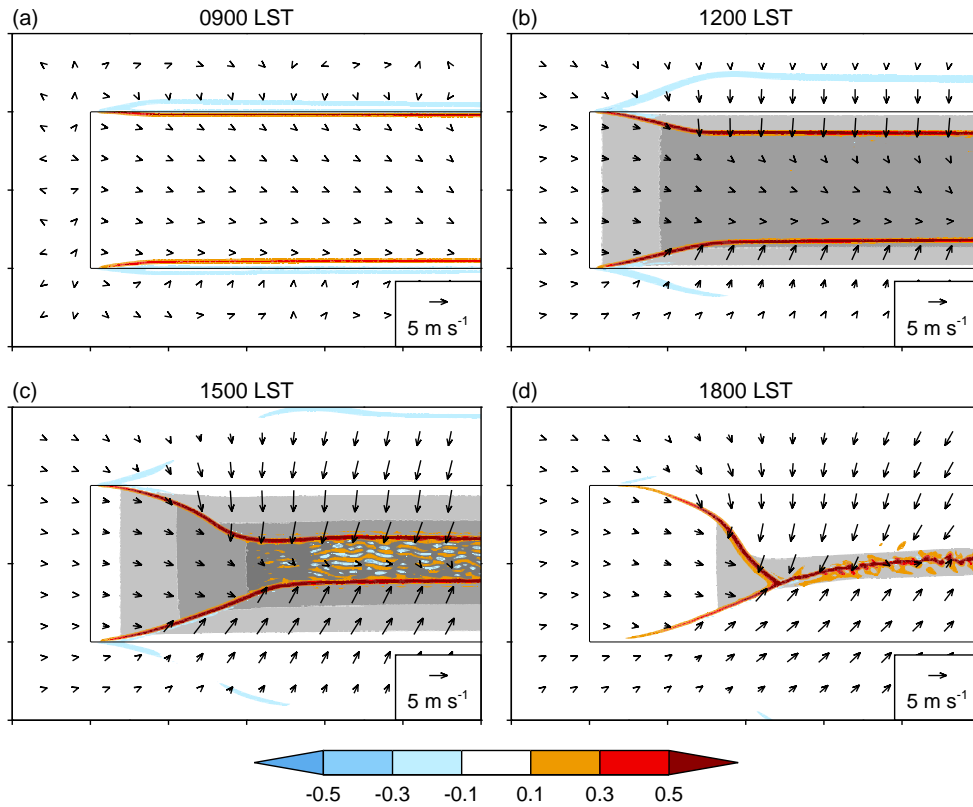


**Figure 5.14** Evolution of the westerly-flow case with  $U_g = 5 \text{ m s}^{-1}$  and  $H_{\text{max}} = 200 \text{ W m}^{-2}$ . Variables shown are the vertical velocity at 600 m (colour shading;  $\text{m s}^{-1}$ ), potential-temperature perturbation at 5 m (grey shading; 1 K intervals starting at 1 K), and perturbation wind velocity ( $\mathbf{u}' = \mathbf{u} - \mathbf{u}_1$  where  $\mathbf{u}_1$  is the velocity field at 0600 LST) at 50 m (vectors). Tick marks on the axes are shown every 50 km.

SBF moves inland slightly faster while the onshore flow behind it is weaker and more angled than that on the north coast. These seemingly contradictory observations can be explained by noting that the ambient wind has a southerly component at low levels due to frictional backing (Figure 5.4). This gives rise to a larger temperature gradient on the north coast, resulting in stronger perturbation winds there (which feeds back on the temperature gradient as discussed in Section 5.2.2). However, the net wind on the north coast is smaller so it takes longer for the veering associated with the Coriolis force to take place. On the south coast, the net onshore flow is stronger causing the SBF there to propagate inland more rapidly. The other notable asymmetry is in the curvature of the SBFs, with the north-coast SBF having a clear inflection point approximately in the centre of the AZ. This is again related to the Coriolis force. Within the AZ, the air behind the SBFs is influenced by both zonal and meridional temperature gradients; hence, the perturbation flow there is initially orientated approximately northwest to southeast on the north side of the peninsula and southwest to northeast on the south side of the peninsula. However, with time the wind veers, resulting in more westerly flow behind the south-coast SBF but more northerly flow behind the north-coast SBF. The latter therefore surges southward close to  $x = x^*$ .

While these observations are interesting in their own right, the most relevant finding

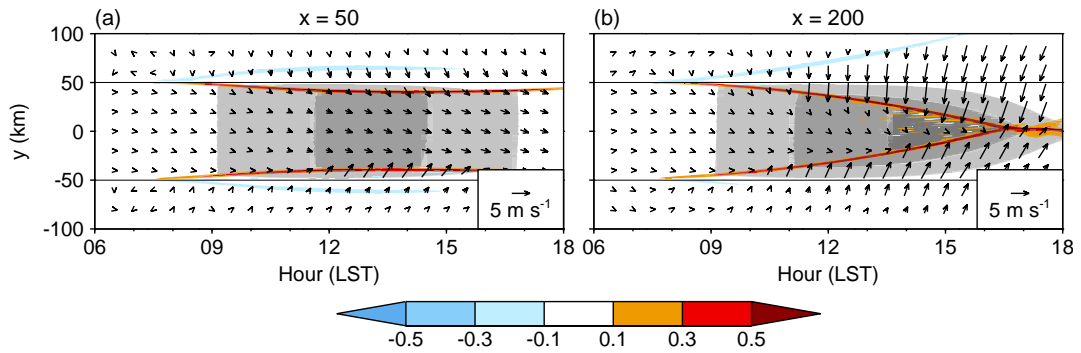


**Figure 5.15** Hovmöller diagrams showing the evolution of the westerly-flow case with  $U_g = 5 \text{ m s}^{-1}$  and  $H_{\text{max}} = 200 \text{ W m}^{-2}$  at (a)  $x = 50 \text{ km}$  and (b)  $x = 200 \text{ km}$ . The variables shown are identical to those in Figure 5.14. Thin horizontal lines show the north and south coastlines.

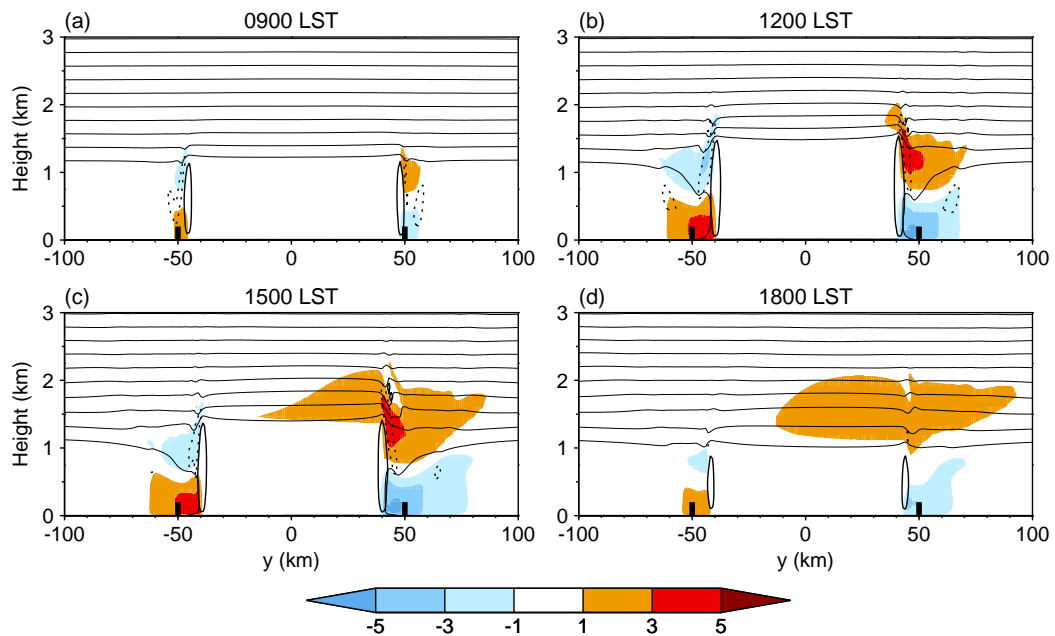


**Figure 5.16** As in Figure 5.7 but for the westerly-flow case with  $U_g = 5 \text{ m s}^{-1}$  and  $H_{\text{max}} = 200 \text{ W m}^{-2}$ . Here, the cross sections are taken at  $x = 50 \text{ km}$  and colour shading shows the meridional perturbation wind velocity.

to the present investigation is that, *within the AZ, the SBFs remain approximately stationary throughout the day*. This behavior can be more clearly seen in Hovmöller diagrams (Figure 5.15). Figure 5.15a shows that at  $x = 50 \text{ km}$ , the SBFs move slowly inland during the morning, gradually decelerating and eventually stalling completely at around 1100 LST, approximately 10 km from the coast. They then remain stationary until  $\sim 1500 \text{ LST}$  after which they retreat slightly. Cross sections taken at this location (Figure 5.16) reveal that the SBCs remain limited in both horizontal and vertical extent and decay towards the end of the day. Farther downstream at  $x = 200 \text{ km}$ , the evolution is similar to that seen for the no-wind case in Figure 5.8a, with the SBFs accelerating inland with time and eventually colliding, in this case slightly north of the centre of the peninsula due to the aforementioned asymmetric propagation speeds (Figure 5.15b).

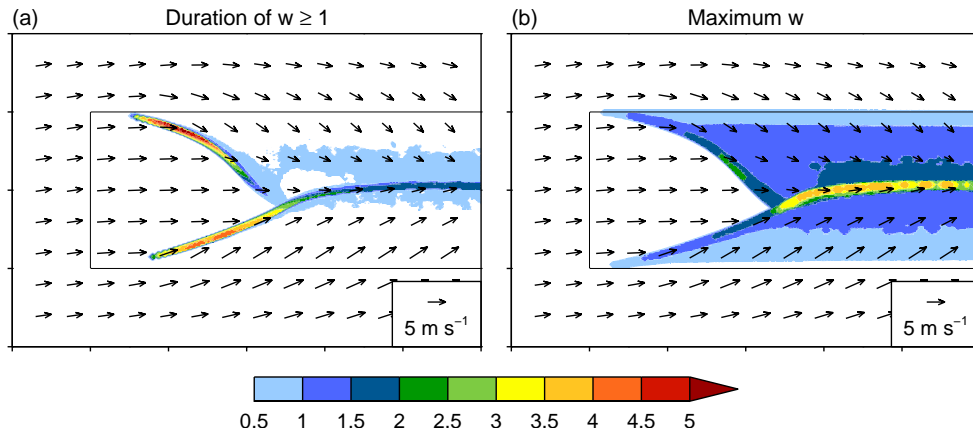


**Figure 5.17** Summary diagnostics for the westerly-flow case with  $U_g = 5 \text{ m s}^{-1}$  and  $H_{\text{max}} = 200 \text{ W m}^{-2}$ : (a) duration of time (hours) where the vertical velocity at 600 m exceeds  $1 \text{ m s}^{-1}$  within 5 km of each grid point; (b) maximum vertical velocity ( $\text{m s}^{-1}$ ) at 600 m within 5 km of each grid point. Vectors show the daytime-mean wind velocity at 50 m. Tick marks on the axes are shown every 50 km.

The inland distance (and thus time) at which the north- and south-coast SBFs become stationary increases with distance from the western edge of the peninsula. This can be seen in Figure 5.17a which shows the length of time for which the vertical velocity at 600 m exceeds  $1 \text{ m s}^{-1}$  within 5 km of each grid point. The stationary portions of the SBFs and the SBF collision zone are visible as contiguous bands where this diagnostic exceeds 1 h. Figure 5.17b meanwhile shows the maximum vertical velocity at 600 m, again within 5 km of a point. Note that the north-coast SBF is characterised by slightly stronger updraughts due to the aforementioned flow asymmetries. Maximum vertical velocities associated with the collision of the two sea breezes are 2–3 times stronger than those along the stationary segments. However, the latter are still around  $1\text{--}2 \text{ m s}^{-1}$  which we know from Chapter 4 is sufficient to trigger deep convection in the presence of a low LCL and weak inhibition. Updraughts of this intensity persist for up to 5 h along the north-coast SBF. Therefore, this setup—steady, along-peninsula flow in the presence of a positive land–sea temperature difference—may be highly favourable to the development of QSCSs.

It is apparent that my original hypothesis regarding quasi-stationary SBFs was incorrect; these features do not require even a weak offshore-directed ambient wind to form. Rather, they are inherent to the upstream portion of a finite-length coastline in the presence of along-shore flow. Upon further consideration, the explanation for their existence becomes quite obvious. The SBGs do in fact move inland along the entire length of the peninsula; however, as they do so, they are advected downstream by the ambient flow. Meanwhile, at the upstream edge of the peninsula, the sea breezes are continually reforming in response to the developing thermal pressure gradient. Within the AZ, the distance the SBGs are able to propagate inland increases with downstream distance, both due to the increasing strength of the onshore flow (associated with increasing  $\Delta T$ ) and the longer time  $\Delta t$  over which it has acted. Hence, in this region, the

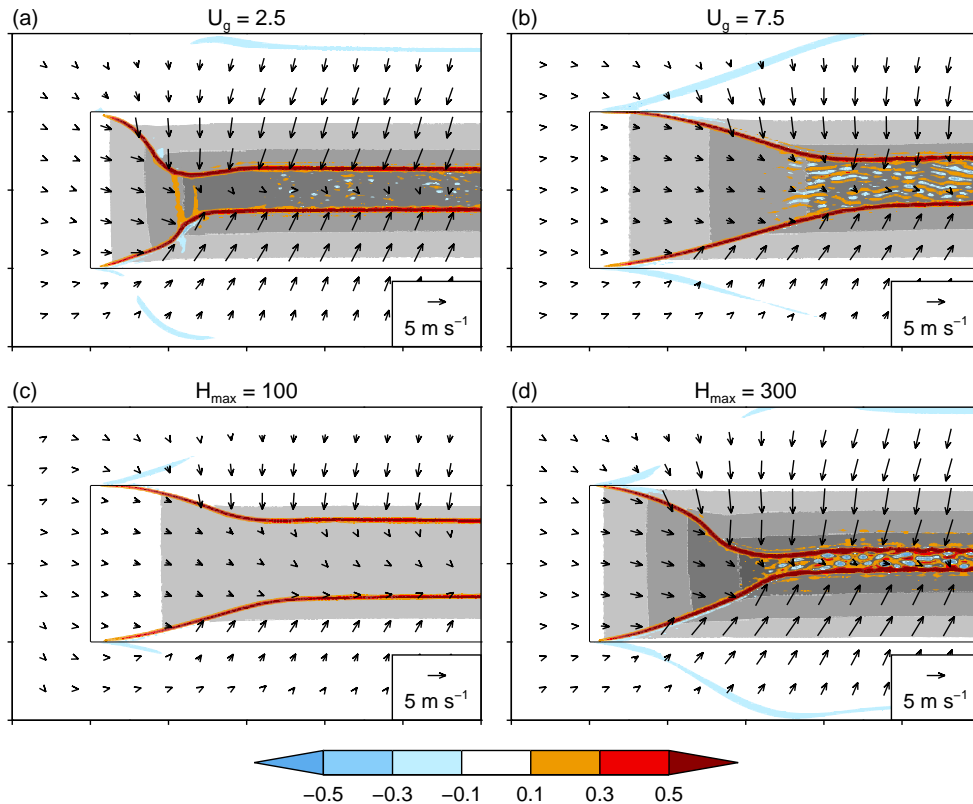


**Figure 5.18** As in Figure 5.14 but comparing along-peninsula-flow simulations with: (a) decreased wind speed ( $U_g = 2.5 \text{ m s}^{-1}$ ); (b) increased wind speed ( $U_g = 7.5 \text{ m s}^{-1}$ ); (c) decreased heat flux ( $H_{\text{max}} = 100 \text{ W m}^{-2}$ ); (d) increased heat flux ( $H_{\text{max}} = 300 \text{ W m}^{-2}$ ). In all cases, data is shown for 1500 LST.

SBFs are quasi-stationary and curve inland with increasing  $x$ , although, as previously discussed, the degree of curvature is modified by the rotation of the winds under the Coriolis force. Beyond the AZ, the onshore flow is approximately constant in  $x$  and has operated for the same length of time  $t - t_1$  so the SBFs are parallel to the coastlines and move inland at a rate which increases with time (due to increasing  $\Delta T$ ) as in the no-flow case. We will see later on that while an offshore-directed ambient wind component is not necessary for the formation of quasi-stationary SBFs, wind direction has a major influence on the location, persistence, and strength of these features.

### Sea breeze sensitivities

Let us now consider how the SBS evolution changes with the strength of the ambient wind and the amplitude of the diurnal cycle of surface heat flux. This is shown in Figure 5.18 which compares the SBS in four runs: two in which only  $U_g$  was changed and two in which only  $H_{\text{max}}$  was changed. Both quantities were increased and decreased by 50% of their original values.

The differences between these runs and the control simulation are highly consistent with the analysis above. Increasing the geostrophic wind speed acts to extend the AZ (since  $x^* = U(t - t_1)$ ), but has relatively little impact on the strength of the SBG and

thus the inland propagation of the SBFs beyond  $x^*$ . Increasing the surface heat flux does not change the horizontal extent of the AZ, but creates stronger onshore flow along the entire length of the peninsula, causing the SBFs to propagate inland more rapidly. This also enhances the vertical velocities at the SBFs (not shown). Both quantities strongly influence the shape of the quasi-stationary portions of the SBFs, with the curvature increasing with decreasing  $U_g$  and increasing  $H_{\max}$  due to an increase in the rate of change of  $\Delta T$  with  $x$ . Other more subtle changes may also be noted. For example, when  $U_g$  is increased to  $7.5 \text{ m s}^{-1}$ , the strength of the southerly wind component associated with frictional backing also increases, resulting in greater asymmetry between the north- and south-coast SBF propagation speeds. When  $U_g$  is decreased to  $2.5 \text{ m s}^{-1}$ , this effect is reduced, but a new asymmetry becomes apparent: a kink in the south-coast SBF around  $x = 50 \text{ km}$ . This is caused by the west-coast SBG which is stronger due to an enhanced west-to-east temperature gradient. The rate of Coriolis-induced veering as a function of  $x$  also increases with decreasing  $U_g$  because at a given distance downstream the flow has spent longer under the influence of the thermal PGF.

The sensitivity of the along-peninsula-flow case to latitude, mixed-layer depth, free-tropospheric stability, and land surface roughness was also explored. The effects of changing these parameters on  $y_{\text{sb}}$  and UMF were virtually identical to those for the no-flow case and therefore are not examined here. However, it is interesting to look at the updraught duration diagnostic (Figure 5.19). This shows that an increase in  $h_{\text{ml}}$  and a decrease in  $\gamma_{\text{ft}}$  both dramatically increase the length of time for which ‘strong’ updraughts are present along the quasi-stationary portions of the SBFs. This is not because the SBFs are stationary for a longer period; rather it simply indicates that the updraughts are stronger, as observed in the no-flow case (Section 5.4.1), and therefore exceed the arbitrary threshold of  $1 \text{ m s}^{-1}$  for a greater portion of the day. All other factors being equal, we might expect QSCSs to be more readily triggered (and potentially longer lived) in the presence of a deeper mixed layer or weaker static stability above the boundary layer. Figure 5.19 also shows that while  $\phi$  and  $z_0$  have little effect of the strength of the updraughts, they do influence the shape and length of the quasi-stationary portions of the SBFs via changes in the background and perturbation winds.

### 5.4.3 Sea breeze scaling

In this section, a method is developed for predicting the inland movement of the north- and south-coast SBFs in the no-wind and along-peninsula-flow cases. This makes use of scaling laws which relate the velocity of winds in the SBG to external parameters. Many of these are based on the work of Steyn (1998) who identified four nondimensional parameters which govern the behavior of sea breezes in the absence of large-scale flow. By apply regression analysis to observations of SBGs in the vicinity of Vancouver, Canada he obtained the following relation:

$$\frac{v_{\text{sb}}}{v_{\text{scale}}} = 1.10 \Pi_1^{-\frac{1}{2}} \Pi_4^{\frac{1}{4}} \quad (5.11)$$

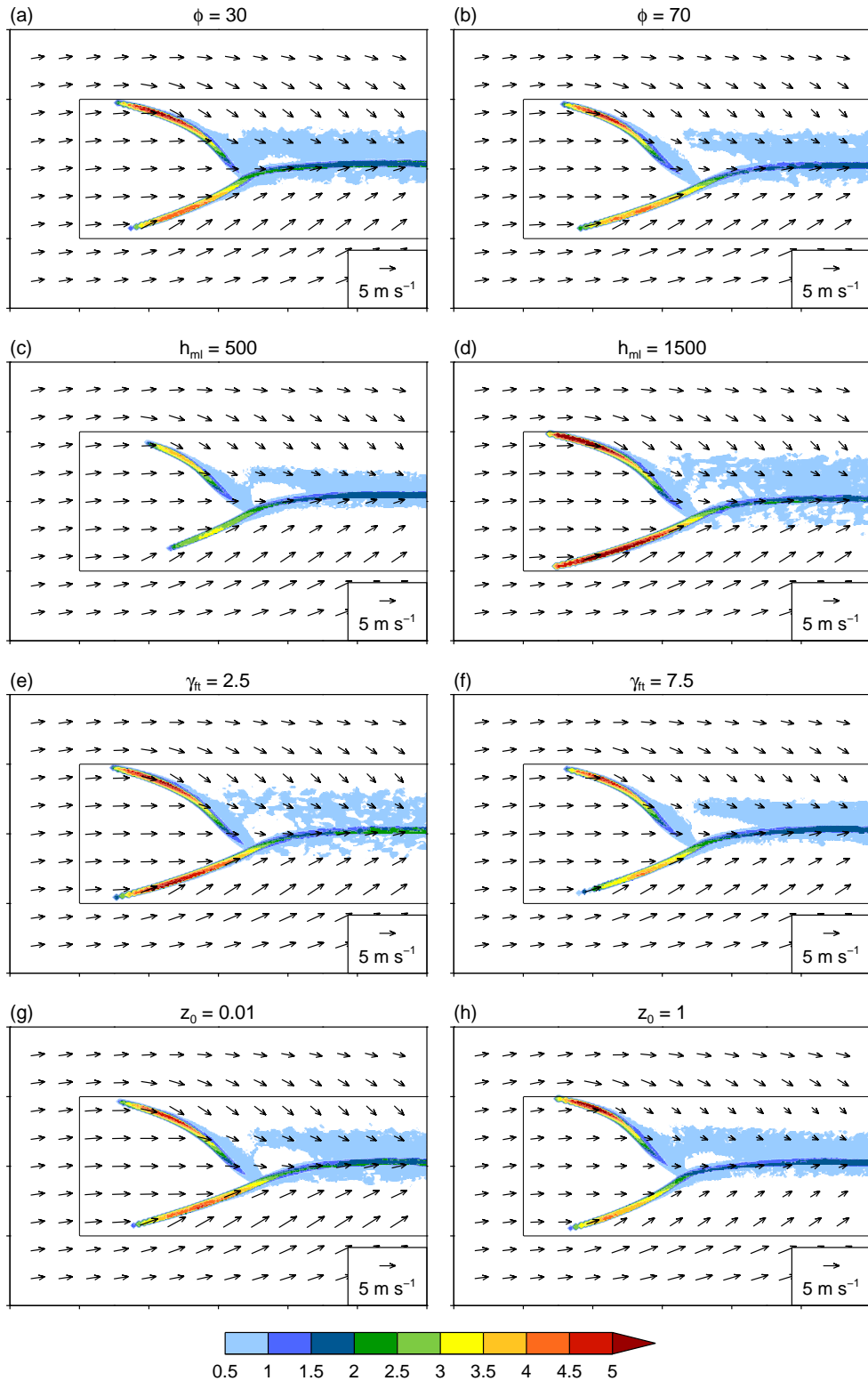


**Figure 5.19** As in Figure 5.17a but for each of the sensitivity runs.

Here,  $v_{sb}$  is the depth-averaged sea-breeze velocity measured close to the coastline,  $v_{scale} = \frac{g\Delta T}{T_0 N}$  is the sea breeze velocity scale (where  $\Delta T$  is the land–sea temperature difference,  $T_0$  is a reference temperature, and  $N$  is the Brunt–Väisälä frequency above the sea breeze layer),  $\Pi_1 = \frac{g\Delta T^2}{NT_0 F_H}$ ,  $\Pi_4 = \frac{N}{\Omega}$ , and  $F_H = (\overline{w'T'})_{sfc}$  is the surface-

layer kinematic sensible heat flux. The other symbols have their usual meanings. Using additional observations from eastern Spain and The Netherlands, Steyn (2003) modified this to

$$\frac{v_{\text{sb}}}{v_{\text{scale}}} = 0.85 \Pi_1^{-\frac{1}{2}} \Pi_2^{-\frac{9}{4}} \Pi_4^{\frac{1}{2}} \quad (5.12)$$

where  $\Pi_2 = \frac{f}{\Omega}$ . In this case,  $F_H$  is replaced with  $\overline{F}_H$ , the time-averaged surface-layer kinematic sensible heat flux

$$\overline{F}_H = \frac{1}{t - t_1} \int_{t_1}^t (\overline{w'T'})_{\text{sfc}} dt \quad (5.13)$$

which gives a better measure of the forcing for the sea breeze (Tijm 1999). Note that an additional nondimensional parameter  $\Pi_3 = \frac{T_0 F_M N}{g \overline{F}_H}$  (where  $F_M$  is the surface-layer kinematic momentum flux) was neglected from both of these analyses because it is related to  $\Pi_1$  via Monin–Obukov scaling (Steyn 1998).

Rearranging Equations 5.11 and 5.12 we obtain expressions for the sea breeze velocity in terms of the external parameters:

$$v_{\text{sb}} = 1.10 (N\Omega)^{-\frac{1}{4}} \left( \frac{g F_H}{T_0} \right)^{\frac{1}{2}} \quad (5.14)$$

$$v_{\text{sb}} = 0.85 (2 \sin \phi)^{-\frac{9}{4}} \left( \frac{g \overline{F}_H}{T_0 \Omega} \right)^{\frac{1}{2}} \quad (5.15)$$

Tijm (1999) modified the first of these and applied it to sea breezes simulated with a 2-D hydrostatic model to obtain a new relation which incorporates latitude dependence:

$$v_{\text{sb}} = 1.7 (1 - 0.5 \cos^3 \phi) (NL)^{-\frac{1}{4}} \left( \frac{g \hat{F}_{\Delta H}}{T_0} \right)^{\frac{1}{2}} \quad (5.16)$$

Here,  $\hat{F}_{\Delta H} = \int_{t_1}^{t_2} \Delta (\overline{w'T'})_{\text{sfc}} dt$  is the differential (land minus sea) surface heat flux integrated over the full period of heating  $L = t_2 - t_1$ . More recently, Porson *et al.* (2007b) derived an alternative version of the Steyn (2003) scaling valid at 50° latitude based on non-hydrostatic 2-D simulations:

$$v_{\text{sb}} = 0.687 (N^2 \Omega)^{-\frac{1}{3}} \left( \frac{g \overline{F}_H}{T_0} \right)^{\frac{1}{2}} \quad (5.17)$$

All four of these expressions show that the sea-breeze velocity depends strongly on the surface heat flux, albeit measured in different ways. Equations 5.14, 5.16, and 5.17 additionally suggest a weak inverse dependence on stability; however, Porson *et al.* (2007b) demonstrate that this can safely be ignored. Those studies in which latitude was also varied agree that it has an effect on the sea-breeze velocity but disagree on the strength of the dependence. For example, increasing  $\phi$  from 30 to 70° reduces  $v_{\text{sb}}$  by a factor of 1.3 with Equation 5.16 but by a factor of 3.5 with Equation 5.15.

Wichink Kruit *et al.* (2004) argue that measurements at a particular location are more likely to be influenced by differences in local topography than latitude, making the role of the latter difficult to assess based on observations. Thus, we might have more confidence in Tijm's model-based scaling (Equation 5.16), although his use of a 2-D hydrostatic configuration with relatively coarse horizontal grid spacing (5 km) may be a source of error.

Based on this previous work, a new scaling was developed which can be applied to sea breezes in conditions of no background flow and flow along a peninsula. The effects of stability and latitude were neglected, so that the only external parameter is the heat flux. I have used the instantaneous time-integrated kinematic heat flux  $\hat{F}_H = \hat{H}/\rho c_p$  as this is more obviously related to the instantaneous sea-breeze velocity than a day-total or time-averaged value. The scaling is then

$$v_{sb} = \alpha v_s \quad (5.18)$$

where  $v_s = \left(g\hat{F}_H/T_0\right)^{\frac{1}{2}}$  is the new scaling velocity and  $\alpha$  is a constant to be determined experimentally. Given a sample of  $v_{sb}$  and  $v_s$  values,  $\alpha$  can be computed using least-squares linear regression as

$$\alpha = \frac{\sum v_s v_{sb}}{\sum v_s^2} \quad (5.19)$$

This calculation was performed using hourly data from 0900–1800 LST (excluding values after the collision of the north- and south-coast SBFs) for the no-flow runs with  $H_{\max} = 100, 200, \text{ and } 300 \text{ W m}^{-2}$ . The reference temperature  $T_0$  was set as the initial surface temperature (288.15 K) and  $\hat{F}_H$  was derived numerically using a time step of 60 s with  $\rho = 1.2 \text{ kg m}^{-3}$ . The sea breeze velocity  $v_{sb}$  was computed by first vertically averaging the meridional perturbation wind velocity  $v'$  (equal to the full meridional velocity  $v$  in the no-flow case) up to the height at which it changed sign (the SBG depth  $z_{sb}$ ). This was done at all grid points where a sign change occurred and  $|v'|$  exceeded  $1 \text{ m s}^{-1}$  both above and below  $z_{sb}$  (i.e. where there was a clear SBG and RC). The resulting set of values were then averaged in  $y$  from 10 km offshore to the position of the SBF (determined as in Section 5.4.1).

As shown in Figure 5.20a,  $v_s$  and  $v_{sb}$  are strongly correlated with  $\alpha = 0.340$  and a Pearson correlation coefficient of 0.99. Looking in more detail, it can be seen that the rate of increase of  $v_{sb}$  with  $v_s$  decreases slightly over time (particularly during the late afternoon) causing the points to drift from the left to the right side of the 1:1 line. This apparent slowing of the sea breeze is in fact a manifestation of its rotation under the influence of the Coriolis force, which transfers cross-shore momentum into the along-shore direction. In a simulation with  $\phi = 0^\circ$ , the rotation does not occur and hence  $v_{sb}/\alpha v_s$  remains almost constant in time (star symbols in Figure 5.20a). Note that a more dramatic decrease in  $v_{sb}$  occurs after the SBFs collide due to the associated sudden decrease of  $\Delta T$ .

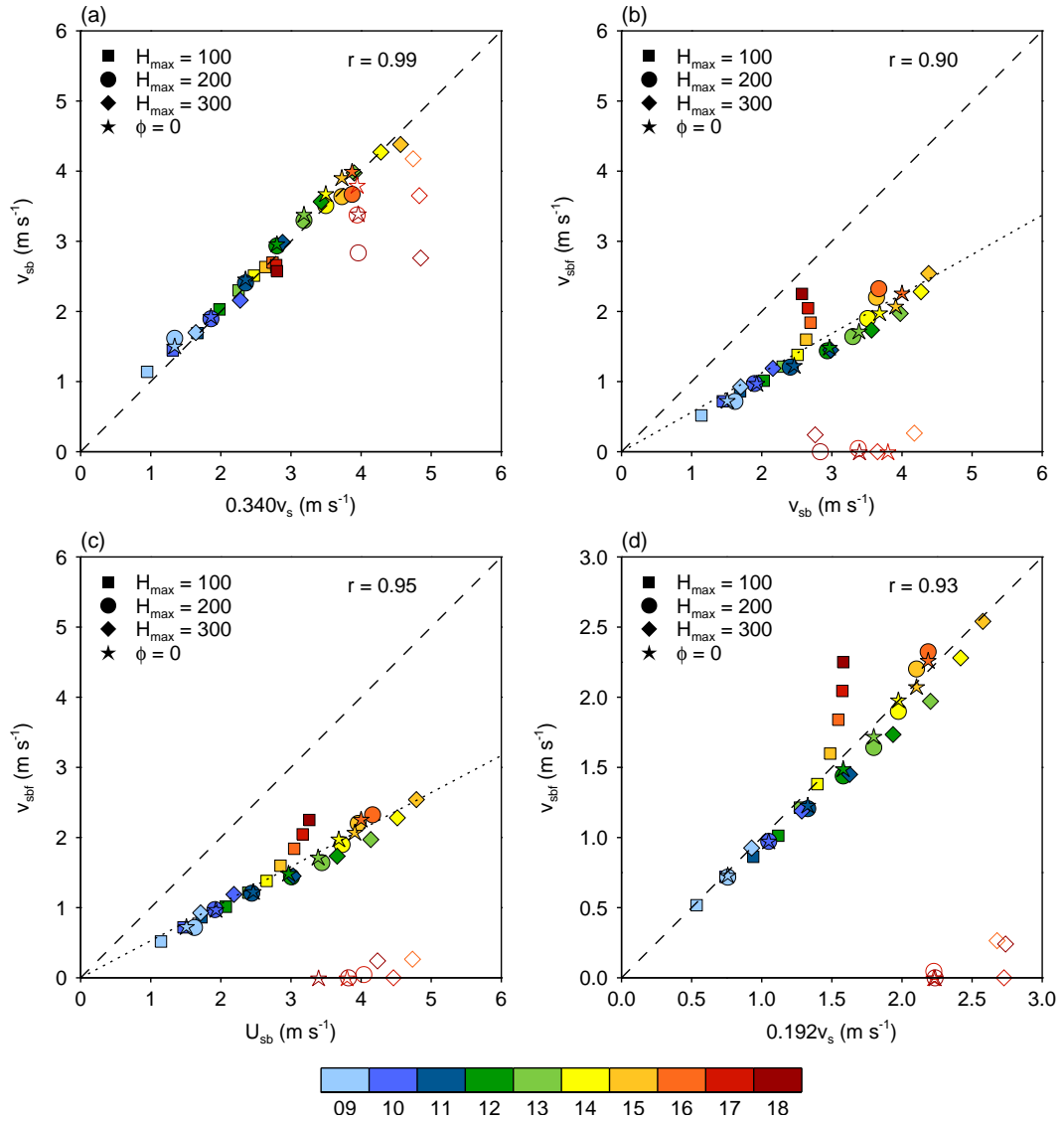


**Figure 5.20** Scatter plots showing the relationship between (a) the sea breeze velocity scale  $v_s$  (multiplied by  $\alpha = 0.340$ ) and the depth-averaged cross-shore sea-breeze velocity  $v_{sb}$ , (b)  $v_{sb}$  and the simulated SBF velocity  $v_{sbf}$ , (c) the depth-averaged total sea-breeze velocity  $U_{sb}$  and  $v_{sbf}$ , and (d)  $v_s$  (multiplied by  $\alpha = 0.192$ ) and  $v_{sbf}$ . Data are shown for the north-coast sea breezes at  $x = 200$  in the no-flow cases with  $H_{\max} = 100 \text{ W m}^{-2}$  (squares),  $H_{\max} = 200 \text{ W m}^{-2}$  (circles),  $H_{\max} = 300 \text{ W m}^{-2}$  (diamonds), and  $\phi = 0^\circ$  (stars). Filled and unfilled symbols show data before and after the SBF collision respectively and colours indicate the time (LST). The dashed lines show a 1:1 relationship and the dotted lines in (b) and (c) shows  $v_{sbf} = 0.562v_{sb}$  and  $v_{sbf} = 0.528U_{sb}$  respectively. Pearson's correlation coefficients  $r$  are given in each panel. Note that the  $\phi = 0^\circ$  run and all values after the SBF collision weren't included in the calculations of  $\alpha$  and  $r$ .

This analysis was also performed for the other eight sensitivity runs presented in Section 5.4.1. The results (not shown) indicate that  $\alpha$  is largely insensitive to latitude, mixed-layer depth, free-tropospheric stability, and land surface roughness, with values ranging from 0.319 (for  $z_0 = 1 \text{ m}$ ) to 0.357 (for  $\phi = 0^\circ$ ).

In order to predict the inland movement of the SBFs, we next need to relate  $v_{sb}$  to the velocity of the front itself  $v_{sbf}$ . Figure 5.20b shows that, at least initially, the SBF

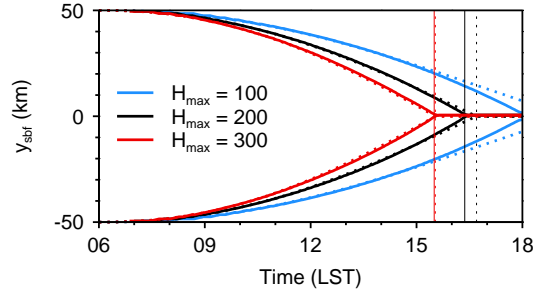


**Figure 5.21** Time series of SBF position  $y_{\text{sbf}}$  at  $x = 200$  km for the no-flow cases with  $H_{\text{max}} = 100 \text{ W m}^{-2}$  (blue),  $H_{\text{max}} = 200 \text{ W m}^{-2}$  (black), and  $H_{\text{max}} = 300 \text{ W m}^{-2}$  (red). Thick solid and dotted lines respectively show the true and scaling-predicted values. Thin vertical lines indicate the time of collision.

moves at approximately half the speed of the depth-averaged flow behind it. However, after around 1400 LST, the rate of change of  $v_{\text{sbf}}$  with  $v_{\text{sb}}$  begins to increase, causing points to drift above the regression line. This is most pronounced in the low heat flux simulation ( $H_{\text{max}} = 100 \text{ W m}^{-2}$ ), where by 1800 LST  $v_{\text{sbf}}$  and  $v_{\text{sb}}$  are almost equal. The drift is reduced and the correlation increased if we plot  $v_{\text{sbf}}$  against the total sea breeze velocity  $U_{\text{sb}} = (u_{\text{sb}}^2 + v_{\text{sb}}^2)^{\frac{1}{2}}$  (Figure 5.20c), indicating that the propagation of the SBF is not significantly affected by the rotation of the perturbation winds. However, some drift remains and becomes more pronounced when we plot the scaling velocity against  $v_{\text{sbf}}$  (Figure 5.20d). Essentially, the SBF is accelerating more rapidly than the increase in  $\hat{H}$  would suggest. It is plausible that this is the same acceleration seen in previous sea breeze studies, which is believed to be associated with the decay of turbulence (Section 5.2.1); however, further analysis is needed to confirm this.

The key result at this stage is that the scaling velocity defined above can provide an accurate estimate of the SBF propagation speed. Specifically, through regression we find that  $v_{\text{sbf}} \approx 0.192v_{\text{s}}$ . By integrating this equation, we can estimate the location of the front  $y_{\text{sbf}}$  as a function of time. This was done for the no-flow simulations with  $H_{\text{max}} = 100, 200, \text{ and } 300 \text{ W m}^{-2}$ ; the results are compared with the true SBF positions in Figure 5.21. The scaling is practically perfect for  $H_{\text{max}} = 300 \text{ W m}^{-2}$ , but its accuracy deteriorates as the maximum heat flux decreases due to the aforementioned acceleration of the SBFs.

The next step is to apply the scaling to the case of along-peninsula flow. As discussed above, in this situation, the integrated heat flux  $\hat{H}$  becomes a function of both time  $t$  and downstream distance  $x = U\Delta t$ . The along-stream velocity  $U$  should be representative of the mean flow over the layer in which heating is applied, i.e. the convective boundary layer. For simplicity, a relation of the form  $U = \beta U_{\text{g}}$  is assumed, where  $\beta$  is constant coefficient whose value is discussed below. For every  $x$  and  $t$ , the sea breeze front velocity is then estimated as

$$v_{\text{sbf}} = \alpha \left( \frac{g\hat{H}}{\rho c_{\text{pd}} T_0} \right)^{\frac{1}{2}} \quad (5.20)$$

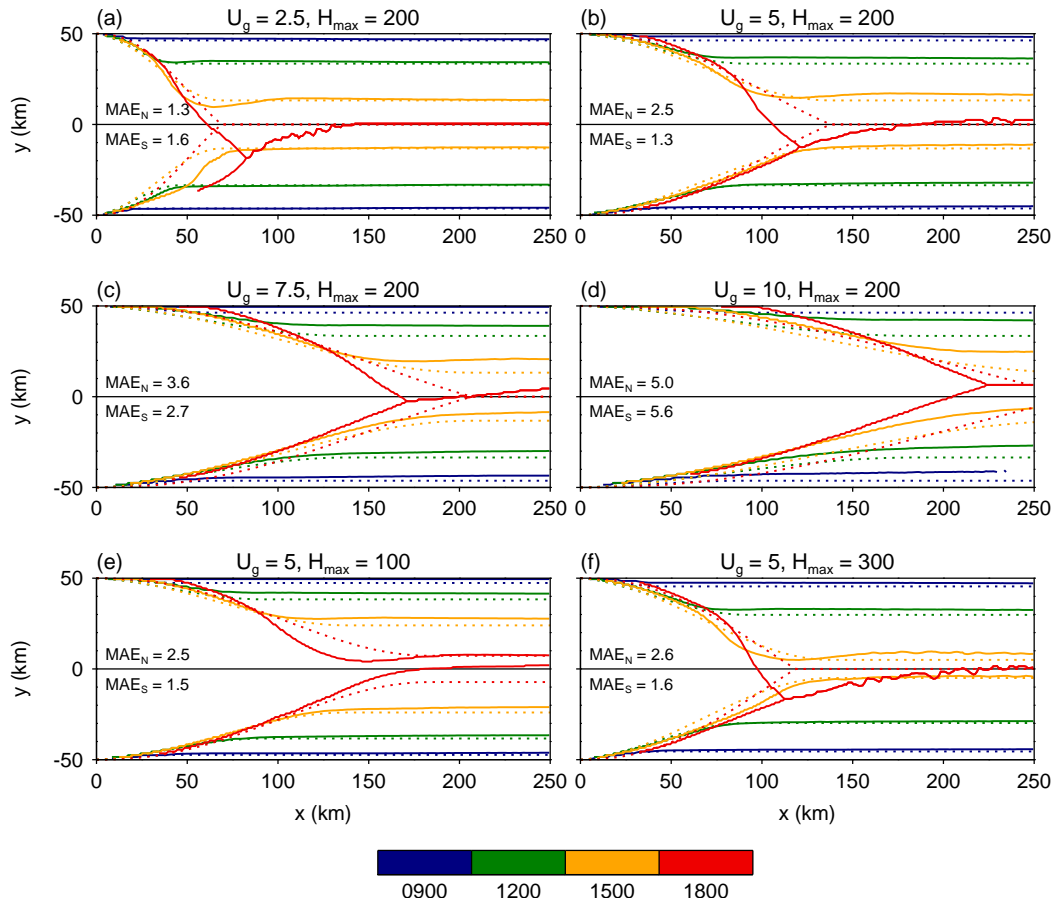


**Figure 5.22** Simulated (solid) and scaling-derived (dashed) SBF positions  $y_{\text{sbf}}$  as a function of time (colours; LST) for along-peninsula-flow runs with: (a)  $U_g = 2.5 \text{ m s}^{-1}$  and  $H_{\text{max}} = 200 \text{ W m}^{-2}$ ; (b)  $U_g = 5 \text{ m s}^{-1}$  and  $H_{\text{max}} = 200 \text{ W m}^{-2}$ ; (c)  $U_g = 7.5 \text{ m s}^{-1}$  and  $H_{\text{max}} = 200 \text{ W m}^{-2}$ ; (d)  $U_g = 10 \text{ m s}^{-1}$  and  $H_{\text{max}} = 200 \text{ W m}^{-2}$ ; (e)  $U_g = 5 \text{ m s}^{-1}$  and  $H_{\text{max}} = 100 \text{ W m}^{-2}$ ; (f)  $U_g = 5 \text{ m s}^{-1}$  and  $H_{\text{max}} = 300 \text{ W m}^{-2}$ . Mean absolute error (MAE) values in km for the north- and south-coast SBFs are given in each panel.

where  $\alpha = 0.192$  and  $\rho$  is set as  $1.2 \text{ kg m}^{-3}$ . The SBF location at a particular time and downstream location is then obtained by integrating along the west-to-east trajectory defined by the background flow:

$$y_{\text{sbf}}(x, t) = y_{\text{sbf}}(x - \delta x, t - \delta t) + \frac{\delta t}{2} [v_{\text{sbf}}(x - \delta x, t - \delta t) + v_{\text{sbf}}(x, t)] \quad (5.21)$$

where  $\delta t = 60 \text{ s}$  is the time interval,  $\delta x = U \delta t$  is the space interval, and  $y_{\text{sbf}} = 0$  for  $x = 0$  or  $t \leq t_1$ .

This calculation was performed for six different runs. The value of  $\beta$  was selected to minimise the total mean absolute error (MAE) in  $y_{\text{sbf}}$  across all runs. The resulting SBF positions are compared with the true positions for four times—0900, 1200, 1500, and 1800 LST—in Figure 5.22. It is instantly apparent that the scaling does a remarkable job of predicting the structure and evolution of the SBFs. MAEs range from 1.3–5.6 km, while instantaneous errors are generally less than 10 km. Since the scaling-derived SBFs

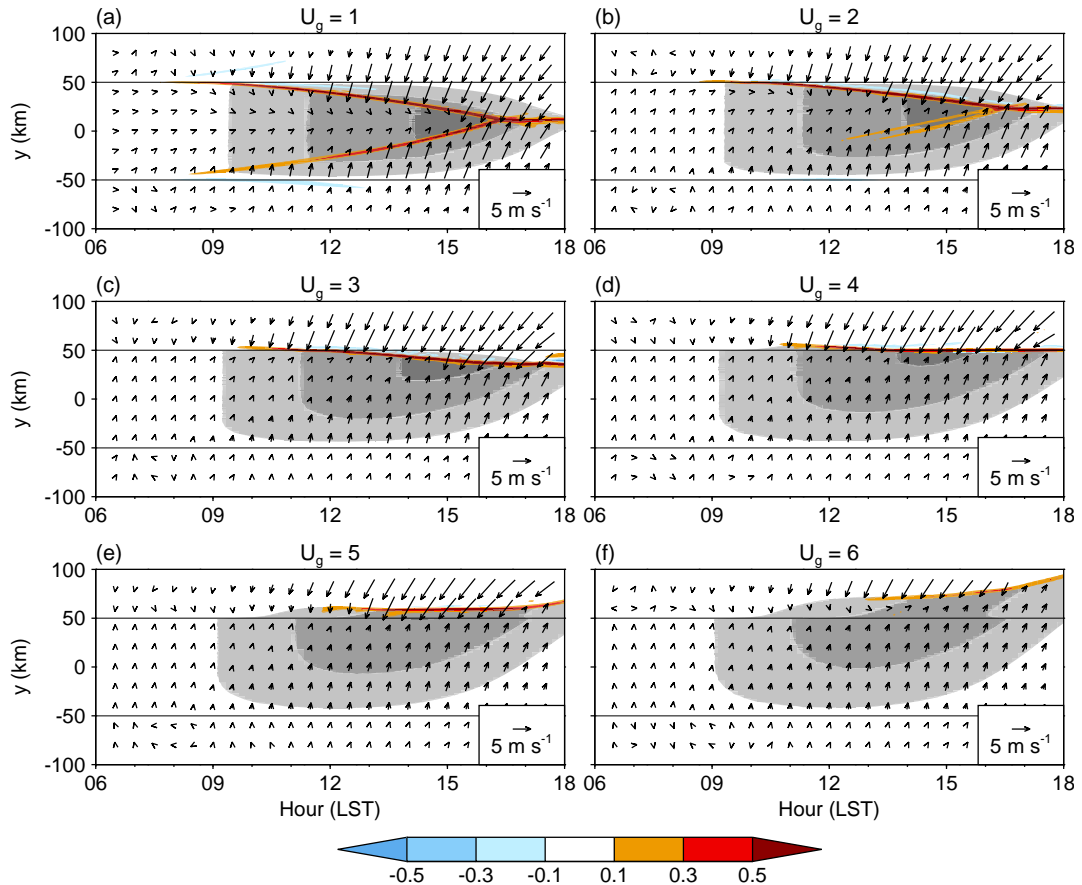


**Figure 5.23** As in Figure 5.15 but for southerly-flow cases with (a)  $U_g = 1 \text{ m s}^{-1}$ , (b)  $U_g = 2 \text{ m s}^{-1}$ , (c)  $U_g = 3 \text{ m s}^{-1}$ , (d)  $U_g = 4 \text{ m s}^{-1}$ , (e)  $U_g = 5 \text{ m s}^{-1}$ , and (f)  $U_g = 6 \text{ m s}^{-1}$ . Values are shown at  $x = 200 \text{ km}$ .

for the north and south coasts are just mirror images of each other, errors are largest where significant asymmetries exist (e.g. at 1800 LST for  $x \approx 80\text{--}150 \text{ km}$  in Figure 5.22b). This partly explains the increase in MAE with increasing  $U_g$ . Another source of error is the assumption of a linear relationship between  $U$  and  $U_g$ . The optimum value of the coefficient  $\beta$  actually decreases with increasing  $U_g$  and increasing  $H_{\max}$ , presumably due to the associated increase in surface drag. Hence, a more sophisticated measure of  $U$  might improve the results.

#### 5.4.4 Cross-peninsula flow

In this section, we will briefly examine the more commonly studied situation of a pure cross-shore geostrophic ambient wind. The flow direction considered herein is southerly ( $\psi_g = 90^\circ$ ). Away from the west coast of the peninsula, the behavior of the sea breeze is virtually identical for northerly flow (not shown). First, let us consider the sensitivity to wind speed. Values of  $U_g$  ranging from 1 to  $6 \text{ m s}^{-1}$  in  $1 \text{ m s}^{-1}$  intervals have been tested. The results are summarised with Hovmöller diagrams in Figure 5.23 and time series of  $w_{\max}$  and UMF in Figure 5.24.

The behavior of the north and south coast sea breezes agrees well with previous

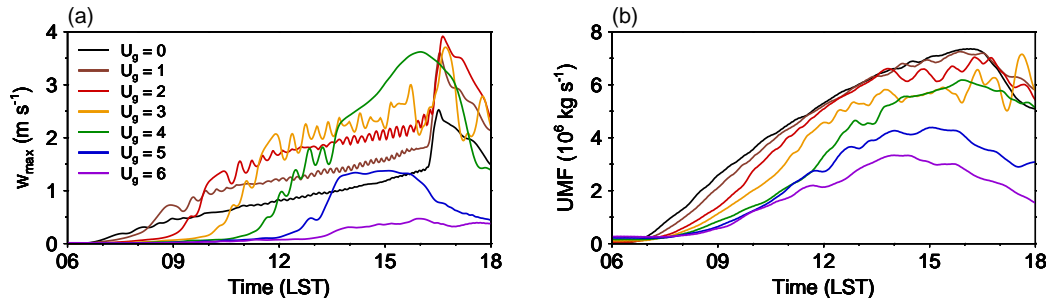


**Figure 5.24** Time series of (a) maximum vertical velocity  $w_{\max}$  and (b) area-integrated updraught mass flux (UMF) at  $x = 200$  km for the no-flow case (black lines) and southerly-flow cases with  $U_g = 1\text{--}6$   $\text{m s}^{-1}$  (coloured lines). The data have a time resolution of 1 min but have been smoothed using a 15 min moving average. The oscillations in  $w_{\max}$  (which are significantly larger in amplitude without the smoothing) appear to be a consequence of representing the continuous movement of the SBF on a discontinuous model grid; the period of each half wave corresponds to the time over which the SBF moves one grid point.

findings for offshore and onshore flow respectively. As  $U_g$  increases, the meridional temperature gradient at the south coast decreases while that at the north coast increases. Consequently, the south-coast SBC weakens and north-coast SBC intensifies. The south-coast SBF becomes very weak once  $U_g = 2$   $\text{m s}^{-1}$  and is completely absent from the Hovmöller plots for  $U_g \geq 3$   $\text{m s}^{-1}$ , although the SBF collision signature is still visible in Figure 5.24a for  $U_g = 3$   $\text{m s}^{-1}$ . Meanwhile, the development and inland propagation of the north-coast SBF is retarded, and the front itself becomes narrower with stronger convergence and ascent. This trend continues up to  $U_g = 4$   $\text{m s}^{-1}$ , at which point the front remains stationary along the coastline for the entire afternoon. The meridional temperature gradient at the north coast is maximised in this case resulting in the strongest perturbation flow, with speeds up to  $9$   $\text{m s}^{-1}$ . Further strengthening of the ambient wind causes the SBF to remain offshore all day, with a dramatic reduction in  $w_{\max}$ . When  $U_g = 5$   $\text{m s}^{-1}$ , the SBF is still stationary for much of the afternoon; however, with  $U_g = 6$   $\text{m s}^{-1}$  it begins to propagate away from the coastline. It is interesting to note that the largest  $w_{\max}$  occurs for  $U_g = 2$   $\text{m s}^{-1}$  and is associated with the SBF collision, although similar values occur at the stationary north-coast SBF for  $U_g = 4$   $\text{m s}^{-1}$ . On the other hand, UMF tends to decrease with increasing  $U_g$ , suggesting that changes in updraught strength are more than compensated for by changes in updraught area.

Recall from Section 5.2.2 that we can define a critical cross-shore ambient wind speed  $U_{\text{crit}}$  above which the sea breeze is unable to propagate inland. In the simulations presented above, this is approximately  $4$   $\text{m s}^{-1}$  which falls at the lower end of the range suggested by previous studies (Crosman and Horel 2010). However,  $U_{\text{crit}}$  is not a constant but a function of the integrated heat flux (Porson *et al.* 2007a). In the present case, this indicates a dependence on both the maximum heat flux  $H_{\max}$  and the peninsula width  $W$ . The latter sets the integration time  $\Delta t = W/U$  where  $U$  is the cross-shore wind speed. These dependencies are illustrated in Figure 5.25. For  $H_{\max} = 100$   $\text{W m}^{-2}$ ,  $U_g = 4$   $\text{m s}^{-1}$  becomes supercritical and the SBF remains offshore, while for  $H_{\max} = 300$   $\text{W m}^{-2}$ ,  $U_g = 4$   $\text{m s}^{-1}$  is subcritical and the SBF is able to propagate

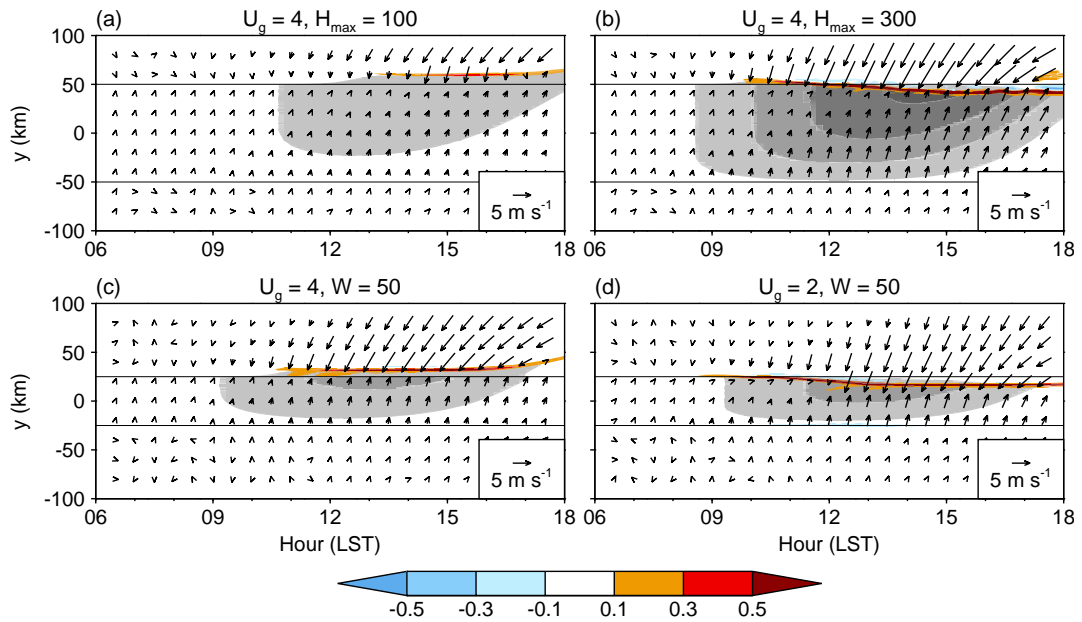


**Figure 5.25** As in Figure 5.15b but for southerly-flow cases with (a)  $U_g = 4 \text{ m s}^{-1}$  and  $H_{\max} = 100 \text{ W m}^{-2}$ , (b)  $U_g = 4 \text{ m s}^{-1}$   $H_{\max} = 300 \text{ W m}^{-2}$ , (c)  $U_g = 4 \text{ m s}^{-1}$  and  $W = 50 \text{ km}$ , and (d)  $U_g = 2 \text{ m s}^{-1}$  and  $W = 50 \text{ km}$ .

a short distance inland. Halving the peninsula width to 50 km again makes  $U_g = 4 \text{ m s}^{-1}$  supercritical. If we also halve  $U_g$  to  $2 \text{ m s}^{-1}$ , we approximately return  $\Delta t$  (and thus  $\hat{H}$ ) to its original value; however, we do not regain the critical configuration of an SBF stationary at the coastline. In fact, comparison of Figures 5.25c and d suggests that with  $W = 50 \text{ km}$ ,  $U_{\text{crit}} \approx 3 \text{ m s}^{-1}$ . This illustrates the highly nonlinear nature of the sea breeze in the presence of an opposing ambient wind and indicates that a simple relationship of the form  $U_{\text{crit}} \propto \hat{H}^{\frac{1}{2}}$  as proposed by Porson *et al.* (2007a) may be inappropriate for a peninsula.

The sensitivity of the cross-peninsula-flow case (with  $U_g = 4 \text{ m s}^{-1}$ ) to  $\phi$ ,  $h_{\text{ml}}$ ,  $\gamma_{\text{ft}}$ , and  $z_0$  was also examined. Results are not shown here as they are highly consistent with those for the no-flow case (Section 5.4.1). A key point to note is that in all cases, the north-coast SBF was stationary and within a kilometre or two of its location in the standard run.

#### 5.4.5 Other wind directions

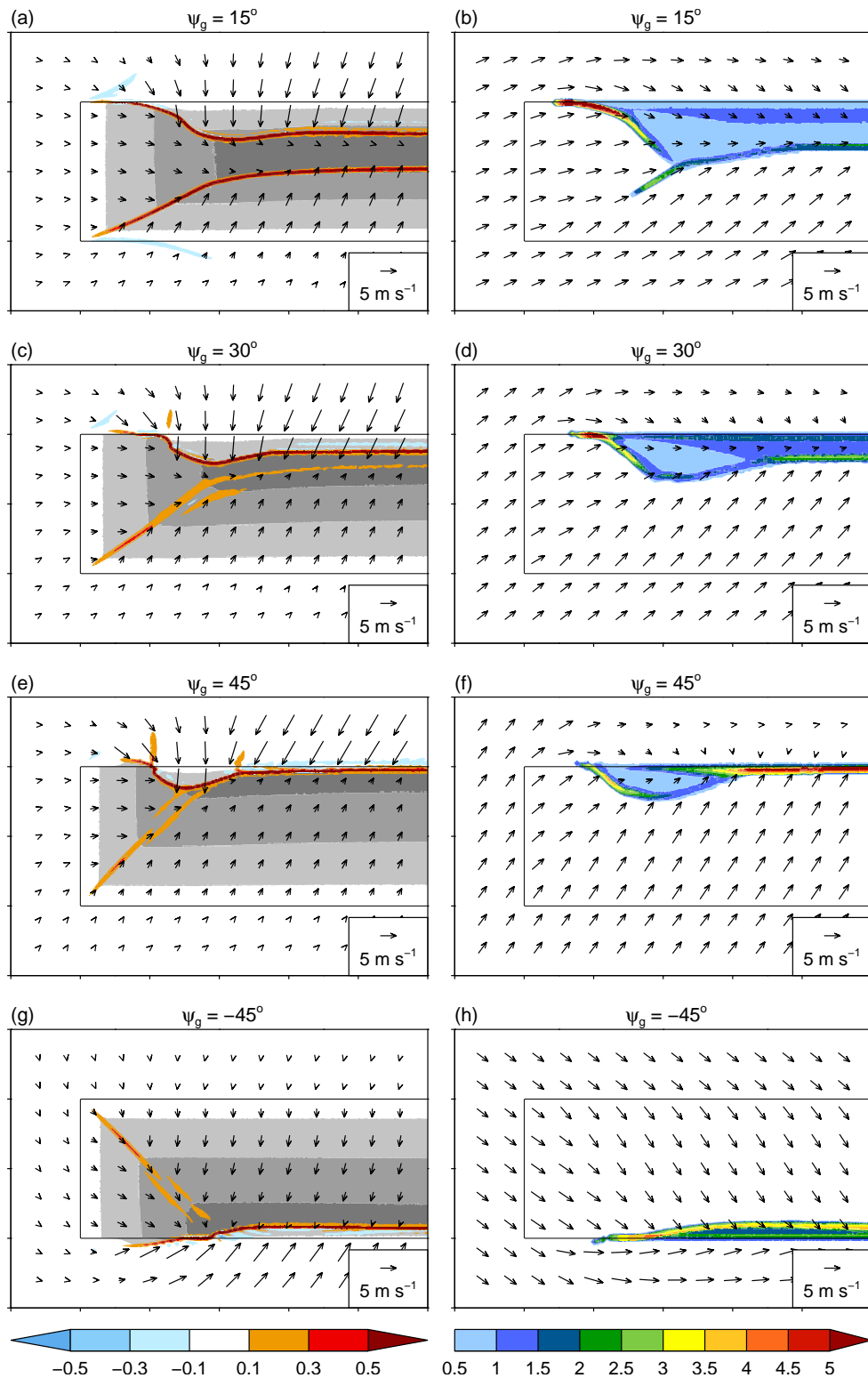
Let us now briefly consider the behavior of the SBS when the geostrophic flow is at an angle to all of the peninsula coastlines. The changes that occur as the wind direction veers from westerly to southwesterly in  $15^\circ$  increments are illustrated in Figure 5.26. As we would expect, strengthening southerly flow causes the south-coast SBF to weaken and move inland more rapidly while the north-coast SBF intensifies and is retarded. The quasi-stationary portion of the SBF on the north coast diminishes in size as the wind veers, and is completely absent when  $\psi_g = 45^\circ$  (Figure 5.26f). In this case, the SBF bulges southward between  $x = 50$  and  $150 \text{ km}$  due to veering of the perturbation flow

from northwesterly to northerly (c.f. the southward surge of the north-coast SBF in the westerly-flow case). Farther west, the SBF remains quasi-stationary along the coastline due to cancellation of the cross-shore component of the perturbation and background flows. It is interesting to note that when the geostrophic flow is from the northwest ( $\psi_g = -45^\circ$ ) the south-coast SBF does not evolve in the same way; rather it propagates a short distance inland and then becomes stationary. This asymmetry is associated with frictional backing which gives a stronger meridional background wind component that more exactly balances the perturbation flow in the southwesterly-flow case. Another feature to note when  $\psi_g = \pm 45^\circ$  is a stationary line of weak ascent extending from the upstream corner of the peninsula associated with convergence between the north-/south- and west-coast SBFs (Figure 5.26e,g).

#### 5.4.6 The role of coastline geometry

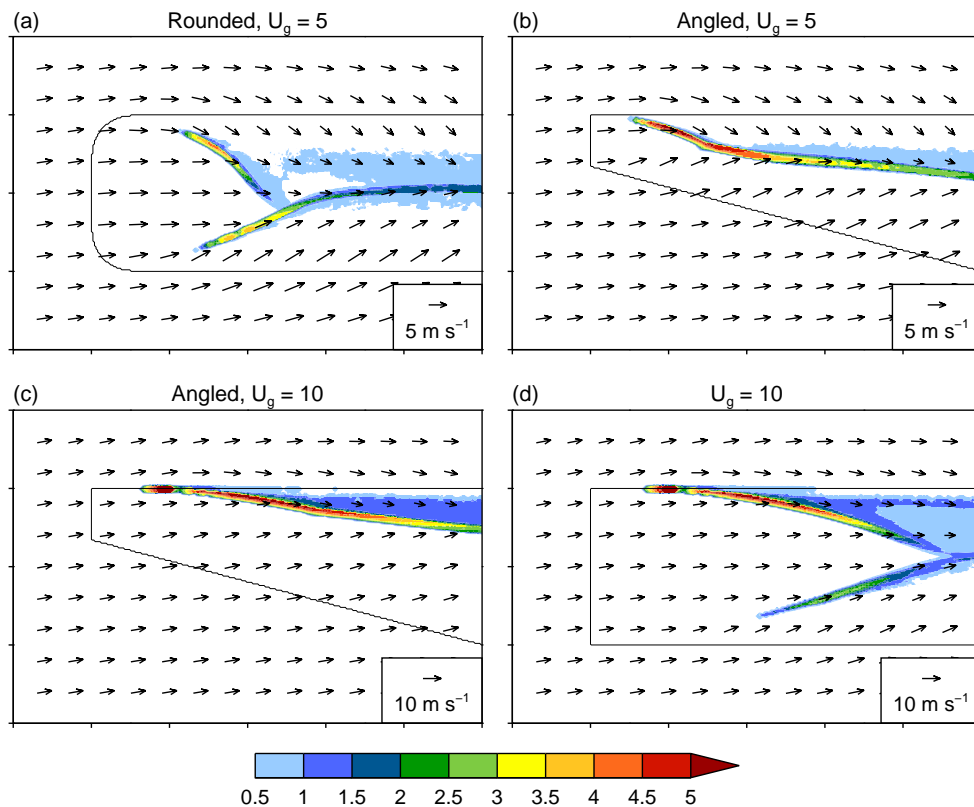
The simulations presented so far have all been performed with a highly idealised coastline geometry. In this section, we will briefly consider how the evolution of the SBS in the along-peninsula-flow case is altered by the use of a slightly more realistic land-mass. Two changes are examined: (1) rounding the corners at the upstream edge of the peninsula, and (2) making the south coast angled with respect to the north coast (i.e. having a peninsula which narrows towards its tip). Simulations with these set-ups will respectively be referred to as ‘rounded’ and ‘angled’ runs. For the former, a circle of radius 25 km was used to define the corners, while in the latter the peninsula was specified to widen from 33 km to the original 100 km between  $x = 0$  and  $x = 250$  km (giving an angle of  $15^\circ$  between the north and south coasts).

Figure 5.27 summarises the results from a rounded run (with  $U_g = 5 \text{ m s}^{-1}$ ) and two angled runs (with  $U_g = 5$  and  $10 \text{ m s}^{-1}$ ). Also included for comparison is a run with the standard peninsula and  $U_g = 10 \text{ m s}^{-1}$ . Comparison of Figure 5.27a with Figure 5.17a shows that rounding the corners reduces convergence along the SBFs at the upstream edge of the peninsula, making the quasi-stationary regions of strong vertical velocity shorter with lower maxima. It thus appears that a less angular coastline may be less favourable for very long-lived QSCSs. Farther downstream, the behavior is unchanged from the control case (Figure 5.17a). In the angled runs, a westerly geostrophic flow is no longer parallel to the south coast: there is an onshore flow component which is enhanced by frictional backing in the boundary layer. Consequently, the south-coast SBF is weaker and more rapidly propagates inland. Furthermore, the distance the north-coast SBF is able to propagate inland before colliding with the south-coast SBF becomes a function of downstream distance. If the wind speed is increased to  $10 \text{ m s}^{-1}$  (Figure 5.27c) these effects are enhanced and the region of persistent strong ascent remains close to the north coast. This final configuration is somewhat reminiscent of the Boscastle and 21 July 2010 QSCS events suggesting that the tapered nature of the UK Southwest Peninsula may have played a role in the organisation of these events. However, in those cases, curvature in the wind field (with rotation of the flow from purely along-shore



**Figure 5.26** (Right column) As in Figure 5.14 but for simulations with  $U_g = 5 \text{ m s}^{-1}$  and (a)  $\psi_g = 15^\circ$ , (c)  $\psi_g = 30^\circ$ , (e)  $\psi_g = 45^\circ$ , and (g)  $\psi_g = -45^\circ$  at 1500 LST. (Left column) As in Figure 5.17a but for simulations with  $U_g = 5 \text{ m s}^{-1}$  and (b)  $\psi_g = 15^\circ$ , (d)  $\psi_g = 30^\circ$ , (f)  $\psi_g = 45^\circ$ , and (h)  $\psi_g = -45^\circ$ .

near the tip of the peninsula to slightly cross-shore farther northeast) appears to have allowed the SBF to remain close to the coastline farther downstream (see Figure 4.16a).



**Figure 5.27** As in Figure 5.17a but for simulations with (a) the rounded peninsula and  $U_g = 5 \text{ m s}^{-1}$ , (b) the angled peninsula and  $U_g = 5 \text{ m s}^{-1}$ , (c) the angled peninsula and  $U_g = 10 \text{ m s}^{-1}$ , and (d) the standard peninsula and  $U_g = 10 \text{ m s}^{-1}$ .

## 5.5 Summary, discussion, and conclusions

This chapter has explored the behaviour of sea breezes over a simple peninsula using idealised numerical simulations. The study was motivated by the observation that under the right conditions, sea-breeze fronts forming along the Southwest Peninsula of the UK can become stationary. If lifting along the front is sufficient to trigger deep convection, a QSCS may result giving the potential for flash flooding. A necessary condition for these stationary SBFs appears to be a large-scale wind directed approximately parallel to the coastline. However, historically, only the shore-perpendicular component of the flow has been considered relevant to the inland propagation of the sea breeze.

Simulations were carried out using an idealised configuration of the Met Office Unified Model with  $1 \text{ km}$  horizontal grid spacing. A  $400 \times 100 \text{ km}$  island was used rather than a peninsula to reduce discontinuities at the fixed lateral boundaries. Vertical profiles of temperature and wind velocity were specified for the initial and boundary conditions while moisture was neglected. The temperature profile included three layers: a neutrally stratified boundary layer, a stably stratified free troposphere, and a stratosphere. The wind profile was initially specified as being constant in height but was allowed to adjust to the roughness of the sea surface. Geostrophic momentum forcing was applied to represent the effect of a uniform pressure gradient, and a diurnally varying heat flux was specified at the land surface. Runs were performed for a range of geostrophic wind

speeds  $U_g$  and directions  $\psi_g$ , and heat flux amplitudes  $H_{\max}$ . The sensitivity to changes in latitude  $\phi$ , mixed-layer depth  $h_{\text{ml}}$ , free-tropospheric stability  $\gamma_{\text{ft}}$ , and land surface roughness  $z_0$  was also investigated.

In the case of no ambient flow, sea breezes develop on all coastlines and move inland to converge at the centre of the peninsula. The collision of the longer north- and south-coast SBFs is accompanied by a sudden increase in maximum vertical velocity providing more favourable conditions for convective initiation. A similar collision of sea breezes over the Florida Peninsula in the USA frequently acts as the trigger for afternoon thunderstorms during the warm season (Byers and Rodebush 1948). The rate of propagation of the SBFs was found to be largely insensitive to changes in  $\phi$ ,  $h_{\text{ml}}$ ,  $\gamma_{\text{ft}}$ , and  $z_0$ , although larger vertical mass fluxes occur in the presence of a deeper mixed layer and weaker stability. On the other hand,  $H_{\max}$  has a strong influence on both the front velocity and updraught intensity, in agreement with previous studies (Crosman and Horel 2010).

Significant changes were found to occur in the presence of along-peninsula (westerly) flow. Air crossing the western edge of the peninsula warms as it travels downstream resulting in an along-shore temperature gradient which extends to a distance  $x^* = U(t - t_1)$ , where  $U$  is the wind speed,  $t$  is time, and  $t_1$  is the time at which heating commenced. This region is referred to as the adjustment zone (AZ). Farther downstream, the time taken for air to travel from the west coast exceeds the time since heating commenced; thus, the temperature here is constant in  $x$ . The AZ expands downstream with time while the temperature gradient within it varies across the diurnal cycle.

In response to the along-shore temperature gradient, the strength of the north- and south-coast sea breezes increases with distance in the AZ but is constant beyond  $x^*$ . A crucial finding is that the SBFs in the AZ remain virtually stationary throughout the day. This occurs despite the absence of a cross-shore wind (other than that due to frictional backing) to counteract the sea breeze. The reason is that the SBGs are advected downstream as they move inland. Consequently, the inland penetration of the SBFs within the AZ is limited to a distance which depends on the relative magnitude of the along-shore (background) and cross-shore (perturbation) flows. Since the latter increases with increasing  $x$ , the SBFs form arcs which gradually expand downstream as the AZ grows. Meanwhile, beyond  $x^*$  the inland penetration of the SBFs is limited only by time; thus, here they move inland parallel to the shoreline and eventually collide as in the no-flow case. Changes in both  $U_g$  and  $H_{\max}$  affect the evolution: an increase in  $U_g$  extends the AZ and thus increases the length of the quasi-stationary SBFs, while an increase in  $H_{\max}$  increases their curvature by driving stronger onshore flow. The sensitivity to other factors was again observed to be small.

These findings demonstrate that, contrary to suggestions from many previous studies, the along-shore component of the large-scale wind can play an important role in determining the inland propagation of the SBF. This will not only be true over peninsulas and elongated islands; any relatively straight stretch of coastline featuring a sharp

angle at one end will develop an along-shore temperature gradient when the wind blows from that direction (provided there is sufficient insolation and large-scale thermal advection is weak). It would be interesting to determine whether the behavior described above is observed in other parts of the UK and the world.

A method was developed to predict the inland movement of the SBFs in both the no-flow and along-peninsula-flow cases. This uses a modified scaling law to estimate the velocity of the front as a function of time and (in the along-peninsula-flow case) downstream distance based on the time-integrated heat flux. The resulting predictions were shown to be remarkably accurate. However, asymmetries between the north- and south-coast SBFs and an afternoon acceleration of the fronts observed for low values of  $H_{\max}$  could not be represented. There is scope for further refining this approach and it would be interesting to test its applicability to real sea breezes (e.g. over the UK Southwest Peninsula) whose behavior is complicated by coastline irregularities and horizontal and temporal variations in the background flow. It might also be useful in predicting the behavior of land breezes and the associated formation of snowbands over lakes (e.g. Niziol *et al.* 1995).

Results for cases with purely cross-shore geostrophic flow largely confirm previous findings. Under southerly flow, the south-coast sea breeze is dramatically weakened while the north-coast sea breeze intensifies and its inland penetration is retarded. For  $U_g = 4 \text{ m s}^{-1}$ , the north-coast SBF remains stationary along the coastline; this represents the so-called critical offshore wind speed  $U_{\text{crit}}$  (e.g. Porson *et al.* 2007a). Further increases in  $U_g$  beyond  $U_{\text{crit}}$  prevent the north-coast SBF from reaching the coastline and weaken the circulation. In agreement with previous studies, the value of  $U_{\text{crit}}$  is found to vary with the time-integrated heat flux, which in this case depends both on  $H_{\max}$  and the peninsula width  $W$ . However, this relationship appears to be more complicated than that suggested by Porson *et al.* (2007a), presumably due to the influence of the sea breeze from the opposing coast. Simulations with intermediate wind directions show a gradual transition in behavior from the along-shore to cross-shore regimes.

It is found that the evolution of the sea breezes depends strongly on the geometry of the peninsula. In particular, if the peninsula tapers towards its end, flow which is parallel to one coastline will have an onshore component on the other. This onshore flow can further limit the inland penetration of the sea breeze on the opposite coast. This effect likely influenced the persistence of the SBFs which triggered the Boscastle and 21 July 2010 QSCSs over the UK Southwest Peninsula, although along-shore variations in the ambient wind also appears to have been important in those cases.

From these results it is apparent that quasi-stationary SBFs may form via three basic mechanisms. The first, the *advection mechanism*, acts in case of primarily shore-parallel flow and is associated with the downstream advection of the sea breeze as it moves inland. This can only occur near the upstream edge of peninsulas or other ‘finite-length’ coastlines as described above. The second, the *collision mechanism*, acts farther downstream in the case of flow along a peninsula or in the presence of weak ( $\lesssim 3 \text{ m s}^{-1}$ ) cross-shore flow over any relatively narrow landmass, and is associated with the collision

of sea breezes from opposing coastlines. Finally, the *cancellation mechanism*, acts when the cross-shore flow is equal and opposite to the sea breeze so that the latter is unable to propagate inland. This can occur over any coastline, but is complicated for peninsulas or other narrow landmass by the sea breeze from the opposing coast. It seems plausible that any of these mechanisms could lead to the formation of a QSCS, provided the wind direction does not change significantly over time. In the Boscastle and 21 July 2010 events, it appears that both the advection and cancellation mechanisms operated: the former near the tip of the peninsula and the latter farther downstream where there was stronger offshore flow. However, in cases where stationary systems form close to the centre of the peninsula or downwind of it (see Figure 3.18), the collision mechanism may be dominant. Further investigation is needed to determine the role that sea breezes play in the formation of QSCSs in other parts of the UK and the world.

## Chapter 6

# Conclusions and future work

### 6.1 Conclusions

This thesis has investigated the physical and environmental characteristics, formation mechanisms, and numerical representation of quasi-stationary convective systems (QSCSs) in the UK. These systems occur when convective cells repeatedly initiate in approximately the same location and subsequently traverse similar paths in a process known as echo training. They may also be viewed as multicell convective systems in which the motion vector components associated with advection (the movement of existing cells) and propagation (the development of new cells) approximately cancel. QSCSs can produce extreme rainfall accumulations which may, depending on various hydrological factors, lead to flash flooding. This has been highlighted in a large number of previous studies of heavy precipitation events and flash floods. However, very little research has been done on these high-impact storms in the UK. Based on this knowledge gap, the following key questions were identified:

1. How common are QSCSs in the UK and how does their occurrence vary geographically, seasonally, diurnally, and with the large-scale meteorological conditions?
2. What are the typical mechanisms by which QSCSs in the UK develop and how well are these understood?
3. How well are QSCSs represented in a high-resolution NWP model?

The following sections will address each of these questions in turn based on the work presented in Chapters 3–5.

#### 6.1.1 Characteristics of QSCSs in the UK

In order to gain a better understanding of how frequently QSCSs occur, their temporal and spatial distributions, and the characteristics of the environments in which they form, a climatology was developed (Chapter 3). First, an algorithm was constructed to identify long-duration convective rain events (LDCREs) using gridded surface rainfall

data from the UK radar network. This was applied to five years' worth of data (2008–2012), resulting in a total of 525 identified events. Of these, 104 were rejected either because they were associated with non-convective precipitation or spurious radar echoes, or because of data quality issues. The remaining 421 were then subjectively placed into six different categories, one of which was QSCSs.

During the five-year period considered, 88 QSCSs were identified over the UK, surrounding waters and near continent, corresponding to a frequency of 17.6 per year. However, these were far from being evenly distributed in time: 75% occurred in the summer (June, July, and August) while none were identified between December and March. There was also significant interannual variability, with the number of events in the most active month of August varying from zero in 2009 to 13 in 2012. The vast majority of QSCSs occurred over land, forming during the early afternoon and dissipating in the late afternoon or early evening. This indicates a strong link with the diurnal cycle. Geographically, the events were widely distributed; however, they appeared to occur more frequently in close proximity to coastlines or areas of prominent orography. A region found to be particularly favourable for QSCS development was the Southwest Peninsula of England, with 13 events identified there during the five-year period. An interesting discovery was that over half (51%) of the events occurred within the same 24 h period as one or more other events. In some of these multi-event cases, the systems were widely separated in space suggesting a link to the large-scale flow.

Reanalysis data was used to examine the properties of the large-scale and local meteorological environments in which QSCSs occur. No particular synoptic patterns were found to favour QSCS formation in general; however, southwest-to-northeast orientated systems over the Southwest Peninsula all occurred in the presence of deep southwesterly flow associated with a trough to the west of the UK. A series of parameters were computed for each event and compared with those for all summertime convective events identified over the southern part of the UK during the same five-year period. The results showed that the environments in which QSCSs form on average feature higher values of convective available potential energy (CAPE) and weaker winds at all levels (with associated weaker shear and greater variability in wind direction). It was hypothesised that larger CAPE may be characteristic not of quasi-stationary storms, but simply those producing large rainfall, since a criterion for the identification of LDCREs was accumulations of at least 15 mm in 3 h. However, the CAPE distribution for events in the other five categories was found to be very similar to that for all convection. Thus, it seems that large CAPE favours the formation of QSCSs; the reasons for this are unclear and require further investigation. The presence of weaker winds may be indicative of the typical mechanisms by which QSCSs in the UK develop, something which is discussed further in the next section.

### 6.1.2 Formation mechanisms of QSCSs in the UK

Previous studies have highlighted many different mechanisms by which convection can be repeatedly initiated in roughly the same location to form a QSCS (see Section 1.3.3). These include mechanical lifting of air impinging on a topographic barrier, thermally driven convergence associated with surface inhomogeneities, isentropic upglide, forced ascent along outflow boundaries, and lifting by convectively generated gravity waves. It is desirable to know the relative contribution of these and other mechanisms to QSCS formation in the UK. Unfortunately, isolating the role of specific processes in the initiation and subsequent evolution of any convective system is a challenging task, and typically requires detailed analysis of high-resolution observations and/or numerical simulations (e.g. Lean *et al.* 2009). It was not feasible to undertake such an investigation for each of the 88 events identified in the climatology. However, some insight can be gleaned simply from the spatial distribution of the systems and the characteristics of their environments. Specifically, the tendency for QSCSs to occur in close proximity to coastlines and orographic features suggests that surface topography frequently plays a role in the repeated initiation of convection. Meanwhile, the predominance of weak winds in QSCS environments suggests that these systems may more commonly be caused by thermally driven circulations than mechanical orographic lifting.

Detailed investigation of a single case was performed in Chapter 4. The system, which occurred on 21 July 2010 over the Southwest Peninsula, showed remarkable similarity to the flash flood-producing Boscastle storm of 16 August 2010, but did not lead to flooding itself. An observation-based comparison of the two events showed that this difference in the hydrological response was associated with significantly lower rainfall totals in the 2010 case (itself a consequence of lower rain rates and a shorter storm duration) and distribution of the rainfall over more river catchments. To investigate the formation of the 2010 QSCS, numerical simulations were performed with the UKV ( $\Delta x = 1.5$  km) configuration of the Met Office Unified Model (UM). These revealed that, like the Boscastle storm, this QSCS was initiated and maintained by lifting along a quasi-stationary sea-breeze front (SBF). The inability of the SBF to propagate inland appeared to be due to a slight offshore-directed component in the ambient wind. For the Boscastle case, it had been suggested that frictional backing over land contributed to this offshore flow (Golding *et al.* 2005); however, the land–sea roughness contrast was not found to have any significant effect in the 2010 case. The same was true of convective outflow and the orography of the Southwest Peninsula.

To further investigate the formation of quasi-stationary SBFs, a series of high-resolution ( $\Delta x = 1$  km) idealised UM simulations were performed and analysed in Chapter 5. These utilised highly simplified topography, a diurnally-varying land surface heat flux of specified amplitude, and imposed vertical profiles of wind velocity and temperature (moisture was not included). The results highlighted three different ways in which SBFs over a peninsula can become quasi-stationary, termed the *advection*, *collision*, and *cancellation* mechanisms. In primarily shore-parallel flow, the sea breezes

which develop near the upstream tip of the peninsula are *advected* downstream as they advance inland, resulting in quasi-stationary SBFs which arc inland with downstream distance. The shape and length of these features was found to be strongly influenced by the wind speed and surface heat flux. Farther downstream, the sea breezes from opposing coasts *collide* forming another stationary zone of convergence and ascent. This also occurs when there is no background flow or a weak ( $\lesssim 3 \text{ m s}^{-1}$ ) cross-peninsula flow. Finally, when the ambient wind velocity has a significant shore-perpendicular component, *cancellation* can occur between this component and the sea breeze on the downstream coast, preventing the latter from propagating inland. The ‘critical’ wind speed at which this occurs depends primarily on the surface heat flux and the peninsula width. It appears that both the advection and cancellation mechanisms may have contributed to the formation of the quasi-stationary SBFs (and thus the QSCSs) in the Boscastle and 21 July 2010 events. In other cases where a QSCS formed near the centre of the Southwest Peninsula, the collision mechanism may have been more important.

Several previous studies (Steyn 1998; Tijn 1999; Steyn 2003; Porson *et al.* 2007b) have proposed scaling relations for the velocity of sea breezes in the absence of background flow. These were adapted for the case of along-peninsula flow using data from the idealised simulations to obtain an expression relating SBF velocity to the time-integrated surface heat flux. Integration of this expression was found to provide a remarkably accurate representation of the evolution of the SBFs under a range of wind speeds and heat fluxes. Although real coastlines and flows are significantly more complex than those considered here, the new scaling may have value as a tool for predicting the behaviour of sea breezes and the associated formation of convective storms.

### 6.1.3 Numerical representation of QSCSs in the UK

The question of how well QSCSs can be simulated is much like the question of how they form, in that it requires analysis of many cases to reach a conclusive answer. Nonetheless, some insight was gained through the case study simulations performed in Chapter 4. Specifically, it was found that the representation of the 21 July 2010 system was significantly improved when the model grid spacing was decreased from 1.5 km to 500 m. This can be attributed in part to the internal convective dynamical processes (updraughts, downdraughts, entrainment, etc.) being better resolved. However, in this case a more crucial factor appears to be the effect of model resolution on the SBF and its associated lifting. With 500 m grid spacing, the change in wind velocity across the SBF was able to occur over a smaller distance, resulting in stronger convergence and, by continuity, larger vertical velocities. This in turn allowed air parcels to more readily reach their level of free convection, promoting earlier and more frequent convective initiation which ultimately helped produce a more realistic-looking system.

This is an important result as it demonstrates that the highest resolutions currently used in operational NWP models may be insufficient to properly represent QSCSs (and other potentially high-impact convective systems) triggered along zones of boundary

layer convergence. In the 21 July 2010 case, the 1.5 km grid-length (UKV) model did capture the repeated initiation of cells, but underestimated the maximum rainfall totals by around a factor of two due to its poor representation of the system structure. However, in some cases, insufficient horizontal resolution can cause a convective event to be missed altogether (e.g. Barthlott *et al.* 2010). This motivates a continuing move towards higher resolution in forecast models.

## 6.2 Future work

There are many possibilities for taking the work presented here forward to further our understanding of and ability to predict QSCSs.

First, the analysis of the QSCS climatology presented in Chapter 3 could be extended. For example, other datasets could be incorporated to develop a better understanding of the characteristics of these events such as their typical cloud top heights (infrared satellite imagery), propensity to produce lightning (sferics), and hydrological impacts (flood reports and/or streamgauge data). It would be particularly interesting to know how many of the 88 identified systems produced flooding of some kind and, similarly, what fraction of flash flood events during the five-year period were caused by QSCSs. Following the approach in Section 3.6, one could also explore the characteristics and environments of the other five types of long-duration convective rain events.

The idealised modelling of peninsula sea breezes could also be taken further. In particular, it would be interesting to include moisture in the simulations to see when and where convection is initiated along the SBFs and what effects this has on their evolution. The complexity of the surface topography could also be increased, with more small-scale coastline details and/or variations in surface height (e.g. a ridge along the peninsula). As noted in the conclusions to Chapter 5, the sea-breeze scaling could also be developed further to represent the effects of non-zero cross-shore flow. Further insight into peninsula sea breezes will likely be gained from the analysis of observations made during the recent Convective Precipitation Experiment (COPE) which took place over the Southwest Peninsula in summer 2013 (<https://www.ncas.ac.uk/index.php/en/cope-home>).

It is worth exploring further the possibility of a fully automated algorithm for the identification of QSCSs. This could be used to extend the UK QSCS climatology or to develop similar climatologies for other countries/regions with good radar coverage. It could also be incorporated into an operational forecasting system to highlight areas of convection with the potential to cause flash flooding in the immediate future, before they produce significant rainfall. As discussed in Section 3.3, such an algorithm would need to be able to identify an approximately fixed initiation location associated with a particular system, or to infer the cancellation of the advection and propagation components of its movement. Diagnosis of initiation locations is possible with the use of a storm tracking algorithm, simply by considering the first point in the track history (e.g. Morel and Senesi 2002). However, if new cells develop in close proximity to the system they might

not be identified as separate entities; thus their initiation would be missed. The second method offers more promise, particularly since cell motion (advection) can already be accurately determined using the cross-correlation method (Section 3.2.4). Propagation would not be easy to diagnose; however, the total system motion could be estimated based on object tracking. A QSCS could then be identified as an object with near-zero system velocity but consistent cell motion. This algorithm could be tested by applying it to the same five-year dataset used here and then comparing the identified events with those in Section 3.6.

More work is needed to understand the mechanisms by which QSCSs in the UK are formed. As noted above, it would be unfeasible to perform a detailed analysis of all 88 cases in the climatology. However, one could investigate a subset of events that appeared to be associated with distinct initiation mechanisms based on their location or observed evolution. The findings of these case studies might then be generalised to similar events in other parts of the UK. Idealised simulations could also be used to explore the sensitivities of a particular mechanism as in Tucker and Crook (2005), Kirshbaum *et al.* (2007), and Bresson *et al.* (2012). However, local factors will always be important, particularly in the case of systems tied to surface topography. To more thoroughly investigate their role in the formation of QSCSs in the UK, one could perform a series of high-resolution, quasi-idealised simulations using the real surface topography but imposed profiles of wind velocity, temperature, and humidity. By varying the forcing within a realistic range, it should be possible to determine favourable locations for stationary systems at different times within the diurnal and seasonal cycles and under different large-scale conditions. Of course the parameter space for this problem is vast. When combined with the need for small horizontal grid spacing (in order to accurately represent topographic forcing and the convection itself), this makes such an investigation highly demanding of both time and computational resources. Nevertheless, it could provide a far more detailed picture of QSCSs in the UK than was possible in the present work.

The role of convective outflow in the formation and persistence of QSCSs is another topic which warrants further research. As discussed in Chapter 1, lifting along a stationary outflow boundary can provide a mechanism for repeated storm initiation in the same location. However, in other cases outflow may disrupt an external forcing mechanism thereby preventing a system from becoming quasi-stationary. Golding *et al.* (2005) hypothesised that the longevity of the Boscastle storm was related to the presence of “weak downdraughts which did not distort the coastal convergence line”. For the similar 21 July 2010 case studied in Chapter 4, the suppression of downdraught formation did not significantly influence the simulated system evolution; however, this may be because they were already relatively weak. It would be interesting to perform sensitivity experiments for these cases with downdraught intensity enhanced (e.g. by increasing the temperature change associated with rain evaporation) to see what effect (if any) this has. A factor which is likely to influence the interaction between convective outflow and a preexisting convergence zone is the cloud-layer wind velocity. Specifically,

the wind speed in the cloud-layer will determine the proximity of mature cells (and their outflow) to their initiation location, while its orientation relative to the convergence line will influence the supply of boundary layer air to developing cells. It is hypothesised that the most favourable configuration for long-lived QSCSs is moderate flow directed along a convergence line (as in the Boscastle and 21 July 2010 cases). This hypothesis could be tested through idealised simulations with low-level convergence either imposed directly or forced via inhomogeneous surface heating (c.f. the sea breeze simulations in Chapter 5).

A final topic for future research is the predictability of quasi-stationary storms and its relation to their formation mechanisms. In general, we would expect systems where the repeated initiation of cells is tied to surface topography to be more predictable than those associated with evolving atmospheric features, such as fronts, or internal forcing mechanisms. Two examples which fit with this hypothesis have been identified. First, for the Boscastle case, Leoncini *et al.* (2013) found a high degree of predictability based on an ensemble of high-resolution simulations containing both model-state perturbations and parameter modifications. Meanwhile, Schumacher *et al.* (2013) found strong sensitivity to initial and lateral boundary conditions in ensemble simulations of flash flood-producing MCSs in Texas and Arkansas, USA, whose formation was strongly tied to previous convective activity. Further such studies are needed to improve our understanding of the predictability of QSCSs and identify ways in which forecasts of these high-impact events can be improved.

# References

- Abbs DJ, Physick WL. 1992. Sea-breeze observations and modelling: A review. *Aust. Meteorol. Mag.* **41**: 7–19.
- Adler RF, Negri AJ. 1988. A satellite infrared technique to estimate tropical convective and stratiform rainfall. *J. Appl. Meteorol.* **27**: 30–51.
- Anagnostou EN. 2004. A convective/stratiform precipitation classification algorithm for volume scanning weather radar observations. *Meteorol. Appl.* **11**: 291–300.
- Antonelli M, Rotunno R. 2007. Large-eddy simulation of the onset of the sea breeze. *J. Atmos. Sci.* **64**: 4445–4457.
- Arakawa A, Lamb VR. 1977. Computational design of the basic dynamical processes of the UCLA general circulation model. *Methods Comp. Phys.* **17**: 173–265.
- Arritt RW. 1993. Effects of the large-scale flow on characteristic features of the sea breeze. *J. Appl. Meteorol.* **32**: 116–125.
- Atallah EH, Bosart LF. 2003. The extratropical transition and precipitation distribution of Hurricane Floyd (1999). *Mon. Wea. Rev.* **131**: 1063–1081.
- Atkins NT, Wakimoto RM, Weckwerth TM. 1995. Observations of the sea-breeze front during CaPE. Part II: Dual-Doppler and aircraft analysis. *Mon. Wea. Rev.* **123**: 944–969.
- Atlas D, Ulbrich CW, Marks FD, Black RA, Amitai E, Willis PT, Samsury CE. 2000. Partitioning tropical oceanic convective and stratiform rains by draft strength. *J. Geophys. Res.* **105**: 2259–2267.
- Austin PM, Bemis AC. 1950. A quantitative study of the "bright band" in radar precipitation echoes. *J. Meteorol.* **7**: 145–151.
- Awaka J, Iguchi T, Kumagai H, Okamoto K. 1997. Rain type classification algorithm for TRMM precipitation radar. In: *Proceedings of the International Geoscience and Remote Sensing Symposium*. Singapore, pp. 1633–1635.
- Baker LH, Gray SL, Clark PA. 2014. Idealised simulations of sting-jet cyclones. *Mon. Wea. Rev.* **140**: 96–110.

- Baldwin ME, Kain JS, Lakshmiarahan S. 2005. Development of an automated classification procedure for rainfall systems. *Mon. Wea. Rev.* **133**: 844–862.
- Banta RM. 1990. The role of mountain flows in making clouds. In: *Atmospheric Processes over Complex Terrain*, Meteorol. Monogr., American Meteorological Society, pp. 229–283.
- Barredo JI. 2007. Major flood disasters in Europe: 1950–2005. *Nat. Hazards* **42**: 125–148.
- Barthlott C, Kirshbaum DJ. 2013. Sensitivity of deep convection to terrain forcing over Mediterranean islands. *Q. J. R. Meteorol. Soc.* **139**: 1762–1779.
- Barthlott C, Schipper JW, Kalthoff N, Adler B, Kottmeier C, Blyth A, Mobbs S. 2010. Model representation of boundary-layer convergence triggering deep convection over complex terrain: A case study from COPS. *Atmos. Res.* **95**: 172–185.
- Bechtold P, Pinty JP, Mascart F. 1991. A numerical investigation of the influence of large-scale winds on sea-breeze- and inland-breeze-type circulations. *J. Appl. Meteorol.* **30**: 1268–1279.
- Bennett LJ, Browning KA, Blyth AM, Parker DJ, Clark PA. 2006. A review of the initiation of precipitating convection in the United Kingdom. *Q. J. R. Meteorol. Soc.* **132**: 1001–1020.
- Bergeron T. 1965. On the low-level redistribution of atmospheric water caused by orography. In: *Proceedings of the International Conference on Cloud Physics*. Tokyo, Japan, pp. 96–100.
- Best M. 2005. Canopy, surface and soil hydrology. Unified Model Documentation Paper 25, Met Office.
- Biggerstaff MI, Listemaa SA. 2000. An improved scheme for convective/stratiform echo classification using radar reflectivity. *J. Appl. Meteorol.* **39**: 2129–2150.
- Bluestein HB, Jain MH. 1985. Formation of mesoscale lines of precipitation: Severe squall lines in Oklahoma during the spring. *J. Atmos. Sci.* **42**: 1711–1732.
- Boer ER, Ramanathan V. 1997. Lagrangian approach for deriving cloud characteristics from satellite observations and its implications to cloud parameterization. *J. Geophys. Res.* **102**: 21 383–21 399.
- Bolton D. 1980. The computation of equivalent potential temperature. *Mon. Wea. Rev.* **108**: 1046–1053.
- Boutle IA, Belcher SE, Plant RS. 2011. Moisture transport in midlatitude cyclones. *Q. J. R. Meteorol. Soc.* **137**: 360–373.

- Bresson E, Ducrocq V, Nuissier O, Ricard D, de Saint-Aubin C. 2012. Idealized numerical simulations of quasi-stationary convective systems over the northwestern Mediterranean complex terrain. *Q. J. R. Meteorol. Soc.* **138**: 1751–1763.
- Browning KA, Eccleston AJ, Monk GA. 1985. The use of satellite and radar imagery to identify persistent shower bands downwind of the North Channel. *Meteorol. Mag.* **114**: 325–331.
- Brümmer B, Hennemuth B, Rhodin A, Thiemann S. 1995. Interaction of a cold front with a sea-breeze front: Observations. *Tellus A* **47**: 383–402.
- Bryan GH, Fritsch MJ. 2000. Moist absolute instability: The sixth static stability state. *Bull. Amer. Meteor. Soc.* **81**: 1207–1230.
- Bryan GH, Wyngaard JC, Fritsch JM. 2003. Resolution requirements for the simulation of deep moist convection. *Mon. Wea. Rev.* **131**: 2394–2416.
- Burt S. 2005. Cloudburst upon Hendrabortnick Down: The Boscastle storm of 16 August 2004. *Weather* **60**: 219–227.
- Bushell AC, Scaife AA, Warner CD. 2013. Non-orographic (spectral) gravity wave parametrization. Unified Model Documentation Paper 34, Met Office.
- Byers HR, Braham Jr RR. 1948. Thunderstorm structure and circulation. *J. Meteorol.* **5**: 71–86.
- Byers HR, Rodebush HR. 1948. Causes of thunderstorms of the Florida peninsula. *J. Meteorol.* **5**: 275–280.
- Caine S, Lane TP, May PT, Jakob C, Siems ST, Manton MJ, Pinto J. 2013. Statistical assessment of tropical convection-permitting model simulations using a cell-tracking algorithm. *Mon. Wea. Rev.* **141**: 557–581.
- Carley JR, Schwedler BR, Baldwin ME, Trapp RJ, Kwiatkowski J, Logsdon J, Weiss SJ. 2011. A proposed model-based methodology for feature-specific prediction for high-impact weather. *Wea. Forecasting* **26**: 243–249.
- Chappell CF. 1986. Quasi-stationary convective events. In: *Mesoscale Meteorology and Forecasting*, American Meteorological Society, pp. 289–310.
- Charney JG, Phillips NA. 1953. Numerical integration of the quasi-geostrophic equations for barotropic and simple baroclinic flows. *J. Meteorol.* **10**: 71–99.
- Charnock H. 1955. Wind stress on a water surface. *Q. J. R. Meteorol. Soc.* **81**: 639–640.
- Clark AJ, Weiss SJ, Kain JS, Jirak IL, Coniglio M, Melick CJ, Siewert C, Sobash RA, Marsh PT, Dean AR, Xue M, Kong F, Thomas KW, Wang Y, Brewster K, Gao J, Wang X, Du J, Novak DR, Barthold FE, Bodner MJ, Levit JJ, Entwistle CB,

- Jensen TL, Correia J. 2012. An overview of the 2010 Hazardous Weather Testbed Experimental Forecast Program Spring Experiment. *Bull. Amer. Meteor. Soc.* **93**: 55–74.
- Collier CG. 1996. *Applications of Weather Radar Systems*. Wiley, 2nd edn.
- Crosman ET, Horel JD. 2010. Sea and lake breezes: A review of numerical studies. *Boundary-Layer Meteorol.* **137**: 1–29.
- Davies T, Cullen MJP, Malcolm AJ, Mawson MH, Staniforth A, White AA, Wood N. 2005. A new dynamical core for the Met Office's global and regional modelling of the atmosphere. *Q. J. R. Meteorol. Soc.* **131**: 1759–1782.
- Davies T, Forbes R, Roadnight C, Beare B, Halliwell C. 2007. Running the unified model in idealised mode. Unified Model Documentation Paper 33, Met Office.
- Davis RS. 2001. Flash flood forecast and detection methods. In: *Severe Convective Storms*, Meteorol. Monogr., American Meteorological Society, pp. 481–525.
- de Rooy WC, Bechtold P, Fröhlich K, Hohenegger C, Jonker H, Mironov D, Pier Siebesma A, Teixeira J, Yano JI. 2013. Entrainment and detrainment in cumulus convection: An overview. *Q. J. R. Meteorol. Soc.* **139**: 1–19.
- Dee DP, Uppala SM, Simmons AJ, Berrisford P, Poli P, Kobayashi S, Andrae U, Balmaseda MA, Balsamo G, Bauer P, Bechtold P, Beljaars ACM, van de Berg L, Bidlot J, Bormann N, Delsol C, Dragani R, Fuentes M, Geer AJ, Haimberger L, Healy SB, Hersbach H, Hólm EV, Isaksen L, Kållberg P, Köhler M, Matricardi M, McNally AP, Monge-Sanz BM, Morcrette JJ, Park BK, Peubey C, de Rosnay P, Tavolato C, Thépaut JN, Vitart F. 2011. The ERA-Interim reanalysis: Configuration and performance of the data assimilation system. *Q. J. R. Meteorol. Soc.* **137**: 553–597.
- Dixon M, Wiener G. 1993. TITAN: Thunderstorm identification, tracking, analysis, and nowcasting—A radar-based methodology. *J. Atmos. Oceanic Technol.* **10**: 785–797.
- Doswell III CA. 1987. The distinction between large-scale and mesoscale contribution to severe convection: A case study example. *Wea. Forecasting* **2**: 3–16.
- Doswell III CA, Brooks HE, Maddox RA. 1996. Flash flood forecasting: An ingredients-based methodology. *Wea. Forecasting* **11**: 560–581.
- Doswell III CA, Rasmussen EN. 1994. The effect of neglecting the virtual temperature correction on CAPE calculations. *Wea. Forecasting* **9**: 625–629.
- Ducrocq V, Nuissier O, Ricard D, Lebeaupin C, Thouvenin T. 2008. A numerical study of three catastrophic precipitating events over southern France. II: Mesoscale triggering and stationarity factors. *Q. J. R. Meteorol. Soc.* **134**: 131–145.

- Edwards JM, Slingo A. 1996. Studies with a flexible new radiation code. I: Choosing a configuration for a large-scale model. *Q. J. R. Meteorol. Soc.* **122**: 689–719.
- Edwards JM, Thelen JC, Ingram WJ. 2004. The radiation code. Unified Model Documentation Paper 23, Met Office.
- Eisenstat SC, Elman HC, Schultz MH. 1983. Variational iterative methods for nonsymmetric systems of linear equations. *Siam J. Numer. Anal.* **20**: 345–357.
- Emanuel KA. 1994. *Atmospheric Convection*. Oxford University Press: New York, NY, USA.
- Essery RLH, Best MJ, Betts RA, Cox PM, Taylor CM. 2003. Explicit representation of subgrid heterogeneity in a GCM land surface scheme. *J. Hydrometeorol.* **4**: 530–543.
- Estoque MA. 1962. The sea breeze as a function of the prevailing synoptic situation. *J. Atmos. Sci.* **19**: 244–250.
- Evans JE, Ducot ER. 1994. The Integrated Terminal Weather System (ITWS). *The Lincoln Laboratory Journal* **7**: 449–474.
- Fankhauser JC. 1988. Estimates of thunderstorm precipitation efficiency from field measurements in CCOPE. *Mon. Wea. Rev.* **116**: 663–684.
- Foken T. 2006. 50 years of the Monin–Obukhov similarity theory. *Boundary-Layer Meteorol.* **119**: 431–447.
- Forbes GS, Merritt JH. 1984. Mesoscale vortices over the Great Lakes in wintertime. *Mon. Wea. Rev.* **112**: 377–381.
- Fovell RG. 2005. Convective initiation ahead of the sea-breeze front. *Mon. Wea. Rev.* **133**: 264–278.
- Fritsch JM, Chappell CF. 1980. Numerical prediction of convectively driven mesoscale pressure systems. Part II. Mesoscale model. *J. Atmos. Sci.* **37**: 1734–1762.
- Gagne DJ, McGovern A, Brotzge J. 2009. Classification of convective areas using decision trees. *J. Atmos. Oceanic Technol.* **26**: 1341–1353.
- Gallus Jr WA, Snook NA, Johnson EV. 2008. Spring and summer severe weather reports over the Midwest as a function of convective mode: A preliminary study. *Wea. Forecasting* **23**: 101–113.
- Garrat JR. 1992. *The atmospheric boundary layer*. Cambridge University Press.
- Golding B. 2005. Boscastle and north Cornwall post flood event study: Meteorological analysis of the conditions leading to flooding on 16 August 2004. Forecasting Research Technical Report 459, Met Office.

- Golding B, Clark P, May B. 2005. The Boscastle flood: Meteorological analysis of the conditions leading to flooding on 16 August 2004. *Weather* **60**: 230–235.
- Golding BW. 1998. Nimrod: A system for generating automated very short range forecasts. *Meteorol. Appl.* **5**: 1–16.
- Grant ALM. 2001. Cloud-base fluxes in the cumulus-capped boundary layer. *Q. J. R. Meteorol. Soc.* **127**: 407–421.
- Gray SL, Dacre HF. 2008. The impact of deformation strain on the formation of banded clouds in idealized modelling experiments. *Q. J. R. Meteorol. Soc.* **134**: 859–874.
- Gregory D, Inness P, Maidens A, Wong R, Stratton R. 2009. Convection scheme. Unified Model Documentation Paper 27, Met Office.
- Gregory D, Rowntree PR. 1990. A mass flux convection scheme with representation of cloud ensemble characteristics and stability-dependent closure. *Mon. Wea. Rev.* **118**: 1483–1506.
- Grisogono B, Ström L, Tjernström M. 1998. Small-scale variability in the coastal atmospheric boundary layer. *Boundary-Layer Meteorol.* **88**: 23–46.
- Gunn KLS, East TWR. 1954. The microwave properties of precipitation particles. *Q. J. R. Meteorol. Soc.* **80**: 522–545.
- Halliwel C. 2007. Subgrid turbulence scheme. Unified Model Documentation Paper 28, Met Office.
- Halliwel C, Lean H, Hanley K, Carter E, Stein T, McBeath K, Nicol J, Hogan R, Plant R. 2013. Progress report on comparisons of convection permitting models with observational data from dymecs and other sources. Technical report, Met Office.
- Han L, Fu S, Zhao L, Zheng Y, Wang H, Lin Y. 2009. 3D convective storm identification, tracking, and forecasting—An enhanced TITAN algorithm. *J. Atmos. Oceanic Technol.* **26**: 719–732.
- Hand WH. 2005. Climatology of shower frequency in the British Isles at 5 km resolution. *Weather* **60**: 153–158.
- Hand WH, Fox NI, Collier CG. 2004. A study of twentieth-century extreme rainfall events in the United Kingdom with implications for forecasting. *Meteorol. Appl.* **11**: 15–31.
- Hanley KE, Plant RS, Stein THM, Hogan RJ, Nicol JC, Lean HW, Halliwel C, Clark PA. 2014. Mixing-length controls on high-resolution simulations of convective storms. *Q. J. R. Meteorol. Soc.* doi:10.1002/qj.2356.
- Harrison DL, Gaussiat N, Pierce C, Norman K. 2012. Radar products for hydrological applications in the UK. *Proc. Inst. Civil Eng. – Water Manag.* **165**: 89–103.

- Harrison DL, Scovell RW, Kitchen M. 2009. High-resolution precipitation estimates for hydrological uses. *Proc. Inst. Civil Eng. – Water Manag.* **162**: 125–135.
- Hartmann DL, Hendon HH, Houze Jr RA. 1984. Some implications of the mesoscale circulations in tropical cloud clusters for large-scale dynamics and climate. *J. Atmos. Sci.* **41**: 113–121.
- Hohenegger C, Schär C. 2007. Predictability and error growth dynamics in cloud-resolving models. *J. Atmos. Sci.* **64**: 4467–4478.
- Holloway CE, Woolnough SJ, Lister GMS. 2012. Precipitation distributions for explicit versus parametrized convection in a large-domain high-resolution tropical case study. *Q. J. R. Meteorol. Soc.* **138**: 1692–1708.
- Hong Y, Kummerow CD, Olson WS. 1999. Separation of convective and stratiform precipitation using microwave brightness temperature. *J. Appl. Meteorol.* **38**: 1195–1213.
- Houghton HG. 1968. On precipitation mechanisms and their artificial modification. *J. Appl. Meteorol.* **7**: 851–859.
- Houze Jr RA. 1997. Stratiform precipitation in regions of convection: A meteorological paradox? *Bull. Amer. Meteor. Soc.* **78**: 2179–2196.
- Houze Jr RA. 2004. Mesoscale convective systems. *Rev. Geophys.* **42**.
- Hoxit LR, Maddox RA, Chappell CF, Zuckerberg FL, Mogil HM, Jones I, Green DR, Scaiffle RE, Scofield RA. 1978. Meteorological Analysis of the Johnstown, Pennsylvania flash flood, 19-20 July 1977. Technical Report ERL 401-APCL 43, NOAA.
- James RP, Markowski PM. 2010. A numerical investigation of the effects of dry air aloft on deep convection. *Mon. Wea. Rev.* **138**: 140–161.
- Jessup SM, Colucci SJ. 2012. Organization of flash-flood-producing precipitation in the northeast United States. *Wea. Forecasting* **27**: 345–361.
- Johnson JT, MacKeen PL, Witt A, Mitchell EDW, Stumpf GJ, Eilts MD, Thomas KW. 1998. The Storm Cell Identification and Tracking Algorithm: An enhanced WSR-88D algorithm. *Wea. Forecasting* **13**: 263–276.
- Jones CD, Macpherson B. 1997. A latent heat nudging scheme for the assimilation of precipitation data into an operational mesoscale model. *Meteorol. Appl.* **4**: 269–277.
- Jonkman SN. 2005. Global perspectives on loss of human life caused by floods. *Nat. Hazards* **34**: 151–175.
- Junker NW, Schneider RS, Fauver SL. 1999. A study of heavy rainfall events during the great Midwest flood of 1993. *Wea. Forecasting* **14**: 701–712.

- Kalman RE. 1960. A new approach to linear filtering and prediction problems. *Trans. AMSE—J. Basic Eng.* **82**: 35–45.
- Kato T, Goda H. 2001. Formation and maintenance processes of a stationary band-shaped heavy rainfall observed in Niigata on 4 August 1998. *J. Meteorol. Soc. Japan* **79**: 899–924.
- Kelway PS. 1975. The rainfall recorder problem. *J. Hydrol.* **26**: 55–77.
- Kim HW, Lee DK. 2006. An observational study of mesoscale convective systems with heavy rainfall over the Korean Peninsula. *Wea. Forecasting* **21**: 125–148.
- Kingsmill DE. 1995. Convection initiation associated with a sea-breeze front, a gust front, and their collision. *Mon. Wea. Rev.* **123**: 2913–2933.
- Kirkpatrick C, McCaul EW, Cohen C. 2011. Sensitivities of simulated convective storms to environmental CAPE. *Mon. Wea. Rev.* **139**: 3514–3532.
- Kirshbaum DJ, Bryan GH, Rotunno R, Durran DR. 2007. The triggering of orographic rainbands by small-scale topography. *J. Atmos. Sci.* **64**: 1530–1549.
- Kirshbaum DJ, Durran DR. 2005. Atmospheric factors governing banded orographic convection. *J. Atmos. Sci.* **62**: 3758–3774.
- Kitchen M, Brown R, Davies AG. 1994. Real-time correction of weather radar data for the effects of bright band, range and orographic growth in widespread precipitation. *Q. J. R. Meteorol. Soc.* **120**: 1231–1254.
- Kodama K, Barnes GM. 1997. Heavy rain events over the south-facing slopes of Hawaii: Attendant conditions. *Wea. Forecasting* **12**: 347–367.
- Lack SA, Fox NI. 2012. Development of an automated approach for identifying convective storm type using reflectivity-derived and near-storm environment data. *Atmos. Res.* **116**: 67–81.
- Laird NF, Walsh JE, Kristovich DA. 2003. Model simulations examining the relationship of lake-effect morphology to lake shape, wind direction, and wind speed. *Mon. Wea. Rev.* **131**: 2102–2111.
- Lakshmanan V. 2012. *Automating the Analysis of Spatial Grids: A Practical Guide to Data Mining Geospatial Images for Human and Environmental Applications*. Springer.
- Lakshmanan V, Hondl K, Rabin R. 2009. An efficient, general-purpose technique for identifying storm cells in geospatial images. *J. Atmos. Oceanic Technol.* **26**: 523–537.
- Lakshmanan V, Rabin R, DeBrunner V. 2003. Multiscale storm identification and forecast. *Atmos. Res.* **67**: 367–380.

- Lakshmanan V, Smith T. 2010. An objective method of evaluating and devising storm-tracking algorithms. *Wea. Forecasting* **25**: 701–709.
- Lean HW, Browning KA. 2013. Quantification of the importance of wind drift to the surface distribution of orographic rain on the occasion of the extreme Cockermouth flood in Cumbria. *Q. J. R. Meteorol. Soc.* **139**: 1342–1353.
- Lean HW, Clark PA, Dixon M, Roberts NM, Fitch A, Forbes R, Halliwell C. 2008. Characteristics of high-resolution versions of the Met Office Unified Model for forecasting convection over the United Kingdom. *Mon. Wea. Rev.* **136**: 3408–3424.
- Lean HW, Roberts NM, Clark PA, Morcrette C. 2009. The surprising role of orography in the initiation of an isolated thunderstorm in southern England. *Mon. Wea. Rev.* **137**: 3026–3046.
- Leoncini G, Plant RS, Gray SL, Clark PA. 2013. Ensemble forecasts of a flood-producing storm: Comparison of the influence of model-state perturbations and parameter modifications. *Q. J. R. Meteorol. Soc.* **139**: 198–211.
- Lilly DK. 1967. The representation of small-scale turbulence in numerical simulation experiments. In: *Proceedings of the IBM Scientific Symposium on Environmental Sciences*. Yorktown Heights, NY, USA, pp. 195–210.
- Lin YL, Chiao S, Wang TA, Kaplan ML, Weglarz RP. 2001. Some common ingredients for heavy orographic rainfall. *Wea. Forecasting* **16**: 633–660.
- Lock A. 2007. The parametrization of boundary layer processes. Unified Model Documentation Paper 24, Met Office.
- Lock AP. 2001. The numerical representation of entrainment in parameterizations of boundary layer turbulent mixing. *Mon. Wea. Rev.* **129**: 1148–1163.
- Lock AP, Brown AR, Bush MR, Martin GM, Smith RNB. 2000. A new boundary layer mixing scheme. Part I: Scheme description and single-column model tests. *Mon. Wea. Rev.* **128**: 3187–3199.
- Lorenz EN. 1969. The predictability of a flow which possesses many scales of motion. *Tellus* **21**: 289–307.
- Luo Y, Gong Y, Zhang DL. 2014. Initiation and organizational modes of an extreme-rain-producing mesoscale convective system along a mei-yu front in East China. *Mon. Wea. Rev.* **142**: 203–221.
- Lyman RE, Schroeder TA, Barnes GM. 2005. The heavy rain event of 29 October 2000 in Hana, Maui. *Wea. Forecasting* **20**: 397–414.
- Machado LAT, Rossow WB, Guedes RL, Walker AW. 1998. Life cycle variations of mesoscale convective systems over the Americas. *Mon. Wea. Rev.* **126**: 1630–1654.

- Maddox RA, Chappell CF, Hoxit LR. 1979. Synoptic and meso- $\alpha$  scale aspects of flash flood events. *Bull. Amer. Meteor. Soc.* **60**: 115–123.
- Maddox RA, Hoxit LR, Chappell CF, Caracena F. 1978. Comparison of meteorological aspects of the Big Thompson and Rapid City flash floods. *Mon. Wea. Rev.* **106**: 375–389.
- Markowski P, Richardson Y. 2010. *Mesoscale Meteorology in Midlatitudes*. Wiley–Blackwell.
- Marshall JS, Palmer WMK. 1948. The distribution of raindrops with size. *J. Meteorol.* **5**: 165–166.
- Martín A, Romero R, De Luque A, Alonso S, Rigo T, Llasat MC. 2007. Sensitivities of a flash flood event over Catalonia: A numerical analysis. *Mon. Wea. Rev.* **135**: 651–669.
- Mastrangelo D, Horvath K, Riccio A, Miglietta MM. 2011. Mechanisms for convection development in a long-lasting heavy precipitation event over southeastern Italy. *Atmos. Res.* **100**: 586–602.
- Mathon V, Laurent H. 2001. Life cycle of Sahelian mesoscale convective cloud systems. *Q. J. R. Meteorol. Soc.* **127**: 377–406.
- Mayes J, Winterton J. 2008. The west Surrey thunderstorm of 13 August 2006. *Weather* **63**: 50–55.
- McBeath K, Field PR, Cotton RJ. 2014. Using operational weather radar to assess high-resolution numerical weather prediction over the British Isles for a cold air outbreak case-study. *Q. J. R. Meteorol. Soc.* **140**: 225–239.
- McCaul Jr EW, Cohen C. 2002. The impact on simulated storm structure and intensity of variations in the mixed layer and moist layer depths. *Mon. Wea. Rev.* **130**: 1722–1748.
- McPherson RD. 1970. A numerical study of the effect of a coastal irregularity on the sea breeze. *J. Appl. Meteorol.* **9**: 767–777.
- Melhauser C, Zhang F. 2012. Practical and intrinsic predictability of severe and convective weather at the mesoscales. *J. Atmos. Sci.* **69**: 3350–3371.
- Metzger J, Barthlott C, Kalthoff N. 2014. Impact of upstream flow conditions on the initiation of moist convection over the island of Corsica. *Atmos. Res.* doi:10.1016/j.atmosres.2014.04.011.
- Miglietta MM, Regano A. 2008. An observational and numerical study of a flash-flood event over south-eastern Italy. *Nat. Hazards Earth Syst. Sci.* **8**: 1417–1430.

- Miller MJ. 1978. The Hampstead storm: A numerical simulation of a quasi-stationary cumulonimbus system. *Q. J. R. Meteorol. Soc.* **104**: 413–427.
- Miller STK, Keim BD, Talbot RW, Mao H. 2003. Sea breeze: Structure, forecasting, and impacts. *Rev. Geophys.* **41**.
- Moore BJ, Neiman PJ, Ralph FM, Barthold FE. 2012. Physical processes associated with heavy flooding rainfall in Nashville, Tennessee, and vicinity during 1–2 May 2010: The role of an atmospheric river and mesoscale convective systems. *Mon. Wea. Rev.* **140**: 358–378.
- Moore JT, Glass FH, Graves CE, Rochette SM, Singer MJ. 2003. The environment of warm-season elevated thunderstorms associated with heavy rainfall over the central United States. *Wea. Forecasting* **18**: 861–878.
- Morel C, Senesi S. 2002. A climatology of mesoscale convective systems over Europe using satellite infrared imagery. II: Characteristics of European mesoscale convective systems. *Q. J. R. Meteorol. Soc.* **128**: 1973–1995.
- Niziol TA, Snyder WR, Waldstreicher JS. 1995. Winter weather forecasting throughout the eastern United States. Part IV: Lake effect snow. *Wea. Forecasting* **10**: 61–77.
- Nuissier O, Ducrocq V, Ricard D, Lebeaupin C, Anquetin S. 2008. A numerical study of three catastrophic precipitating events over southern France. I: Numerical framework and synoptic ingredients. *Q. J. R. Meteorol. Soc.* **134**: 111–130.
- Ogawa S, Sha W, Iwasaki T, Wang Z. 2003. A numerical study on the interaction of a sea-breeze front with convective cells in the daytime boundary layer. *J. Meteorol. Soc. Japan* **81**: 635–651.
- Pankiewicz GS. 1997. Neural network classification of convective airmasses for a flood forecasting system. *Int. J. Remote Sensing* **18**: 887–898.
- Passarelli Jr RE, Braham Jr RR. 1981. The role of the winter land breeze in the formation of Great Lake snow storms. *Bull. Amer. Meteor. Soc.* **62**: 482–492.
- Pastor F, Gómez I, Estrela MJ. 2010. Numerical study of the October 2007 flash flood in the Valencia region (Eastern Spain): The role of orography. *Nat. Hazards Earth Syst. Sci.* **10**: 1331–1345.
- Peak JE, Tag PM. 1994. Segmentation of satellite imagery using hierarchical thresholding and neural networks. *J. Appl. Meteorol.* **33**: 605–616.
- Petersen WA, Carey LD, Rutledge SA, Knievel JC, Johnson RH, Doesken NJ, McKee TB, Vonder Haar T, Weaver JF. 1999. Mesoscale and radar observations of the Fort Collins flash flood of 28 July 1997. *Bull. Amer. Meteor. Soc.* **80**: 191–216.

- Pierce CE, Hardaker PJ, Collier CG, Haggett CM. 2000. GANDOLF: A system for generating automated nowcasts of convective precipitation. *Meteorol. Appl.* **7**: 341–360.
- Pontrelli MD, Bryan G, Fritsch JM. 1999. The Madison County, Virginia, flash flood of 27 June 1995. *Wea. Forecasting* **14**: 384–404.
- Porson A, Steyn DG, Schayes G. 2007a. Formulation of an index for sea breezes in opposing winds. *J. Appl. Meteorol. Climatol.* **46**: 1257–1263.
- Porson A, Steyn DG, Schayes G. 2007b. Sea-breeze scaling from numerical model simulations, Part I: Pure sea breezes. *Boundary-Layer Meteorol.* **122**: 17–29.
- Price C, Yair Y, Mugnai A, Lagouvardos K, Llasat MC, Michaelides S, Dayan U, Dietrich S, Galanti E, Garrote L, Harats N, Katsanos D, Kohn M, Kotroni V, Llasat-Botija M, Lynn B, Mediero L, Morin E, Nicolaidis K, Rozalis S, Savvidou K, Ziv B. 2011. The FLASH Project: Using lightning data to better understand and predict flash floods. *Environ. Sci. Policy* **14**: 898–911.
- Renshaw R, Francis PN. 2011. Variational assimilation of cloud fraction in the operational Met Office Unified Model. *Q. J. R. Meteorol. Soc.* **137**: 1963–1974.
- Ricard D, Ducrocq V, Auger L. 2012. A climatology of the mesoscale environment associated with heavily precipitating events over a northwestern Mediterranean area. *J. Appl. Meteorol. Climatol.* **51**: 468–488.
- Rinehart RE, Garvey ET. 1978. Three-dimensional storm motion detection by conventional weather radar. *Nature* **273**: 287–289.
- Roberts NM, Lean HW. 2008. Scale-selective verification of rainfall accumulations from high-resolution forecasts of convective events. *Mon. Wea. Rev.* **136**: 78–97.
- Robinson FJ, Patterson MD, Sherwood SC. 2013. A numerical modeling study of the propagation of idealized sea-breeze density currents. *J. Atmos. Sci.* **70**: 653–668.
- Romero R, Doswell III CA, Ramis C. 2000. Mesoscale numerical study of two cases of long-lived quasi-stationary convective systems over eastern Spain. *Mon. Wea. Rev.* **128**: 3731–3751.
- Rosenfeld D, Amitai E, Wolff DB. 1995. Classification of rain regimes by the three-dimensional properties of reflectivity fields. *J. Appl. Meteorol.* **34**: 198–211.
- Rusjan S, Kobold M, Mikoš M. 2009. Characteristics of the extreme rainfall event and consequent flash floods in W Slovenia in September 2007. *Nat. Hazards Earth Syst. Sci.* **9**: 947–956.
- Scaife AA, Butchart N, Warner CD, Swinbank R. 2002. Impact of a spectral gravity wave parameterization on the stratosphere in the Met Office Unified Model. *J. Atmos. Sci.* **59**: 1473–1489.

- Schmidli J, Billings B, Chow FK, de Wekker SF, Doyle J, Grubišić V, Holt T, Jiang Q, Lundquist KA, Sheridan P, Vosper S, Whiteman CD, Wyszogrodzki AA, Zängl G. 2011. Intercomparison of mesoscale model simulations of the daytime valley wind system. *Mon. Wea. Rev.* **139**: 1389–1409.
- Schumacher RS. 2009. Mechanisms for quasi-stationary behavior in simulated heavy-rain-producing convective systems. *J. Atmos. Sci.* **66**: 1543–1568.
- Schumacher RS, Clark AJ, Xue M, Kong F. 2013. Factors influencing the development and maintenance of nocturnal heavy-rain-producing convective systems in a storm-scale ensemble. *Mon. Wea. Rev.* **141**: 2778–2801.
- Schumacher RS, Johnson RH. 2005. Organization and environmental properties of extreme-rain-producing mesoscale convective systems. *Mon. Wea. Rev.* **133**: 961–976.
- Schumacher RS, Johnson RH. 2006. Characteristics of US extreme rain events during 1999–2003. *Wea. Forecasting* **21**: 69–85.
- Schumacher RS, Johnson RH. 2008. Mesoscale processes contributing to extreme rainfall in a midlatitude warm-season flash flood. *Mon. Wea. Rev.* **136**: 3964–3986.
- Schwartz BE, Chappell CF, Togstad WE, Zhong XP. 1990. The Minneapolis flash flood: Meteorological analysis and operational response. *Wea. Forecasting* **5**: 3–21.
- Segal M, Leuthold M, Arritt RW, Anderson C, Shen J. 1997. Small lake daytime breezes: Some observational and conceptual evaluations. *Bull. Amer. Meteor. Soc.* **78**: 1135–1147.
- Seko H, Kato T, Saito K, Yoshizaki M, Kusunoki KI, Maki M. 1999. Analytical and numerical studies of a quasi-stationary precipitation band observed over the Kanto area associated with Typhoon 9426 (Orchid). *J. Meteorol. Soc. Japan* **77**: 929–948.
- Sénési S, Bougeault P, Chêze JL, Cosentino P, Thepenier RM. 1996. The Vaison-La-Romaine flash flood: Mesoscale analysis and predictability issues. *Wea. Forecasting* **11**: 417–442.
- Sha W, Kawamura T, Ueda H. 1991. A numerical study on sea/land breezes as a gravity current: Kelvin-Helmholtz billows and inland penetration of the sea-breeze front. *J. Atmos. Sci.* **48**: 1649–1665.
- Sha W, Kawamura T, Ueda H. 1993. A numerical study of nocturnal sea breezes: Pre-frontal gravity waves in the compensating flow and inland penetration of the sea-breeze cutoff vortex. *J. Atmos. Sci.* **50**: 1076–1088.
- Shepherd DJ, Colquhoun JR. 1985. Meteorological aspects of an extraordinary flash flood event near Dapto, New South Wales. *Aust. Meteorol. Mag.* **33**: 87–102.

- Sibley A. 2009. Coastal thunderstorms in Kent 21 August 2007. *Weather* **64**: 199–203.
- Sibley A. 2010. Analysis of extreme rainfall and flooding in Cumbria 18–20 November 2009. *Weather* **65**: 287–292.
- Simpson JE. 1994. *Sea Breeze and Local Wind*. Cambridge University Press.
- Simpson JE, Mansfield DA, Milford JR. 1977. Inland penetration of sea-breeze fronts. *Q. J. R. Meteorol. Soc.* **103**: 47–76.
- Skamarock WC, Smolarkiewicz PK, Klemp JB. 1997. Preconditioned conjugate-residual solvers for Helmholtz equations in nonhydrostatic models. *Mon. Wea. Rev.* **125**: 587–599.
- Smagorinsky J. 1963. General circulation experiments with the primitive equations: I. The basic experiment. *Mon. Wea. Rev.* **91**: 99–164.
- Smith JA, Baeck ML, Zhang Y, Doswell III CA. 2001. Extreme rainfall and flooding from supercell thunderstorms. *J. Hydrometeorol.* **2**: 469–489.
- Smith RNB. 1990. A scheme for predicting layer clouds and their water content in a general circulation model. *Q. J. R. Meteorol. Soc.* **116**: 435–460.
- Smolarkiewicz PK, Margolin LG. 1994. Variational elliptic solver for atmospheric applications. Technical Report LA-12712-MS, Los Alamos National Laboratory.
- Soderholm B, Ronalds B, Kirshbaum DJ. 2014. The evolution of convective storms initiated by an isolated mountain ridge. *Mon. Wea. Rev.* **142**: 1430–1451.
- Staniforth A, White A, Wood N, Thuburn J, Zerroukat M, Cordero E, Davies T, Diamantakis M. 2006. Joy of U.M. 6.3. – Model formulation. Unified Model Documentation Paper 15, Met Office.
- Steenburgh WJ, Onton DJ. 2001. Multiscale analysis of the 7 December 1998 Great Salt Lake-effect snowstorm. *Mon. Wea. Rev.* **129**: 1296–1317.
- Steiner M, Houze Jr RA, Yuter SE. 1995. Climatological characterization of three-dimensional storm structure from operational radar and rain gauge data. *J. Appl. Meteorol.* **34**: 1978–2007.
- Steyn DG. 1998. Scaling the vertical structure of sea breezes. *Boundary-Layer Meteorol.* **86**: 505–524.
- Steyn DG. 2003. Scaling the vertical structure of sea breezes revisited. *Boundary-Layer Meteorol.* **107**: 177–188.
- Strangeways IC. 1996. Back to basics: The ‘met. enclosure’: Part 2 (b) – Raingauges, their errors. *Weather* **51**: 298–303.

- Stull RB. 1988. *An Introduction to Boundary Layer Meteorology*. Kluwer Academic Publishers.
- Sui CH, Tsay CT, Li X. 2007. Convective–stratiform rainfall separation by cloud content. *J. Geophys. Res.* **112**.
- Sun J, Lee TY. 2002. A numerical study of an intense quasi-stationary convection band over the Korean Peninsula. *J. Meteorol. Soc. Japan* **80**: 1221–1245.
- Tang Y, Lean HW, Bornemann J. 2013. The benefits of the Met Office variable resolution NWP model for forecasting convection. *Meteorol. Appl.* **20**: 417–426.
- Tao WK, Lang S, Simpson J, Adler R. 1993a. Retrieval algorithms for estimating the vertical profiles of latent heat release: Their applications for TRMM. *J. Meteorol. Soc. Japan* **71**: 685–700.
- Tao WK, Simpson J, Sui CH, Ferrier B, Lang S, Scala J, Chou MD, Pickering K. 1993b. Heating, moisture, and water budgets of tropical and midlatitude squall lines: Comparisons and sensitivity to longwave radiation. *J. Atmos. Sci.* **50**: 673–690.
- Tijm ABC. 1999. Sea-breeze studies. PhD thesis, University of Utrecht.
- Tijm ABC, van Delden AJ. 1999. The role of sound waves in sea-breeze initiation. *Q. J. R. Meteorol. Soc.* **125**: 1997–2018.
- Tijm ABC, van Delden AJ, Holtslag AAM. 1999. The inland penetration of sea breezes. *Contrib. Atmos. Phys.* **72**: 317–328.
- Tokay A, Short DA. 1996. Evidence from tropical raindrop spectra of the origin of rain from stratiform versus convective clouds. *J. Appl. Meteorol.* **35**: 355–371.
- Tucker DF, Crook NA. 2005. Flow over heated terrain. Part II: Generation of convective precipitation. *Mon. Wea. Rev.* **133**: 2565–2582.
- Ulbrich CW, Atlas D. 2002. On the separation of tropical convective and stratiform rains. *J. Appl. Meteorol.* **41**: 188–195.
- Vila DA, Machado LAT, Laurent H, Velasco I. 2008. Forecast and Tracking the evolution of Cloud Clusters (ForTraCC) Using satellite infrared imagery: Methodology and validation. *Wea. Forecasting* **23**: 233–245.
- Warner CD, McIntyre ME. 2001. An ultrasimple spectral parameterization for nonorographic gravity waves. *J. Atmos. Sci.* **58**: 1837–1857.
- Warren RA, Kirshbaum DJ, Plant RS, Lean HW. 2014. A ‘Boscastle-type’ quasi-stationary convective system over the UK Southwest Peninsula. *Q. J. R. Meteorol. Soc.* **140**: 240–257.

- Webster S. 2004. Gravity wave drag. Unified Model Documentation Paper 22, Met Office.
- Webster S, Brown AR, Cameron DR, Jones CP. 2003. Improvements to the representation of orography in the Met Office Unified Model. *Q. J. R. Meteorol. Soc.* **129**: 1989–2010.
- Weisman ML, Klemp JB. 1982. The dependence of numerically simulated convective storms on vertical wind shear and buoyancy. *Mon. Wea. Rev.* **110**: 504–520.
- Wichink Kruit RJ, Holtslag AAM, Tijn ABC. 2004. Scaling of the sea-breeze strength with observations in the Netherlands. *Boundary-Layer Meteorol.* **112**: 369–380.
- Wiernga J. 1993. Representative roughness parameters for homogeneous terrain. *Boundary-Layer Meteorol.* **63**: 323–363.
- Wilkinson J, Wilson D, Forbes R. 2010. The large-scale precipitation parametrization scheme. Unified Model Documentation Paper 26, Met Office.
- Wilks DS. 2011. *Statistical methods in the atmospheric sciences*. Academic Press, 3rd edn.
- Williams M, Houze Jr RA. 1987. Satellite-observed characteristics of winter monsoon cloud clusters. *Mon. Wea. Rev.* **115**: 505–519.
- Wilson D, Morcrette C. 2010. The large-scale cloud scheme and saturated specific humidity. Unified Model Documentation Paper 29, Met Office.
- Wilson DR, Ballard SP. 1999. A microphysically based precipitation scheme for the UK Meteorological Office Unified Model. *Q. J. R. Meteorol. Soc.* **125**: 1607–1636.
- Wilson DR, Bushell AC, Kerr-Munslow AM, Price JD, Morcrette CJ. 2008. PC2: A prognostic cloud fraction and condensation scheme. I: Scheme description. *Q. J. R. Meteorol. Soc.* **134**: 2093–2107.
- Wilson JW, Foote GB, Crook NA, Fankhauser JC, Wade CG, Tuttle JD, Mueller CK, Krueger SK. 1992. The role of boundary-layer convergence zones and horizontal rolls in the initiation of thunderstorms: A case study. *Mon. Wea. Rev.* **120**: 1785–1815.
- Wilson JW, Schreiber WE. 1986. Initiation of convective storms at radar-observed boundary-layer convergence lines. *Mon. Wea. Rev.* **114**: 2516–2536.
- Wilson JW, Weckwerth TM, Vivekanandan J, Wakimoto RM, Russell RW. 1994. Boundary layer clear-air radar echoes: Origin of echoes and accuracy of derived winds. *J. Atmos. Oceanic Technol.* **11**: 1184–1206.
- Wulfmeyer V, Behrendt A, Bauer HS, Kottmeier C, Corsmeier U, Blyth A, Craig G, Schumann U, Hagen M, Crewell S, Di Girolamo P, Flamant C, Miller M, Montani

- A, Mobbs S, Richard E, Rotach MW, Arpagaus M, Russchenberg H, Schlüssel P, König M, Gärtner V, Steinacker R, Dorninger M, Turner DD, Weckwerth T, Hense A, Simmer C. 2008. The Convective and Orographically induced Precipitation Study. *Bull. Amer. Meteor. Soc.* **89**: 1477–1486.
- Xu KM. 1995. Partitioning mass, heat, and moisture budgets of explicitly simulated cumulus ensembles into convective and stratiform components. *J. Atmos. Sci.* **52**: 551–573.
- Yang Y, Chen X, Qi Y. 2013. Classification of convective/stratiform echoes in radar reflectivity observations using a fuzzy logic algorithm. *J. Geophys. Res.* **118**: 1896–1905.
- Yoshikado H. 1992. Numerical study of the daytime urban effect and its interaction with the sea breeze. *J. Appl. Meteorol.* **31**: 1146–1164.
- Young M. 2011. Torrential downpours in southern England 15 September 2009. *Weather* **66**: 231–234.
- Yuter SE, Houze Jr RA. 1995. Three-dimensional kinematic and microphysical evolution of Florida cumulonimbus. Part II: Frequency distributions of vertical velocity, reflectivity, and differential reflectivity. *Mon. Wea. Rev.* **123**: 1941–1963.
- Zhang F, Bei N, Rotunno R, Snyder C, Epifanio CC. 2007. Mesoscale predictability of moist baroclinic waves: Convection-permitting experiments and multistage error growth dynamics. *J. Atmos. Sci.* **64**: 3579–3594.
- Zhang F, Odins AM, Nielsen-Gammon JW. 2006. Mesoscale predictability of an extreme warm-season precipitation event. *Wea. Forecasting* **21**: 149–166.
- Zhang F, Snyder C, Rotunno R. 2003. Effects of moist convection on mesoscale predictability. *J. Atmos. Sci.* **60**: 1173–1185.
- Zhang M, Zhang DL. 2012. Subkilometer simulation of a torrential-rain-producing mesoscale convective system in east China. Part I: Model verification and convective organization. *Mon. Wea. Rev.* **140**: 184–201.
- Zhong S, Leone Jr JM, Takle ES. 1991. Interaction of the sea breeze with a river breeze in an area of complex coastal heating. *Boundary-Layer Meteorol.* **56**: 101–139.